



University of Bradford eThesis

This thesis is hosted in [Bradford Scholars](#) – The University of Bradford Open Access repository. Visit the repository for full metadata or to contact the repository team



© University of Bradford. This work is licenced for reuse under a [Creative Commons Licence](#).

Acoustic and Thermal Properties of Recycled Porous Media

Sararat Mahasaranon

**Submitted for the degree
Of Doctor of Philosophy**

School of Engineering, Design and Technology

University of Bradford

2011

Acoustic and Thermal Properties of Recycled Porous Media

Abstract

This thesis is concerned with developing porous materials from tyre shred residue and polyurethane binder for acoustic absorption and thermal insulation applications. The resultant materials contains a high proportion of open, interconnected cells that are able to absorb incident sound waves through viscous friction, inertia effects and thermal energy exchanges. The materials developed are also able to insulate against heat by suppressing the convection of heat and reduced conductivity of the fluid locked in the large proportion of close-cell pores. The acoustic absorption performance of a porous media is controlled by the number of open cells and pore size distribution. Therefore, this work also investigates the use of catalysts and surfactants to modify the pore structure and studies the influence of the various components in the chemical formulations used to produce these porous materials. An optimum type and amounts of catalyst are selected to obtain a high chemical conversion and a short expanding time for the bubble growth phase. The surfactant is used to reduce the surface tension and achieve a homogenous mixing between the solid particulates tyre shred residue, the water, the catalyst and the binder. It is found that all of the components significantly affect the resultant materials structure and its morphology. The results show that the catalyst has a particularly strong effect on the pore structure and the ensuing thermal and acoustical properties. In this research, the properties of the porous materials developed are characterized using standard experimental techniques and the acoustic and thermal insulation performance underpinned using theoretical models.

The important observation from this research is that a new class of recycled materials with pore stratification has been developed. It is shown that the pore stratification can have a positive effect on the acoustic absorption in a broadband frequency range. The control of reaction time in the foaming process is a key function that leads to a gradual change in the pore size distribution, porosity, flow resistivity and tortuosity which vary as a function of

sample depth. It is shown that the Pade approximation is a suitable model to study the acoustic behaviour of these materials. A good agreement between the measured data and the model was attained.

Keywords: Porous media, acoustic absorption, waste recycling, pore stratification, thermal insulation.

Acknowledgements

I would like to sincerely thank my supervisors, Professor Kirill Horoshenkov and Professor Hadj Benkreira for all their continued support and encouragement during my PhD study. I am thankful to them for giving me the opportunity to attend international conferences and for their sincere advice. I would also like to thank my colleague, Dr. Amir Khan in the acoustic laboratory for his help and coaching with the acoustical measurements techniques. Thank you also to all the staff and students in the Polymer Engineering and the Acoustic laboratories. They have been very supportive and good friends.

I would like to extend thanks to my good friend, Dr. Gareth Ross for the proof reading of my first draft. Special thanks also to my best friend Sukunya Juikham for all her support and encouragement, and to my family for giving me a tremendous amount of support.

My sponsors, the Ministry of Science and Technology of Thailand and Naresuan University, Phitsanulok, Thailand, deserve special acknowledgements as without their financial support, I would not have been able to carry this research.

Table of Contents

1	Introduction.....	16
1.1	Problem Statement and Motivation.....	16
1.2	Aim and Objective.....	17
1.3	The Structure of Thesis.....	18
2	Literature Review and Theoretical Background.....	21
2.1	Introduction.....	21
2.2	Plastic Waste Recycling.....	21
2.3	Acoustic Materials.....	26
2.4	Acoustic Absorption in Porous Materials.....	29
2.5	Polyurethane Foaming Process.....	31
2.5.1	Raw Material for Polyurethane Foaming.....	32
2.5.2	Manufacturing Process of Polyurethane foam.....	36
3	Design of the Effective Porous Materials.....	39
3.1	Introduction.....	39
3.2	Waste Stream Selection.....	40
3.3	Particle Size Distribution of Tyre Shred Residue.....	41
3.3.1	Particle Sieve Analysis.....	41
3.3.2	Filament Fibres Length Measurement.....	45
3.4	Control of Structure of Porous Materials by Chemical Reaction Methods.....	49
3.4.1	Experimental Procedure.....	50
3.4.2	Measurement of Reaction Rate.....	54
3.4.3	Measurement of Absorption coefficient.....	57
3.4.4	Measurement of Non-acoustical Properties.....	59
3.5	Effect of the Contents of Tyre Shred Residue for Production Porous Material.....	65
3.6	Effect of the Contents of Water for Production Porous Material.....	70
3.7	Effect of the different Particle Size of Tyre Shred Residue for Production Porous Material.....	74
3.8	Effect of Catalysts on the Porous Material Structure.....	79
3.9	Effect of Surfactant on the Porous Material Structure.....	91
3.10	Effect of Catalyst and Surfactant on the Porous Material Structure.....	95

3.11	Conclusions.....	101
4.	Modelling of the Acoustical Properties of Recycled Porous Media	105
4.1	Introduction	105
4.2	Johnson-Champoux-Allard Model.....	107
4.3	Pade Approximation	110
4.4	Modelling of Porous Materials Produced with Variable Amounts of Catalyst and Surfactant	113
4.4.1	The effect of catalyst.....	111
4.4.2	The effect of catalyst and surfactant.....	122
4.5	Conclusions.....	137
5	The Porous Materials with Stratification	138
5.1	Introduction	138
5.2	Sample Preparation Procedure	139
5.3	Experimental Results.....	145
5.3.1	Non-Acoustical Properties of Samples manufactured with Method 1.....	146
5.3.2	Acoustic Absorption Coefficient of Samples manufactured with Method 1..	152
5.3.3	Non-Acoustical Properties of Samples manufactured with Method 2.....	157
5.3.4	Acoustic Absorption Coefficient of Samples manufactured with Method 2..	162
5.4	Modeling of the Porous Materials Using Pade Approximations.....	166
5.4.1	Acoustical Absorption Coefficient of individual sub-layers.....	166
5.5	Acoustical modelling of porous media with stratification	175
5.6	Conclusion.....	179
6	Study the Thermal property of Porous Materials	182
6.1	Introduction	182
6.2	Literature Review and Theoretical Background	182
6.2.1	Thermal insulation	182
6.2.2	Theoretical Basis	184
6.3	Thermal Conductivity Measurement	188
6.4	Effect of the Catalysts on Thermal Conductivity	191
6.5	Effect of Surfactants on the Thermal Conductivity	194
6.6	Conclusion.....	196

7	Summary and Conclusion	198
8	Recommendation and Further Work	203
	Reference	205
	APPENDIX A	216
	APPENDIX B	218

List of Figures

Figure 2.1: Plastic identification codes [4]	22
Figure 2.2: Absorption mechanisms and characteristics outline. [23].....	27
Figure 2.3: Illustration of three main types of porous absorbing materials and a cross section of a porous solid material [25]	28
Figure 2.4: Interaction of sound waves with materials [31].....	29
Figure 2.5: Sound incidence conditions [32]	30
Figure 2.6: illustration of chemical reaction	35
Figure 3.1: Experiment set up for sieve analysis.....	42
Figure 3.2: Illustration of tyre shred residue on the different size of screen capture.....	42
Figure 3.3: Illustration of granulated rubber, nylon staple fibre and nylon filament fibres bonded with rubber	43
Figure 3.4: Images of tyre shred residue from the different hole size of the screen capture	44
Figure 3.5: Weight distribution of the particle size for tyre shred residue	45
Figure 3.6: Microscope with camera setup for filament fibres length measuring	46
Figure 3.7: Examples of filament fibres collected from 6 different sieves	47
Figure 3.8: Filament fibres length distribution	48
Figure 3.9: Cumulative percentage of filament fibres length	49
Figure 3.10: The rectangular mould for preparation the porous materials samples	52
Figure 3.11: Illustration of the porous material sample and location of areas selected for cutting the specimens	52
Figure 3.12: Illustration of how to find the slope for reactant and production	55
Figure 3.13: Experimental setup for measuring the reaction rate for the porous samples	56
Figure 3.14: Illustration of finding the rate of polyurethane polymerization from slope of the cumulative volume CO ₂ curve	57
Figure 3.15: Illustration of layout for test equipment [43]	58
Figure 3.16: Illustration of the impedance tube equipment.....	59
Figure 3.17: Flow resistivity measuring apparatus.....	61
Figure 3.18: Experimental setup for the measurement of porosity [45].....	63
Figure 3.19: (a) Image of porous material sample before set up threshold, (b) Image highlighting the pores used to determine the pore size distribution.....	64
Figure 3.20: Calculation of the mean pore diameter by fitting the pore centroid.	65
Figure 3.21: Reaction rate of the porous materials produced by the different contents of tyre shred residue	67
Figure 3.22: Microscopic images of porous materials produced with different amount of tyre shred residue: (a) 20%, (b) 40%, (c) 60% and (d) 80%.....	68
Figure 3.23: The probability density function of the pore size for the porous materials produced with different amounts of tyre shred residue.....	68
Figure 3.24: The normal incidence, plane wave absorption coefficient spectra for the porous materials produced with variable amounts of tyre shred residue	69

Figure 3.25: The reaction rate of the porous materials produced with different amounts of water	71
Figure 3.26: Microscopic images porous materials manufactured with different amounts of water: (a) 20%, (b) 30% and (c) 40%	72
Figure 3.27: The probability density function of the pore size for the porous materials produced using different amounts of water	73
Figure 3.28: The absorption coefficient spectra for the porous materials produced using different amounts of water.....	74
Figure 3.29: Reaction rate of the porous materials produced by the different particle size of tyre shred residue	76
Figure 3.30: Microscopic images of the porous materials produced from different particle sizes of tyre shred residue: (a) P0, (b) P05, (c) P1, (d) P2, (e) P3, (f) P4 and (g) P6.....	78
Figure 3.31: Probability density function of the pore size for the porous materials produced by the different particle size of tyre shred residue	78
Figure 3.32: Absorption coefficient spectra for the porous materials produced by the different particle size of tyre shred residue	79
Figure 3.33: The reaction rate of the polyurethane binder (Flexilon 457) in the presence of different amounts of catalyst.....	81
Figure 3.34: The reaction rate of polyurethane binder (Flexilon 1109) in the presence of different amounts catalyst.....	81
Figure 3.35: The effect of catalyst on the activation energy [52]	82
Figure 3.36: The energy in molecules in the absence and presence of a catalyst [51]	83
Figure 3.37: Microscopic images of the porous materials produced with polyurethane binder Flexilon 457 and with different amount of catalysts: (a) C0_M457, (b) C1_M457, (c) C2_M457 and (d) C3_M457	86
Figure 3.38: Microscopic images of the porous materials produced with polyurethane binder Flexilon 1109 and different amount of catalysts: (a) C0_M1109, (b) C1_M1109, (c) C2_M1109 and (d) C3_M1109.....	87
Figure 3.39: The probability density function of the pore size for the porous materials produced with polyurethane binder Flexilon 457 and different amount of catalysts.....	87
Figure 3.40: The probability density function of the pore size for the porous materials produced with polyurethane binder Flexilon 1109 and different amount of catalysts.....	88
Figure 3.41: Absorption coefficient spectra for the porous materials produced by polyurethane binder (Flexilon 457) and the different content of catalysts ...	90
Figure 3.42: Absorption coefficient spectra for the porous materials produced by polyurethane binder (Flexilon 1109) and the different content of catalysts ..	90
Figure 3.43: The reaction rate of the porous materials produced with different concentration of surfactant.....	92
Figure 3.44: Photos of the porous materials produced by the different content of surfactants; (a) S0, (b) S2, (c) S4, (d) S6, (e) S8, (f) S10 and (g) S12	93
Figure 3.45: The pore size probability density function for the porous materials produced with different concentration of surfactant.	94
Figure 3.46: The absorption coefficient spectra for the porous materials produced with different concentration of surfactant.	94

Figure 3.47: Reaction rate of the porous materials produced by the different content of surfactants at 3% catalyst.....	97
Figure 3.48: Photos of the porous materials produced by the different content of surfactants at 3% catalyst; (a) C3S0, (b) C3S1, (c) C3S2, (d) C3S3, (e) C3S4 and (f) C3S5	98
Figure 3.49: Probability density function of the pore size for the porous materials produced by the different content of surfactants at 3% catalyst.....	98
Figure 3.50: The absorption coefficient spectra for the porous materials produced with different concentration of surfactants and by adding 3% of catalyst.	99
Figure 3.51 Comparasion of absorption spectra for the developed porous materials and commercial products	100
Figure 4.1: The measured and predicted absorption coefficient of the porous specimen without catalyst (sample C0_M457); (a) JCA model and (b) Pade model.....	115
Figure 4.2: The measured and predicted absorption coefficient of the porous specimen with 1% catalyst (C1_M457); (a) JCA model and (b) Pade model	116
Figure 4.3: The measured and predicted absorption coefficient of the porous specimen with 2% catalyst (C2_M457); (a) JCA model and (b) Pade model	117
Figure 4.4: The measured and predicted absorption coefficient of the porous specimen with 3% catalyst (C3_M457); (a) JCA model and (b) Pade model	118
Figure 4.5: The measured and deduced flow resistivity data for samples produced with different concentration of catalyst.	122
Figure 4.6: The measured and deduced porosity data for samples produced with different concentration of catalyst	123
Figure 4.7: A comparison of the deduced tortuosity data of two models for samples produced with different concentration of catalyst	123
Figure 4.8: The deduced data of viscous length and thermal length for samples produced with different concentration of catalyst	124
Figure 4.9: The deduced standard deviation of pore size for samples produced with different concentration of catalyst	124
Figure 4.10: The measured and predicted absorption coefficient for porous specimen without surfactant produced with 3% of catalyst (sample C3S0); (a) JCA model and (b) Pade model.....	126
Figure 4.11: The measured and predicted absorption coefficient for porous specimen with 1% of surfactant produced with 3% of catalyst (sample C3S1); (a) JCA model and (b) Pade model.....	127
Figure 4.12: The measured and predicted absorption coefficient for porous specimen with 2% of surfactant produced with 3% of catalyst (sample C3S2); (a) JCA model and (b) Pade model.....	128
Figure 4.13: The measured and predicted absorption coefficient for porous specimen with 3% of surfactant produced with 3% of catalyst (sample C3S3); (a) JCA model and (b) Pade model.....	129
Figure 4.14: The measured and predicted absorption coefficient for porous specimen with 4% of surfactant produced with 3% of catalyst (sample C3S4); (a) JCA model and (b) Pade model.....	130
Figure4.15: The measured and predicted absorption coefficient for porous specimen with 5% of surfactant produced with 3% of catalyst (sample C3S5); (a) JCA model and (b) Pade model.....	131

Figure 4.16: The measured and deduced flow resistivity values for porous samples produced by varying the concentration of surfactant and with 3% of catalyst.....	134
Figure 4.17: The measured and deduced porosity values for porous samples produced by varying the concentration of surfactant and with 3% of catalyst.....	135
Figure 4.18: A comparison of deduced tortuosity values of two models for porous samples produced by varying the concentration of surfactant and with 3% of catalyst.....	135
Figure 4.19: The deduced data of viscous length and thermal length for porous samples produced by varying the concentration of surfactant and with 3% of catalyst.....	136
Figure 4.20: The deduced standard deviation of pore size for porous samples produced by varying the concentration of surfactant and with 3% of catalyst.....	136
Figure 5.1: The polyurethane polymerization reaction	140
Figure 5.2: Chemical reaction of polyurethane polymerisation with polyol	142
Figure 5.3: photographs of the resultant material sample; (a) whole, (b) topside of whole sample and (c) bottom side of whole sample	143
Figure 5.4: The procedure for splitting a 140mm sample into individual sub-layers: (a) original sample, (b) splitting in two 70mm layers, (c) splitting in four 35mm sub-layers.....	144
Figure 5.5: On the selection of the analysis area to determine the pore size distribution in a material specimen	145
Figure 5.6: Microscopic images of the porous material with stratification for sample ST1; (a) sub-layer C, top side, (b) sub-layer C, bottom side, (c) sub-layer D, top side, (d) sub-layer D, bottom side, (e) sub-layer E, top side, (f) sub-layer E, bottom side, (g) sub-layer F, top side and (h) sub-layer F, bottom side.....	147
Figure 5.7: Microscopic images of the porous material with stratification for sample ST2: (a) Sub-layer C, top side, (b) sub-layer C, bottom side, (c) sub-layer D, top side, (d) sub-layer D, bottom side, (e) sub-layer E, top side, (f) sub-layer E, bottom side, (g) sub-layer F, top side and (h) sub-layer F, bottom side.....	148
Figure 5.8: The probability density functions of the pore size for each of the four sub-layer of sample ST1.	148
Figure 5.9: The probability density functions of the pore size of each of the four sub-layer of sample ST2.	149
Figure 5.10: The dependence of the porosity and density on sample depth for samples ST1 and ST2.....	150
Figure 5.11: The dependence of the flow resistivity and porosity on layer depth for samples ST1 and ST2.....	152
Figure 5.12: Absorption coefficient spectra of 140 mm thick sample of stratified porous materials (ST1 and ST2).....	155
Figure 5.13: Absorption coefficient spectra of layer A and B of ST1 and ST2	155
Figure 5.14: The absorption coefficient spectra of sub-layers C, D, E and F of: (a) sample ST1, and (b) sample ST2	156
Figure 5.15: Microscopic images of the porous material with stratification for sample SP1: (a) sub-layer C, top side; (b) sub-layer C, bottom side; (c) sub-layer D, top side; (d) sub-layer D, bottom side; (e) sub-layer E, top side; (f) sub-layer	

E, bottom side; (g) sub-layer F, top side; and (h) sub-layer F, bottom side.	160
Figure 5.16: Microscopic images of the porous material with stratification for sample SP2: (a) sub-layer C, top side; (b) sub-layer C, bottom side; (c) sub-layer D, top side; (d) sub-layer D, bottom side; (e) sub-layer E, top side; (f) sub-layer E, bottom side; (g) sub-layer F, top side; and (h) sub-layer F, bottom side.	161
Figure 5.17: The probability density function of the pore size of each sub-layer of sample SP1	161
Figure 5.18: Probability density function of the pore size of each sub-layer of SP2	162
Figure 5.19: The absorption coefficient spectra of 140mm thick samples SP1 and SP2	164
Figure 5.20: The absorption coefficient spectra of sub-layer A and B of samples SP1, SP2	164
Figure 5.21: The absorption coefficient spectra of sub-layers C, D, E and F of: (a) sample SP1; (b) sample SP2	165
Figure 5.22: Comparison between the predicted data and experimental data of each sub-layer for SP1; (a) sub-layer C (normal), (b) sub-layer C (reverse), (c) sub-layer D (normal), (d) sub-layer D (reverse), (e) sub-layer E (normal), (f) sub-layer E (reverse), (g) sub-layer F (normal) and (h) sub-layer F (reverse)	168
Figure 5.23: Comparison between the predicted data and experimental data of each sub-layer for SP2; (a) sub-layer C (normal), (b) sub-layer C (reverse), (c) sub-layer D (normal), (d) sub-layer D (reverse), (e) sub-layer E (normal), (f) sub-layer E (reverse), (g) sub-layer F (normal) and (h) sub-layer F (reverse)	169
Figure 5.24: The dependence of the flow resistivity on the layer depth	171
Figure 5.25: The dependence of porosity on the layer depth	172
Figure 5.26: The dependence of the tortuosity on the layer depth	174
Figure 5.27: Standard deviation of pore size for SP1 and SP2	175
Figure 5.28: Illustration of sound wave incident to N-layers	176
Figure 5.29: Comparison between the predicted and measured absorption coefficient spectra of the stratification material sample (SP1) in two different orientations	178
Figure 5.30: Comparison between the predicted and measured absorption coefficient spectra of the stratification material sample (SP2) in two different orientations	178
Figure 6.1: Illustration of thermal conductivity apparatus [88]	190
Figure 6.2: Experimental setup for determination thermal conductivity	190
Figure 6.3: The influence of variable amount of catalyst on the thermal conductivity	193
Figure 6.4: A comparison of the influence of the variable amount of catalyst on the density and porosity	193
Figure 6.5: The influence of variable amount of surfactant on thermal conductivity	195
Figure 6.6: Comparison of the influence of variable amount of surfactant on density and porosity	196
Figure B.1: Absorption coefficient spectra for the porous materials produced by the variable tyre shred residue; (a) 20%, (b) 40%, (c) 60% and (d) 80%	219

Figure B.2 Absorption coefficient spectra for the porous materials produced by the variable water; (a) 20%, (b) 30% and (c) 40%	220
Figure B.3 Absorption coefficient spectra for the porous materials produced by tyre shred residue sieved having the different particle size followed on hole of screen capture (mm); (a) no sieve, (b) <0.5, (c) 1.0, (d) 2.0, (e) 3.35, (f) 4.0 and (g) > 6.67	220
Figure B.4 Absorption coefficient spectra for the porous materials produced by polyurethane binder (Flexilon 457) and the variable catalyst; (a) 0%, (b) 1%, (c) 2% and (d) 3%	221
Figure B.5 Absorption coefficient spectra for the porous materials produced by polyurethane binder (Flexilon 1109) and the variable catalyst; (a) 0%, (b) 1%, (c) 2% and (d) 3%	222
Figure B.6 Absorption coefficient spectra for the porous materials produced by the variable surfactant; (a) 0%, (b) 2%, (c) 4%, (d) 6%, (e) 8%, (f) 10% and (g) 12%	222
Figure B.7 Absorption coefficient spectra for the porous materials produced by the variable surfactant at 3% catalyst; (a) 0%, (b) 1%, (c) 2%, (d) 3%, (e) 4% and (f) 5%.....	223

List of Tables

Table 3.1: Weight fraction of the particle/fibre size for tyre shred residue	44
Table 3.2: The average filament fibre length as a function of the sieve size	48
Table 3.3: Formulation for producing the porous materials containing the different tyre shred residue.....	52
Table 3.4: Formulation for producing the porous materials containing the different water	53
Table 3.5: Formulation for producing the porous materials using the different particle	53
Table 3.6: Formulation for producing the porous materials containing the different catalyst	53
Table 3.7: Formulation for producing the porous materials containing the different surfactant	54
Table 3.8: Formulation for producing the porous materials containing the different surfactant at 3% catalyst	54
Table 3.9: Summary of non-acoustical properties for the porous materials produced by the different amount of tyre shred residue.....	67
Table 3.10: The non-acoustical properties of the porous materials produced with different amounts of water.	71
Table 3.11: The non-acoustical properties of the porous materials produced of tyre shred residue with different particle sizes.	76
Table 3.12: Non-acoustical properties of the porous materials with different catalysts	80
Table 3.13: The non-acoustical properties of the porous materials produced with different concentration of surfactant.....	91
Table 3.14: The non-acoustical properties for the porous materials produced with different concentration of surfactants and by adding 3% of catalyst.....	97
Table 4.1: The deduced non-acoustical properties by JCA model for the porous materials produced by varying the concentration of catalysts	119
Table 4.2: The deduced non-acoustical properties by Pade model for the porous materials produced by varying the concentration of catalysts	119
Table 4.3: The deduced non-acoustical properties by JCA model for the porous materials produced by varying the concentration of surfactants at constant catalyst 3%	132
Table 4.4: The deduced non-acoustical properties by Pade model for the porous materials produced by varying the concentration of surfactants at constant catalyst 3%	132
Table 5.1: The composition of the reactants	141
Table 5.2: The composition of the material mix.....	143
Table 5.3: The positions of areas on the image selected for the pore size distribution analysis (x,y) in terms of the sample radius R = 50mm.	145
Table 5.4: Summary of the porosity and density for ST1 and ST2.....	150
Table 5.5: The flow resistivity data for samples ST1 and ST2.....	151
Table 5.6: The porosity and density for sample SP1and SP2.	159

Table 5.7: The flow resistivity for samples SP1 and SP2	160
Table 5.8: The non-acoustical properties of all sub-layer of SP1 from Padé approximation.....	170
Table 5.9: The non-acoustical properties of all sub-layers of SP2 from Padé approximation.....	170
Table 6.1: The thermal conductivity of the porous materials produced with the polyurethane binder with a higher concentration of isocyanate (Flexilon 457) and concentration of catalyst.....	192
Table 6.2: The thermal conductivity of the porous materials produced with polyurethane binder with a lower concentration of isocyanate (Flexilon 1109) and variable amount of catalyst.	192
Table 6.3: The physical properties and thermal conductivity of commercial products.	194
Table 6.4: The thermal conductivity of the porous materials produced by varying the amount of surfactant	195
Table 7.1 The trends of the structural, acoustical and thermal properties for the effective porous materials when the composition increased.....	202
Table 7.2 The trend of the non-acoustical and acoustical properties for the recycled porous materials with stratification produced by method 1.....	202
Table 7.3 The trend of the non-acoustical and acoustical properties for the recycled porous materials with stratification produced by method 2.....	202

Chapter 1

1 Introduction

1.1 Problem Statement and Motivation

The disposal of plastic waste has been the subject of many studies in recent years. There are many reasons for this work. Plastic waste is difficult to decompose; natural resources become scarce because of increasing demand and there are many negative environmental effects from dumping plastic waste. In general, plastic waste cannot be decomposed by micro-organisms in a short time because plastics are macromolecular particulate inert compounds. This very slow decomposition and the huge amount of waste generated by both manufacturers and consumers has resulted in the increase of plastic waste being dumped in landfill and the environment in general causing long-term ground and air contamination. Efficient methods for plastics waste recycling are thus highly desirable because it is attractive to make further use of their good mechanical, chemical properties and processability properties.

Another important problem which affects the quality of the environment and life is noise pollution which has serious effects on health both psychologically and physiologically. As population increases and cities around the world get larger and larger exposure to noise pollution from traffic (cars, trains, airplanes, etc.) will increase and demand for abating this problem will increase. There is also noise exposure in the work place from machineries and in building and housing from human activities. For good building and machineries noise insulation will increasingly become the norm and indeed is

now increasingly regulated. Demand on acoustic materials will thus increase and finding sustainable new materials, from waste plastics for example, will be highly desirable as this will provide a solution to plastic waste disposable and generate new sustainable and cheaper alternative to conventional acoustic materials such as wool and glass fibers and foams fabricated from raw hydrocarbons. This is precisely the objective of this research; to use such waste plastic residues and process them into forming porous structures that are suitable for noise absorption and if possible also heat insulation. By adding the heat insulation element, the research will contribute to finding solutions to reducing the green house effect, the major concern of our times. The idea of using plastic waste for this purpose is not new [1] and is further reviewed later but creating the optimum structure with *residues* is new and the subject of this research. By residues, it is meant effectively dust and other un-recyclable particulates as will be fully described later.

1.2 Aim and Objective

As explained above, this research proposes new acoustic and thermal insulation solutions which are based on porous materials manufactured from granulated tyre waste residue. Here, the porous structure is formed by binding the waste particulates with a foaming polyurethane binder. A chemical reaction with the release of gas through a binder that can be elastic or rigid is thus developing during processing. If well designed and controlled, the process should result in a porous material of a structure that can be optimized to offer a considerable thermal and acoustic performance, low density, low cost and environmentally sound solution. As required for good noise insulation the structure must be highly porous with *open* cells. Where required, the process

can be manipulated to develop structures with *closed* cells for good thermal insulation. One particular objective of this research is to attempt some form of *stratification* of the cells as this is in principle conducive to enhancing acoustic absorption. The ultimate objective of this study is thus to engineer the structure of this porous material to optimize acoustic and heat insulating performances and develop new technology in the foaming of elastomeric waste residues.

The specific objectives of this research are:

1. To study the effect of the basic physical properties of mixtures of recycled granulated tyre waste, polyurethane binder and water.
2. To produce new porous materials with chemical reagents such as catalysts and surfactants by controlling the number of open cell and their size distribution.
3. To produce porous materials with pore stratification in order to improve the sound absorption in a broad frequency band.
4. To study the acoustical and non-acoustical properties of the stratification porous materials as a function of sample depth by experimental analysis and via theoretical modelling.
5. To study the effect of catalysts and surfactants on the thermal conductivity of the manufactured porous samples.

1.3 The Structure of Thesis

The problem statement, motivation and objective of this research have already been presented in this chapter.

Chapter 2 presents the literature review of methods for waste recycling and acoustic material theory and discusses the key mechanisms of sound

absorption in porous media. In this chapter, the mechanisms of the polyurethane foaming process are also described

Chapter 3 presents the experimental method for producing the porous materials from the recycled tyre shred residue and polyurethane foaming binder. The physical characteristics of the particulates such as particle size and fibre length, the sample preparation and all the measuring methods are described. These include measurements of structural properties (porosity, tortuosity, air flow resistivity and material elasticity) and performance properties (noise absorption and impact sound insulation) using standard methods.

Chapter 4 introduces the basic theory of Johnson-Champoux-Allard and Pade approximation and makes use of these models to predict the acoustic behaviour of the porous materials manufactured during this research and make comparison with measured data.

Chapter 5 presents the work on materials with pore stratification. The first part of this chapter presents various manufacturing methods which have been developed as a part of this work and material characterisation methods. The second part of this chapter presents the non-acoustical properties and acoustic absorption coefficient as a function of sample depth. The last part of this chapter focuses on the use of the Pade approximation model for studying the acoustic behaviour of porous media with stratification.

Chapter 6 reviews the literature on materials used for thermal insulation and describes the experimental method used in this research for measuring thermal conductivity. The data obtained are then presented and the various effects on composition including catalyst and surfactant discussed.

Finally, chapter 7 and 8 present the general conclusions and recommendations of future work, respectively.

The complete list of publications authored or co-authored during my PhD work and directly relevant to the material discussed here, are provided in Appendix A.

Chapter Two

2 Literature Review and Theoretical Background

2.1 Introduction

This chapter describes the theoretical background and reviews literature that relates to this study. More specifically, this chapter touches on the methods of waste recycling, types of materials used for noise control and polyurethane foaming process. The following section presents tyre waste recycling and describes the differences between the tertiary and quaternary recycling. It is followed up with a section which presents a classification of acoustic materials including materials made from recycling plastic. Here we describe the key physical mechanisms by which the acoustic energy is dissipated in a porous material. The final section describes polyurethane foaming process, the details of raw materials and manufacturing.

2.2 Plastic Waste Recycling

Recycling plastic is a sustainable method of reducing waste which has increased significantly in recent years. Key several benefits of recycling are: protection of the environment and natural resources, its low cost, added value attained at the end of this process, financial and energy savings. Efficient plastic waste recycling can be achieved through the following five steps [2]. : (i) plastic collection; (ii) plastic sorting; (iii) fine separation; (iv) plastic processing; (v) remanufacturing. During step (i), used plastics are collected by providing the collection areas and used plastic containers, e.g. recycling boxes and recycling

bins. After that the collected plastic waste is sorted (step (i)) and separated (step (ii)) by several technologies that are able to identify and sort different types of plastics. The recycling plastic codes help to identify the plastic waste in the sorting and separating processes, which is a numerical coding system (shown in figure 2.1). The plastic codes usually can be found at the bottom or on a side of most plastic products. These sorting and separating techniques make use of the difference in the physical, optical, chemical and electrical properties of the various plastics [3]. Some of these techniques include density-based sorting (float-sink method followed by dry separation and centrifugal sorting), optical sorting, electrostatic sorting techniques (using triboelectric drum separator and corona charging belt separator) and sorting by melting temperature and selective dissolution.

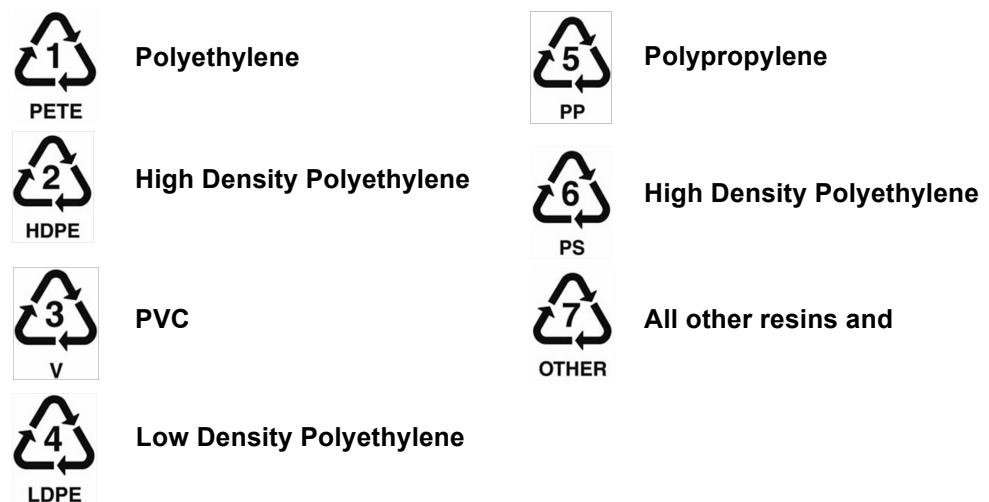


Figure 2.1: Plastic identification codes [4]

Step (iv), the fourth (reprocessing) step works continuously with the final step (manufacturing). During step (iv) and step (v), the plastic waste is melted by heat in order to injection mould or extrude new products. The plastic waste which is thermoplastic, can be melted by a heating process. This melting

process for thermoset plastics is rarely successful and this type of plastics requires alternative technologies for reprocessing and manufacturing.

Recycling process can be divided into four types: primary, secondary, tertiary and quaternary. In primary recycling, the plastic waste is converted back into the original product, called “reuse product”. In secondary recycling, the waste is reprocessed into a new product that has different characteristics from the original product. Primary and secondary recycling are types of mechanical recycling [5] composed of sorting, separating, size reducing (granulating) and melting (by extruder) steps.

Tertiary recycling of plastic waste is chemical recycling in which the plastic is cracked with the long molecular chains transforming into monomers, oligomers which can be used as petro-chemical feedstock and fuels. The tertiary recycling has various technologies classified as depolymerisation for thermoplastics and devulcanisation for thermosets and rubbers leading to the production of monomers and oligomers which can be used again to manufacture new products with properties similar to those made with the virgin material. Thermolysis process can produce petro-chemical feedstock and fuels from all types of plastic waste by using high temperatures to break the bonds in the molecular chains of the polymer. This can be divided into three processes: pyrolysis, hydrogenation and gasification [3]. When the plastic waste is cracked with heat and air together that is called pyrolysis or thermal cracking process. If the thermal process of plastic waste recycling is performed in atmosphere of hydrogen gas, then the hydrogenation or hydrocracking process takes place. If this recycling process is controlled by the addition of oxygen in which a mixture of gases is produced (also called syngas), then this process is known as

gasification. In quaternary recycling, the plastic waste is converted into energy by burning or combustion including incineration of waste. The quaternary recycling has been investigated when any plastic waste cannot be sensibly recycled by mechanical recycling due to excessive contamination, separation difficulties, etc. Examples include plastic waste containing organic materials, medical plastic waste and plastic waste with electronic components etc. Recovery of energy from plastic waste is used routinely in power plants, solid fuel fired boilers and electric generation.

This study uses tyre shred residue as filler in the production of porous materials. Therefore, this section describes tyre waste recycling that has differences in details to more conventional plastic waste recycling. The raw materials of which tyres are made are natural and synthetic rubbers that are thermoset plastics having cross-linked structure. Recycling of tyre waste involves tyre shredding, plastic sorting and separation [3]. The next step here is the size reduction of tyre waste into 2x2 inch or 1x1inch chips. Mechanical grinding can produce high-quality rubber particles (approx. 1.7 mm diameter). This method consists of four main steps: shredding (25mmx25mm chips), separating (remove steel), granulating (particles 1.7mm) and final sorting (remove steel, textile and dust). Cryogenic grinding uses liquid nitrogen (temperature -195.7 °C approximately) to cool the tyre waste chips which are then mechanically broken into fine rubber particles and nylon fibres. The tyre waste is reduced by these techniques and the steel is removed already, which is called ground rubber crumb or rubber crumb that is filler used in various applications such as filler products, bound rubber products [6] and rubber crumb with thermoplastic binder. The ground tyre rubber crumbs are mixed with

recycled high-density polyethylene (HDPE) to produce composite materials for structural application [7, 8, 9]. Rubber waste powder which has its surface modified by allylamine solution is used in order to improve the compatibility of polypropylene/rubber composites [10]. Ground rubber is used as a filler in the rubber compound of natural rubber (NR) and styrene butadiene rubber (SBR) to improve the mechanical properties and abrasion property [11].

Chemical recycling of natural and synthetic rubber uses mainly two processes, reclaiming and devulcanisation. In reclaiming, scrap rubber is cleaved to produce long molecular chains, which lowers the rubber molecular weight. The reclaiming process is a mechanical recycling using high pressure and high temperature for cleaving the molecular chains of the rubber. In devulcanisation, the cross-linked chains (C-S bond or S-S bond) are cleaved to produce rubber having the same properties as virgin rubber. Devulcanisation is carried out through various technologies that can be grouped into chemical, ultrasonic, microwave, biological devulcanisation or desulfurization [12] in order to make new products [13]. Tyre waste can be used as fuels for cement kilns, boilers and electrical generation. Tyre waste is however difficult to burn in comparison with plastic waste because it is relatively highly resistant to heat. Pyrolysis of tyre waste cracks the molecular structure by using high temperatures and catalysts [14]. The products from this process are carbon black and pyrolytic oil that is a feedstock for the refinery industry.

The tyre shred residue material used in this study was composed of small rubber particles and nylon fibres free from any steel wire. The particles and the fibre in this residue can be in discrete form or bond together. The fibres are a mixture of nylon 6 and nylon 6, 6 [15].

2.3 Acoustic Materials

Acoustical materials belong to a class of materials which are used to absorb or reflect sound, dampen or insulate against vibrations. Materials used for vibration damping are designed to dissipate the vibrational energy. A good vibration damper converts the mechanical energy of vibrations into heat by molecular relaxation mechanism. When the energy of the incident sound wave is equal to the energy of molecular motion, the damping is particularly pronounced. Materials used to damp vibrations are commonly viscoelastic substances. Some polymers which are especially effective include polydienes, urethane-epoxy networks, cross-poly (vinyl methyl ether)-inter-cross-polystyrene [16], polymer foam, fibrous materials, melamine foam [17], wood flour filled polypropylene composites [18], polyurethane compositions with soft and hard segments [19] and advanced fibre reinforced plastic [20].

Airborne sound transmission can be controlled by interrupting the sound transmission path and minimising the energy in the transmitted sound wave. The transmission loss performance of a sound barrier material depends on its thickness and material density. Material which are used routinely as acoustic barriers include gypsum board, plywood, concrete, polyurethane composite [19], nitrile butadiene rubbers (NBR) with carbon black [21,22].

Sound absorbing materials (sound absorbers) are essentially energy transducers (sinks) which convert the acoustic energy in an incident sound wave into heat. Sound absorbers can be divided into three types as is shown in the Figure 2.2.

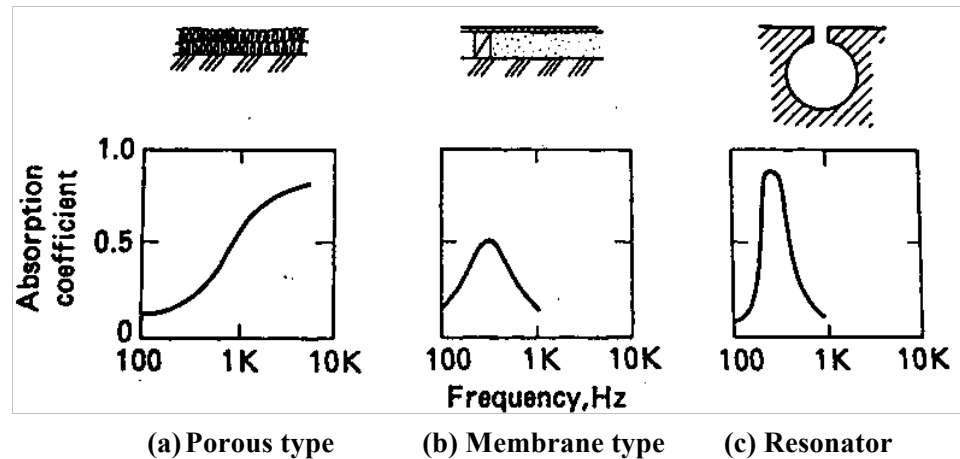


Figure 2.2: Absorption mechanisms and characteristics outline. [23]

Here the physical mechanism is absorber-specific, but the energy transformation is similar. There are many requirements to good-quality acoustic absorbers. These materials are expected to be lightweight, strong, durable, fire resistant, low cost and environmentally friendly. Examples include macro perforated poro-elastic materials [24], micro-perforated panels, porous absorbing material, porous fibrous material, porous asphalt [25], polymer microparticles and polyurethane (PU) foam [26], polypropylene (PP) foam [27], polyolefin foam [28] and nonwoven composites [29,30]. There are three common types of porous absorbing materials: cellular, fibrous and granular materials. These types are illustrated in Figure 2.3.

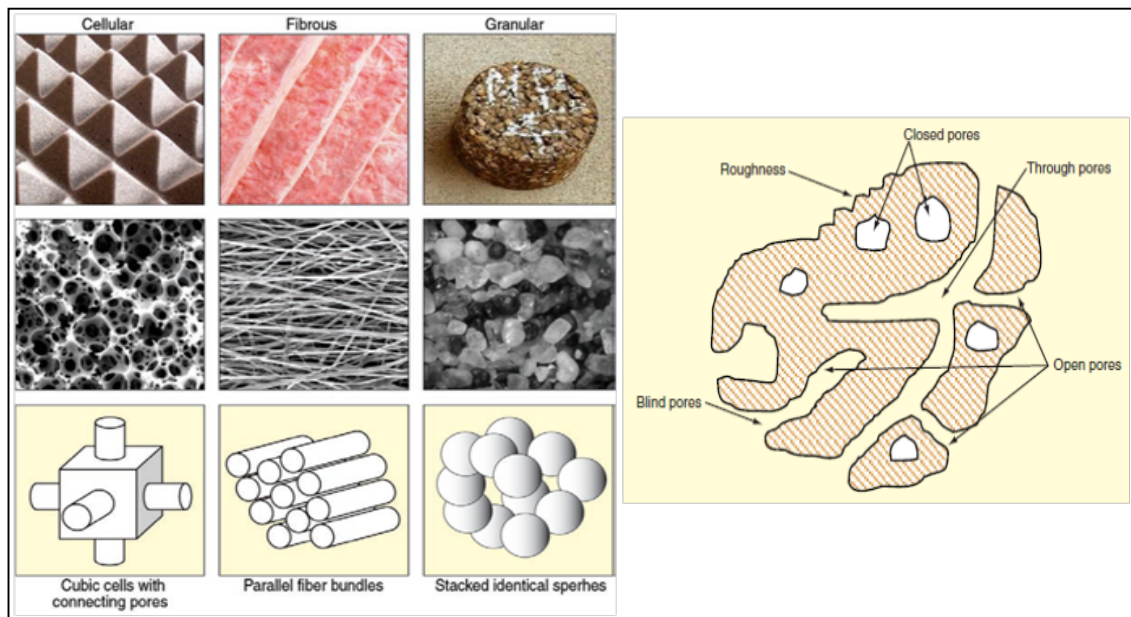


Figure 2.3: Illustration of three main types of porous absorbing materials and a cross section of a porous solid material [25]

Porous materials are composed of a solid matrix (cell ligaments, fibres or granules) and the air with which this matrix is filled. This air oscillates under the influence of the incident sound wave in a limited porous space in which the frictional and viscous losses occur. In this process, a considerable amount of sound energy in the incident wave is converted into heat. Figure 2.3 shows examples of open pore structures which typically exhibit high acoustic absorption. The most important characteristics of a porous material which control its acoustic performance are the pore size and open porosity. The pore size has an influence on the material permeability to air and determines the magnitude of the viscous and frictional losses within porous materials. The pore size distribution and open porosity have a strong influence on the flow resistivity and tortuosity of porous materials that directly affects to change of sound pressure within pore structure.

On the other hand, pores that are isolated from their neighbors are called closed pores. A material which is composed of closed pores has a better

thermal insulation efficiency than a material with the same porosity, but composed of open pores. The main differences here are in the diffusion and convection. The heat transferred by convection within porous materials is created by air moving, which is low due to air trapped within closed pores.

The amount of heat which is transferred from molecule to molecule in a porous material is lower if there is a lower volume fraction of solid frame. This directly relates to the material density and porosity. Typically, a material with lower density (i.e. with a higher porosity) exhibits a better thermal insulation than that of a higher density.

2.4 Acoustic Absorption in Porous Materials

When a porous material is exposed to an incident sound wave with the incident energy (E_i), some of this energy is reflected, some is absorbed within the material pores and some is transmitted through the material. This energy balance is illustrated in Figure 2.4.

$$E_i = E_r + E_t + E_a \quad (2.1)$$

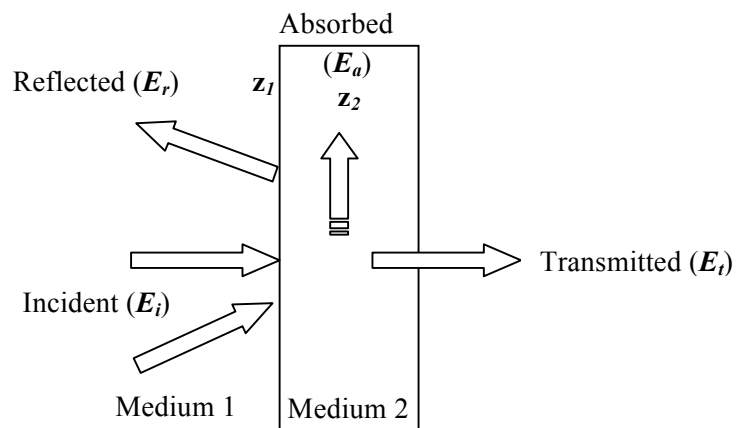


Figure 2.4: Interaction of sound waves with materials [31]

The ability of a material to absorb sound energy is characterised by its sound absorption coefficient which is defined as the ratio between the absorbed (including the transmitted energy) and the incident acoustical energies

$$\alpha = \frac{E_{\alpha+t}}{E_i} \quad , \quad (2.2)$$

The sound absorption coefficient depends on the frequency and the angle of incidence of the sound waves. As shown in Figure 2.5

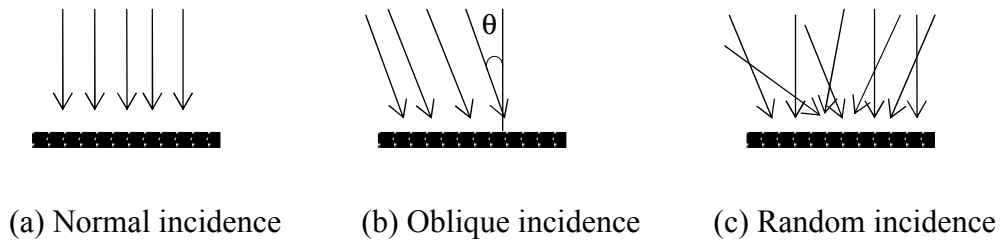


Figure 2.5: Sound incidence conditions [32]

The energy reflection coefficient is defined as

$$\alpha_r = \frac{E_r}{E_i} \quad , \quad (2.3)$$

where E_r is the energy in the reflected sound wave.

The reflected coefficient can be expressed in terms of the sound pressure reflection coefficient (r) to be determined.

$$\alpha_r = r^2 = \left| \frac{p_r}{p_i} \right|^2 \quad , \quad (2.4)$$

where p_r and p_i represent sound pressures in the reflected and incident sound waves, respectively. Therefore, the absorption coefficient is given by

$$\alpha = 1 - r^2 \quad (2.5)$$

The acoustical characteristic impedance (z_c) is one of the most important properties of a material, which can be defined in terms of the ratio of sound pressure to the particle velocity. It depends on the bulk density of the medium (ρ_b) and sound speed in the medium (c_b), i.e.

$$z_c = \left(\frac{P}{u_x} \right)_{x=0} = \rho_b c_b \quad (2.6)$$

In case of sound wave propagating from medium 1 to medium 2 as shown in Figure 2.4, the reflection coefficient can be calculated by the characteristic impedance of medium.

$$r^2 = \left| \frac{P_r}{P_i} \right|^2 = \left| \frac{z_2 - z_1}{z_2 + z_1} \right|^2 \quad (2.7)$$

where z_1 is z_2 the characteristic impedance of medium 1 and medium 2, respectively. If the medium 1 is layer air and medium 2 is a porous material, then its absorption coefficient can be expressed in term of the normalised surface impedance (z_s):

$$\alpha = 1 - \left| \frac{z_s - 1}{z_s + 1} \right|^2 \quad (2.8)$$

where z_s is the normalized surface impedance of the porous layer.

2.5 Polyurethane Foaming Process

Polyurethane (PU), which is a thermoset, has been used in various modes, as an elastomer, a coating, an adhesive, or for fibres and foams

formation. The use in different applications depends on the structure, chemical and physical properties of the particular PU.

2.5.1 Raw Material for Polyurethane Foaming

In this study, PU foam is based on the following raw materials [33]:

- **Isocyanate:** isocyanate is a key raw material that indicates the important characterisation of the final products. The isocyanates basically have at least two functional reactive groups, which have two types: aliphatic isocyanates and aromatic isocyanates. The aliphatic isocyanates are used to produce the flexible fibres, elastomers and coating polyurethanes, for example hexamethylene diisocyanate. Most polyurethane foam uses the aromatic isocyanate, for example diphenylmethane diisocyanate (MDI) and tolylene diisocyanate (TDI). The isocyanates used may be in the form of monomers or pre-polymers. Industry uses generally pre-polymers, a form of PU ready for foaming. A pre-polymer with a high molecular weight and low isocyanate content results in a flexible PU foam containing a high proportion of open cells. A more rigid PU foam is produced by using a pre-polymer with a low molecular weight, low viscosity and high isocyanate content [34].

- **Polyols or Oligomerols:** These are compounds that have long and flexible molecular chains, a molecular weight of ~500-12000 and hydroxyl-terminated groups (OH groups ≥ 2). Polyols can be further classified into polyester polyols and polyether polyols, which are used to modify the structure of polyurethane in order to achieve all requirements. For example, polyols with long molecular chains are used to add flexibility to foams.

- **Chain extenders and Cross-linking agents:** These are diol and diamine compounds having low molecular weight, for example, ethylene glycol,

diethylene glycol, propylene glycol, 1,4-butanediol, 1,4-cyclohexanediol, hexamethylenediamine, 4,4'-diamino diphenylmethane and m-phenylenediamine . The hard or rigid segments of PU are used to modify the mechanical properties of the foam by using chain extenders and cross-linking agents in order to create crystalline structures or cross-linking.

- **Catalysts:** Those used for producing PU foam are classified into two main groups [35]: amine compounds and organometallic compounds, for example, dicyclohexyl methylamine, dimethylethanolamine, N-cocomorphiline, N-methylmorpholine, dibutyltin diacetate, dibutyltin dimaleate and dibutyltinlaurate. The use of catalyst in chemical processes has the main objective of increasing the product yield or material conversion rate. The yield can be described in term of ratio of actual yield and theoretical yield as [36]

$$\frac{\text{actual - yield(grams)}}{\text{theoretical - yield(grams)}} \times 100\% = \% \text{ yield} \quad (2.9)$$

Here, the theoretical yield is the amount of product after the reaction is fully complete and the calculations are based on the stoichiometry of the reaction within standard condition of temperature and pressure (STP). The STP condition or ideal condition is 293.15 Kelvin or 20 °C and 101.325 kPa or 1 atm pressure. The actual yield is the actual amount of product from the experiment in the laboratory which normally is not completed reaction due to different conditions. Therefore, the use of a catalyst helps to improve the product yield. Furthermore, the catalyst affects the reaction rate and reaction time in the production of PU foam. In the PU foaming process, the reaction time is the period from the nucleating to expanding. If the foaming reaction has a long reaction time this means it has a long expanding time allowing the bubbles to

expand to a large size and form large pores. As a result, the pore size of PU foam depends on the expanding time.

- **Surfactants:** These are additives which help to improve the production of PU foam. Basically, a surfactant is an ionic and non-ionic compounds used to reduce the surface tension and interface tension of at the liquid-liquid, liquid-solid interface. Surfactants are widely used in the foaming process [37], for example, polysiloxane-polyether copolymer, silicone oils, oxyethylenated alkylphenols, fatty acid, sulphonated hydrocarbons, sodium salts of alkoxyglycols and etc. In this study, surfactants have been used at each step of the PU foaming process: In the pre-mixing step of water, catalyst and tyre shred residues, a surfactant is used to improve the wetting of tyre shred residues. Surfactants also help to reduce the polymer viscosity and ensure good mixing of the ingredients. Adding a surfactant helps to reduce the surface tension in the liquid phase and increase the nucleating rate of the gas bubbles resulting in a higher proportion of open cells. In the absence of a surfactant the developed porous sample was prone to shrinkage caused by the collapse of the resultant cell structure prior to its solidification. Adding a surfactant helps to stabilise the bubbles and prevents their premature collapse.

- **Blowing agents:** In the foaming process, blowing or foaming agents make up the gas phase that can be expanded into the polymer melt phase. Blowing agents can be divided into two types [38]. The first type includes chemical blowing agents, which are solid or liquid materials decomposed to create a gas at and above the polymer melt temperature. This gas can be of various compositions depending on the chemistry of the particular blowing agent. For example, the decomposition of azodicarbonamide has

residual materials and gas composition of 65% N₂, 24% CO, 5% CO₂ and 5% NH₃. The second type of blowing agents are volatile organic compounds called physical blowing agents which have the following important properties: (i) low boiling point; (ii) inert gases; (iii) low permeability and solubility into polymer melt phase; and (iv) they are safe and environmentally friendly. Hydrocarbon compounds are a type of physical blowing agents that can be easily volatilised at low temperatures and examples include butane, pentane, isopropyl alcohol, methyl chloride, hydrochlorofluorocarbons (HCFCs) and chlorofluorocarbons (CFCs). These blowing agents have been widely used because they are non-flammable except butane but CFCs are environmentally unfriendly and cause the destruction of the Earth ozone layer. Nitrogen (N₂) and carbon dioxide (CO₂) gases have been investigated as alternatives to be used in foaming processes. The advantages of CO₂ are: non-flammable, low solubility and low vapor thermal conductivity. It also is the reaction product of polyurethane polymerisation [39]. In this study, water has been used to trigger the chemical reaction with isocyanate group of polyurethane binder to produce carbon dioxide gas (CO₂) at room temperature. The chemical reaction of PU foam [40] is shown in Figure 2.6.

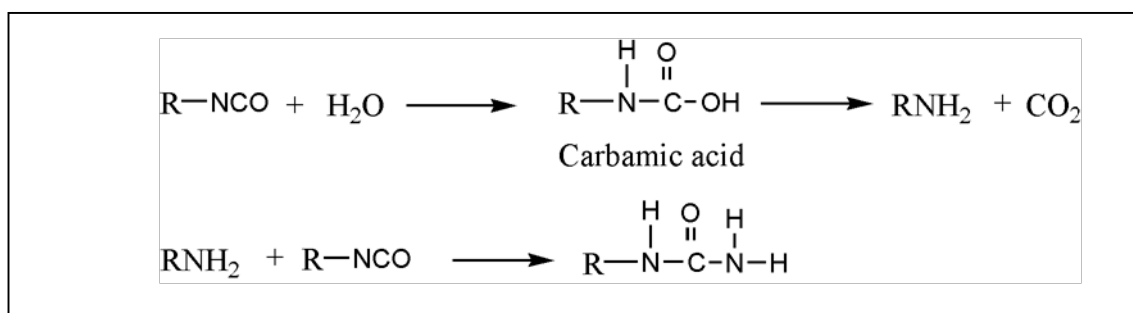


Figure 2.6: illustration of chemical reaction

- **Other additives:** These include fillers (particle, fibrous and flaky), flame retardants and pigments used to improve the physical and mechanical properties of PU foam. In this study, tyre shred residue may be considered as a filler although it is the important bulk material used.

2.5.2 Manufacturing Process of Polyurethane foam

Manufacturing of PU foam can be generally divided into two types of processes, continuous or batch. The continuous process has commonly two elements, foam formation and product shaping such as in reactive injection moulding (RIM). In the continuous process, the raw materials are the pre-polymer having isocyanate groups, polyols, catalysts, blowing agents and fillers. These ingredients are mixed in a mixing head chamber. For 'slabstock' process, the mixtures are laid down onto a paper strip transported by a belt conveyor. In case of RIM process, the mixtures from the mixing head chamber are injected into a mould with automatic control solidifying and curing the product. The batch process uses moulds and is classified into hot or cold moulding with either an open or close mould. The close mould uses the machine to fill the mixture components whereas in the open mould the mixture components are filled manually.

The mechanism of the foaming process has four steps; nucleation, bubble growth, bubble coalescence and rupture, and solidification and curing [38].

- **Nucleating step:** In batch reactive processes of PU foam, foaming occurs whilst the PU reacts. Nucleation sites are created from the mixing of the components and reaction rate. The mixing of the components

induces turbulence nucleation mechanism and the reaction rate is a main factor in a simple reactive foaming.

- **Bubble Growth:** the bubble growth rate depends on the diffusion of gas, melt viscosity of polymer and surface tension. Bubbles of low viscosity and low surface tension are easily expanded to a large size, whereas, the diffusion decreases due to the concentration of gas is decreased when there is a large volume of bubbles. When the polymer melt during foaming cools down into a solid phase, the diffusion of gas is slow. In particular, temperature has an effect on the gas diffusivity or diffusion coefficient as described by the Arrhenius thermal dependency equation [38]

$$D = D_0 \exp\left(-\frac{\Delta E}{RT}\right) \quad , \quad (2.10)$$

D_0 is the maximum diffusion coefficient at infinite temperature, ΔE is the activation energy for diffusion, T is the absolute temperature and R is the gas constant. The skin that forms on the surface of foam as a result of natural cooling at room temperature causes resistance to bubble growth. Also when the polymer melt has a high melt strength bubble growth is limited.

- **Bubble Coalesce and Rupture:** The resulting of over-expansion of bubble growth causes the cells wall to rupture and this creates an open cell. As PU foaming process develops a continuous reaction to produce CO_2 , continuous expansion between neighboring bubbles may occurs leading to the bubbles coalescence and thinner cell walls. If cell walls are weakened, then an open-faced structure is likely to occur. In theory, polyurethane polymerisation is an exothermic reaction. Thus, the heat generated in the

exothermic reaction and cross-linking helps to expand and open cells without collapsing.

- **Solidification and Curing:** Once foamed, the PU is solidified after complete polymerisation. Heat from the exothermic reaction of PU foam needs time in order to cool because of PU foam having poor thermal conductivity. The cooling time depends on the dimensions of the PU foam products. The cooling system induces CO₂ within PU foam into a stable state. Curing of PU foam helps to improve mechanical properties by curing moisture [41]. The strength of PU foam is increased by the formation of hydrogen bonds between water molecules and the isocyanate segments.

Chapter Three

3 Design of the Effective Porous Materials

3.1 Introduction

Materials which contain a large proportion of open, interconnected pores have good performance as acoustic absorbers. The use of granulated tyre waste blended with polyurethane binder in the production of acoustic materials can help to resolve problems of both waste disposal and noise pollution. Therefore, this work has been focused on producing recycled porous materials for sound absorption applications. The non-acoustical properties of the materials have a strong influence to sound absorption performance. The amount of the acoustic energy which a porous material is able to dissipate depends generally on the open porosity, mean cell size and cell size distribution. The control of the time and surface tension in the foaming process is a key to creating open and interconnected cells of the right size. Therefore, this work investigates the influence of catalysts and surfactants on the foaming process. More specifically, this chapter studies the influence of the various ingredients used to produce the recycled materials on their resultant acoustical and non-acoustical properties. Suitable theoretical models for the acoustical properties of porous media are used to inform the material production process and to infer the key non-acoustical parameters of the porous structure.

3.2 Waste Stream Selection

This study has investigated the use of tyre waste in order to develop a porous media for sound absorption; there are several reasons for the selection of tyre waste. Problems of landfill for tyre waste are reduced by recycling. Waste recycling is now one of the most important issues with regards environmental protection. Furthermore, waste recycling has more benefits in part of reduced consumption of energy, reduced amounts of solid waste and reduction of resources. In case of recycling plastic waste, it is placed into raw material or feedstock in order to produce new materials by reprocessing. Vehicle tyres are produced by natural rubber and synthetic rubbers, which have cross-linkers in the molecular chains. Therefore, the tyre waste cannot be break down their cross-linked chains by reprocessing with only heat. It is now known that tyre waste can be recycled by a decross-linking agent or reclaim agent, pressure and steam (called devulcanization and reclaiming rubber). This method has a high cost of operation and uses a highly technical process. The work proposed here is concerned with compounding shredded tyre waste with a foaming agent to produce a porous material. In this study, the tyre shred residue used contains a mixture of granulated rubber bonded to fibres and nylon fibres. Fibres and wools are good absorbers, which is used widely in sound absorbing. Therefore, the use of tyre shred residue help to improve performance of sound absorption and has low cost of production in porous material.

3.3 Particle Size Distribution of Tyre Shred Residue

The tyre shred residue used in this study was supplied by Credential Tyre Recycling Ltd. and came in a granulated form as a mixture of nylon fibres and rubber grains bonded to the fibres. In this section, the tyre shred residue particle size distribution was determined by sieve analysis and fibre length by microscope. The details of the experiment procedure and data analysis are presented below.

3.3.1 Particle Sieve Analysis

In order to understand better the composition of tyre shred residue which was used to produce acoustic absorbers, experiments were carried out to determine its particle size and fibre length distributions. The tyre shred residue grain size distribution was determined with a sieving machine. This machine consists of a shaker and 12 sieves with different screen apertures of <0.063, 0.063, 0.15, 0.25, 0.50, 1.00, 2.00, 3.35, 4.00, 6.70, 8.00 and 10.00 mm which are depicted in Figure 3.1. Five samples of the original tyre shred residue material were sieved to obtain a statistical average and its standard deviation. The weight of each of the 5 material samples was 200 grams. The shaker was set to operate for 60 minutes. After the completion of one shaker cycle, the sieved sample in each screen was weighted with a standard laboratory scale and the grain size probability density function (weight fraction) was calculated. Figure 3.2 presents images of the sieved samples which correspond to each of the 12 sieve screens. It is clear that tyre shred residue is a complex material which consists of the granulated rubber, nylon staple fibres and nylon filament

fibres bonded to rubber. Figure 3.3 presents photograph of the three ingredients which constitute tyre shred residue. Figure 3.4 presents photographs of the material fractions which were removed from the 12 sieves at the end of this experiment. Table 3.1 presents the average weight fraction as a function of the sieve size and its standard deviation.



Figure 3.1: Experiment set up for sieve analysis

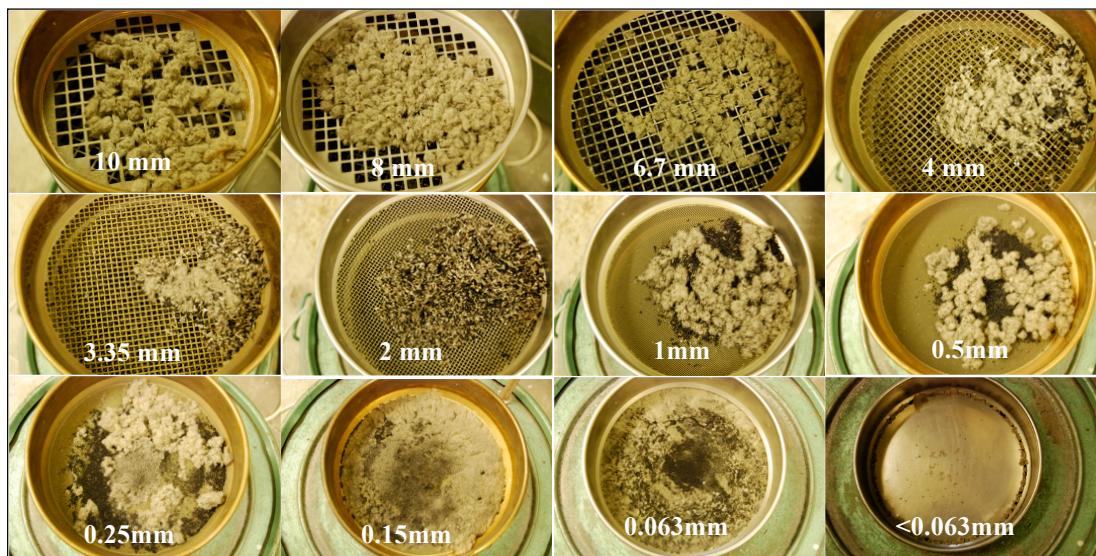


Figure 3.2: Illustration of tyre shred residue on the different size of screen capture

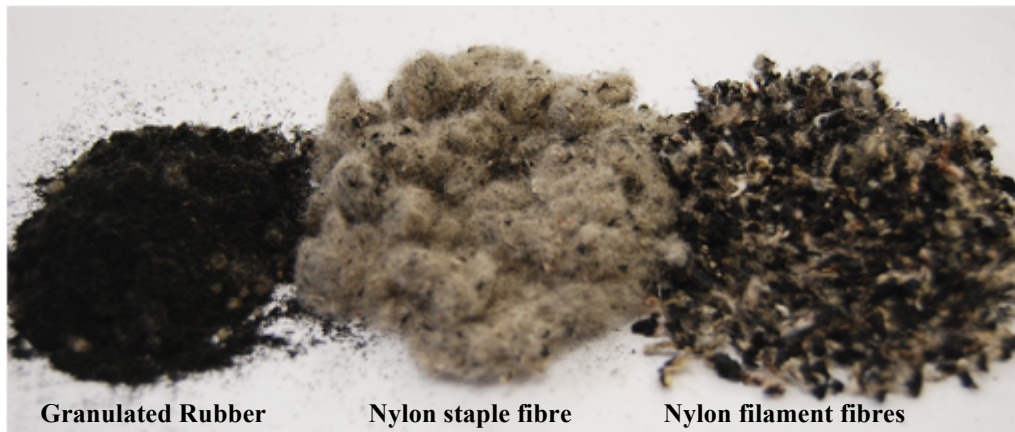


Figure 3.3: Illustration of granulated rubber, nylon staple fibre and nylon filament fibres bonded with rubber

Tyre shred residue captured with the sieves with the $<0.50\text{mm}$ hole sizes consists mainly of granulated rubber and nylon staple. The material which passed through the sieve sizes in the range of $0.50\text{mm} - 6.67\text{mm}$ contains a mixture of nylon fibres, rubber and staple. The material captured with the $>6.67\text{mm}$ hole size screens consists mainly of shredded rubber and nylon staple fibres. The particle size probability density function (weight fraction) of sieved in tyre shred residue is shown graphically in Figure 3.5. It is found that the highest proportion of tyre shred residue fall within the particle range of $0.5 - 4.0\text{mm}$. This fact is illustrated with the photographs in Figure 3.4, which show that in this particle size range a large part of nylon filament fibres are bonded with rubber.

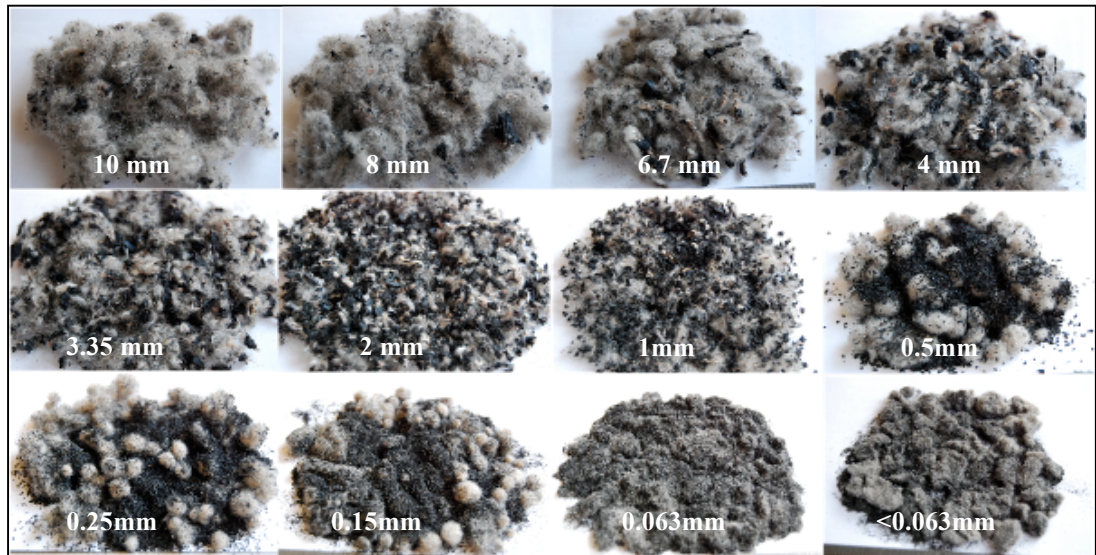


Figure 3.4: Images of tyre shred residue from the different hole size of the screen capture

Table 3.1: Weight fraction of the particle/fibre size for tyre shred residue

Sieve aperture (mm)	Average weight fraction
10.00	0.083±0.046
8.00	0.037±0.020
6.70	0.037±0.007
4.00	0.097±0.033
3.35	0.115±0.020
2.00	0.206±0.023
1.00	0.193±0.024
0.50	0.096±0.014
0.25	0.053±0.007
0.15	0.053±0.006
0.063	0.027±0.006
<0.063	0.003±0.003

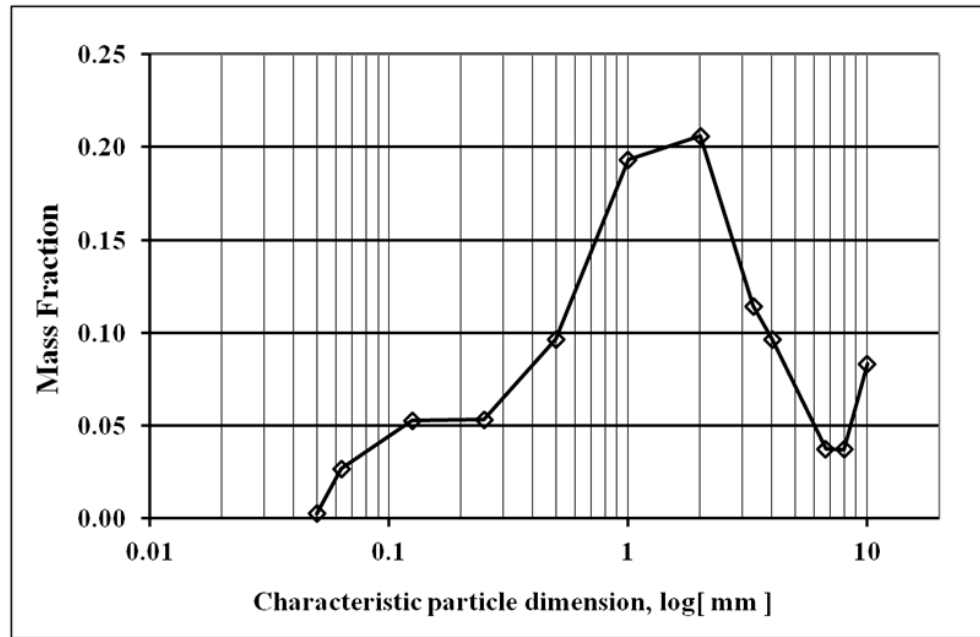


Figure 3.5: Weight distribution of the particle size for tyre shred residue

3.3.2 Filament Fibres Length Measurement

The length of recycled fibres is an important parameter in the material manufacturing process which controls the ability of the fibres to mix. This section describes the procedure for measuring the length of the nylon filament fibres bonded with rubber. The material studied in this section was obtained from sieve analysis of the tyre shred residue using the sieve sizes of 1.00, 2.00, 3.35, 4.00 and 6.67 mm. A sample of filament fibres in each screen capture was taken randomly from the twenty samples. Therefore, the total sample of these filament fibres is the 100 samples from 5 screens captures. A microscope with a digital camera (see Figure 3.6) was used in order to zoom in on the specimen until a suitable magnification was achieved to measure accurately the length of the filament fibre sample to the accuracy of 1mm. Figure 3.7 presents examples of the filament fibres samples of the different lengths photographed with this equipment. The length data obtained for 20 fibres in each screen capture were used to calculate the average fibre length, L , and its standard deviation as

function of the sieve size (Table 3.2). The probability density function for the filament fibre length was calculated by placing the filament fibres of the same length into individual bins. The bins were sorted by the smallest ($L=1.00\text{mm}$) to the largest values ($L=30\text{mm}$). The number of samples in each of the bins was counted and normalized by dividing by the total number of filament fibre measured to give the probability density value. Figure 3.8 shows the probability density values versus the filament fibre length. The corresponding cumulative filament fibre length (the probability density value multiplied by 100) is plotted in Figure 3.9.

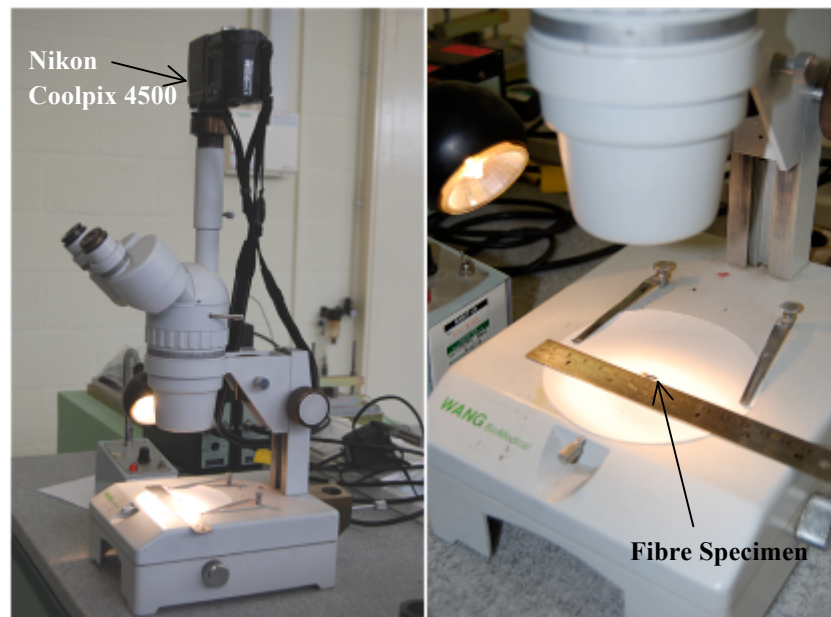


Figure 3.6: Microscope with camera setup for filament fibres length measuring

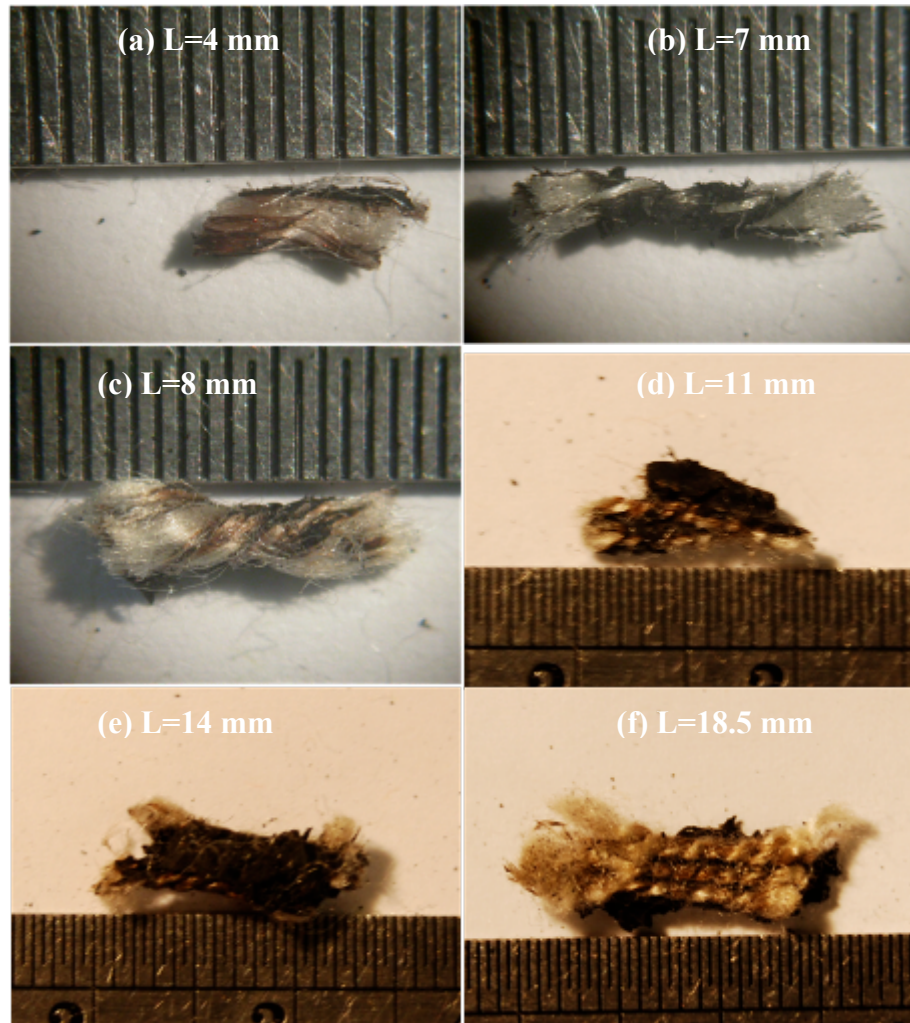


Figure 3.7: Examples of filament fibres collected from 6 different sieves

The results presented in Table 3.2 and Figures 3.8, 3.9 suggest that the length of fibres in tyre shred residue is in the range of 3.00mm-29.00mm. The length of filament fibres in a given capture is 3-6 times greater than the corresponding sieve size. The filament fibre length distribution is wide and its probability density function peaks around 6.00mm. The cumulative percentage of filament fibres length can be used to estimate that 50% of the filament fibres in tyre shred residue have the fibre length in the range of 3.00-900mm. The filament fibres length in the range of 10.00-17.00mm is only 40% and only 10%

of fibres are 18.00-29.00 mm long. This corresponds with the probability density function of filament fibres (shown in figure 3.8) that presents 0-0.02

Table 3.2: The average filament fibre length as a function of the sieve size

Hole Size of Screen Capture	Average fibre length, L , (mm)
1.00 mm.	6.67 \pm 4.02
2.00 mm.	7.59 \pm 3.16
3.35 mm.	10.60 \pm 2.45
4.00 mm.	13.95 \pm 3.36
6.67 mm.	18.92 \pm 6.07

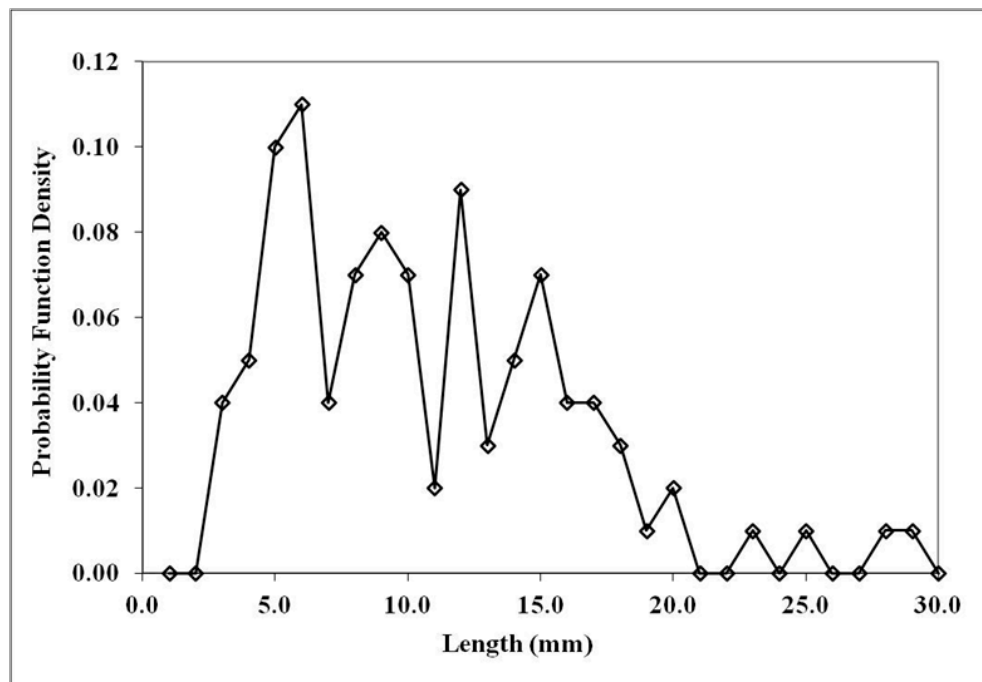


Figure 3.8: Filament fibres length distribution

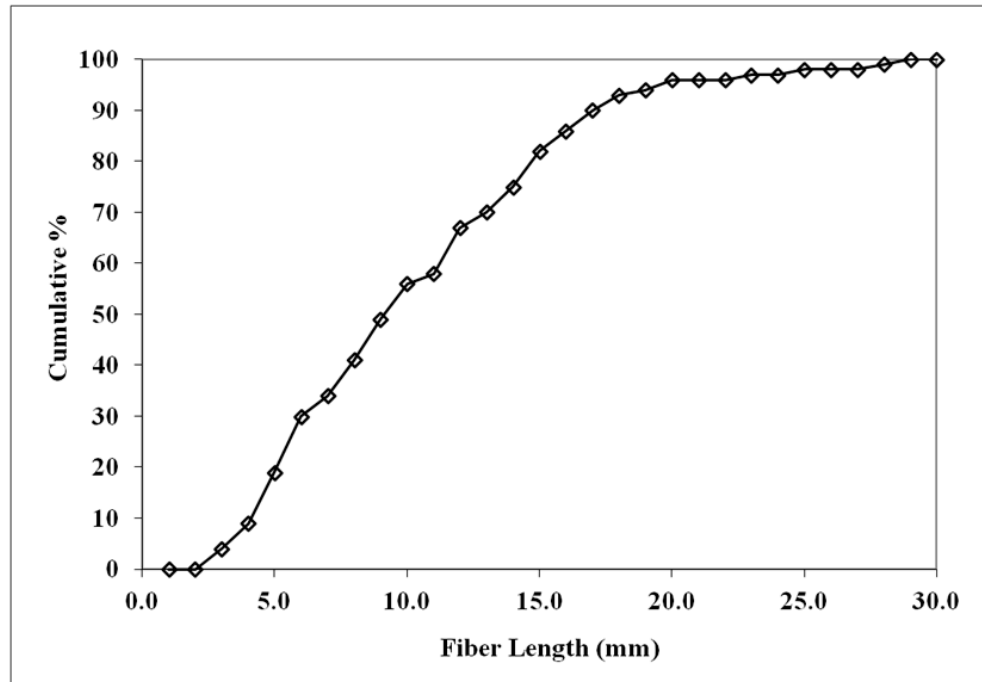


Figure 3.9: Cumulative percentage of filament fibres length

3.4 Control of Structure of Porous Materials by Chemical Reaction Methods

This section studies the effect of the compositions used in order to find the optimum formulation for producing effective porous materials. These compositions are tyre shred residue, water, the particle size of tyre shred residue, catalyst and surfactant, which directly effects the non-acoustical properties. The open porosity and pore size distribution which are important non-acoustical properties considered in this study, which have a strong influence on sound propagation into pore media and relate directly to sound absorption performance. Furthermore, this study has been concerned in the low production cost, environment friendly and performance of the produce. This section described the details of the experimental procedure (materials, sample

preparation and material characterisation), results and discussion of the composition of the porous materials as follows.

3.4.1 Experimental Procedure

Materials and Sample Preparation: The raw materials for the production of this material sample are:

- Polyurethane (PU) binder (Flexilon 457) supplied by Rosehill Polymers Ltd. This binder is based on methylene diphenyl diisocyanate (MDI), which contains 9.8-10.8% of isocyanate and has 1300-1600 cps of viscosity at 25^oC
- Polyurethane (PU) binder (Flexilon 1109) supplied by Rosehill Polymers Ltd. This binder is based on methylene diphenyl diisocyanate (MDI), which contains 8.5-9.5% of isocyanate and has 2500-3300 mPas of viscosity at 25^oC.
- Tyre shred residue supplied by Credential Tyre Recycling Ltd. and comes in the granulated form, which is a mix of nylon fibres and rubber grains bonded to the fibres. The sieve analysis data for tyre shred residue are shown in section 3.2.
- Catalyst supplied by BASF The Chemical Company. The chemical name is 2,2'-Dimorpholinyl-diethylether (DMDEE).
- Surfactant supplied by Cognis Corporation. The chemical name is β -alanine, N-coco alkyl derivs. (Sodium salts K280).
- Water is the one important reactant that reacts with MDI binder at room temperature. It produces carbon dioxide gases (CO₂). In this way, the water was used as a blowing agent in the foaming process.

The preparation of all samples for this study has the same step, which explains as follows. However, the preparation in each case has different compositions shown in tables 3.3-3.8. Accordingly, the calculation of the ratio in the variation column of each case was based on 100 percentages of polyurethane binder. Follows are the details of sample preparation for T20. The first step, the tyre shred residue and water listed in Table 3.3 were mixed in a 2 liter beaker until tyre shred residue wetted. The next step, the wetted tyre shred residue and MDI binder were mixed with a spatula for 60 seconds. The mixtures were poured in a rectangular mould and then covered with a lid on the top surface. The dimension of this mould was 200mm x 200mm and its height was 50mm as is shown in figure 3.10. In this way, the polyurethane polymerisation reaction occurred in this mould, which has a chemical reaction as shown in figure 2.6 (section 2.3 in chapter 2). The CO₂ by products from this polymerisation reaction were trapped inside the polymer matrix. It was estimated that the polymerisation reaction for T20 sample took on average 120 mins to complete, resulting in a fully consolidated sample. The polymerisation reaction time in each case depends on the compositions of each sample, which was explained the details of measurement for reaction time and reaction rate in the next section. The samples shown in table 3.3-3.8 were reproduced three times.

The completely consolidated sample was removed from this mould, shown in figure 3.11(a). In this way, this resultant sample was cut to form a 29mm diameter by 30mm thickness for four specimens and a 100mm diameter by 30mm thickness for one specimen and the area selected for their specimens is shown in figure 3.11(b). These specimens were used for measuring non-

acoustical properties (porosity, density, flow resistivity) and acoustic absorption coefficient.

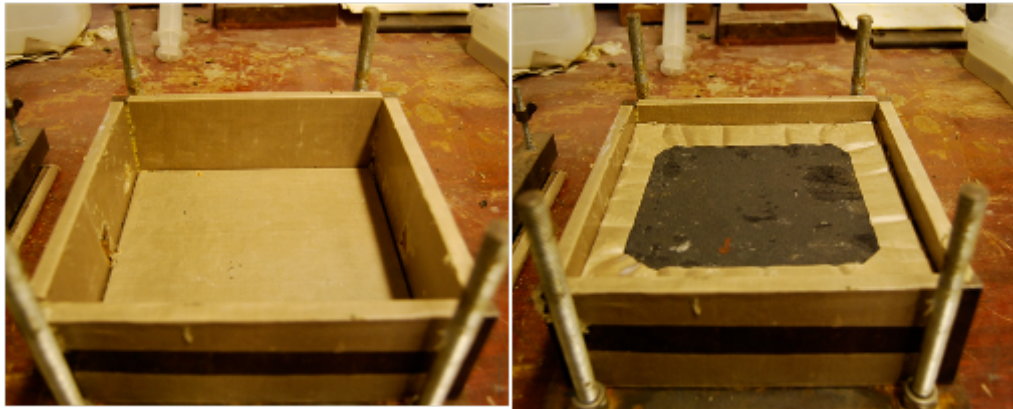


Figure 3.10: The rectangular mould for preparation the porous materials samples

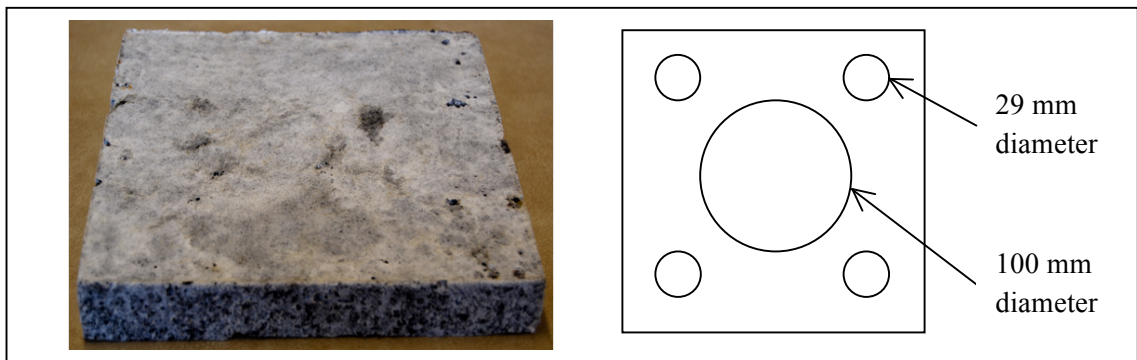


Figure 3.11: Illustration of the porous material sample and location of areas selected for cutting the specimens

Table 3.3: Formulation for producing the porous materials containing the different tyre shred residue

Samples	Variation	Reactants(kilograms)			Total (kilograms)
	Tyre shred residue (%)	MDI (Flexilon 457)	Tyre shred residue	Water	
T20	20	0.20	0.04	0.06	0.30
T40	40	0.20	0.08	0.06	0.34
T60	60	0.20	0.12	0.06	0.38
T80	80	0.20	0.16	0.06	0.42

Table 3.4: Formulation for producing the porous materials containing the different water

Samples	Variation	Reactants(kilograms)			Total (kilograms)
	Water (%)	MDI (Flexilon 457)	Tyre shred residue	Water	
H20	20	0.20	0.12	0.04	0.36
H30	30	0.20	0.12	0.06	0.38
H40	40	0.20	0.12	0.08	0.40

Table 3.5: Formulation for producing the porous materials using the different particle

Samples	Variation	Reactants(kilograms)			Total (kilograms)
	Hole size of screen capture	MDI (Flexilon 457)	Tyre shred residue	Water	
P0	No sieve	0.20	0.12	0.06	0.38
P05	≤0.05mm	0.20	0.12	0.06	0.38
P1	1.00mm	0.20	0.12	0.06	0.38
P2	2.00mm	0.20	0.12	0.06	0.38
P3	3.35mm	0.20	0.12	0.06	0.38
P4	4.00mm	0.20	0.12	0.06	0.38
P6	≥6.67mm	0.20	0.08*	0.06	0.34

Note: * the use of tyre shred residue in the sample is less than other samples because it contains the large part of nylon staple fibre which has a light weight.

Table 3.6: Formulation for producing the porous materials containing the different catalyst

Samples	Variation	Reactants(kilograms)				Total (kilograms)
	Catalyst (%)	MDI (Flexilon 457)	Tyre shred residue	Water	Catalyst	
C0_M457	0	0.20	0.12	0.06	0.000	0.380
C1_M457	1	0.20	0.12	0.06	0.002	0.382
C2_M457	2	0.20	0.12	0.06	0.004	0.384
C3_M457	3	0.20	0.12	0.06	0.006	0.386
		(Flexilon 1109)				
C0_M1109	0	0.20	0.12	0.06	0.000	0.380
C1_M1109	1	0.20	0.12	0.06	0.002	0.382
C2_M1109	2	0.20	0.12	0.06	0.004	0.384
C3_M1109	3	0.20	0.12	0.06	0.006	0.386

Table 3.7: Formulation for producing the porous materials containing the different surfactant

Samples	Variation	Reactants(kilograms)				Total (kilograms)
	Surfactant (%)	MDI (Flexilon 1109)	Tyre shred residue	Water	Surfactant	
S0	0	0.20	0.12	0.06	0.000	0.380
S2	2	0.20	0.12	0.06	0.004	0.384
S4	4	0.20	0.12	0.06	0.008	0.388
S6	6	0.20	0.12	0.06	0.012	0.392
S8	8	0.20	0.12	0.06	0.016	0.396
S10	10	0.20	0.12	0.06	0.020	0.400
S12	12	0.20	0.12	0.06	0.024	0.404

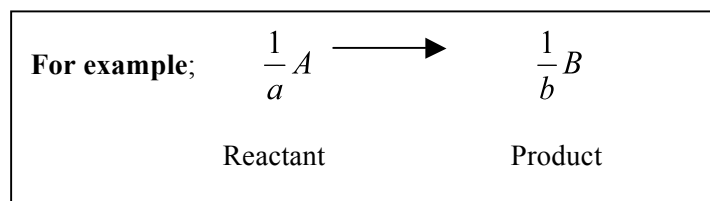
Table 3.8: Formulation for producing the porous materials containing the different surfactant at 3% catalyst

Samples	Variation	Reactants(kilograms)					Total (kilograms)
	Surfactant (%)	MDI (Flexilon 457)	Tyre shred residue	Water	Catalyst	Surfactant	
C3S0	0	0.20	0.12	0.06	0.006	0.000	0.386
C3S1	1	0.20	0.12	0.06	0.006	0.002	0.388
C3S2	2	0.20	0.12	0.06	0.006	0.004	0.390
C3S3	3	0.20	0.12	0.06	0.006	0.006	0.392
C3S4	4	0.20	0.12	0.06	0.006	0.008	0.394
C3S5	5	0.20	0.12	0.06	0.006	0.010	0.396

3.4.2 Measurement of Reaction Rate

Reaction rate is one factor that relates directly with expanding time in foaming processes. The expanding time is a key parameter controlling the cell size of the porous materials. In particular, the reaction rate is defined in terms of the change in the concentration of reactant or product in the unit time (Keeler and Worthers, 2008) [42].

$$Rate = \frac{\text{change in concentration during the interval } \Delta t}{\Delta t} \quad (3.1)$$



The decreased concentration of reactant and the increased concentration of product are plotted as function of time [42], which is shown in figure 3.12. The reaction rate can be found from slope of the graph in figure 3.12

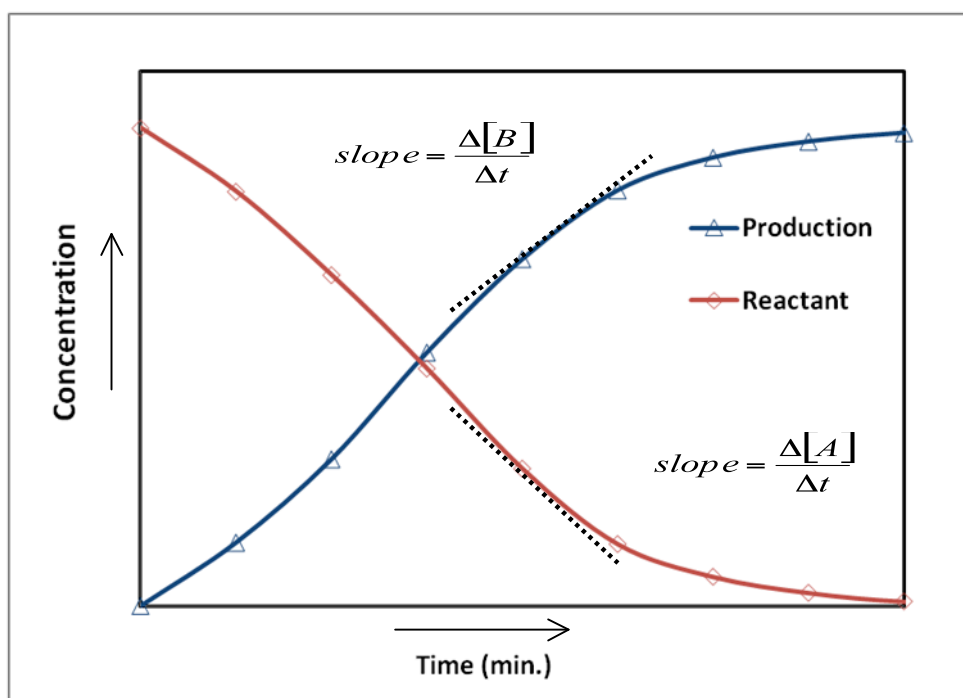


Figure 3.12: Illustration of how to find the slope for reactant and production

Therefore:

$$\text{Reaction rate} = \frac{1}{a} \times \text{slope of a plot of } [A] \text{ against time} \quad (3.2)$$

where $\frac{1}{a}$ is the stoichiometric coefficient of A (reactant) in the balanced chemical equation. In this work, the reaction rate can be measured by the amount of CO₂ products, which obtain from the polyurethane polymerization. The chemical reaction of this polymerisation is shown in Figure 2.6 (chapter 2,

section 2.5). Figure 3.13 illustrates the experimental setup for measuring reaction rate and reaction time of the polyurethane polymerisation.

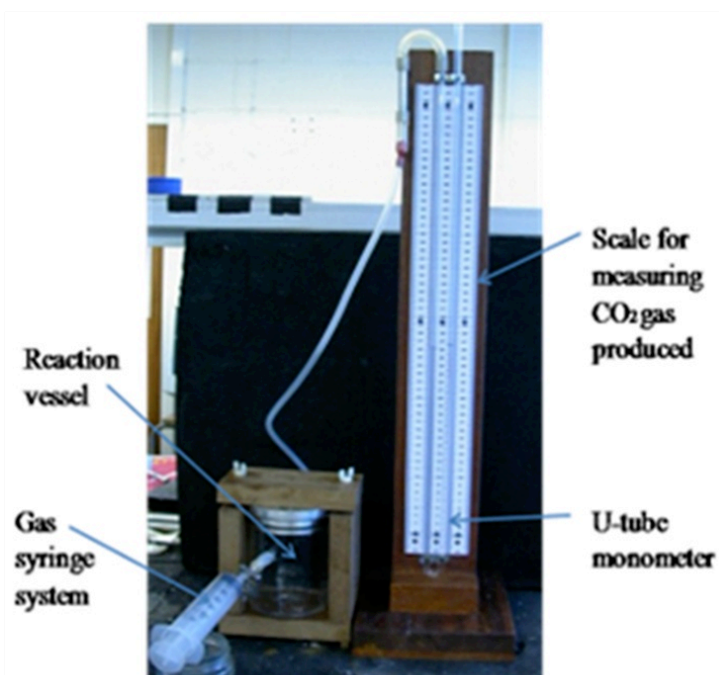


Figure 3.13: Experimental setup for measuring the reaction rate for the porous samples

The CO₂ obtained from this reaction and the volume is measured in the cm³ unit. In this experiment, the volumes of CO₂ were recorded in each minute until the complete of the reaction. It means the volume of CO₂ is zero. The volume of CO₂ for all samples was measured under atmospheric pressure and room temperature. In this study, the rate of reaction was determined from slope of the graph plotted between cumulative CO₂ volume and time as is shown in Figure 3.14 for example;

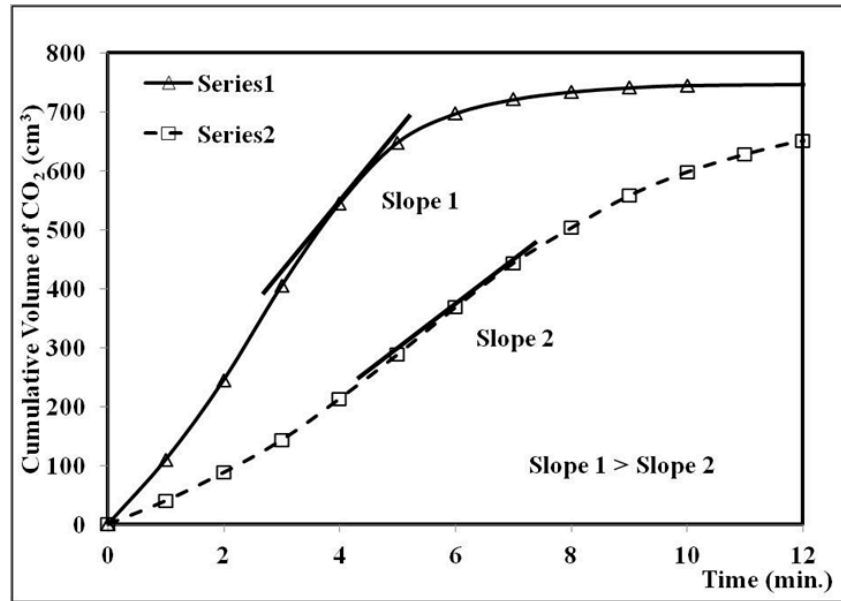


Figure 3.14: Illustration of finding the rate of polyurethane polymerization from slope of the cumulative volume CO₂ curve

In this study, the reaction rate in each case was measured three times. Three cumulative CO₂ data points were obtained and the average calculated in each case, which was plotted as function of time and then it was presented and discussed in the next section.

3.4.3 Measurement of Absorption coefficient

The acoustic absorption coefficients of the material samples were measured in this study by using a standard BS EN ISO 10534-2 [43]. This method uses an impedance tube with a sound source connected to one end and the test sample mounted in the tube at the other end. Figure 3.15 presents layout of test equipment for determination of sound absorption coefficient and impedance in impedance tube. In this test method, plane waves are generated in a tube by the sound source, and the decomposition of the interference field is realised by the measurement of acoustic pressures at two fixed locations using a wall-mounted microphones and subsequent calculation of the sound absorption coefficient and the normal acoustic impedance.

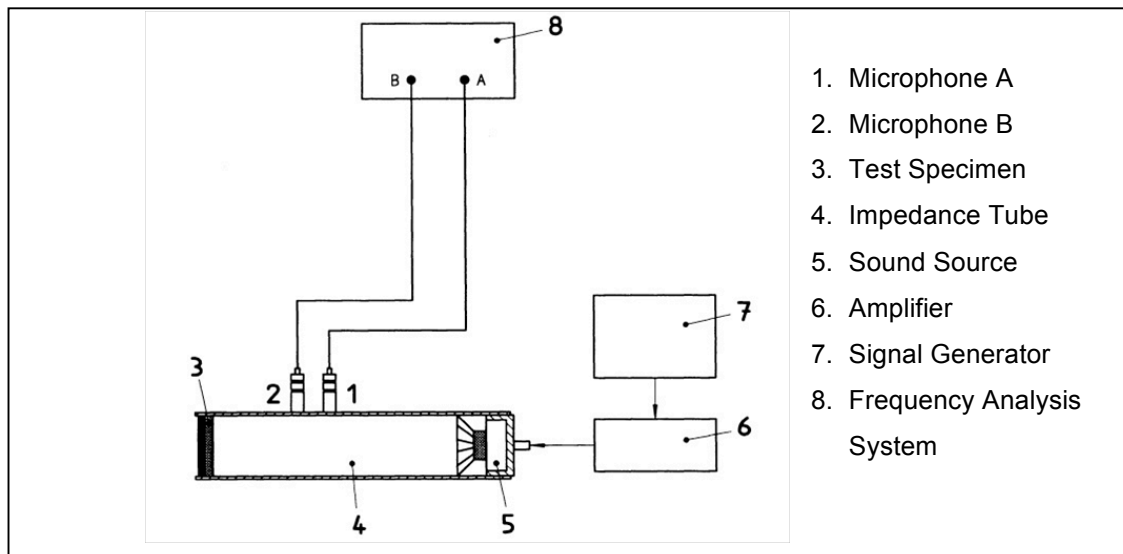


Figure 3.15: Illustration of layout for test equipment [43]

This study was carried out in a two-microphone Bruel Kjael (BK4206) impedance tube (shown in figure 3.16) at a normal angle of incidence and in the frequency range of 200-6400 Hz. The software Bruel Kjael *"PULSE" version 14.0* was used to control the experiment and to measure the normal incidence absorption coefficient of the material samples. This study used the small tube for testing all of the materials samples in this section. Three specimens of 29mm diameter and 30mm thickness in each case were measured the absorption coefficient. Here, the absorption coefficient spectra of the average and standard deviation calculated by three absorption coefficient data obtained, which are presented in the appendix B. The average values of the absorption coefficient in each case are discussed in the next section.

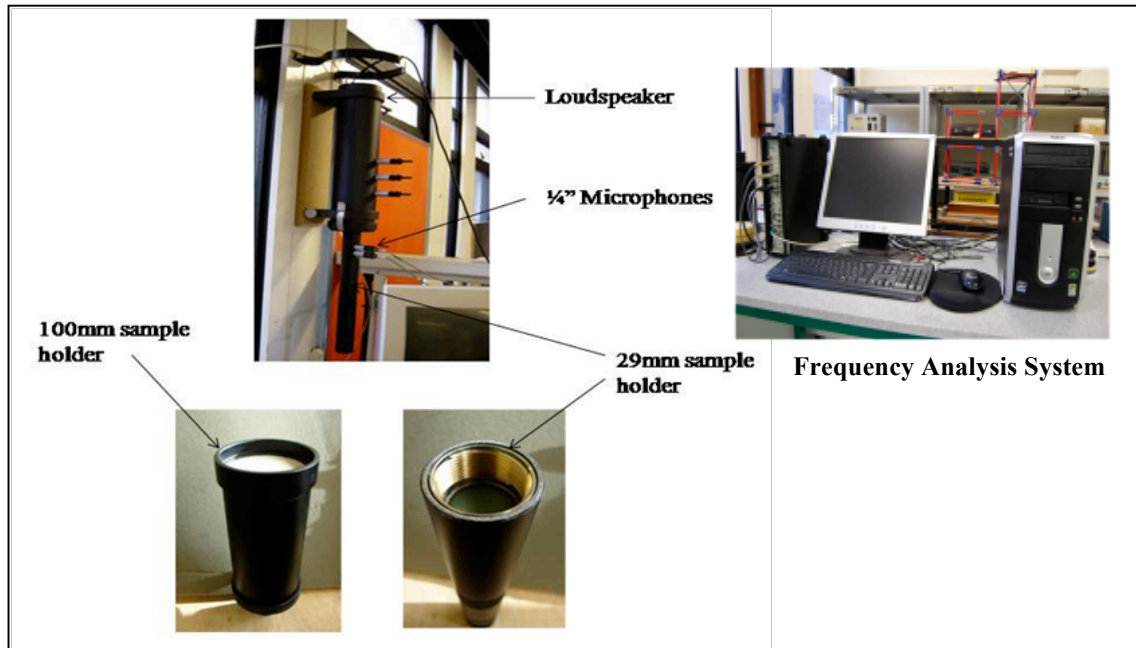


Figure 3.16: Illustration of the impedance tube equipment

3.4.4 Measurement of Non-acoustical Properties

The key non-acoustical properties of porous materials used for sound absorption applications are: (i) flow resistivity; (ii) porosity; (iii) pore size distribution. These parameters are can be used in theoretical and semi-empirical models to predict the acoustic characteristic impedance, complex wave number and absorption coefficient of porous media.

3.4.4.1 Flow resistivity

The flow resistivity of the acoustical materials is important non-acoustic property which related to the pore size and pore connectivity. The flow resistivity is the resistance which the material exhibits to a flow of air through its pores. In this study, the specific flow resistivity (σ) was measured by using a standard ISO 9053 method detailed in [44], which can be expressed as:

$$\sigma = \frac{(\Delta P)\pi r^2}{q_f(\Delta x)} \quad \left[\frac{Pa.s}{m^2} \right] \quad (3.3)$$

Where ΔP is the air pressure difference across the test specimen, q_f is the volumetric air flow rate in m^3/s , Δx and r are the thickness and the radius of the test specimen, respectively. The experimental setup for measurement of the specific flow resistivity is presented in Figure 3.17. It consists of three differential pressure transducers, laminar flow element, conical glass tube and a sample holder. Two differential pressure transducers are used to measure the pressure drop across the specimen, ΔP , in the range of 0-20 Pa and 0-100Pa. The other pressure transducer is connected to the laminar flow element and calibrated to measure volumetric flow rate through the specimen in the range of 0-30 litres/min. The outputs of these transducers are connected to a PC via a NI UBS-6008 data acquisition card. The pressure drop is measured for a range of flow velocities which are typically kept below 1mm/sec. The flow resistivity is then calculated according to equation (3.3) as the best fit to the experimentally obtained dependence $\Delta P = f\left(q_f / (\pi r^2)\right)$ which normally reduces to a linear regression analysis.

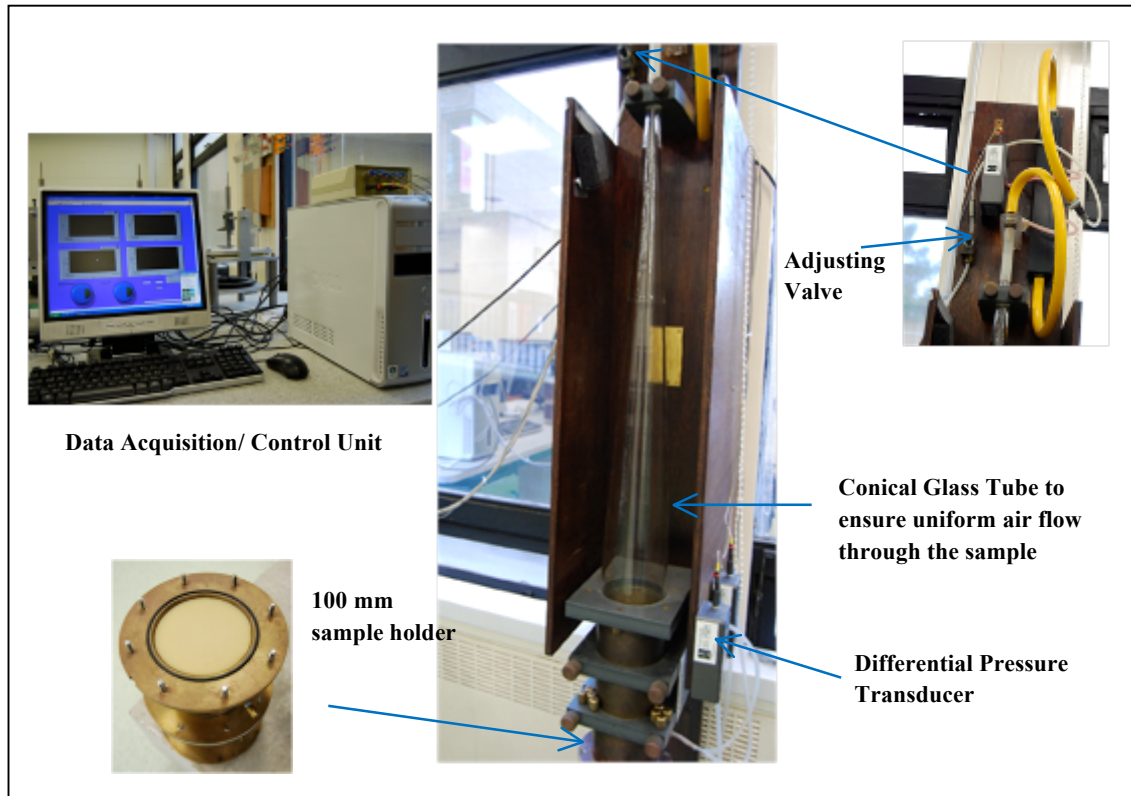


Figure 3.17: Flow resistivity measuring apparatus

3.4.4.2 Porosity

The pore space in the porous materials can be occupied by closed and open pores. The porosity, which is of importance to the acoustical absorption performance of a porous material specimen, is the volume fraction occupied by air in the network of open (interconnected) pores. The porosity can be expressed in terms of the ratio of the volume of the voids in the material to its total volume.

$$\phi = \frac{V_a}{V_T}, \quad (3.4)$$

where V_a is the volume of air in the open pores and V_T is total volume of the porous material sample.

The porosity in this study was measured by the method based on the ideal gas laws, which was proposed by Leclaire *et al* [45]. Figure 3.18 illustrates an experimental setup for measuring the porosity of a material sample. This apparatus consists of two air-tight chambers: reference chamber and measurement chamber. These chambers are connected to two sides of a U-tube manometer filled with water. The bottom of the U-tube is connected to a water-drawing piston, which can be moved forward and back with a piston. The porous material specimen is placed in the measurement chamber. At this stage, the two chambers and manometer valves A and B are opened so that the pressures in them are equal to the atmospheric pressure. Then, the valves and chambers are closed. The air volume in the measurement chamber has been decreased compared to its original volume because of the presence of the porous specimen. When the water in the U-tube manometer is drawn with the piston, the pressure in the two chambers changes and varies depending upon the chamber volume. The pressure equalisation of the two chambers is achieved by moving the calibration piston until the difference in the pressure difference between the two manometer tubes is zero and it no longer depends on the position of the piston. The volume in the measurement piston is equal to the volume occupied by the frame and closed pores in the porous specimen. The volume of open interconnected pores in the porous material specimen can then be calculated according to

$$V_a = V_T - V_s \quad , \quad (3.5)$$

where V_a is the volume of air in the porous specimen, V_T is the total volume of the porous specimen, V_s is the volume of solid in the porous specimen

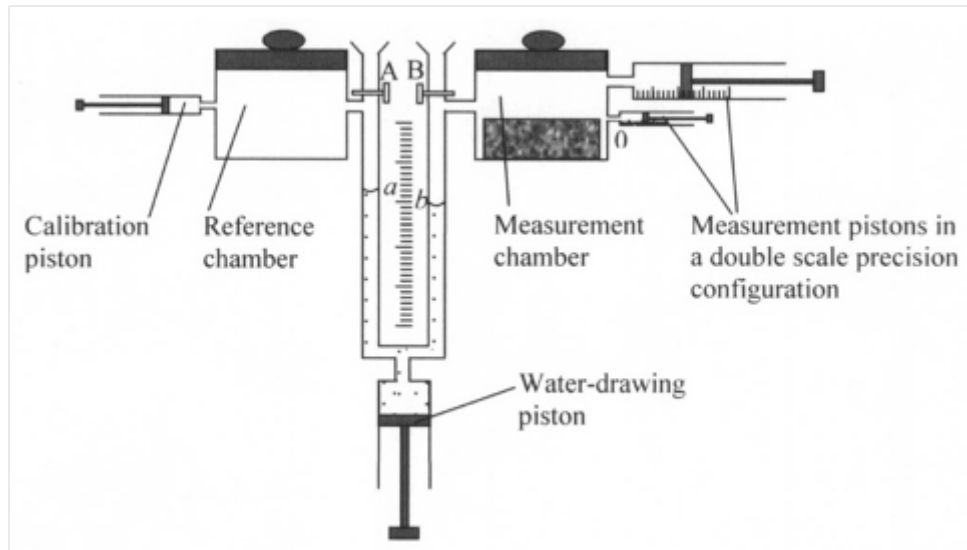


Figure 3.18: Experimental setup for the measurement of porosity [45]

In this study, it was common to use four 29 mm diameter material specimens to measure the porosity with the described method. Four values of the porosity were determined, the average and standard deviation were calculated.

3.4.4.3 Density

Material density is a very important parameter which relates to the porosity and amount of solid material which is needed to manufacture a specific volume of porous absorber. In this study, four specimens of 29mm diameter and 30mm thickness were used to measure the average material density. The weight of these specimens was measured by placing each specimen on the laboratory scales and dividing the recorded specimen mass by its volume. Four values of the density were calculated so that the average and its standard deviation could be obtained.

3.4.4.4 The Pore size and Pore size distribution

The pore size and pore size distribution determine the acoustic behaviour of the porous medium. The sound wave propagation is controlled

by the pore size, cell density and by the porosity. The pore size distribution is a main parameter which determines the viscous and thermal characteristic length [46]. Commonly, the smaller pores control the viscous dissipation and inertial effects and the larger pores control the thermal dissipation effects in the oscillatory flow between the pores.

In this study, the pore size distribution was measured using the optical method proposed described in the work by Pispola et al. [47]. An enhanced microscopic image of a porous structure taken with the microscope and digital camera is shown in Figure 3.6. Two 20x20mm non-equidistantly spaced areas were selected from each microscopic photograph for analysis with Optimax image processing software [48].

The analysis procedure was following. Firstly, the software was calibrated by an image of a 1mm graticule taken at 2.5x magnification under the optical microscope. Secondly, the threshold of image sample was set in order to focus on the pores as is shown in Figure 3.19.

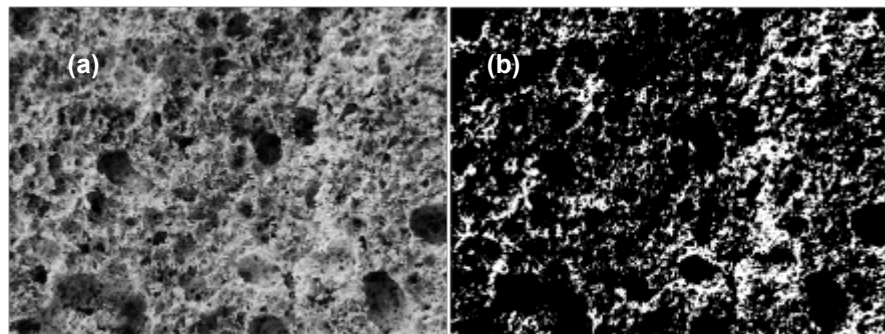


Figure 3.19: (a) Image of porous material sample before set up threshold, (b) Image highlighting the pores used to determine the pore size distribution

Thirdly, optimax software was used to detect the pores and measure the average pore diameter by fitting the pore's centroid to each of the detected pores. In this process, the mean pore diameter was calculated as the average

of the diagonals taken at 2 degree intervals and passing through this centroid as illustrated in Figure 3.20.

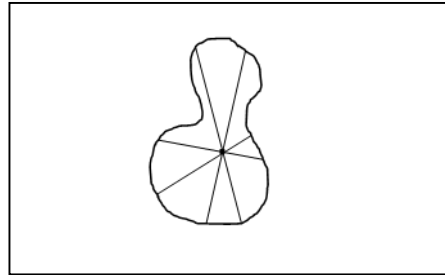


Figure 3.20: Calculation of the mean pore diameter by fitting the pore centroid.

Finally, the pore size distribution histogram was constructed by placing the pores of the similar size into individual bins. The number of samples in each of the bins was counted and the data was normalised by dividing by the total number of pores so that the probability density function (PDF) of pore size was determined as a function of the logarithm of the pore radius.

3.5 Effect of the Contents of Tyre Shred Residue for Production Porous Material

This section studies the effect of tyre shred residue on the non-acoustical and acoustical properties of the porous material. Tyre shred residue is one component in production of the porous material samples which was used as a filler. The porous material samples were produced by according to the formulations listed in Table 3.3. In this study the amount of tyre shred residue was: 20% (T20), 40% (T40), 60% (T60) and 80% (T80). The tyre shred residue ratio by weight to polyurethane binder was calculated.

The non-acoustical properties of these samples such as reaction time, density, porosity and flow resistivity were measured and these are presented in Table 3.9. Figure 3.21 presents the reaction rate of the polyurethane

polymerisation for different amounts of tyre shred residue. The reaction rate was determined by the slope of the graph shown in Figure 3.21. It was found that the reaction rate increases and reaction time decrease with the increased amount of tyre shred residue. The difference in reaction time between sample T20 (the lowest amount of tyre shred residue) and sample T80 (the highest amount of tyre shred residue) is 32 minutes. This is a significant difference that can be explained by the fact that the surface area of active sites in the polymerisation reaction increased with the increased amount of tyre shred residue. Therefore, sample T80 that contains the largest amount of tyre shred residue has the shortest reaction time and the highest reaction rate. In particular, expanding time is the period of time for bubble growth in the foaming process, which is an important factor in controlling the pore size of the porous materials which are produced with the foaming process. The expanding time in the foaming process relates directly to reaction time and reaction rate of polymerisation reaction. In this study, microscopic images of the materials (see Figure 3.22) produced in this work suggest that the porous structure consists of micro- and meso-pores. These images were used to measure the pore size distribution of samples T20, T40, T60 and T80. Figure 3.23 present the mean pore size distribution data for all the four samples. The pore size distribution data illustrates clearly that the proportion of smaller pores increases with increasing amount of tyre shred residue. Sample T80 contains a larger proportion of smaller pores, which has the highest value of PDF in the micro-pore range (0.1 mm). The pore size distribution determined for samples T20 and T40 is similar. Here, the PDF of the meso-pore (1.00 mm) for these two samples is a higher value than the micro-pore (0.1 mm). But sample T20 has

the highest value of PDF in the meso-pore (1.00 mm). In the case of samples T20, T40 and T60, the pore size distribution is clearly bi-modal and it peaks around 1mm (meso-pores) and 0.1mm (micro-pores).

Table 3.9: Summary of non-acoustical properties for the porous materials produced by the different amount of tyre shred residue

Sample	Composition of Tyre Shred Residue (%)	Reaction time (min)		Density (kg/m ³)		Porosity		Flow Resistivity [N.m.s ⁻⁴]
		average	STD	average	STD	average	STD	
T20	20%	122	2.0	194	21	0.87	0.015	4381
T40	40%	120	1.5	274	20	0.84	0.013	8852
T60	60%	95	2.4	303	24	0.82	0.016	27522
T80	80%	90	2.5	423	20	0.67	0.018	54578

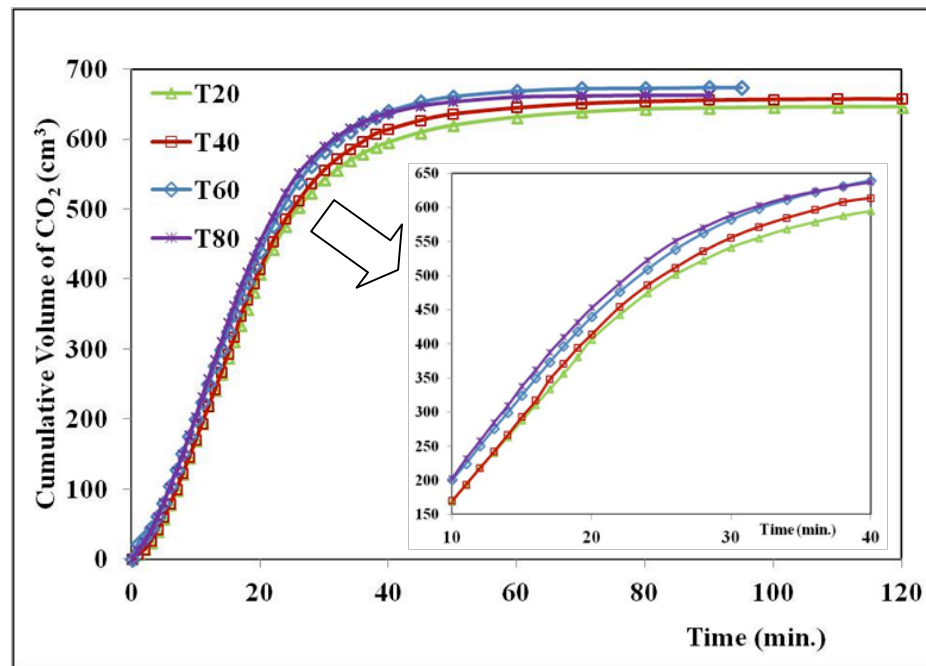


Figure 3.21: Reaction rate of the porous materials produced by the different contents of tyre shred residue

The density and flow resistivity of samples T20, T40, T60 and T80 increase as more tyre shred residue is added. It was found that the porosity of these samples reduces with the increased amount of tyre shred residue. The difference in the density, porosity and flow resistivity between samples T20 and

T80 is 218%, 77% and 1245%, respectively. These results illustrate clearly that the amount of tyre shred residue has an obvious effect on the reaction time, reaction rate, density, porosity and flow resistivity.

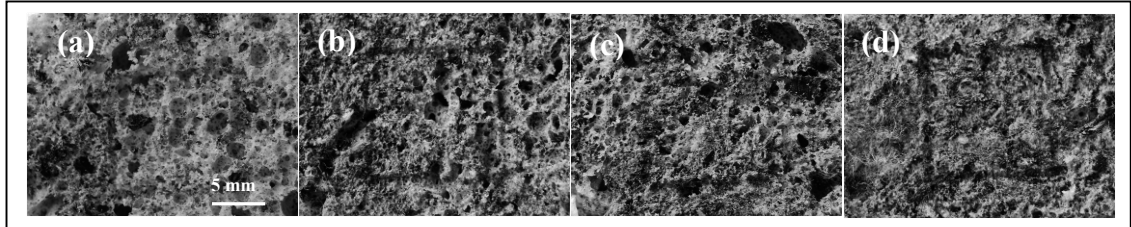


Figure 3.22: Microscopic images of porous materials produced with different amount of tyre shred residue: (a) 20%, (b) 40%, (c) 60% and (d) 80%

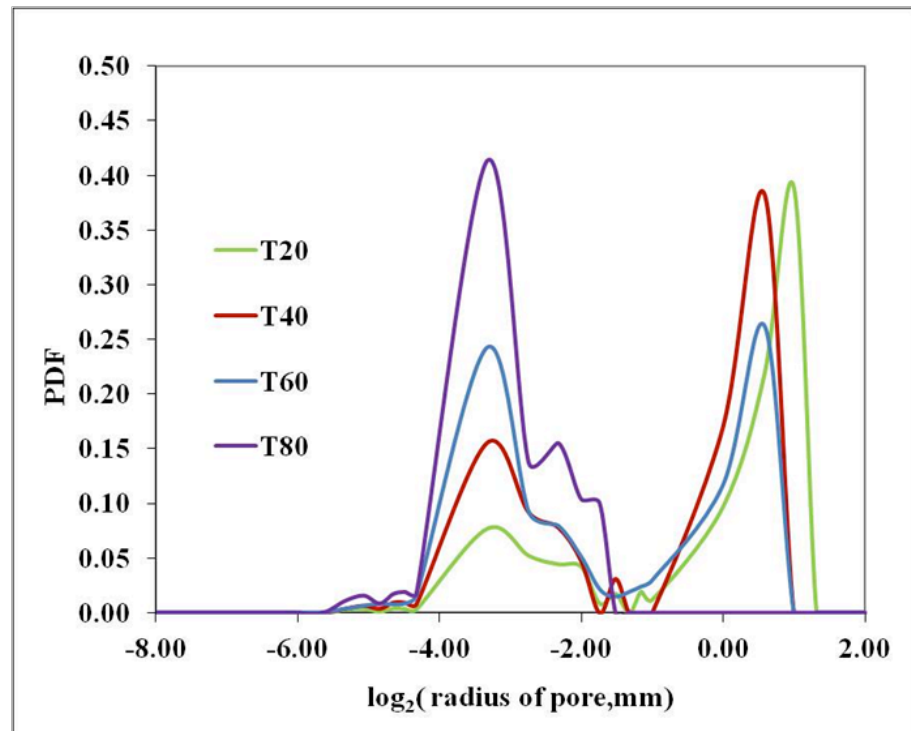


Figure 3.23: The probability density function of the pore size for the porous materials produced with different amounts of tyre shred residue.

Figure 3.24 shows the acoustical absorption coefficient spectra of samples T20, T40, T60 and T80. The samples T20 and T40 have similar spectra of absorption coefficient which peak in the frequency range of 1300-

3000 Hz and around 4300 Hz. The similarity in the absorption coefficient spectra can be explained by the similarity in the pore size distribution in samples T20 and T40 which contain similar proportions of meso-pores (>1mm). In the case of sample T60, the maximum in the absorption coefficient spectrum shifts towards the low frequency range and peaks around 700-1300 Hz. This is explained by the pore size distribution in sample T60, which contains a higher proportion of the micro-pores (0.10mm) than samples T20 and T40. The absorption coefficient of sample T80 is limited. It can be explained by its limited porosity (67%) and a relatively high flow resistivity (54578 Pas m⁻²). The pore size distribution in this sample suggests that it consists entirely of micro-pores which are less than 100 μm.

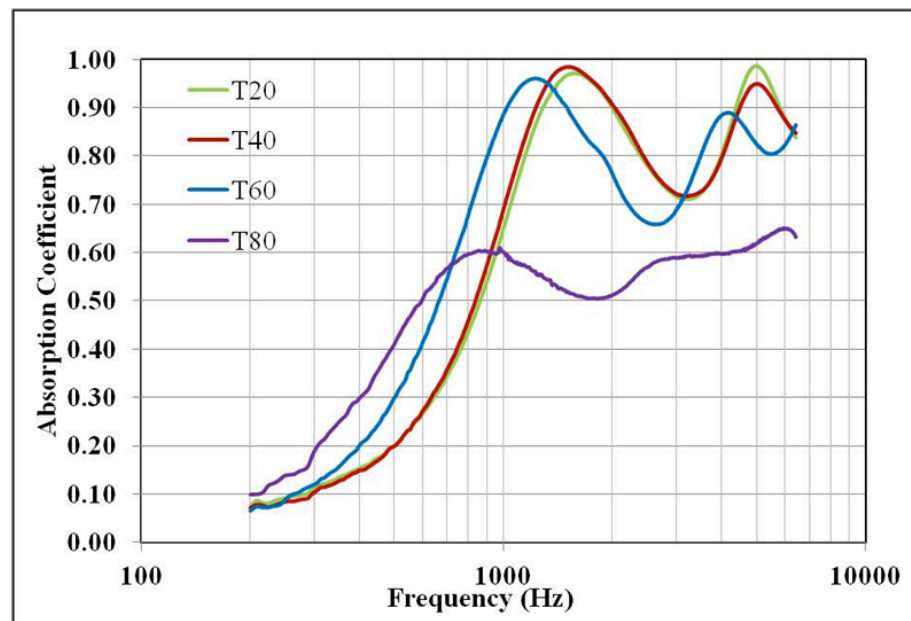


Figure 3.24: The normal incidence, plane wave absorption coefficient spectra for the porous materials produced with variable amounts of tyre shred residue

This part of the study indicates that the amount of tyre shred residue strongly affects the non-acoustical and acoustical properties of porous materials manufactured with this process. Increasing the amount of tyre shred residue

beyond 60% results in a higher reaction rate which leads to porous samples with a lower values of porosity and higher flow resistivity. Therefore, the amount of tyre shred residue must be carefully controlled in order to produce the effective porous materials.

3.6 Effect of the Contents of Water for Production Porous Material

This section studies the effect of water on the non-acoustical and acoustical properties of the porous material. Water is an important reagent in the production of the porous material samples using the foaming process. Here water is used as a blowing agent for the production of polyurethane foam at room temperature. In this work porous samples were produced using material formulations listed in Table 3.4. The amount of water was varied in three steps from 20% to 40%: 20% (H20), 30% (H40) and 40% (H40). The percentage of water was presented as a ratio of weight of water to that of polyurethane binder. The non-acoustical properties of these three samples are presented in Table 3.10. This table lists the reaction time, density, porosity and flow resistivity. Figure 3.25 represents the data on the amount of CO₂ produced during the foaming process as a function of time for different amounts of water. The reaction rate of samples H20, H30 and H40 is determined by the slope of the graphs shown in Figure 3.25. The reaction rate increases with the increased water content. The difference in the reaction times in this experiment is small. In particular, polymerisation reaction of polyurethane in this study has two main functional groups, which are isocyanate group (from MDI) and hydroxy group (from water). This polymerisation reaction is created by these functional groups, which has multiple steps. It is a complex reaction which can be divided into two basic reaction types: an addition reaction and a self-addition reaction

[49]. The isocyanate groups in polyurethane binder enable both of these reactions. Therefore, stoichiometry ratio of this polymerisation reaction between isocyanate group (from MDI) and hydroxy group (from water) is not 1:1. This is a main reason which can be used to explain why the addition of more water has little or no influence on the reaction rate. It is clear that there is a threshold which corresponds to approximately 20% of water so that the reaction rate and reaction time of the samples H30 and H40 have very close values. As a result, measured values of non-acoustical properties of these two material samples are similar.

Table 3.10: The non-acoustical properties of the porous materials produced with different amounts of water.

Sample	Composition of Water (%)	Reaction time (min)		Density (kg/m ³)		Porosity		Flow Resistivity [N.m.s ⁻⁴]
		average	STD	average	STD	average	STD	
H20	20	100	2.0	339	13	0.78	0.020	40621
H30	30	95	2.4	303	24	0.82	0.016	27522
H40	40	94	1.5	292	18	0.83	0.012	29746

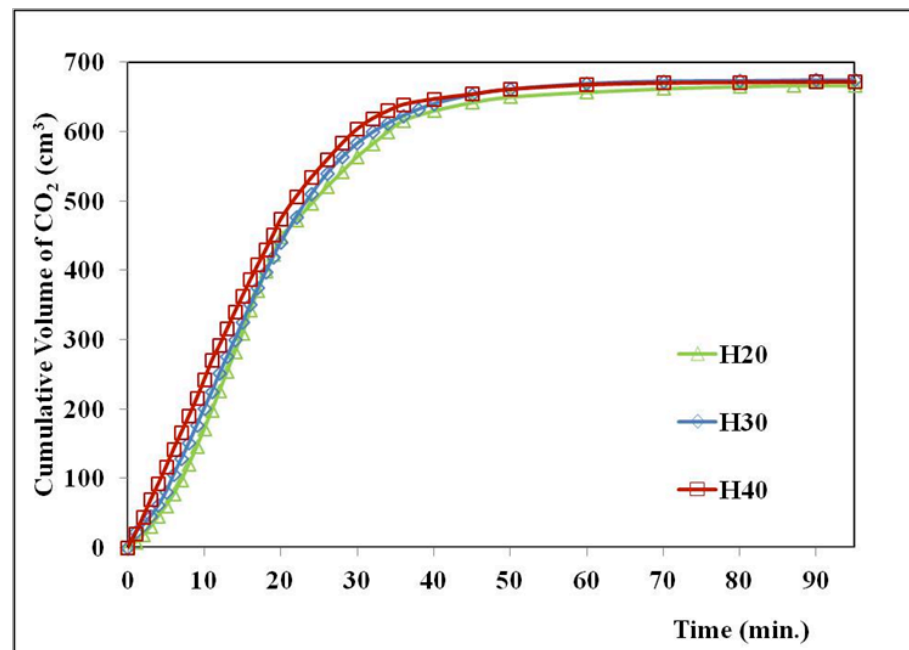


Figure 3.25: The reaction rate of the porous materials produced with different amounts of water

Figure 3.26 shows microscopic images of the surface of samples H20, H30 and H40. The pore size distribution of these samples is shown in Figures 3.27. It was found that all these materials consist of micro- and meso-pores. The pore size distribution data illustrates clearly that the proportion of meso-pores increases with increasing water. Samples H30 and H40 consist of pores of similar sizes. There are clear bi-modal peaks around near pore sizes of 1mm (meso-pores) and 0.1mm (micro-pores). Sample H20 consists of smaller pores than samples H30 and H40. This can be explained by the related small amount of water used for the production of sample H20. Therefore, the polymerisation reaction of sample H20 produced a smaller amount of CO₂ and resulted in the material sample with smaller pores in the solid polymer matrix.

The density and flow resistivity of samples H20, H30 and H40 decreases slightly as the amount of water increases. It was found that porosity of these samples remained relatively constant and unaffected by the variable amount of water. The differences in density, porosity and flow resistivity between sample H20 (the lowest amount of water) and sample H40 (the highest amount of water) are 86%, 106% and 73%, respectively. In case of samples H30 and H40, the density, porosity and flow resistivity values are close. It can be explained by the fact that the pore size distribution in these materials is similar (see Figure 3.26 and 3.27).

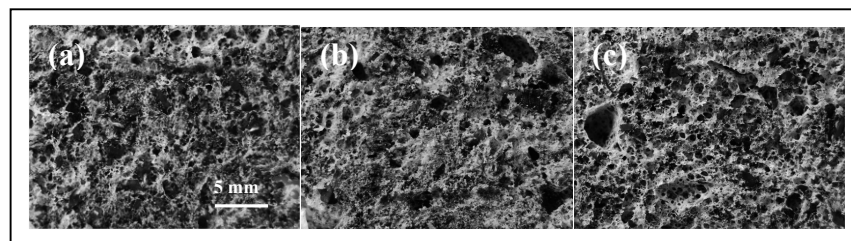


Figure 3.26: Microscopic images porous materials manufactured with different amounts of water: (a) 20%, (b) 30% and (c) 40%

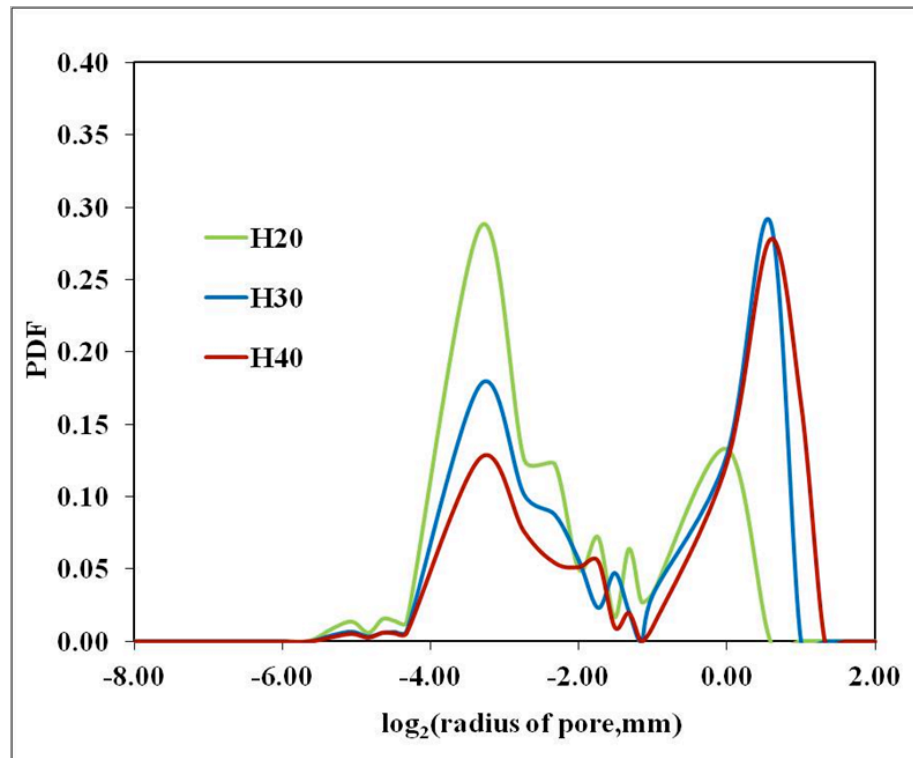


Figure 3.27: The probability density function of the pore size for the porous materials produced using different amounts of water

Figure 3.28 shows the acoustical absorption coefficient spectra of samples H20, H30 and H40. Sample H20 exhibits the lowest values of absorption coefficient. This phenomenon is consistent with the behaviour of non-acoustical properties: the highest density, lowest porosity, highest flow resistivity and the PDF biased towards the micro-pores ($<0.10\text{mm}$). The samples H30 and H40 have close absorption coefficient spectra which peak in the frequency range of 800-3000 Hz and around 4300 Hz. The observed similarity in the acoustical properties can be explained by the close values of the non-acoustical properties of samples H30 and H40: presence of larger pores, broader pore size PDF, lower density, higher porosity and a lower flow resistivity.

The results of the non-acoustical and acoustical properties in this case, indicate that the amount of water used for the production of the porous

materials has an upper limit and depends on stoichiometry ratio of this polymerisation reaction. Excess of water in the polymerisation reaction of polyurethane may be present in the material sample that contains higher moisture. It has an effect on the acoustical absorption performance which, in this case, can be limited.

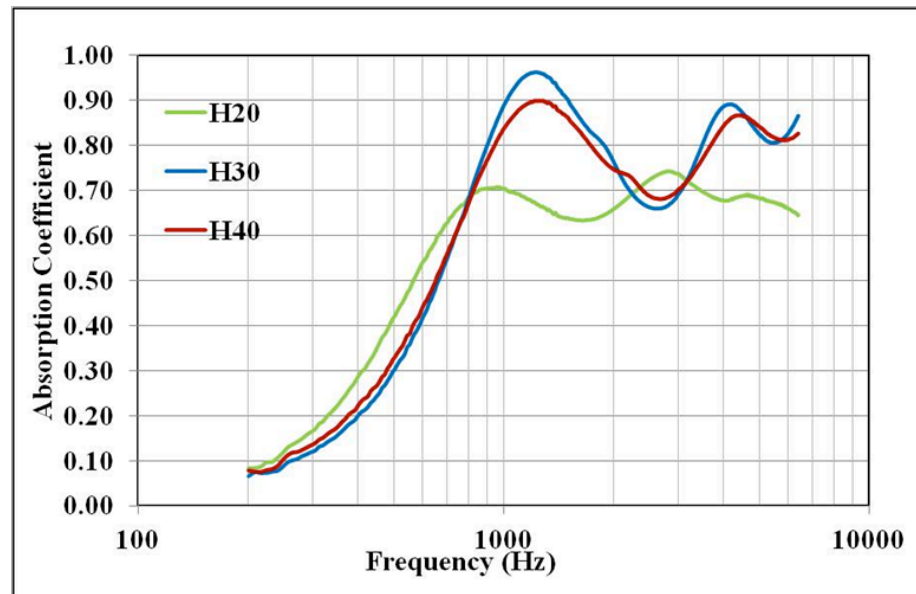


Figure 3.28: The absorption coefficient spectra for the porous materials produced using different amounts of water.

3.7 Effect of the different Particle Size of Tyre Shred Residue for Production Porous Material

This section studies the effect of particle size of tyre shred residue on the non-acoustical and acoustical properties of the porous material which are produced with the foaming process. Tyre shred residue was sieved using a set of sieves with the following mesh sizes: 0.05mm, 1.00mm, 2.00mm, 3.35mm, 4.00mm and 6.67mm. The material formulations which correspond to the tyre shred residue fractions obtained with the sieve separation process are presented in Table 3.5. These formulations were used to produce the porous

samples P0, P05, P1, P2, P3, P4 and P6 (see Table 3.5). The ratio by weight of tyre shred residue to polyurethane binder for all samples was 0.6 except sample P6. The ratio of 0.4 was used to produce sample P6, which was based on the tyre shred residue fractions with particle sizes greater than 6.67 mm. This screen capture contained a large amount of nylon staple fibre that was a relatively light weight material.

The non-acoustical properties of these samples (P0, P05, P1, P2, P3, P4 and P6) such as reaction time, density, porosity and flow resistivity are presented in Table 3.11. Figure 3.29 presents the amount of CO₂ gas released during the polyurethane polymerisation reaction as a function of the reaction time. This graph was used to determine the reaction rate as a function of the particle size of tyre shred residue.

The results show that the reaction rate is by and large independent of the particle size. The reaction rate in the case of sample P05 is slightly higher than in the case of other samples. It can be explained by the fact that the surface area of active site in this polymerisation reaction was relatively high because this formulation contained a larger proportion of small rubber granulates (<0.5mm).

Figure 3.30 shows microscopic images of the surface of the seven material samples produce with particles of variable size. The pore size distribution of these samples is shown in Figure 3.31. It is clear that these samples are composed of micro- and meso-pores. The pore size distribution in samples P0, P05 and P6 is clearly bi-modal and it peaks around 1mm (meso-pores) and 0.1mm (micro-pores). Increasing the particle size in the mix results in samples P1, P2, P3 and P4 in which the pore size distribution is biased

towards larger pores. The pore size distribution of samples P1, P2, P3 and P4 is more close to log-normal and it peaks for pores with sizes around 1mm (meso-pore).

Table 3.11: The non-acoustical properties of the porous materials produced of tyre shred residue with different particle sizes.

Sample	Hole size of screen capture (mm)	Composition of Tyre Shred Residue (%)	Reaction time (min)		Density (kg/m ³)		Porosity		Flow Resistivity [N.m.s ⁻⁴]
			average	STD	average	STD	average	STD	
P0	No sieve	0.6	93	1.5	307	18	0.82	0.010	25462
P05	≤0.05	0.6	88	2.1	311	13	0.80	0.009	32959
P1	1.00	0.6	90	1.5	261	9	0.84	0.008	21633
P2	2.00	0.6	93	1.5	264	15	0.84	0.007	22127
P3	3.35	0.6	94	1.5	273	31	0.86	0.012	18735
P4	4.00	0.6	94	2.1	279	16	0.86	0.005	16861
P6	≥6.67	0.4	89	2.5	255	7	0.87	0.006	16467

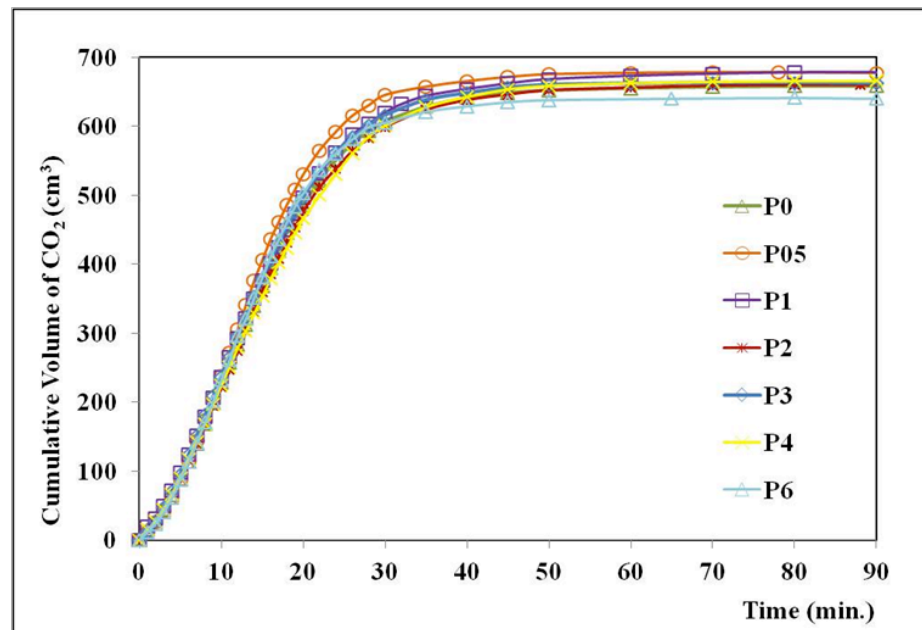


Figure 3.29: Reaction rate of the porous materials produced by the different particle size of tyre shred residue

The density and flow resistivity of samples P05, P1, P2, P3, P4 and P6 reduced when the particle size was increased. It was found that the porosity of these samples increased only slightly with increasing the particle size, whereas the flow resistivity decreased. The differences in the density, porosity and flow

resistivity between sample P05 (smallest particle size) and sample P6 (the largest particle size) were 122%, 92% and 200%, respectively. The sample P05 was prepared by the large proportion of granulated rubber (from screen capture $\leq 0.5\text{mm}$), which has a higher weight. Therefore, this sample has the highest density, lowest porosity and highest flow resistivity. In case of sample P6, it was prepared by with a large proportion of the nylon staple fibres (from screen capture $\geq 6.67\text{mm}$), which has a lighter weight. Therefore, sample P6 has the lowest density, highest porosity and lowest flow resistivity. The sample P0 was prepared from unsieved tyre shred residue. This tyre shred residue is a mixture of three components, which are granulated rubber (20%w/w), nylon staple fibre (20%w/w) and nylon filament fibres bonded with rubber (60%w/w). It was found that sample P0 has slightly lower density and flow resistivity than sample P05 and has slightly higher porosity than sample P05. This study indicates that the particle size of tyre shred residue and the ratio of granulated rubber, nylon staple fibre and nylon filament fibres bonded with rubber has an obvious affect on pore size, pore distribution, density, porosity and flow resistivity of the porous materials.

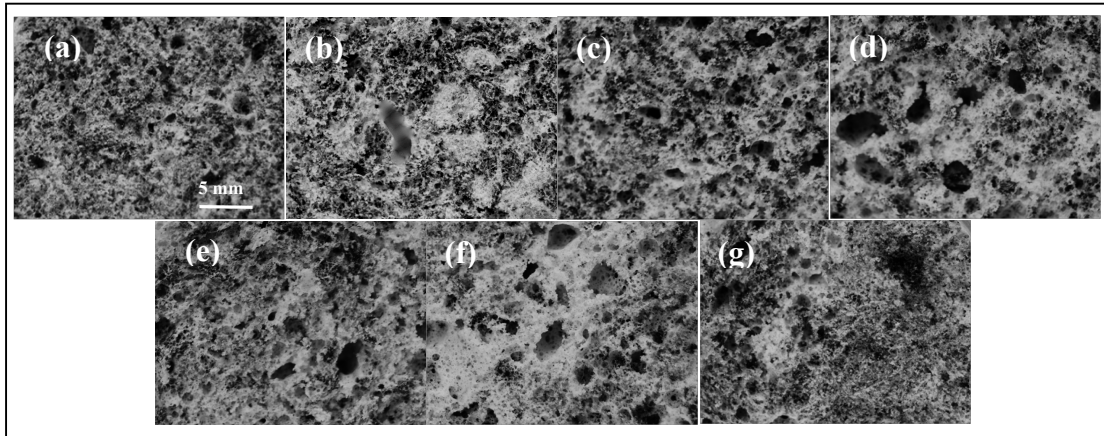


Figure 3.30: Microscopic images of the porous materials produced from different particle sizes of tyre shred residue: (a) P0, (b) P05, (c) P1, (d) P2, (e) P3, (f) P4 and (g) P6.

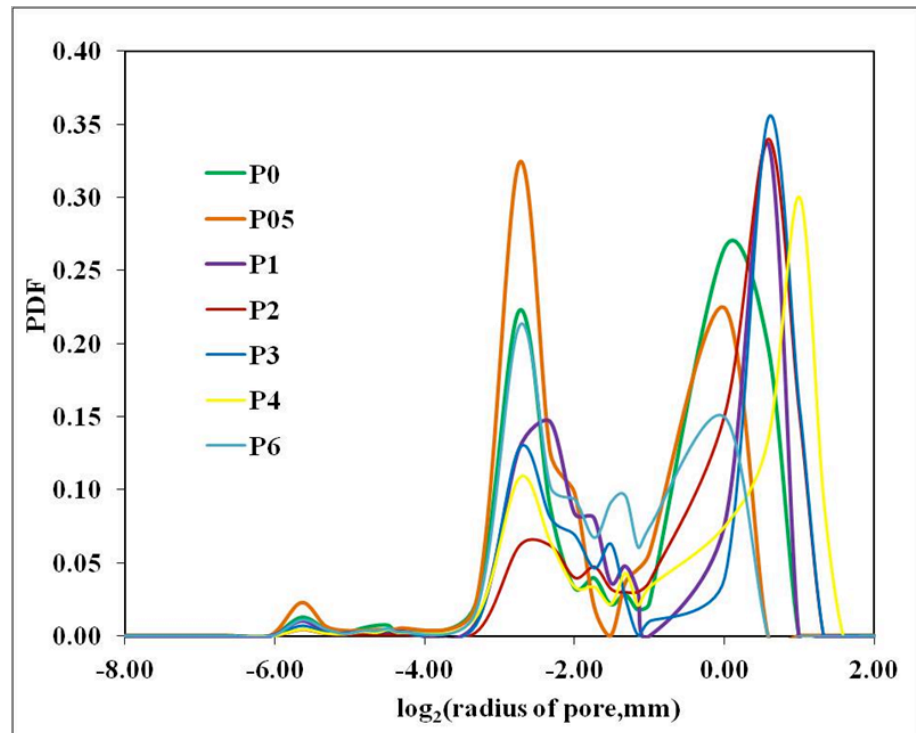


Figure 3.31: Probability density function of the pore size for the porous materials produced by the different particle size of tyre shred residue

Figure 3.32 shows the acoustical absorption coefficient spectra of samples: P0, P05, P1, P2, P3, P4 and P6. There is only small difference in the acoustic absorption performance of the seven material samples produced from tyre shred residue of variable particle size. The 1st maximum in the absorption

coefficient spectrum shifts slightly towards the higher frequency range because of the decrease in the flow resistivity with the increased particle size.

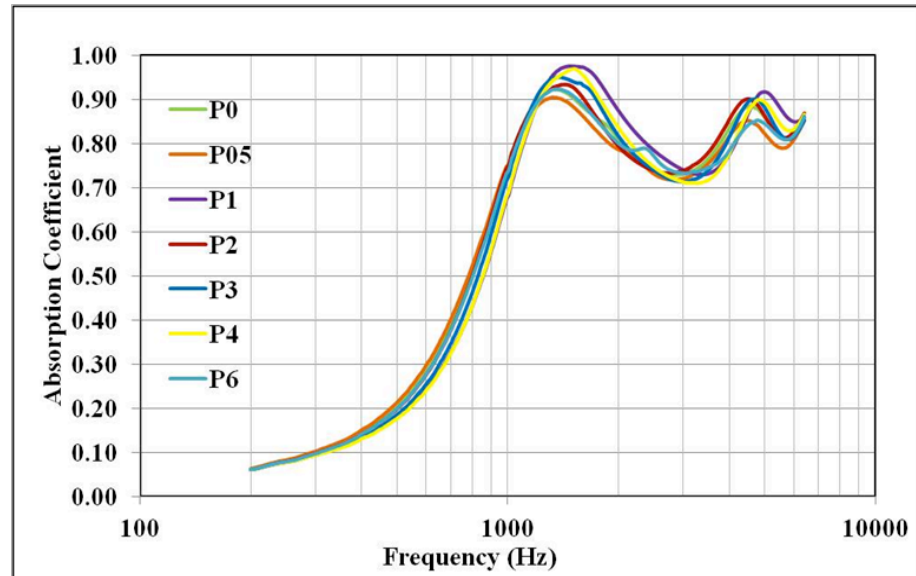


Figure 3.32: Absorption coefficient spectra for the porous materials produced by the different particle size of tyre shred residue

3.8 Effect of Catalysts on the Porous Material Structure

This section studies the effect of catalysts on the non-acoustical and acoustical properties of the porous material. A catalyst is a substance that changes reaction rate, reaction time and mechanism of a chemical reaction. In this study catalysts were used to control the rate of reaction and expanding time in foaming process. Expanding time in the foaming process is a key parameter, which determines the size of cells which are produced in the foaming process. In this work, the porous material samples were produced by using polyurethane binder, which has two different amounts of isocyanate: Flexilon 457 (higher isocyanate) and Flexilon 1109 (lower isocyanate). Table 3.6 lists the ingredients and their quantities which were used in this experiment. Here we

varied the amount of catalysts (2,2'-Dimorpholinyl diethylether, DMDEE) which proportion constituted 0%, 1%, 2% and 3% of the polyurethane binder weight. The C0_M457, C1_M457, C2_M457 and C3_M457 samples were produced by higher isocyanate and the samples produced by lower isocayante are C0_M1109, C1_M1109, C2_M1109 and C3_M1109. The non-acoustical properties of these samples (C0_M457, C1_M457, C2_M457, C3_M457, C0_M1109, C1_M1109, C2_M1109 and C3_M1109) such as reaction time, density, porosity and flow resistivity are presented in Table 3.12. Figures 3.33-3.34 represents reaction rate in terms of the amount of CO₂ produced by the polyurethane polymerisation for the variable content of catalyst.

Table 3.12: Non-acoustical properties of the porous materials with different catalysts

Sample	Composition of Catalyst (%)	Reaction time (min)		Density (kg/m ³)		Porosity		Flow Resistivity [N.m.s ⁻⁴]
		average	STD	average	STD	average	STD	
C0_M457	0	95	2.4	303	12	0.82	0.006	27522
C1_M457	1	44	0.8	281	11	0.84	0.007	34875
C2_M457	2	22	1.0	268	14	0.85	0.009	41420
C3_M457	3	18	1.0	241	12	0.87	0.010	47956
C0_M1109	0	58	1.3	195	12	0.90	0.009	10071
C1_M1109	1	28	1.0	186	12	0.91	0.008	15738
C2_M1109	2	24	0.8	151	8	0.94	0.006	20527
C3_M1109	3	14	1.3	133	8	0.96	0.008	26502

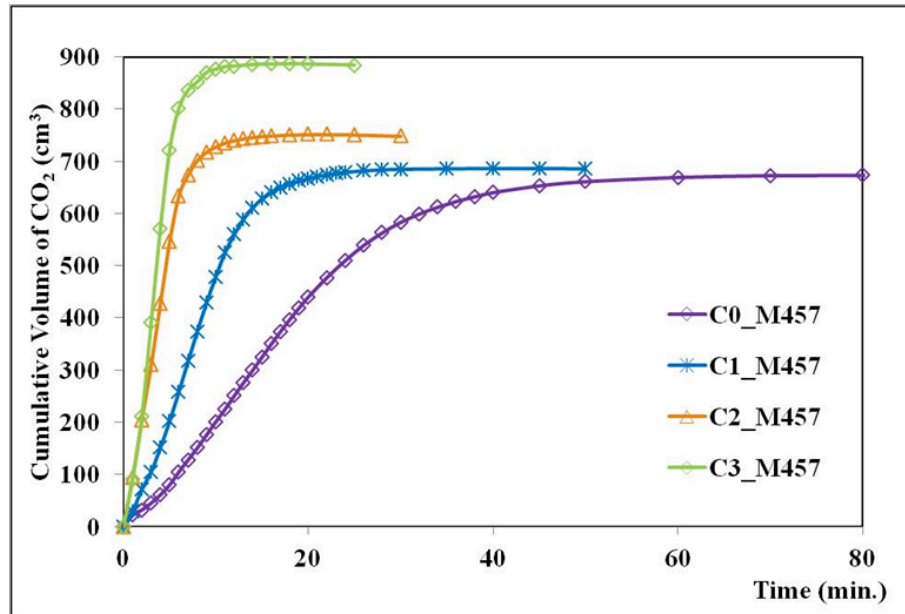


Figure 3.33: The reaction rate of the polyurethane binder (Flexilon 457) in the presence of different amounts of catalyst

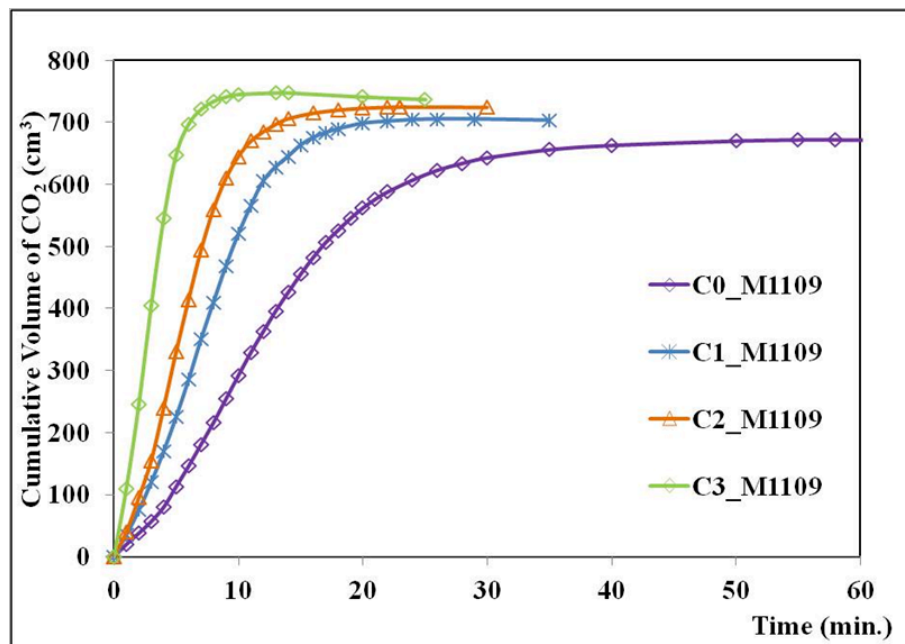


Figure 3.34: The reaction rate of polyurethane binder (Flexilon 1109) in the presence of different amounts catalyst

It was found that the reaction rate of samples is faster in the case of higher catalyst concentrations. The reaction in the case of the samples without

catalyst (samples C0_M457 and C0_M1109) was 77 minutes. The reaction time in case of samples with the highest amount of catalyst (C3_M457 and C3_M1109) was 44 minutes. These are large differences which can be explained by the fact that the activation energy in this polymerisation reaction decreases with the increasing amount of catalyst. In particular, the presence of catalyst increases the rate of reaction by providing an alternative reaction path with a lower activation energy (E_a) [50] as it is illustrated in Figure 3.35. When the lower activation energy pathway is available, a greater proportion of molecules possess sufficient kinetic energy to react so that the reaction rate increases [51] (see Figure 3.36). Therefore, the use of catalyst in the reaction helps to improve the percent yield producing it more effective.

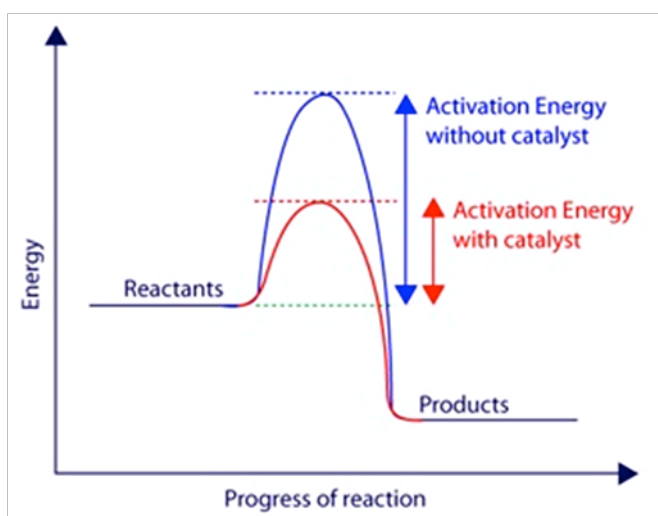


Figure 3.35: The effect of catalyst on the activation energy [52]

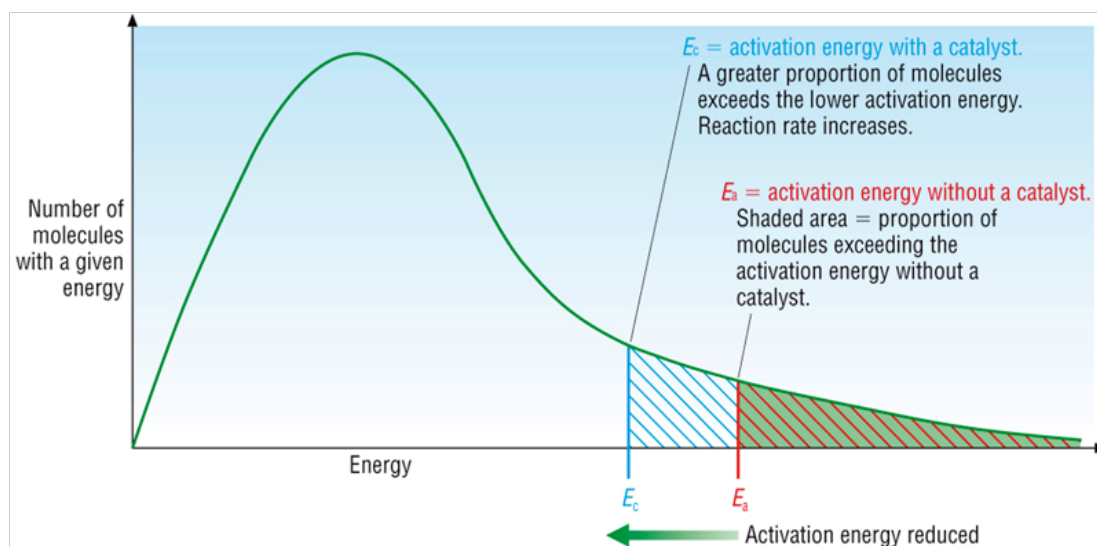


Figure 3.36: The energy in molecules in the absence and presence of a catalyst [51]

As a result, the reaction time in the case of samples C3_M457 and C3_M1109, produced with a larger amount of catalyst, was the shortest while the reaction rate was the highest. The reaction rate is higher in case of polyurethane binder that has a higher concentration of isocyanate than that in the case of binder with the lower concentration of isocyanate. This phenomenon can be explained by the collision theory which suggests that the reaction only occurs when two molecules collide with a kinetic energy greater than the activation energy required for that reaction [51]. An increase in the concentration of reactant means that there are more molecules with the energy greater than or equal to the activation energy. As a result, the reaction time of sample C0_M457 is higher than sample C0_M1109 because of the difference in the isocyanate concentration in the binders used for their production.

The relationship between reaction time and expanding time is described in section 3.5. The reaction time is a key factor for controlling the pores size distribution in the porous material. The results of this work illustrate clearly that

the pore size distribution in these porous materials is controlled by the reaction time of the foaming process. Microscopic images of the porous materials produced with variable concentration of catalyst as shown in Figure 3.37 and 3.38. Figures 3.39 and 3.40 present the corresponding pore size distribution data obtained from the image analysis. It was found that almost of these materials are composed of micro- and meso-pores. In materials produced with binder of a higher isocyanate the proportion of smaller pores increases with the increased amount of catalyst. Sample C3_M457 (the highest amount of catalyst) contains the largest proportion of micro-pores. The pore size PDF of sample C2_M457 is similar to that of sample C3_M457 because the reaction times in the case of these samples were close. The pore size distribution in samples C1_M457 and C0_M457 is clearly bi-modal and it peaks around 1mm (meso-pores) and 0.1mm (micro-pores). In case of the samples C0_M1109, C1_M1109, C2_M1109 and C3_M1109 produced with binder of a lower isocyanate, the proportion of smaller pores increases with the increasing concentration of catalyst. The pore size distribution in these samples is clearly bi-modal. The porous material samples were produced by this polyurethane binder, which obtained a lower cross-linking density in the molecular structure. The CO₂ produced as a result of this polyurethane polymerisation reaction can be able to expand faster and in across greater space within the polymer matrix. Therefore, samples C0_M1109, C1_M1109, C2_M1109 and C3_M1109 contain a larger proportion of larger pores. Samples C0_M457, C1_M457, C2_M457 and C3_M457 produced with polyurethane binder with a higher concentration of isocyanate have a higher cross-linking density in the molecular structure. Free

expansion of CO₂ in that polymer matrix is more difficult. Therefore, these material samples contain a higher proportion of smaller pores.

The density, porosity and flow resistivity of samples C0_M457, C1_M457, C2_M457, C3_M457, C0_M1109, C1_M1109, C2_M1109 and C3_M1109 are summarized in Table 3.12. It was found that the density of these materials is reduced when more catalyst is added. The porosity and flow resistivity tend to increase with the increased concentration of catalyst. The differences in the density, porosity and flow resistivity of sample without catalyst (C0_M457) and sample with the highest concentration of catalyst (C3_M457) are 79%, 106% and 174%, respectively. Similarly, the difference between these quantities in the case of samples C0_M1109 and C3_M1109 is 68%, 107% and 263%, respectively. Small changes in the catalyst concentration cause marginal variations in the measured values of the non-acoustical properties of the resultant porous media. In comparison of porosity between samples with 2% catalyst and samples with 3% catalyst, it was found that the increase of porosity is only 2%. This case can be explained as follows. The sample with 3% catalyst was produced by the fast reaction. Therefore, it contains a larger proportion of smaller pores and some part of closed pore, which found collapse of some part of cell structure. The flow resistivity of these samples increases when more catalyst is added. It can be explained by the fact that a larger proportion of smaller pores is created with when more catalyst is added.

A comparison of the pore size and pore size distribution, density, porosity and flow resistivity between the samples produced by a higher isocyanate (C0_M457, C1_M457, C2_M457 and C3_M457) and the samples produced by

a lower isocyanate (C0_M1109, C1_M1109, C2_M1109 and C3_M1109), it was found that the pore size and pore size distribution of the samples produced by higher isocyanate has a larger proportion of smaller pores in the micro-pore (see Figure 3.39). But the samples produced by lower isocyanate illustrate clearly that the pore size and pore size distribution has a larger proportion of larger pores in the meso-pore (see Figure 3.40). The samples produced by higher isocyanate are a higher density, a higher flow resistivity and a lower porosity than the samples produced by lower isocyanate. It can be explained by the effect of pore size and cross-linking density. The porous material sample produced by higher isocyanate has a higher cross-linking density in the molecular structure, therefore the CO₂ bubbles is difficult to be expanded in polymer matrix of these samples. So that, the samples with a higher cross-linking density have a smaller pore size, a higher density, a lower porosity and a higher flow resistivity.

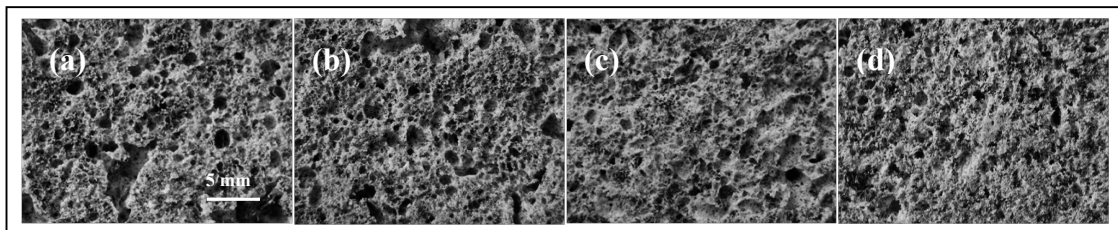


Figure 3.37: Microscopic images of the porous materials produced with polyurethane binder Flexilon 457 and with different amount of catalysts: (a) C0_M457, (b) C1_M457, (c) C2_M457 and (d) C3_M457

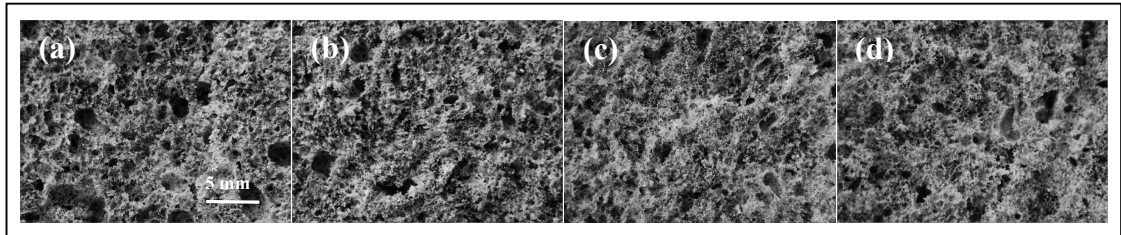


Figure 3.38: Microscopic images of the porous materials produced with polyurethane binder Flexilon 1109 and different amount of catalysts: (a) C0_M1109, (b) C1_M1109, (c) C2_M1109 and (d) C3_M1109

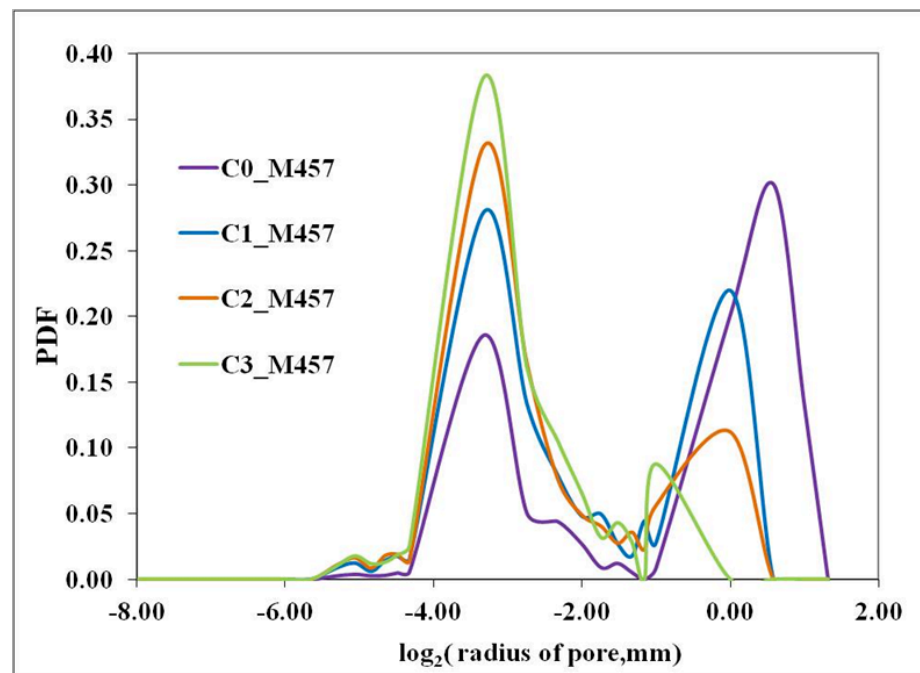


Figure 3.39: The probability density function of the pore size for the porous materials produced with polyurethane binder Flexilon 457 and different amount of catalysts.

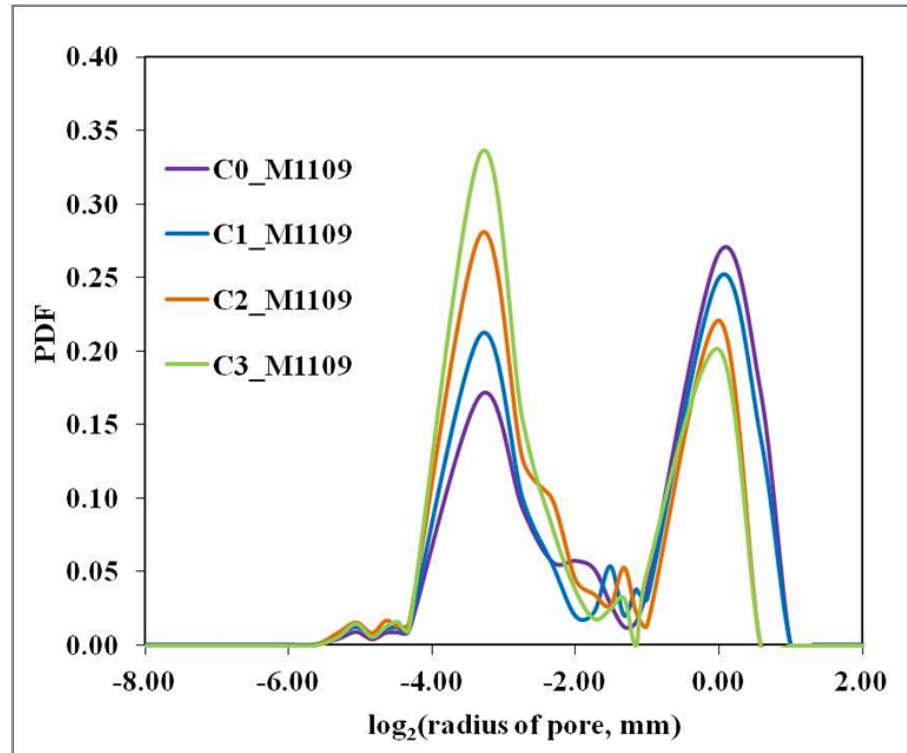


Figure 3.40: The probability density function of the pore size for the porous materials produced with polyurethane binder Flexilon 1109 and different amount of catalysts.

Figures 3.41 and 3.42 show the acoustical absorption coefficient spectra of samples: C0_M457, C1_M457, C2_M457, C3_M457, C0_M1109, C1_M1109, C2_M1109 and C3_M1109. In general, the absorption coefficient spectra move towards the lower frequency range with the increasing amount of catalyst. It can be explained by the increase in the proportion of smaller pores produced in materials in the presence of more catalyst. The largest difference between the absorption coefficient spectra is sound in the case of sample without catalyst (C0_M457) and sample with 3% catalyst (C3_M457). Here, the absorption of material C3_M457 is generally lower because of its relatively large flow resistivity. This difference is attributed to the fact that there are more smaller pores in the sample with 3% catalyst (C3_M457) and there are more

larger pores in the sample without a catalyst (C0_M457). In case of the samples produced with a binder with less isocyanate, the difference of absorption spectrum between the sample without catalyst (C0_M1109) and the sample with 3% catalyst (C3_M1109) is the same trend with the samples produced by higher %isocayante. Because the pore size distribution data in Figure 3.40 illustrate clearly that the highest proportion of smaller pores is in the sample produced with 3% of catalyst (C3_M1109) and that the lowest proportion of smaller pores is in the sample made with no catalyst (C0_M1109).

This study proves that the amount of catalyst added during the polyurethane polymerisation reaction has a strong influence on % yield, reaction rate, reaction time and pore size. Furthermore, it was found that the reaction time determines the pore size distribution in the resultant material samples. The pore distribution is a main non-acoustical property, which has a direct effect on porosity, flow resistivity and acoustic absorption in a porous sample. Polyurethane binder is a major component that has an influence on the morphological and structural properties of the porous material produced as a result.

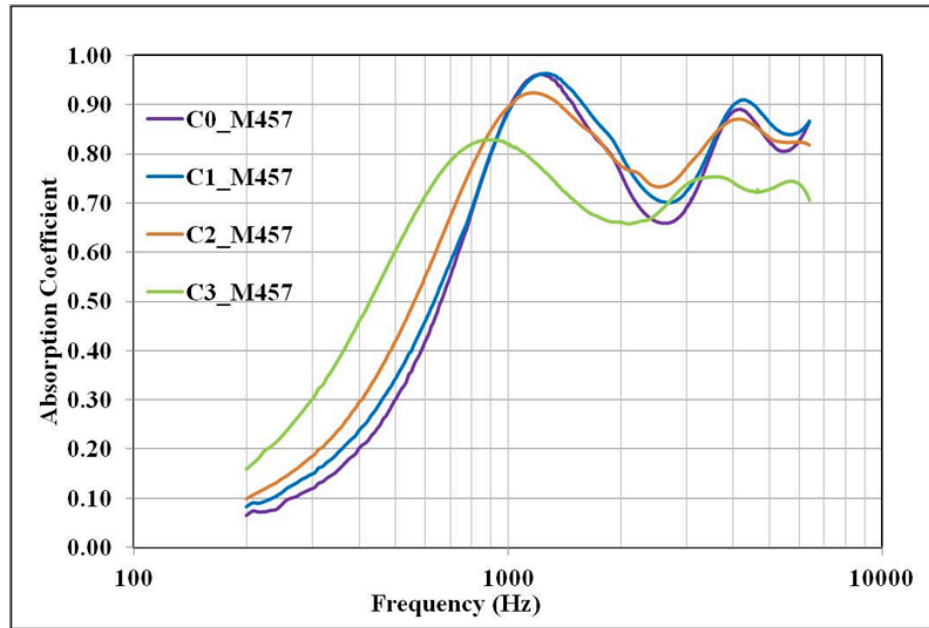


Figure 3.41: Absorption coefficient spectra for the porous materials produced by polyurethane binder (Flexilon 457) and the different content of catalysts

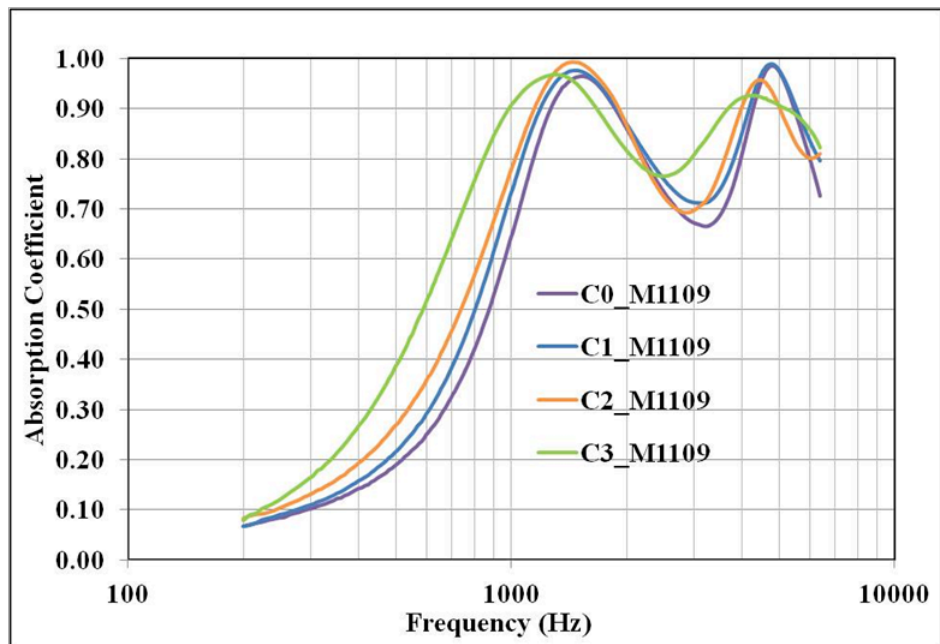


Figure 3.42: Absorption coefficient spectra for the porous materials produced by polyurethane binder (Flexilon 1109) and the different content of catalysts

3.9 Effect of Surfactant on the Porous Material Structure

This section studies the effect of surfactants on the non-acoustical and acoustical properties of the porous material produced as a result of polyurethane polymerisation reaction. Surfactant is an additive in the foaming process which helps a more thorough mixing of the polyurethane mixture components, decreases the surface tension enhances the foam stability, degree of openness of cell structure and prevents bubbles of gas from coalescing. In this work, the porous material samples were produced according to the formulations listed in Table 3.7. In this experiment the surfactant concentration (β -alanine, N-coco alkyl derivs. (Sodium salts K280)) was varied from 0% to 12% in the following steps: 0%(S0), 2%(S2), 4%(S4), 6%(S6), 8%(S8), 10%(S10) and 12%(S12). The surfactant concentration was calculated as the ratio of the surfactant weight to the weight of polyurethane binder. The non-acoustical properties of the samples prepared with a variable amount of surfactant (samples S0, S2, S4, S6, S8, S10 and S12) were measured and their values are presented in Table 3.13. Figure 3.43 represents the reaction of the polyurethane polymerisation reaction for different concentrations of surfactant.

Table 3.13: The non-acoustical properties of the porous materials produced with different concentration of surfactant.

Sample	Composition of Surfactant (%)	Reaction time (min)		Density (kg/m ³)		Porosity		Flow Resistivity [N.m.s ⁻⁴]
		average	STD	average	STD	average	STD	
S0	0	58	1.3	195	12	0.90	0.009	10071
S2	2	62	1.2	198	5	0.90	0.007	10201
S4	4	66	1.0	203	4	0.89	0.008	10503
S6	6	67	1.3	205	10	0.88	0.009	10076
S8	8	70	1.0	214	8	0.85	0.009	9850
S10	10	72	0.8	223	8	0.82	0.010	9045
S12	12	76	1.0	233	5	0.81	0.010	8953

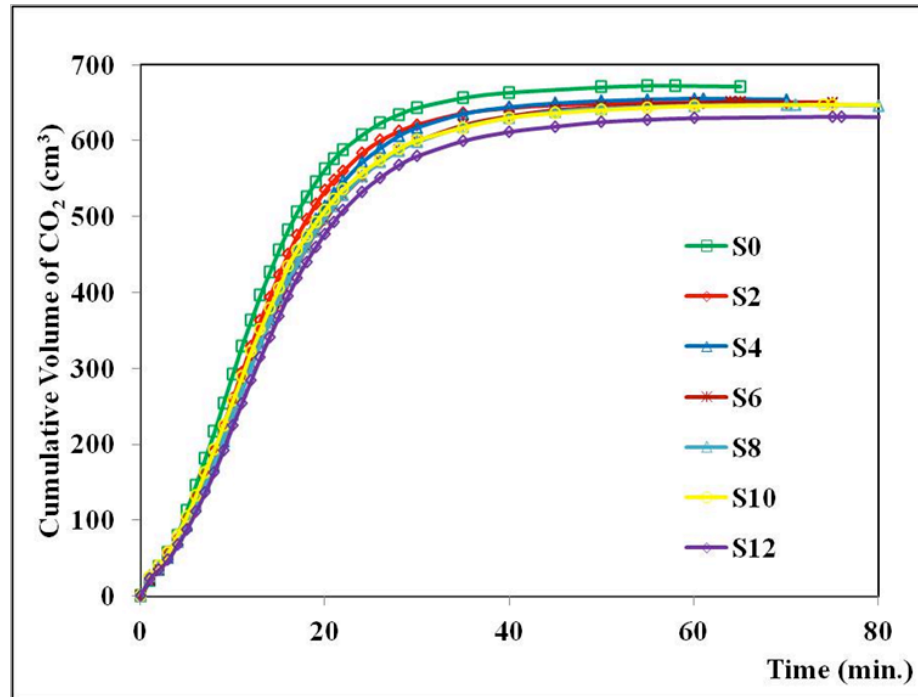


Figure 3.43: The reaction rate of the porous materials produced with different concentration of surfactant.

It was found that the reaction rate reduces when the amount of surfactant is increased. The difference in the reaction time between the sample without surfactant (S0) and the sample with the highest amount of surfactant (S12) is 18 minutes. It is clear that the polymerisation reaction in this study is slowed down by the presence of surfactant. This has an effect on the non-acoustical properties of the developed porous materials and their micro-structure. Figure 3.44 shows microscopic images of the porous surface of samples S0, S2, S4, S6, S8, S10 and S12. The pore size distribution data determined from these images is shown in Figure 3.45. It was found that these materials are composed of micro- and meso-pores. The proportion of larger pores increases with an increased concentration of surfactant. Sample S0 (material produced without surfactant) contains a larger proportion of smaller pores. The PDF of these samples is clearly bi-modal and peaks around 1-2mm (meso-pores) and

0.1mm (micro-pores). The increase in the size of meso-pores is observed when more surfactant is added. This can be explained by an increase in the surface tension reduction effect.

The change in the surfactant concentration has a relatively little effect on the density, porosity and flow resistivity of the developed samples (see Table 3.13). Materials which are produced with more surfactant tend to be slightly denser than those produced with no or little surfactant. A small decrease in the porosity and flow resistivity is observed when more surfactant is added. The reaction time increases with the increased concentration of surfactant, as a result a lower density of larger cells is observed (see Figure 3.44) causing the porosity and flow resistivity to decrease.

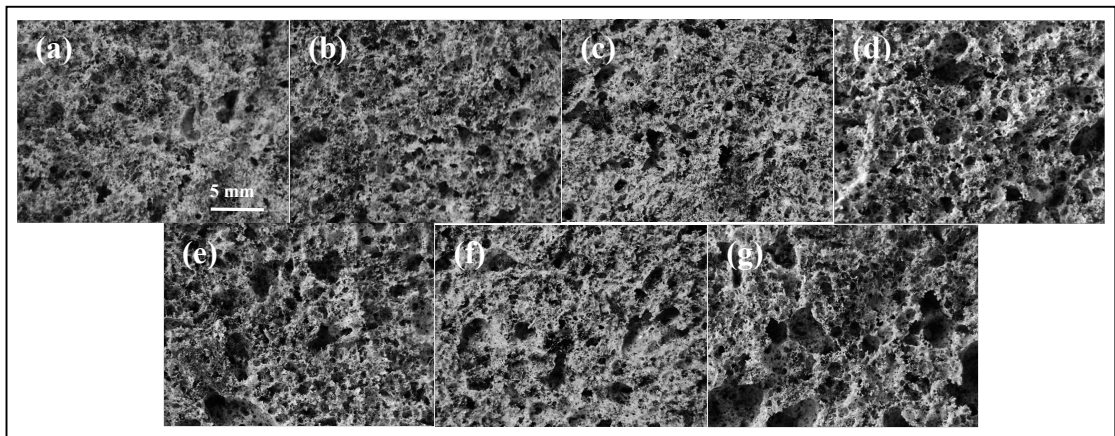


Figure 3.44: Photos of the porous materials produced by the different content of surfactants; (a) S0, (b) S2, (c) S4, (d) S6, (e) S8, (f) S10 and (g) S12

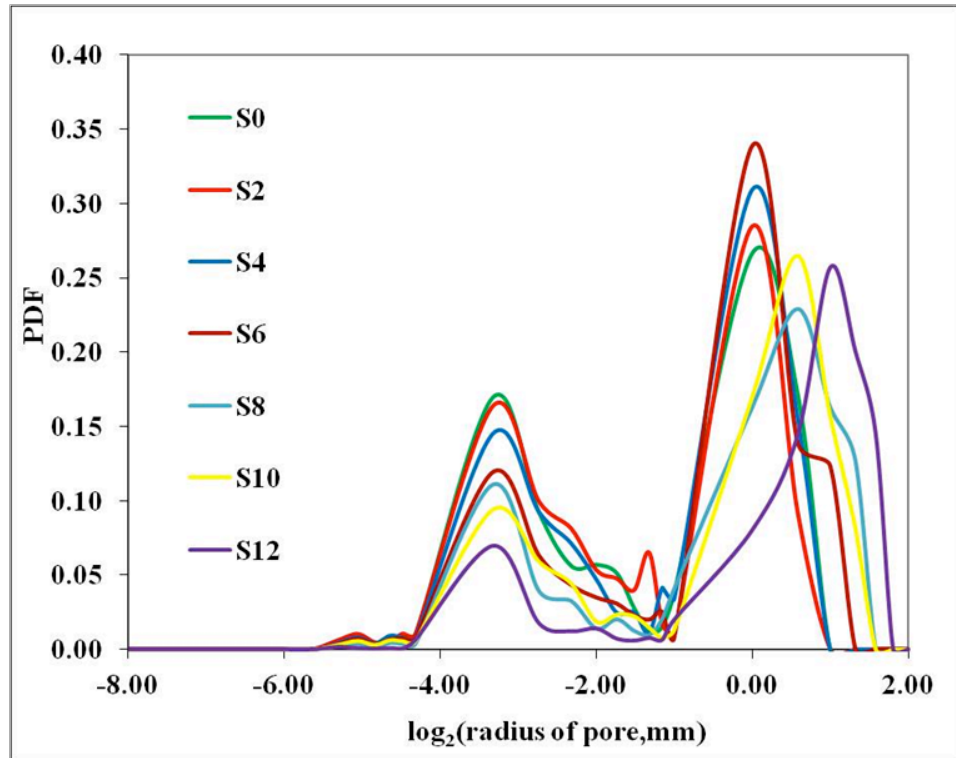


Figure 3.45: The pore size probability density function for the porous materials produced with different concentration of surfactant.

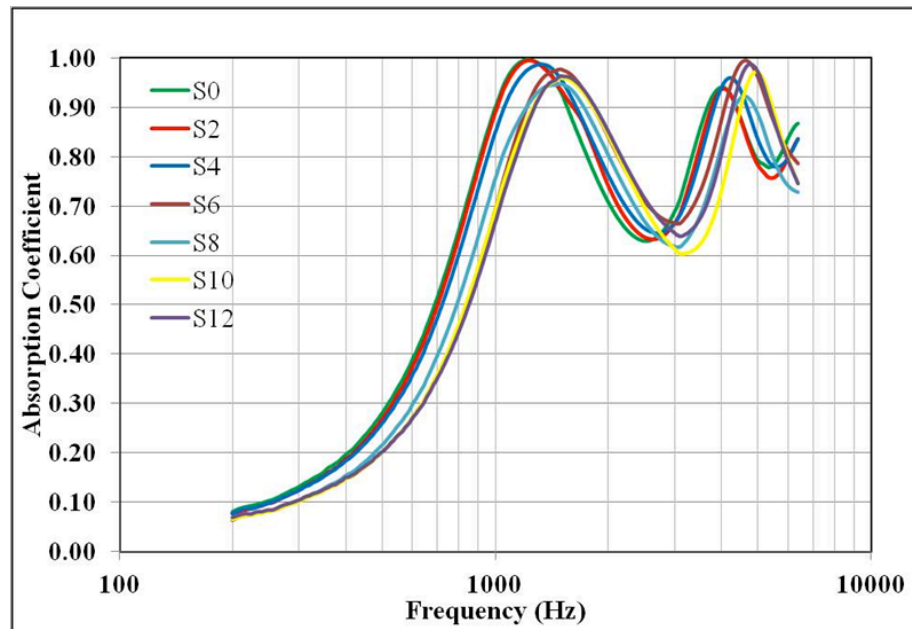


Figure 3.46: The absorption coefficient spectra for the porous materials produced with different concentration of surfactant.

Figure 3.45 shows the acoustical absorption coefficient spectra of samples S0, S2, S4, S6, S8, S10 and S12. These spectra are remarkably similar. The frequency of the 1st maximum in the absorption spectrum increases slightly when more surfactant is added. This effect is explained by the reduced flow resistivity due to the presence of a higher proportion of larger pores with an increasing amount of surfactant.

3.10 Effect of Catalyst and Surfactant on the Porous Material Structure

This section studies the effect of both catalyst and surfactant on the non-acoustical and acoustical properties of the developed porous materials. In this experiment, porous material samples were produced with 3% of catalyst. The samples produced with this amount of catalyst have been characterised by predominately smaller pores some of which are partly closed and not connected. Therefore, surfactant was used to open these cells by improving the consistency of the material mixture and to decrease the proportion of bubble collapses resulting in closed and semi-closed pores.

In this study, the formulations listed in Table 3.8 were used. Following concentrations of surfactant (β -alanine, N-coco alkyl derivs. (Sodium salts K280)) were used: 0%(C3S0), 1%(C3S1), 2%(C3S2), 3%(C3S3), 4%(C3S4) and 5%(C3S5). The concentration of surfactant was calculated as the ratio between the weights of surfactant and polyurethane binder added to the mix. The non-acoustical properties of these samples are presented in Table 3.14. Figure 3.47 represents the reaction rate of the polyurethane polymerisation for

different concentrations of surfactant and for 3% of catalyst added to the material mix.

It was found that the reaction rate for these is largely independent of the surfactant concentration (see Figure 3.47). In this section, the polymerisation reaction with catalyst and surfactant is delayed less than the polymerisation reaction with the surfactant only (in the section 3.9). The reduction of CO₂ products between the sample without surfactant (C3S0) and the sample with the highest amount of surfactant (C3S5) is illustrated clearly in figure 3.47. It can be explained by the %yield of these samples was reduced when surfactant increased. Figure 3.48 shows microscopic images of the porous surface of the samples developed with these formulations. The pore size distribution obtained from the analysis of these images is shown in Figure 3.49. These figures illustrate that the proportion of micro-pores depends on the concentration of surfactant. The proportion of micro-pores reduces when the concentration of surfactant increases. The proportion of meso-pores increases with the increases concentration of surfactant. In other samples, the proportion of meso-pores is relatively small and the pore size distribution resembles long-normal. The increase of large pores can be explained by surface tension reduction by the same reason as given in section 3.9.

Table 3.14: The non-acoustical properties for the porous materials produced with different concentration of surfactants and by adding 3% of catalyst.

Sample	Composition of Surfactant (%)	Reaction time (min)		Density (kg/m ³)		Porosity		Flow Resistivity [N.m.s ⁻⁴]
		average	STD	average	STD	average	STD	
C3S0	0	18	1.0	241	20	0.87	0.010	47956
C3S1	1	18	0.6	278	9	0.83	0.007	42311
C3S2	2	18	0.6	295	12	0.81	0.005	45025
C3S3	3	18	0.6	310	17	0.81	0.010	37943
C3S4	4	19	0.6	323	8	0.80	0.006	39872
C3S5	5	20	1.2	333	4	0.79	0.004	41684

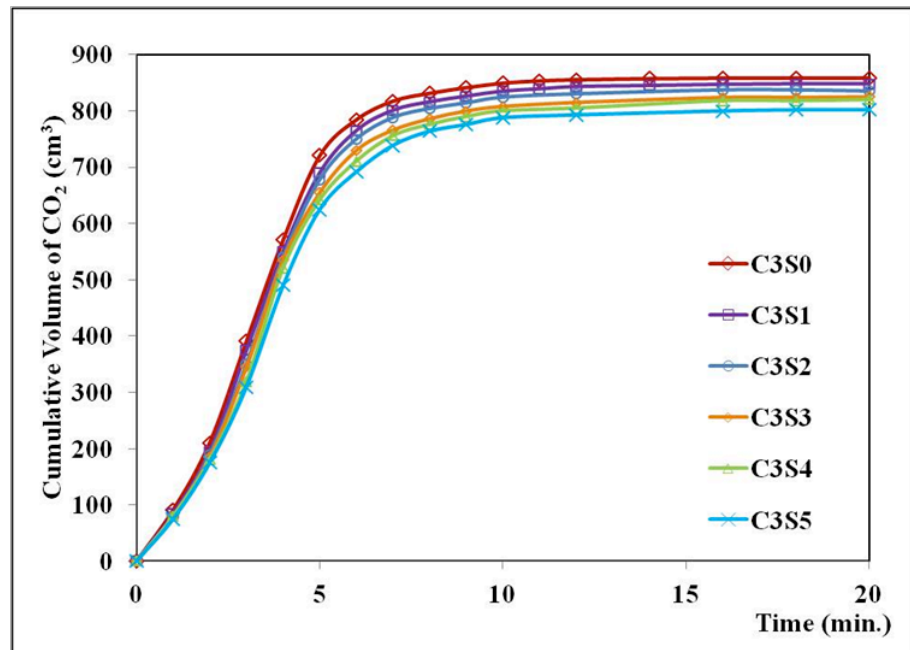


Figure 3.47: Reaction rate of the porous materials produced by the different content of surfactants at 3% catalyst

There is a relatively small variation in the density, porosity and flow resistivity (see Table 3.14). There is a small increase in the density when more surfactant is added. In this case, a small reduction in the porosity is also observed. The variation of the flow resistivity as a function of the surfactant concentration is complex and its is relatively small. The largest differences are

between the sample without surfactant (C3S0) and sample with 5% surfactant (C3S5) in terms of the density and porosity: 138% and 91%, respectively. This is the effect of decreasing of reaction rate between these two samples. It affects to these non-properties.

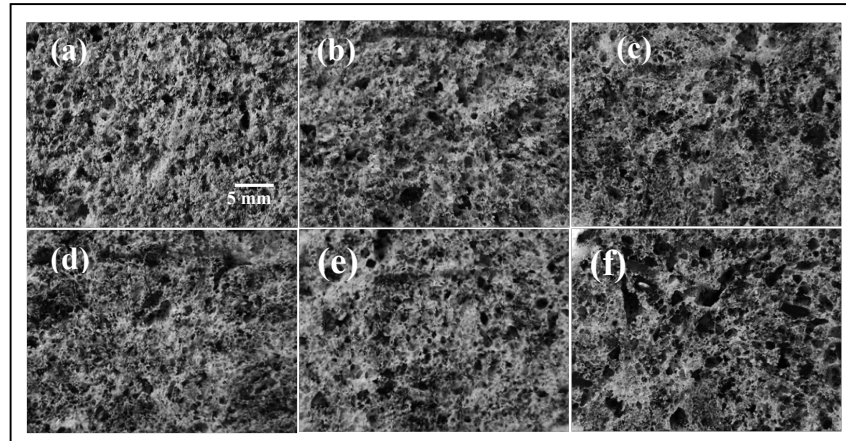


Figure 3.48: Photos of the porous materials produced by the different content of surfactants at 3% catalyst; (a) C3S0, (b) C3S1, (c) C3S2, (d) C3S3, (e) C3S4 and (f) C3S5

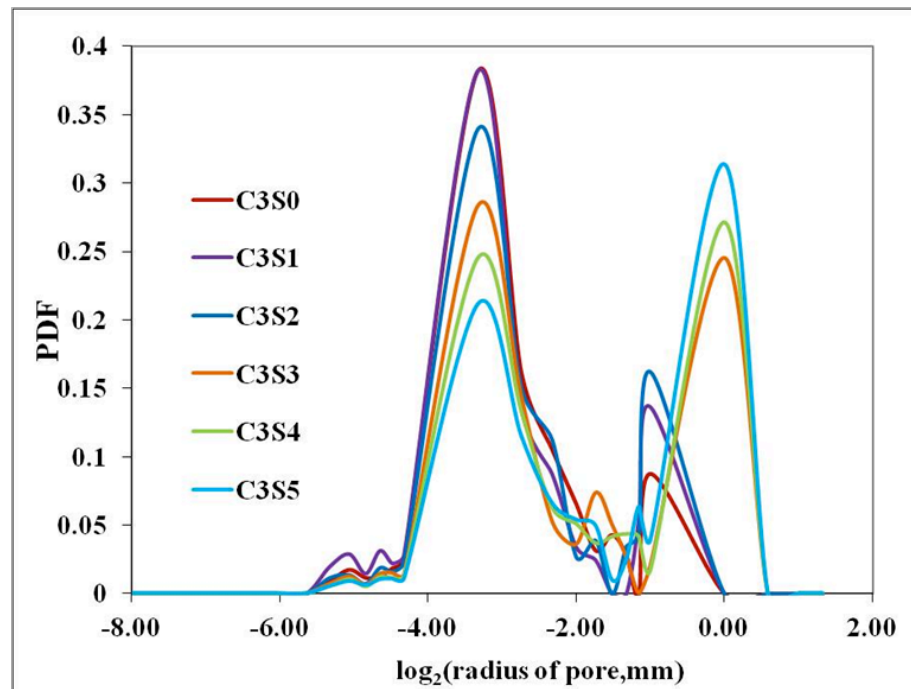


Figure 3.49: Probability density function of the pore size for the porous materials produced by the different content of surfactants at 3% catalyst

Figure 3.50 shows the acoustical absorption coefficient spectra of samples C3S0, C3S1, C3S2, C3S3, C3S4 and C3S5, which tend to shift towards the higher frequency range and when more surfactant is added. This is consistent with the fact that the proportion of larger pores increases when more surfactant is added. It is the excessive use of surfactant that causes the sample C3S5 to have higher moisture.

This study indicates as the amount of surfactant is increased it affects the non-acoustical and acoustical properties of the developed porous media. The surfactant helps to produce more large pores of the porous material sample, which was produced with 3% catalyst. Surfactant uses to excess that it affects the % yield and reaction rate of polymerisation. Therefore, the amount of surfactant must be suitable for production the porous materials.

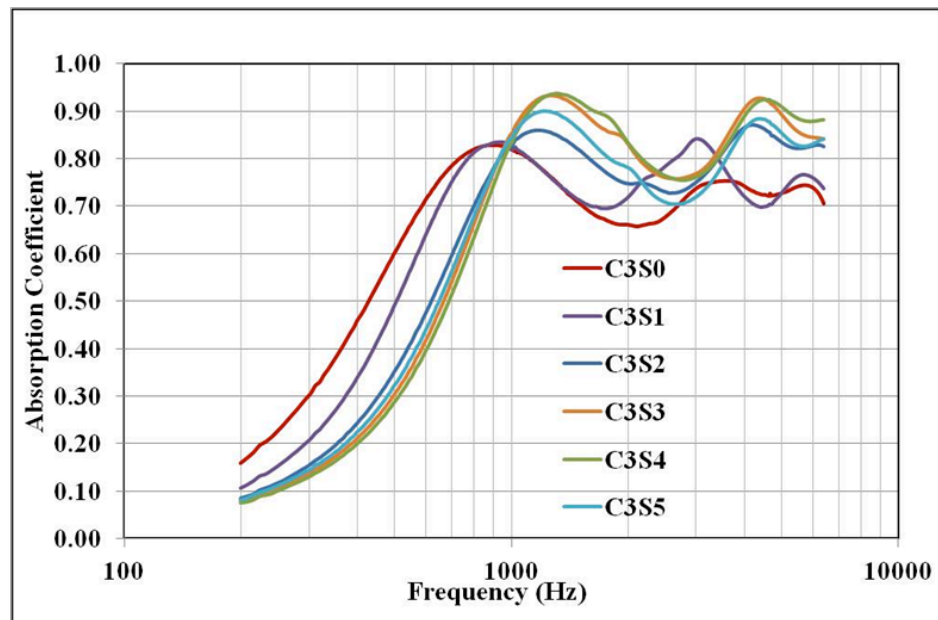


Figure 3.50: The absorption coefficient spectra for the porous materials produced with different concentration of surfactants and by adding 3% of catalyst.

The acoustical absorption coefficient spectra of the developed porous materials (C3_M457 and C3S2) produced in this study were compared with other products, such as Rayon and AFS, and shown in figure 3.51. The Rayon sample proposed by Khan and et al. [53] is based on tyre shred residue produced by a novel extrusion process and the AFS sample is a commercial product developed by Armacell UK LTD., which is based on the recycled nitrile rubber. It was found that the developed porous materials: C3_M457 and C3S2 have higher absorption coefficient than the Rayon and AFS samples at low frequency range (200- 1500 Hz). It can be explained by the larger proportion of smaller pores in these samples: C3_M457 and C3S2. In addition, the porosity of C3_M457 (porosity=0.87) and C3S2 (porosity=0.81) have a higher value than AFS sample (porosity=0.79) and however, they have slightly lower value than Rayon sample (porosity=0.89).

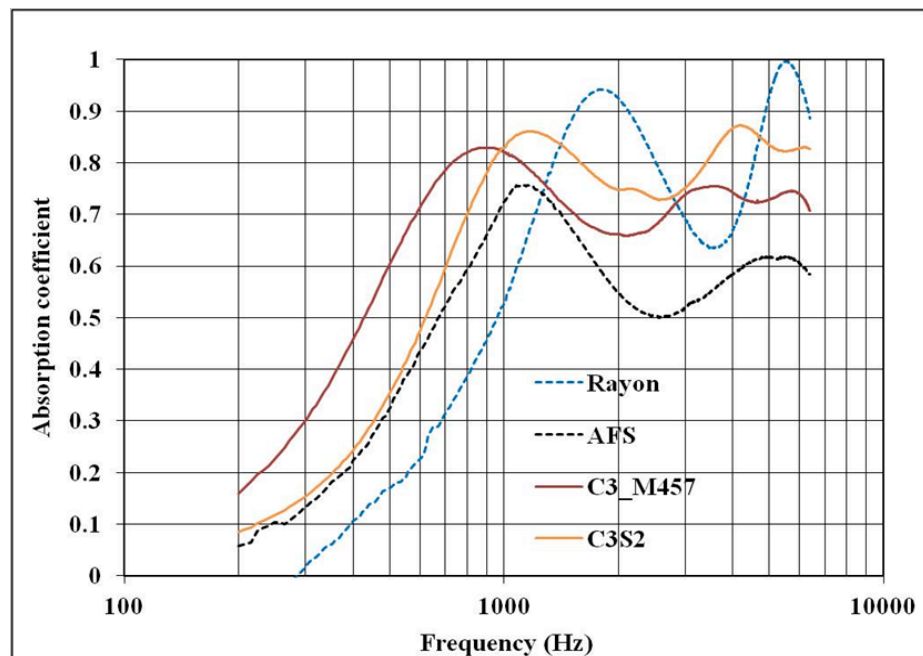


Figure 3.51 Comparison of absorption spectra for the developed porous materials and commercial products

These developed porous materials produced by using catalyst and surfactant has a lower cost of the raw materials, energy, maintenance and labour than commercial products. These materials used recycled tyre rubber that is very cheap. The use of additives in production for these materials is only 3% catalyst and 2% surfactant that are not expensive. In addition, the polyurethane polymerization occurs at room temperature. Therefore, this production has a low energy cost.

3.11 Conclusions

The results of a study into the effect of chemical formulations used to produce porous recycled materials suggest that the amount of each component has influence on the non-acoustical and acoustical properties of the porous materials. The experimental results of each composition clearly show a strong relationship between the reaction rates, reaction time and pore size. The pore size and pore size distribution have a dominant effect on density, porosity and flow resistivity. These non-acoustical properties control sound propagation in porous media.

It has been found that amount of each component in the production the porous material has an upper limit due to several reasons that follow.

As the amount of tyre shred residue increases, the rate reaction increases, while the pore size decreases. The sample used an excess of tyre shred residue, which has a lower absorption coefficient. For example, the sample (T80) with 80% tyre shred residue has the highest density, the lowest porosity, the highest flow resistivity and the lowest absorption coefficient

spectrum. Therefore, the amount of tyre shred residue must be carefully selected in order to produce acoustically effective porous materials. In this study, the samples produced with 60% tyre shred residue still show a higher absorption coefficient spectrum, smaller pores, a lower density, a higher porosity and a lower flow resistivity.

The amount of water used in the production process controls the stoichiometry of the polymerisation reaction. But the stoichiometry ratio between isocyanate group from polyurethane binder and hydroxy group from water is not 1:1 due to the complex polymerisation reaction. In this case, it was found that acoustically efficient porous materials can be produced with 30% of water. This sample is characterised by a higher porosity, lower density and a lower flow resistivity.

Tyre shred residue used in this study was sieved by different screen capture of a sieving machine. Tyre shred residue sieved from each screen capture contains three components (granulated rubber, nylon staple fibre and nylon filament fibres bonded with rubber) in the different ratios. It was found that these samples produced by sieved-tyre shred residue have a slight change in the non-acoustical and acoustical properties. These sample were produced by using tyre shred residue sieved with increasing hole size of screen capture that has the increasing proportion of the nylon staple fibres and nylon filament fibres bonded to rubber, which have a increasing proportion of larger pores, a slight increase in porosity and a slight decrease in density and flow resistivity. But the sample produced with the smaller particle size of granulated rubber in screen capture $\leq 0.5\text{mm}$ helps to increase rate reaction and decrease reaction time and smaller pores. However, this sample shows a slightly lower

acoustical absorption coefficient, a higher density, a lower porosity and a higher flow resistivity. Therefore, the use of tyre shred residue in the form of a mixture of three components for the production the porous material still provides good non-acoustical and acoustical properties.

A catalyst is an important component which is used in the production of porous materials. This component has a strong effect on the rate of reaction, the results in decreasing reaction time and increasing % yield. Catalyst can be used to control the pore size distribution that directly relates to the reaction time. It has been found that the samples with 3% of catalyst have the highest proportion of smaller pores, lowest density, highest porosity and a relatively high flow resistivity. The result show that this sample achieved to improve the absorption performance in the low frequency.

The surfactant in this study helps to decrease surface tension in order to produce an open cell. Additionally, the use of surfactant illustrates especially, which is a good mixing and a stabilizing bubbles. But as surfactant is increased this has an effect on properties; decreasing rate reaction, increasing reaction time, decreasing % yield and increasing the number of larger pore sizes. Therefore, the amount of surfactant used must be upper limit in order to avoid % yield decreasing.

Another objective of this chapter was the production the effective porous materials. Both catalyst and surfactant were used for controlling the pore size and pore size distribution. The experimental results of the samples produced with increased surfactant at 3% catalyst show the increasing larger pore size and increasing open pore. But the rate reaction, density and porosity slightly

reduce. Therefore, the use of surfactant should be $\leq 3\%$ in order to obtain a good absorption of the porous material.

Chapter Four

4. Modelling of the Acoustical Properties of Recycled Porous Media

4.1 Introduction

The acoustic behavior of porous media can be related to the non-acoustical parameters, which describe the morphological characteristics of the porous space in which sound wave propagates. A good understanding of this link can help to design materials with high absorption coefficient, low density and low embedded energy

The correct choice of the acoustic model is of importance. Several researchers have focused on studying and developing theoretical modeling tools for acoustic behaviour of porous media. Stinson and Champoux [54] have studied the sound propagation in model pore materials having simple pore geometries. Rigid-frame porous material containing uniform pores of specific cross-sectional shapes: circular, rectangular and triangular cross section has been investigated in this work. Two model porous materials were constructed, which were composed of pores with a rectangular cross and triangular cross-sections. The authors proposed exact theoretical expression which can describe accurately the acoustical behaviour of these model porous materials. The non-acoustical parameters used by this expression for predicting are flow resistivity, porosity and tortuosity. Attenborough [55,56] developed a model which predicts the acoustical behaviour porous materials via the pore shape factor ratio (s_p) which must be take a value of 0.5 for all pore shapes at low

frequencies and a value that depends on the pore shape at high frequencies. This model requires the data of flow resistivity, porosity and tortuosity and it is in a good agreement with the exact theoretical expression for all frequencies [57,58]. Champoux and Stinson [59] studied sound propagation in rigid-frame porous materials (including ceramic materials) saturated with air. A model porous material with a large variation in pore cross-sectional area was proposed. The flow resistivity and tortuosity of this model material are average due to the variation in pore shape. This model was an improvement to the existing models (e.g. Biot-Chapoux-Allard model [60, 61, 62] and Attenborough model [55, 56]). The authors here proposed a new approach in which a pore is represented as a capillary tube of arbitrary shape and area. The prediction of this approach agreed very well with the measured data for porous materials studied in this work. This theoretical model required two different shape factors to treat the effect of pore shape on both the viscous and thermal functions.

Allard and Champoux [46] proposed new empirical equations for sound propagation in rigid frame fibrous materials that were an improvement to the phenomenological equations by Delany and Bazley [63]. The new expression is based on the general frequency dependency of the viscous forces in porous materials as described by Johnson *et al* [64] and an additional term which predicts the dynamic bulk modulus of air. The new model predicts the dynamic density and bulk modulus as a function of the bulk material density and fibre diameter. In this work Champoux and Allard [65] introduced a new characteristic length for determination the dynamic tortuosity and the dynamic bulk modulus at high frequency.

The work presented in this chapter makes use of the Johnson-Champoux-Allard model (JCA model) [46, 63,66] and Pade Approximations [67] to characterise the morphology of the porous material samples produced with various catalysts and surfactants as described in sections 3.8 and 3.10 of chapter 3. The porous material samples in this study consist of polyurethane-frame and tyre shred residue rubber-filler. The JCA model requires the knowledge of five non-acoustical parameters: flow resistivity, porosity, tortuosity, viscosity and thermal characteristic lengths. In case of Pade approximations, four non-acoustical parameters required are flow resistivity, porosity, tortuosity and standard deviation of pore size distribution. In this study the porosity and flow resistivity were measured directly. The unknown parameters here were the tortuosity, two characteristics lengths (for the JCA model) and standard deviation of pore size distribution (for Pade model), which can be inferred from these models via an optimisation analysis.

4.2 Johnson-Champoux-Allard Model

The Johnson-Champoux-Allard model (JCA model) is used widely to study the acoustical behaviour of the rigid framed porous materials. The JCA model describes sound propagation in a porous material in which two characteristic pore dimensions are assumed to relate to the high-frequency behaviour of the viscous forces and thermal exchanges [65]. The dynamic density function is used to describe the viscous effects which can be defined in expression (4.1) [46]

$$\rho(\omega) = \rho_0 \alpha_\infty \left[1 + \frac{\sigma \phi}{i \alpha_\infty \rho_0 \omega} \left(1 + \frac{4i \alpha_\infty^2 \eta \rho_0 \omega}{\sigma^2 \Lambda^2 \phi^2} \right)^{1/2} \right] \quad (4.1)$$

where ρ_0 is the equilibrium air density, η is the viscosity of air, ϕ is the porosity, σ is the flow resistivity, α_∞ is the tortuosity, ω is the angular frequency, $i = \sqrt{-1}$ and Λ is a viscous characteristic length which is parameter introduced by Johnson *et al* [64]

$$\Lambda = \frac{2 \int_V |v(r)|^2 dV}{\int_A |v(r_w)|^2 dA} \quad (4.2)$$

where $v(r)$ is the velocity of an inviscid fluid, the integral in the numerator is over the volume V of the pore and $v(r_w)$ is the velocity of the same inviscid fluid at the surface of the pore wall, the integral in the denominator is over the surface A of the pore. The viscous characteristic length, Λ relates with the quantities: $\sigma, \phi, \alpha_\infty, \eta$ as follows:

$$\Lambda = s \left(\frac{8\alpha_\infty \eta}{\sigma \phi} \right)^{1/2} \quad (4.3)$$

where s^2 is the shape factor, a parameter that depends on the pore geometry and its value lies between 0.1 and 10 for a majority of most porous materials [64]. The viscous characteristic length has strong influence on the dynamic density function in the narrow sections of the pore. The dynamic bulk modulus is used to describe the thermal effects which are accounted for by Champoux and Allard model [65]

$$K(\omega) = \gamma P_0 \left(\gamma - \frac{\gamma - 1}{1 - \left(\frac{i\sigma'\phi}{\rho_0 \alpha_\infty N_{pr} \omega} \left(1 + \frac{4i\alpha_\infty^2 \eta \rho_0 N_{pr} \omega}{\sigma'^2 \Lambda'^2 \phi^2} \right)^{1/2} \right)} \right)^{-1}, \quad (4.4)$$

where P_0 is the atmospheric pressure, N_{pr} is the Prandtl number, γ is the fluid specific heat ratio $= c_p/c_v$, $\sigma' \leq \sigma$ if the heat losses in widest parts, and Λ' is the thermal characteristic length which is defined by

$$\Lambda' = \left(\frac{8\eta\alpha_\infty}{\sigma'\phi} \right)^{1/2}. \quad (4.5)$$

The above equation can be written as

$$\Lambda' = s' \left(\frac{8\eta\alpha_\infty}{\sigma'\phi} \right)^{1/2}, \quad (4.6)$$

where $s' = \left(\frac{\sigma}{\sigma'} \right)^{1/2}$. The thermal characteristic length can be defined in terms of the volume to pore surface ratio (expression 4.7). The thermal characteristic length has a strong effect on the dynamic bulk modulus in the wider sections of the pore

$$\Lambda' = \frac{2 \int_V dV}{\int_A dA}. \quad (4.7)$$

The acoustic surface impedance Z_s of a material sample of thickness d can be calculated from the following equation

$$Z_s = Z(\omega) \coth \Gamma(\omega) d, \quad (4.8)$$

where $Z(\omega)$ is the characteristic impedance at normal angle of incidence and $\Gamma(\omega)$ is the propagation constant. The characteristic impedance and propagation constants are given by the following expressions

$$Z(\omega) = [\rho(\omega) K(\omega)]^{1/2} \quad (4.9)$$

and
$$\Gamma(\omega) = i 2\pi f [\rho(\omega) K(\omega)]^{1/2}, \quad (4.10)$$

respectively. The normal-incidence absorption coefficient of the porous materials can then be calculated as

$$\alpha = 1 - \left| \frac{Z_s - \rho_0 c_0}{Z_s + \rho_0 c_0} \right|^2. \quad (4.11)$$

4.3 Pade Approximation

Pade approximation for the acoustical properties of porous media with pore size distribution close to a log-normal was proposed by Horoshenkov *et al* [68]. This model assumes that the pore size distribution

$$e(s) = f(\varphi) \frac{d\varphi}{ds} \quad (4.12)$$

is log-normal, i.e.

$$f(\varphi) = \frac{1}{\sigma_\varphi \sqrt{2\pi}} e^{\left(-\frac{(\varphi - \langle \varphi \rangle)^2}{2\sigma_\varphi^2} \right)} \quad (4.13)$$

where $\varphi = -\log_2 s$ is the pore size, $\langle \varphi \rangle = \log_2 \langle s \rangle$ is the mean pore size, $\langle s \rangle$ is median value of s and σ_φ is the standard deviation which is a measure of the deviation in the pore size s . The Pade model [68] is based on the equivalent fluid model in which the fluid is characterised with a normalised, complex, frequency dependent characteristic impedance of the bulk medium (expression 4.14) and a bulk medium wave number (expression 4.15)

$$z_b = \frac{\omega \rho_b(\omega)}{k_b(\omega)} = \sqrt{\rho_b(\omega)/c_b(\omega)} \quad (4.14)$$

$$k_b = \omega \sqrt{\rho_b(\omega) c_b(\omega)} \quad (4.15)$$

where $c_b(\omega) = \phi \bar{c}_x(\omega)$ is defined as the bulk medium complex compressibility and $\bar{c}_x(\omega)$ is the complex compressibility of air in a single pore (expression 4.16), $\rho_b(\omega)$ represents the bulk medium dynamic complex density, which is defined as expression (4.17).

$$\bar{c}_x(\omega) = \frac{1}{\gamma P_0} \left(\gamma - \frac{\rho_0 (\gamma - 1)}{\rho_x(N_{pr}, \omega)} \right) \quad (4.16)$$

In the above expression P_0 is the atmospheric pressure, γ is the ratio of specific heat, ρ_0 is the equilibrium density of air, N_{pr} is the Prandtl number and $\bar{\rho}_x = \rho_b(\omega) \phi / \alpha_\infty$ represents the effective dynamic density.

$$\rho_b(\omega) = \frac{\alpha_\infty}{\phi} \left(\rho_0 - \frac{\phi \sigma}{i \omega \alpha_\infty} \bar{F}(\omega) \right) \quad (4.17)$$

where ϕ is the porosity, α_∞ is the tortuosity, σ is the flow resistivity and $\bar{F}(\omega)$ is the viscosity correction function which is given by the following expression [68]

$$\bar{F}(\omega) \cong \frac{1 + a_1 \varepsilon + a_2 \varepsilon^2}{1 + b_1 \varepsilon}, \quad (4.18)$$

where the coefficients in this model are; $a_1 = \frac{\theta_1}{\theta_2}$, $a_2 = \theta_2$, $b_1 = a_1$ and $\varepsilon = \sqrt{-i\omega\rho_0\alpha_\infty/\sigma\phi}$. The values of θ_1 and θ_2 are real and depend on the pore geometries. In particular, the pores in the materials have a variable shape such as slit-like pore, equilateral triangle and circular pore. In this study, the pore shapes were assumed in the form of triangular pores, therefore these are defined as;

$$\theta_1 = \frac{10}{7} e^{4\xi} - 1 \quad (4.19)$$

$$\theta_2 = \sqrt{\frac{3}{5}} e^{\frac{3}{2}\xi} \quad (4.20)$$

where $\xi = (\sigma_\varphi \ln 2)^2$ is a measure of the deviation from the mean pore size.

The absorption coefficient of these porous materials can be calculated from the following expression.

$$\alpha = 1 - \left| \frac{z_s - 1}{z_s + 1} \right|^2 \quad (4.21)$$

where z_s is the normal acoustic surface impedance (expression 4.22) and d is thickness of these material sample layer.

$$z_s = z_b \coth(-ik_b d) \quad (4.22)$$

4.4 Modelling of Porous Materials Produced with Variable Amounts of Catalyst and Surfactant

This section studies the acoustical properties of porous material samples presented in Chapter 3. The Johnson-Champoux-Allard model (JCA model) and Pade approximations are used here. The first case studied the porous material samples produced by varying the amount of catalyst as detailed in the section 3.4.1. These samples in question are C0_M457, C1_M457, C2_M457 and C3_M457. In the second case, the porous materials are C3S0, C3S1, C3S2, C3S3, C3S4 and C3S5. These materials were produced by varying the amount of surfactant with a constant 3% catalyst content as detailed in the section 3.4.1. The values of porosity (ϕ) and flow resistivity (σ) for these materials are quoted in Tables 3.12 and 3.14. These parameters were used in the JCA and Pade models. The deduced values of the non-acoustical properties and the acoustical absorption coefficient of these samples were presented and discussed in the next sections.

4.4.1 The effect of catalyst

The results of the modeling of the acoustic absorption coefficient of the four material samples produced by varying the amount of catalyst are presented in Figures 4.1– 4.4. The above model was used in combination with a standard optimisation algorithm [69] to determine sets of non-acoustical parameters which minimise the difference

$$F(x) = \sum_{n=1}^N \left| \alpha^{\text{exp}}(f_n) - \alpha^{\text{th}}(f_n, x) \right| \rightarrow \min , \quad (4.23)$$

where f_n is the frequency of sound, $\alpha^{\text{exp}}(f_n, x)$ is the measured absorption coefficient spectrum, $\alpha^{\text{th}}(f_n, x)$ is the absorption coefficient spectrum predicted using expression (4.11) and (4.21) for a given design variable vector, in JCA model $x = \{\sigma, \phi, \alpha_\infty, \Lambda, \Lambda'\}$ and in case of Pade model $x = \{\sigma, \phi, \alpha_\infty, \sigma_\psi\}$. The optimisation algorithm was based on the Nelder-Mead direct search optimisation method detailed in ref. [69]. The Nelder-Mead method determined the parameters of the best fit between the measured data of absorption coefficient and predicted data by JCA and Pade models. This parameter inversion was carried out for N is equal to 800 in the frequency range of below 6400 Hz that corresponds to the standard operational range for an impedance tube with a 29mm diameter. It was found that both JCA model and Pade model provided a good fit for acoustic absorption coefficient of these samples, the Pade model shows a slightly better agreement than JCA model.

The relative error between the measured and predicted absorption data was calculated from the following expression

$$E = \frac{\sum_{n=1}^N |\alpha^{\text{exp}}(f_n) - \alpha^{\text{th}}(f_n, x_0)|}{\sum_{n=1}^N \alpha^{\text{exp}}(f_n)} \times 100\% \quad , \quad (4.24)$$

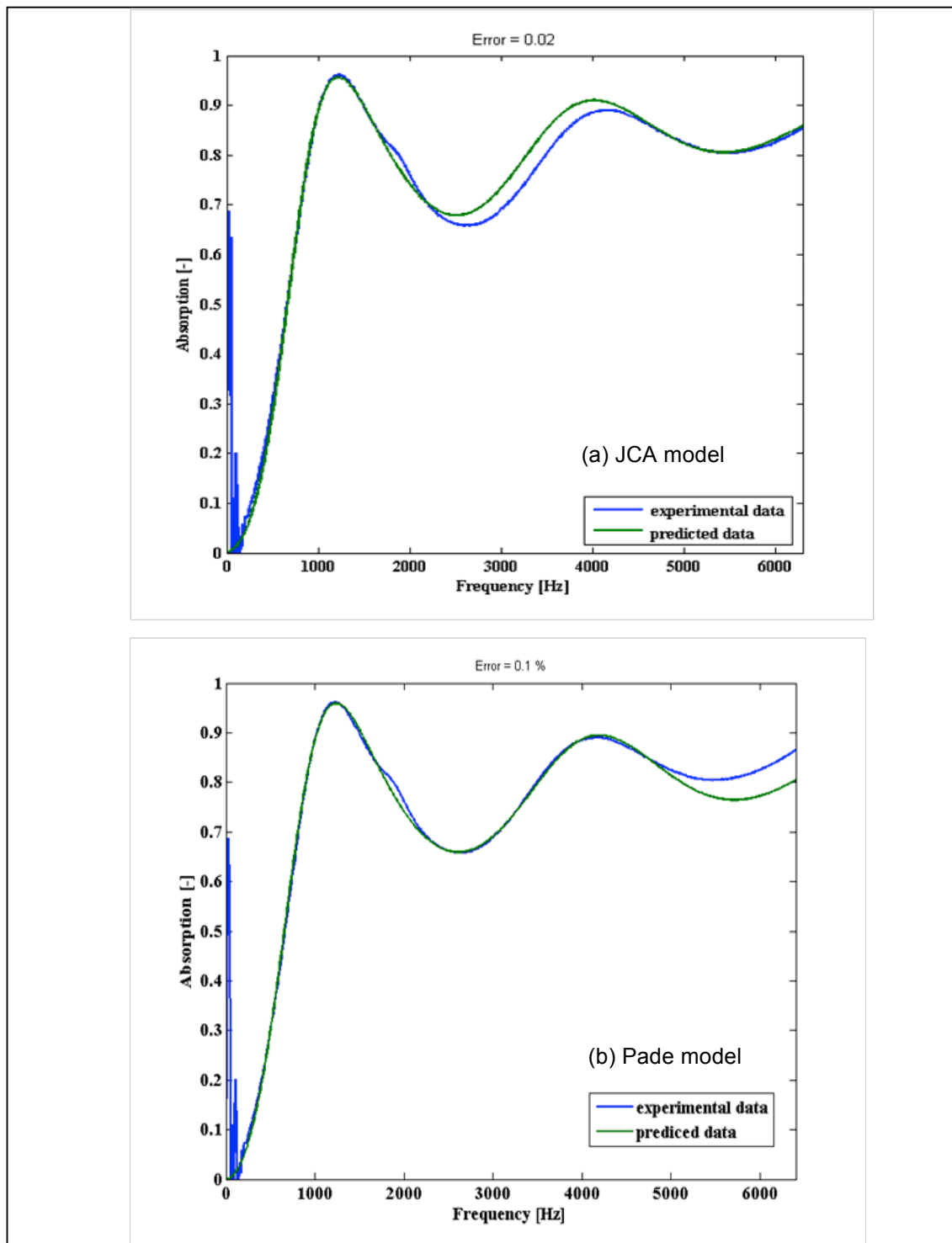


Figure 4.1: The measured and predicted absorption coefficient of the porous specimen without catalyst (sample C0_M457); (a) JCA model and (b) Pade model

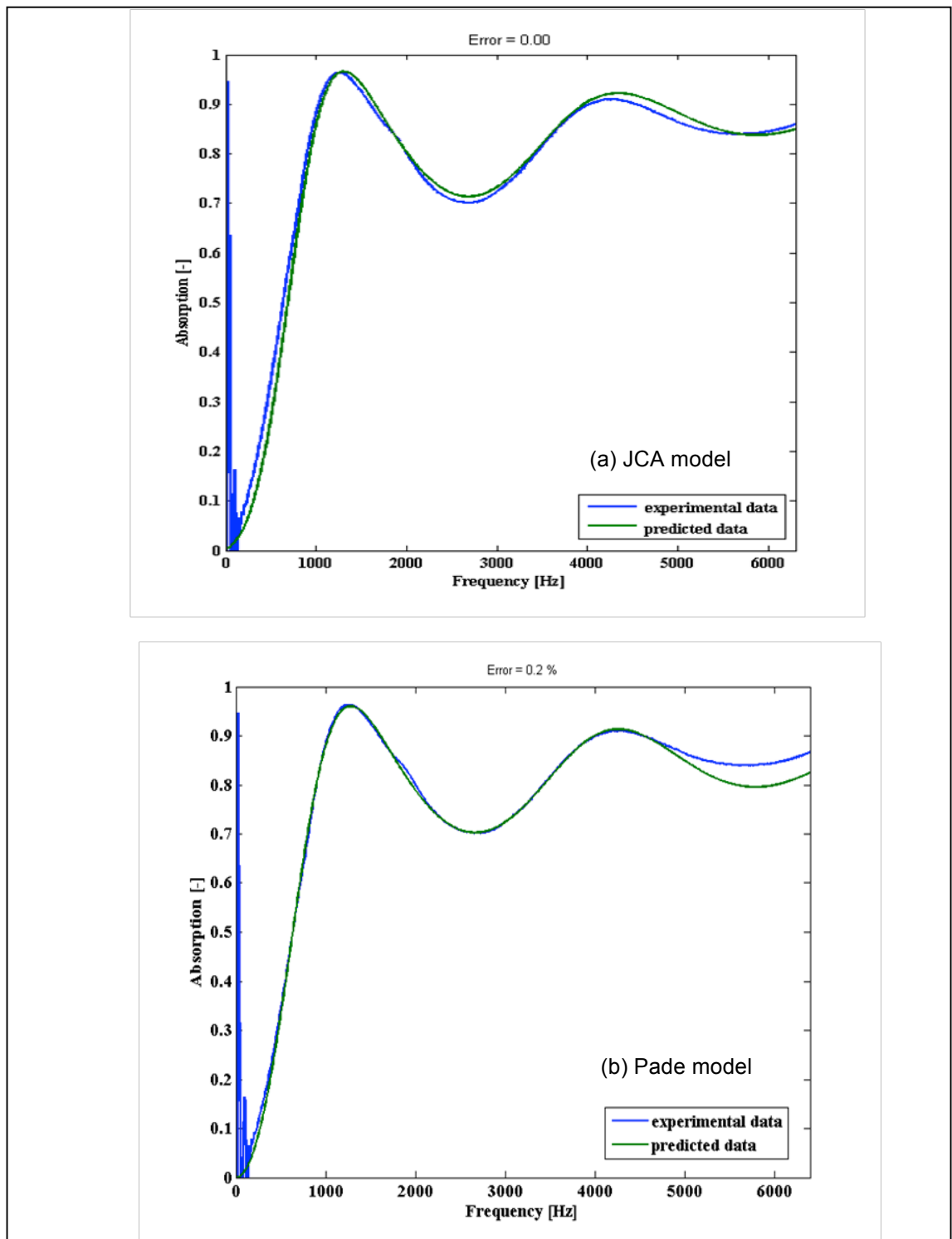


Figure 4.2: The measured and predicted absorption coefficient of the porous specimen with 1% catalyst (C1_M457); (a) JCA model and (b) Pade model

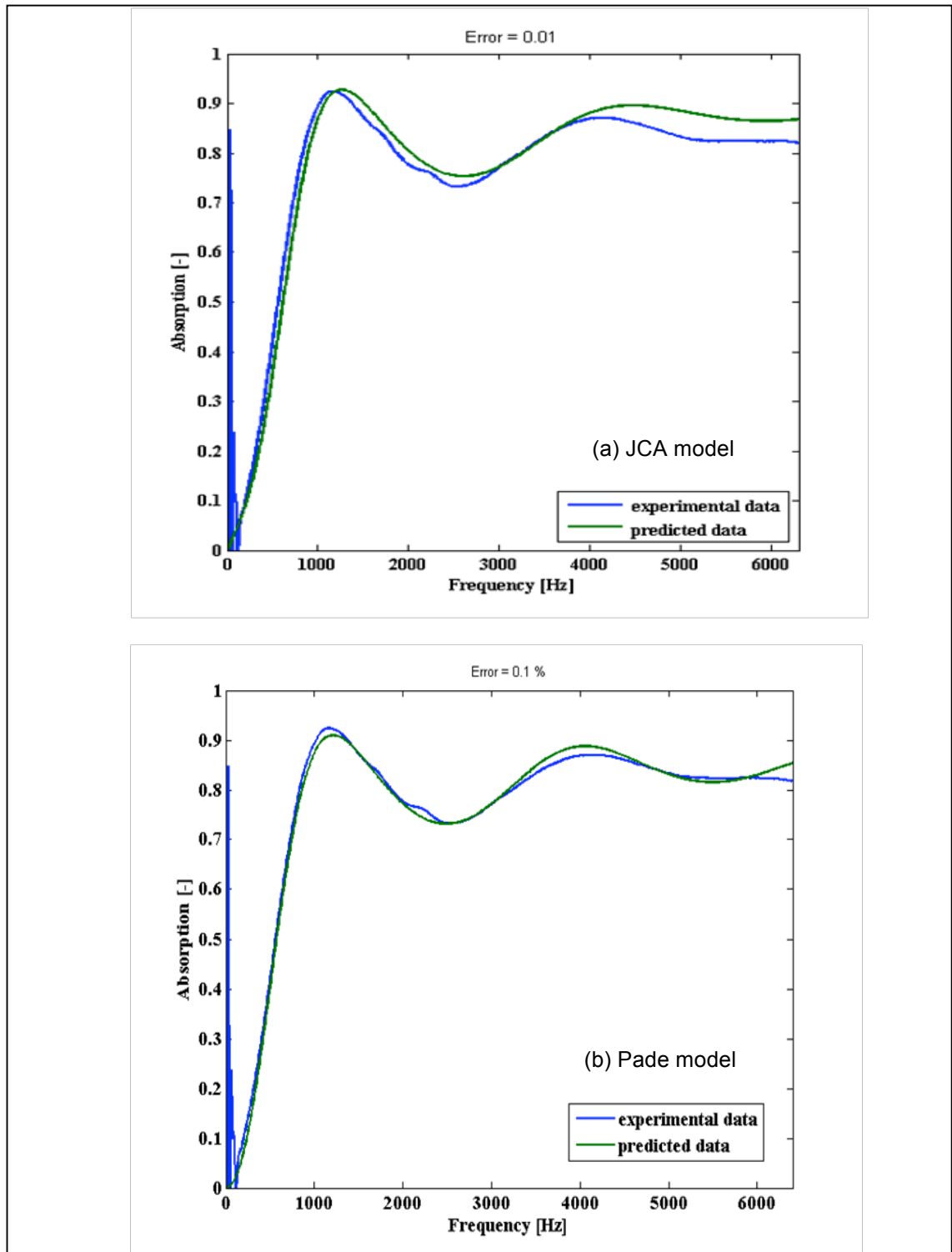


Figure 4.3: The measured and predicted absorption coefficient of the porous specimen with 2% catalyst (C2_M457); (a) JCA model and (b) Pade model

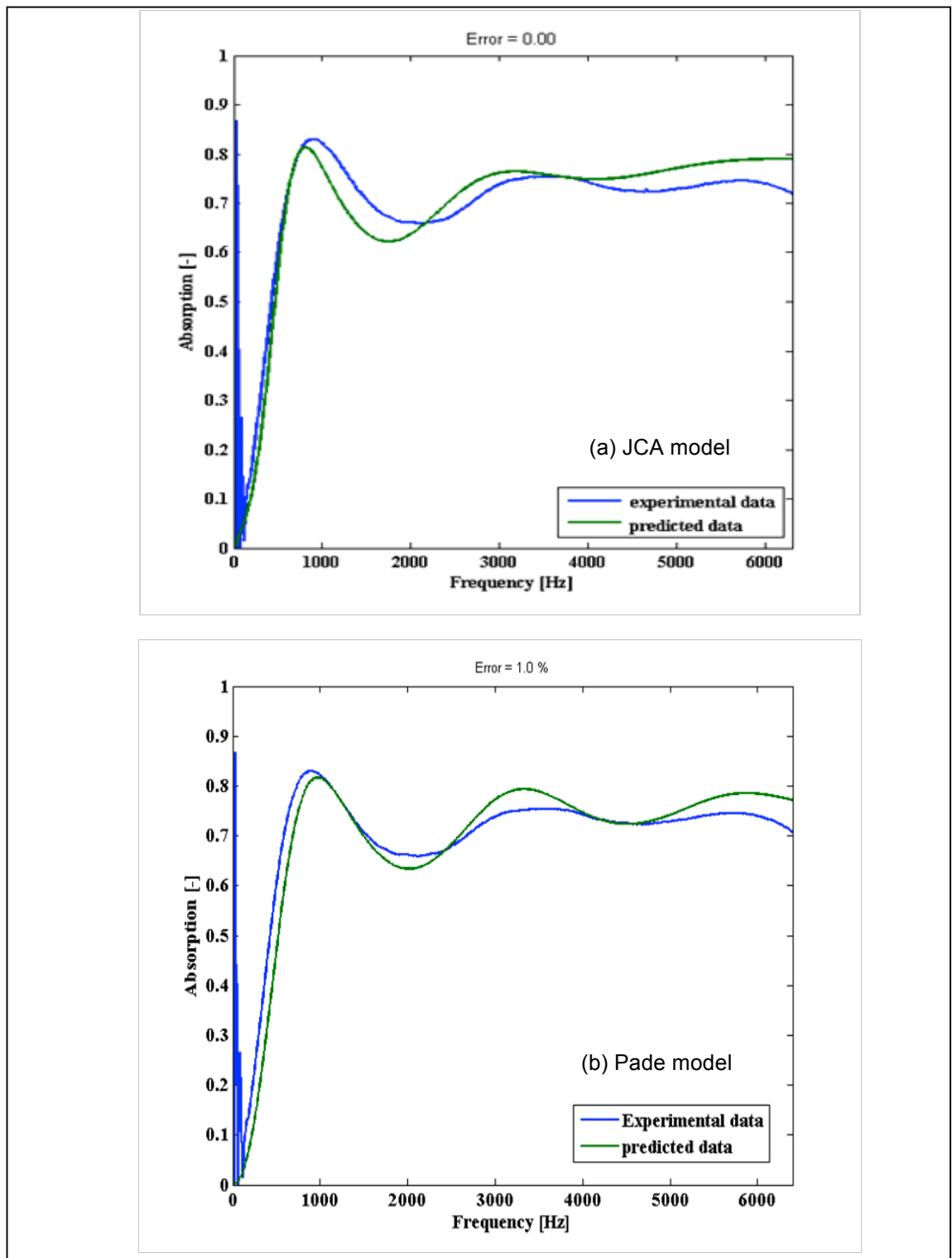


Figure 4.4: The measured and predicted absorption coefficient of the porous specimen with 3% catalyst (C3_M457); (a) JCA model and (b) Pade model

The deduced values of the non-acoustical parameters for samples C0_M457, C1_M457, C2_M457 and C3_M457 are listed in Table 4.1 and 4.2. In this study, the JCA model assumed the measured porosity is accurate. Therefore, the deduced values shown in table 4.1 were obtained from JCA model, which have only four non-parameters such as flow resistivity, tortuosity and two characteristic lengths. Figures 4.5 and 4.6 present a comparison of the measured and deduced data of flow resistivity and porosity. Figure 4.7, 4.8 and 4.9 present the behaviour of the tortuosity, two characteristic lengths and standard deviation of pore size, respectively. These parameters are plotted as a function of the amount of catalyst.

Table 4.1: The deduced non-acoustical properties by JCA model for the porous materials produced by varying the concentration of catalysts

Sample	Variation of catalyst (%)	Flow Resistivity (N.s.m ⁻⁴)	Porosity (measuring)	Tortuosity	Viscous Characteristic Length	Thermal Characteristic Length
C0_M457	0	20784	0.82	2.51	4.88E-05	3.77E-04
C1_M457	1	26733	0.84	1.71	2.87E-05	2.28E-04
C2_M457	2	30414	0.85	1.19	1.99E-05	5.38E-04
C3_M457	3	33774	0.87	1.60	1.18E-05	5.87E-04

Table 4.2: The deduced non-acoustical properties by Pade model for the porous materials produced by varying the concentration of catalysts

Sample	Variation of catalyst (%)	Flow Resistivity (N.s.m ⁻⁴)	Porosity	Tortuosity	Standard deviation of pore size
C0_M457	0	19652	0.73	2.56	0.89
C1_M457	1	24930	0.76	2.40	0.68
C2_M457	2	36052	0.76	2.34	0.62
C3_M457	3	51287	0.75	3.76	0.68

The flow resistivity of these samples from the measured data shows the same trend as the flow resistivity data by modeling. The measured flow resistivity of these samples shows higher values than the deduced data from

both the JCA and Pade models (shown in figure 4.5). It can be explained by the different dimensions of specimens between flow resistivity testing has a 100mm diameter and acoustic absorption testing has a 29mm diameter. The specimen having a larger surface area (100mm diameter) presents more variability in the microstructure in these samples. The measured flow resistivity of these materials has a higher value than the deduced value predicted by the specimen having a smaller surface area (29mm diameter). Another reason is these samples have a wide pore size distribution (see figure 3.39). Therefore, the deduced flow resistivity from the JCA model is lower than the measured values because of the JCA model is designed for relatively uniform pores with similarly sized pore volumes and pore neck diameters. In the case of sample (C3_M457) with the highest catalyst content (3%), the deduced flow resistivity by Pade model shows the highest value. It is the effect of the larger proportion of smaller pores (figure 3.39) and the highest deduced tortuosity value (3.76). The impact of the predicted flow resistivity between sample without catalyst (C0_M457) and sample with the highest catalyst (C3_M457) is 163% of JCA model and 261% of Pade model. The measured and deduced results show clearly that the flow resistivity increased with increasing catalyst content and this can be explained by decrease seen in pore size (figure 3.39). This is inversed to the porosity, which shifts to higher value with increased catalyst content. The deduced values of porosity by the Pade model (shown in figure 4.6) are lower than the measured values. This is because these samples contain micro-pores (0.1mm) and meso-pores (1mm) and have a broad pore size distribution (see figure 3.39). Therefore, Pade model has predicted only

porosity of meso-pore. This affects the deduced porosity giving a lower value than the measured data.

The high deduced value of tortuosity for these samples can be explained by a more complex interconnectivity between pores of different sizes and the more complex pore geometry than those assumed in the JCA and Pade models (see Figure 3.39). The deduced tortuosity from Pade model has a higher value than the JCA model (shown in figure 4.7). It can be explained by the different porosity between two models. The deduced porosity from Pade model is low that causes tortuosity to be high. In the case of C3_M457, the deduced tortuosity from Pade model is the highest. This sample was produced by a very fast reaction and has very complex pore geometry.

Furthermore, increasing the concentration of catalyst results in decreased viscous characteristic length and increased thermal characteristic length. This indicates that the characteristic dimension of the pores increases but the pore necks become smaller resulting in the apparent increase in the flow resistivity. The thermal characteristic length of all samples shown in table 4.1 and figure 4.8 illustrates clearly that is larger than the viscous characteristic length. The impact of the viscous and thermal characteristic lengths between sample without catalyst (C0_M457) and sample with the highest catalyst (C3_M457) is 24% and 155%, respectively. This illustrates the amount of catalyst has an influence on the pore dimensions and connectivity. Clearly, there are more pores of smaller diameter and the larger pores appear somewhat longer (see Figure 3.37). This fact is reflected in small (5%) increase in the porosity and a lower deduced tortuosity by JCA model (57%) in comparison with the case when no catalyst was added.

The standard deviation of pore size of these samples has a high value in a range of 0.89-0.62 (see figure 4.9). It corresponds with the wide pore size distribution of these samples shown in figure 3.39. The sample without catalyst (C0_M457) has the highest value of standard deviation. Because the pore behaviour of this sample presents obviously bi-modal, which consists of micro-pore and meso-pore. Therefore, the different pore size affects directly to standard deviation increasing.

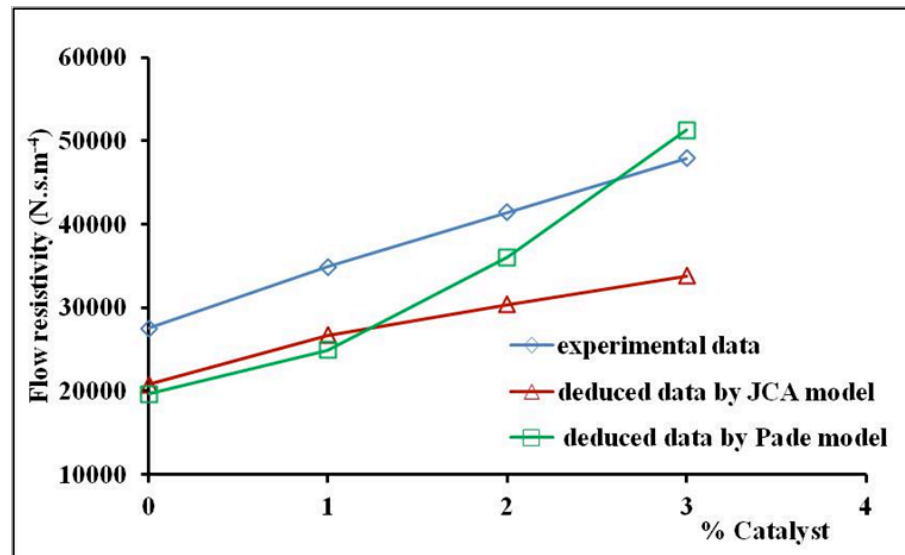


Figure 4.5: The measured and deduced flow resistivity data for samples produced with different concentration of catalyst.

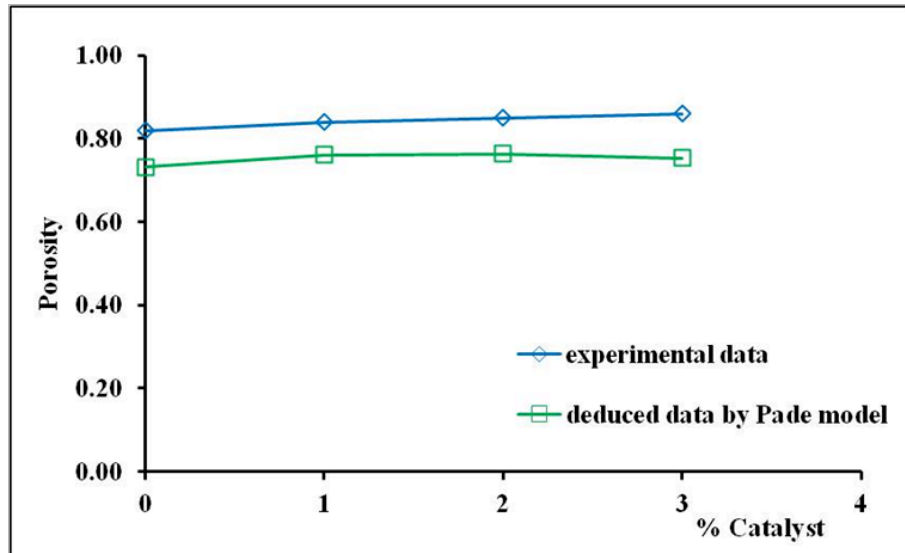


Figure 4.6: The measured and deduced porosity data for samples produced with different concentration of catalyst

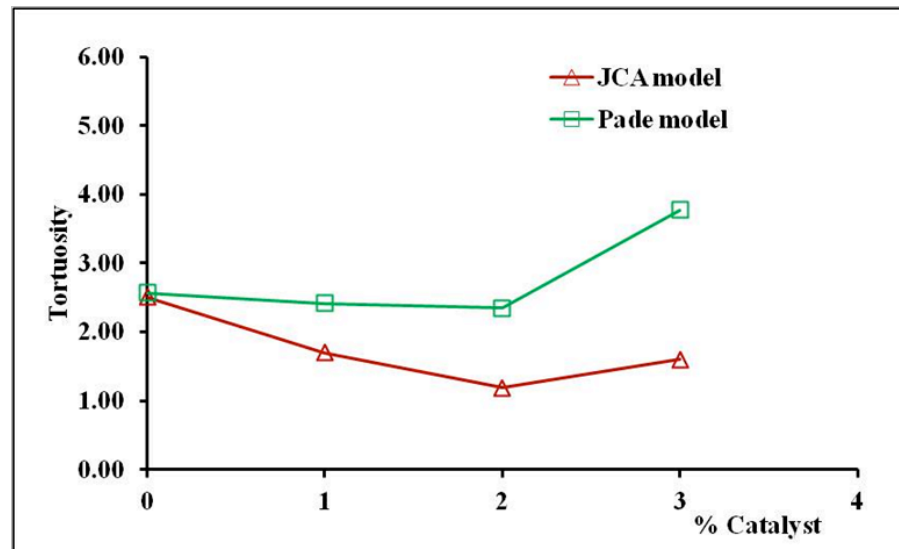


Figure 4.7: A comparison of the deduced tortuosity data of two models for samples produced with different concentration of catalyst

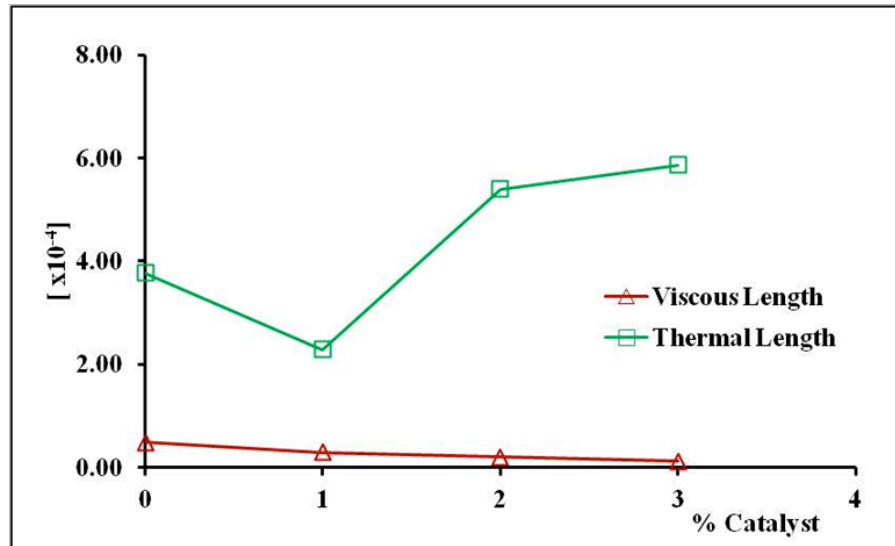


Figure 4.8: The deduced data of viscous length and thermal length for samples produced with different concentration of catalyst

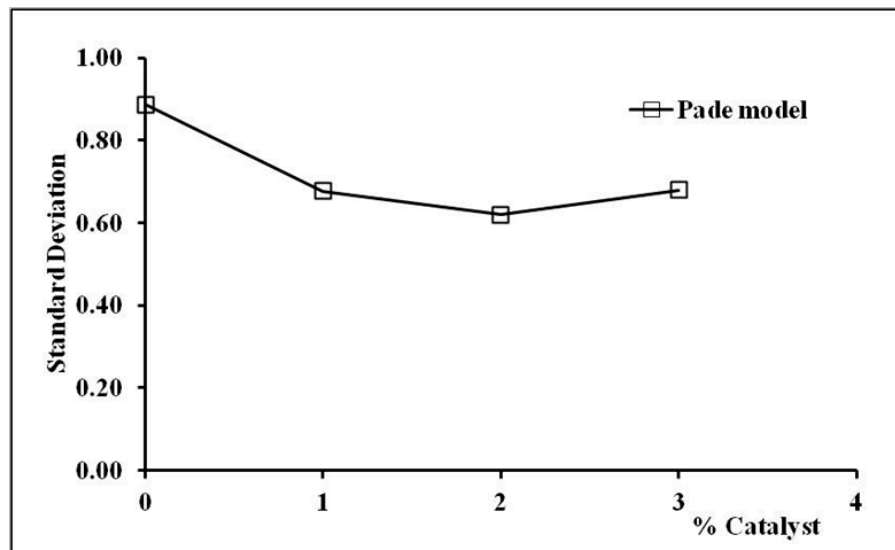


Figure 4.9: The deduced standard deviation of pore size for samples produced with different concentration of catalyst

4.4.2 The effect of Catalyst and Surfactant

This section examines the effect of catalyst and surfactant; we adopted the JCA and Pade models to predict the acoustic behaviour of material samples C3S0, C3S1, C3S2, C3S3, C3S4 and C3S5 manufactured by varying the concentration of catalyst and surfactant. Figures 4.10-4.15 present the

measured and predicted values of the absorption coefficient for the six material specimens. The predicted results were obtained via the optimisation method described in previous section. There is a generally good agreement between the predicted spectra by JCA model and measured spectra for the absorption coefficient. The JCA model does not fully explain the complexity in the behavior of the measured absorption coefficient at frequencies above 1000 Hz. This discrepancy is relatively small (5-10%) and it can be explained by the broad pore size distribution presented in Figure 3.49. Pade model provided very good agreement for acoustic absorption coefficient of these materials in this case. Figures 4.11-4.15 show clearly the deduced data of absorption coefficient spectra from Pade model have better agreement than JCA model over the frequency range.

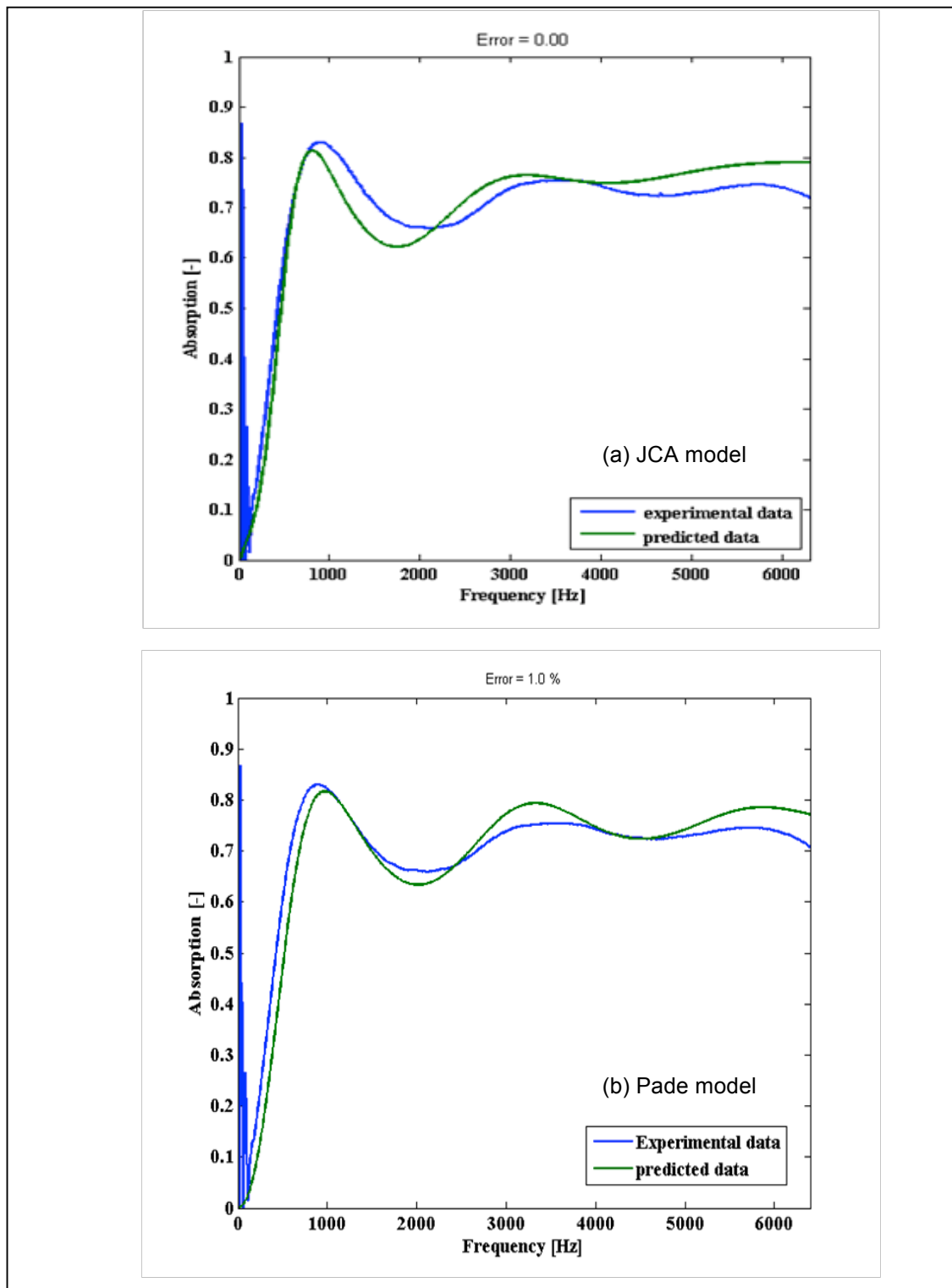


Figure 4.10: The measured and predicted absorption coefficient for porous specimen without surfactant produced with 3% of catalyst (sample C3S0); (a) JCA model and (b) Pade model

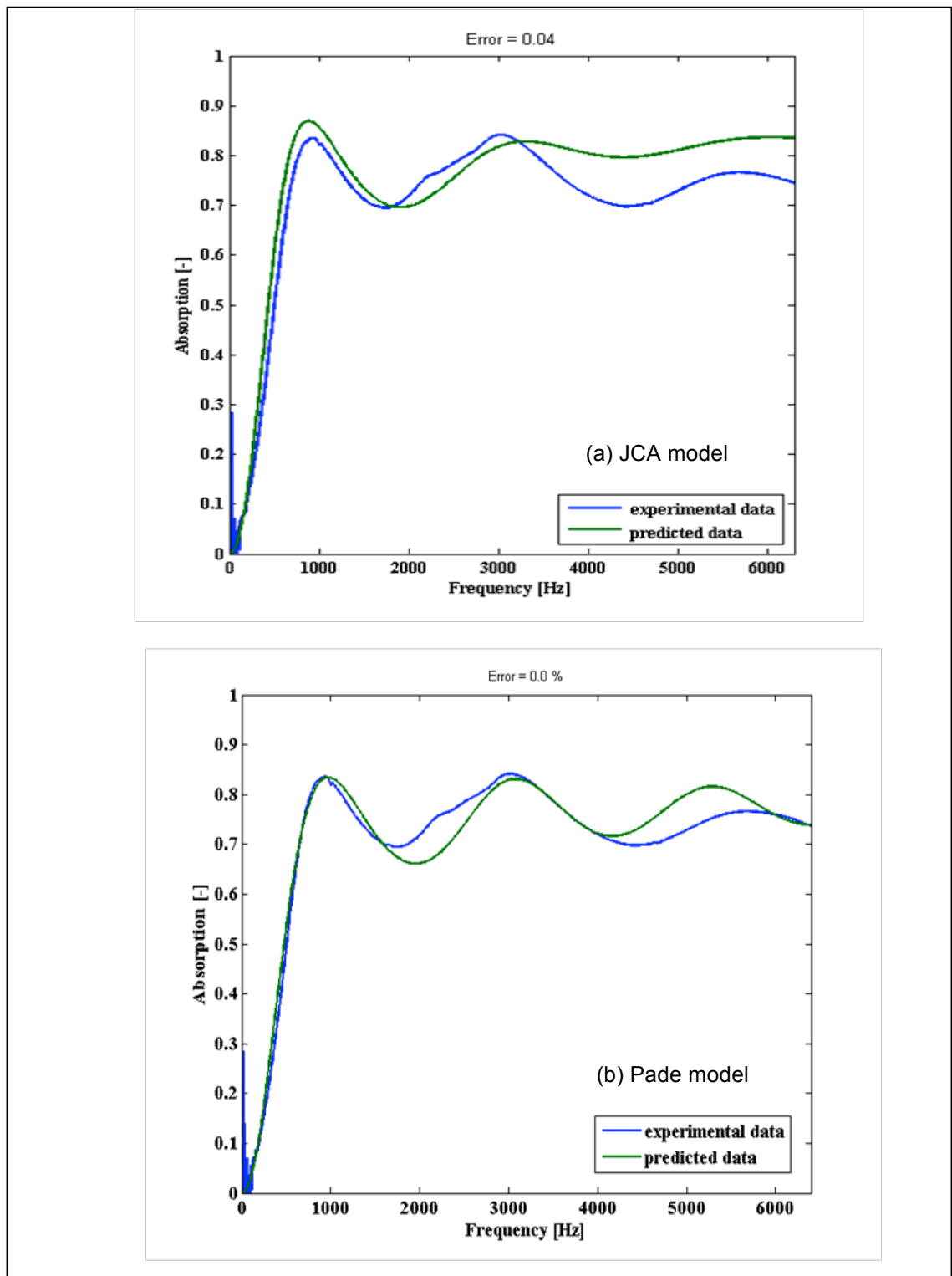


Figure 4.11: The measured and predicted absorption coefficient for porous specimen with 1% of surfactant produced with 3% of catalyst (sample C3S1); (a) JCA model and (b) Pade model

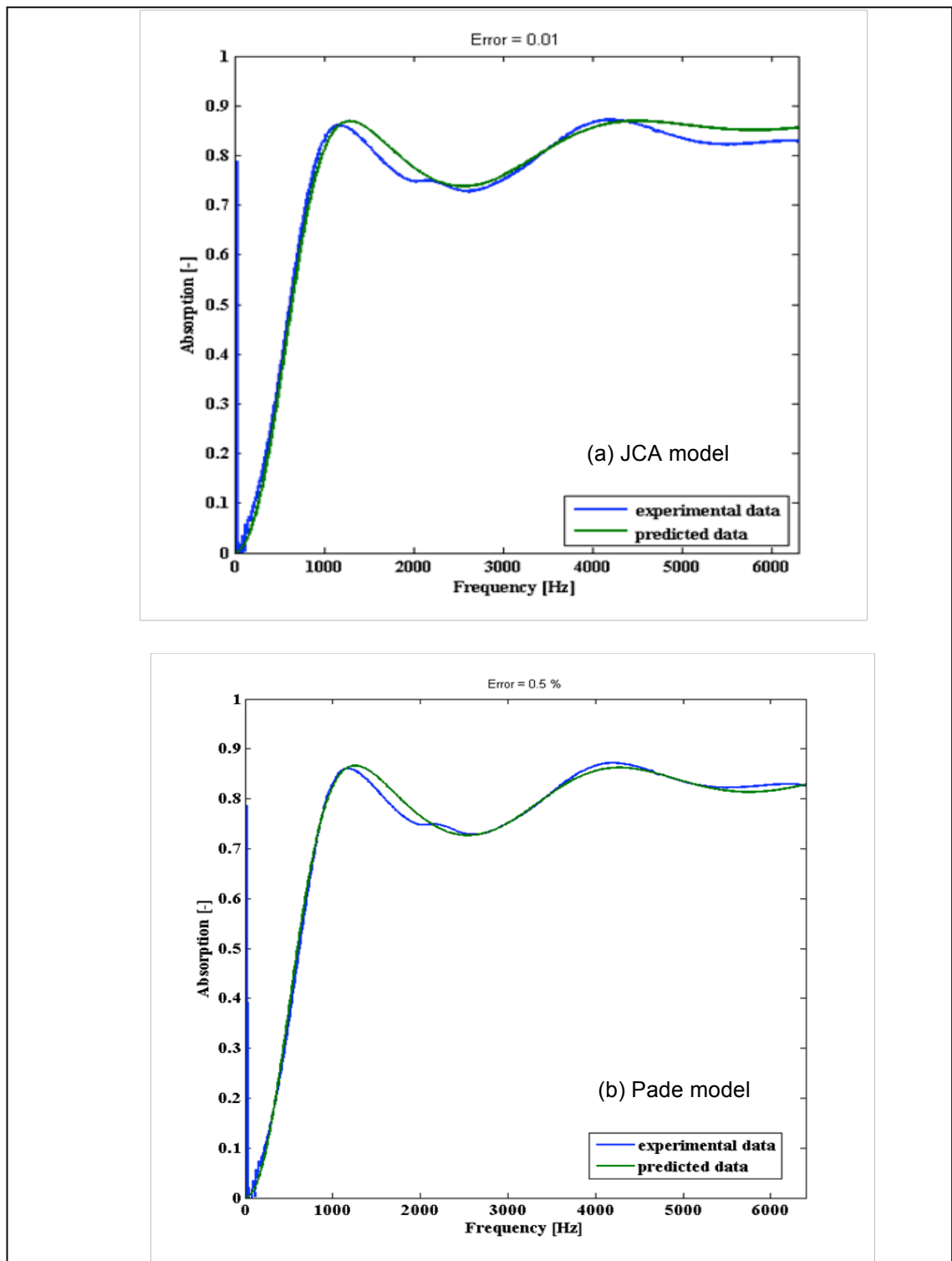


Figure 4.12: The measured and predicted absorption coefficient for porous specimen with 2% of surfactant produced with 3% of catalyst (sample C3S2); (a) JCA model and (b) Pade model

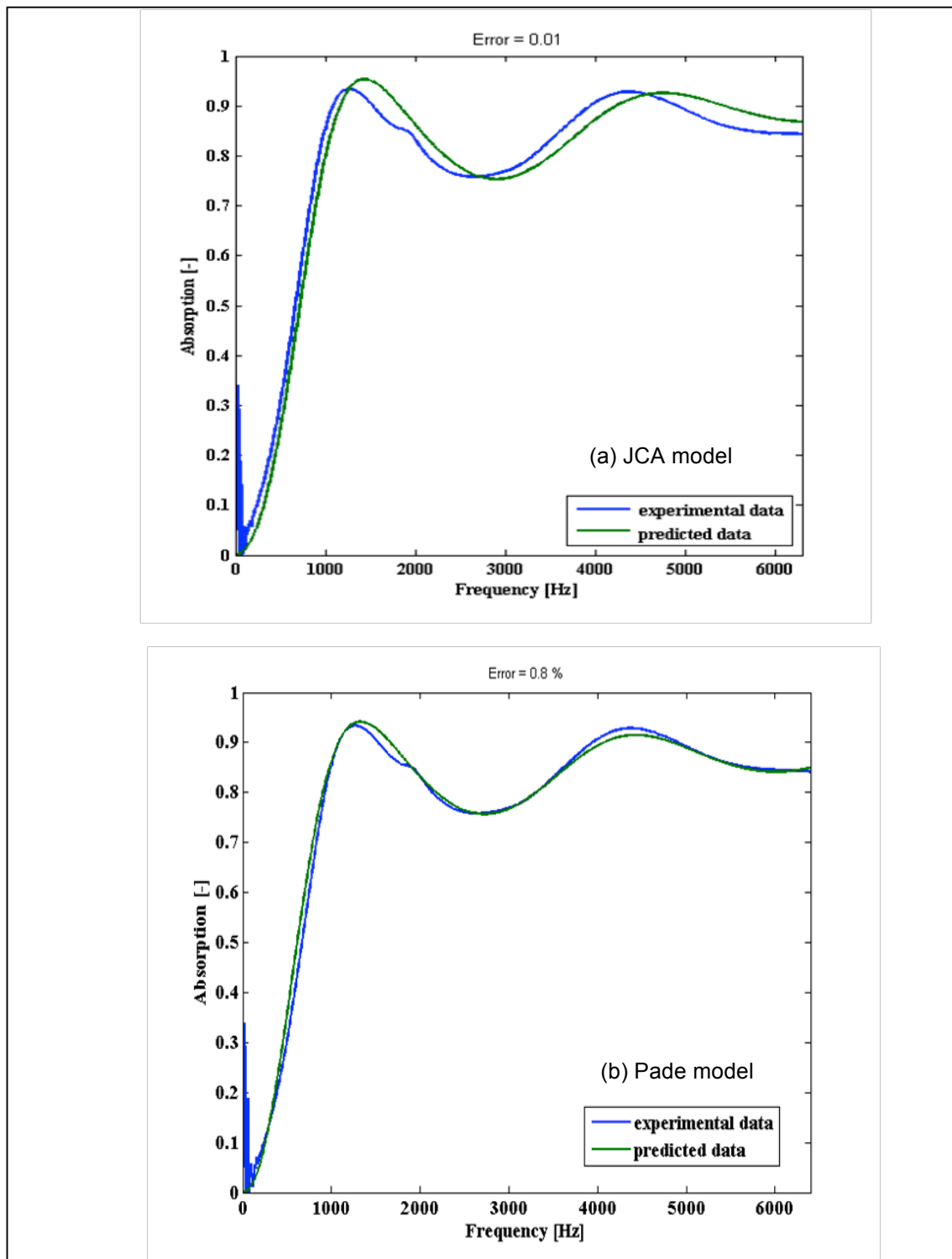


Figure 4.13: The measured and predicted absorption coefficient for porous specimen with 3% of surfactant produced with 3% of catalyst (sample C3S3); (a) JCA model and (b) Pade model

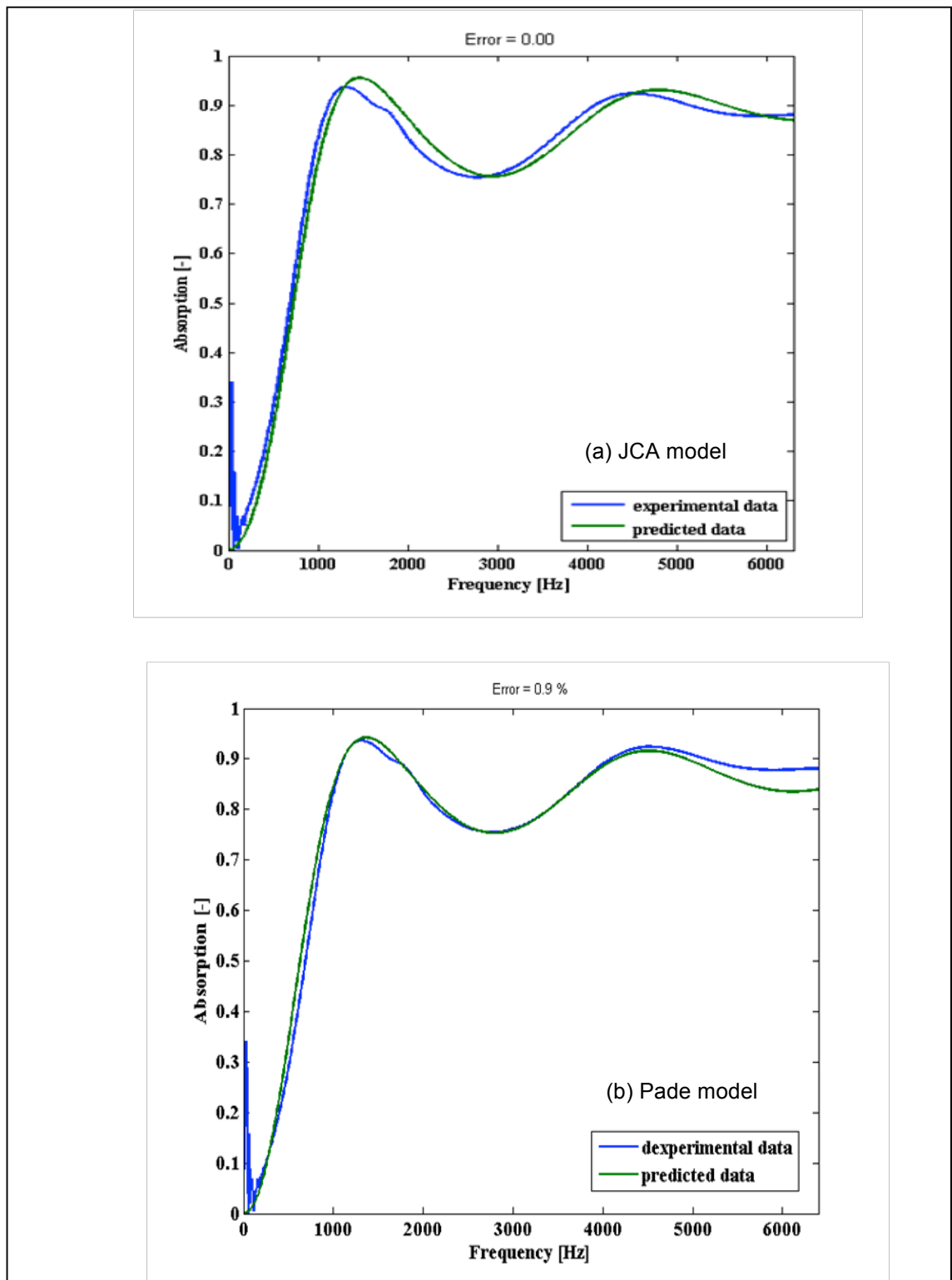


Figure 4.14: The measured and predicted absorption coefficient for porous specimen with 4% of surfactant produced with 3% of catalyst (sample C3S4); (a) JCA model and (b) Pade model

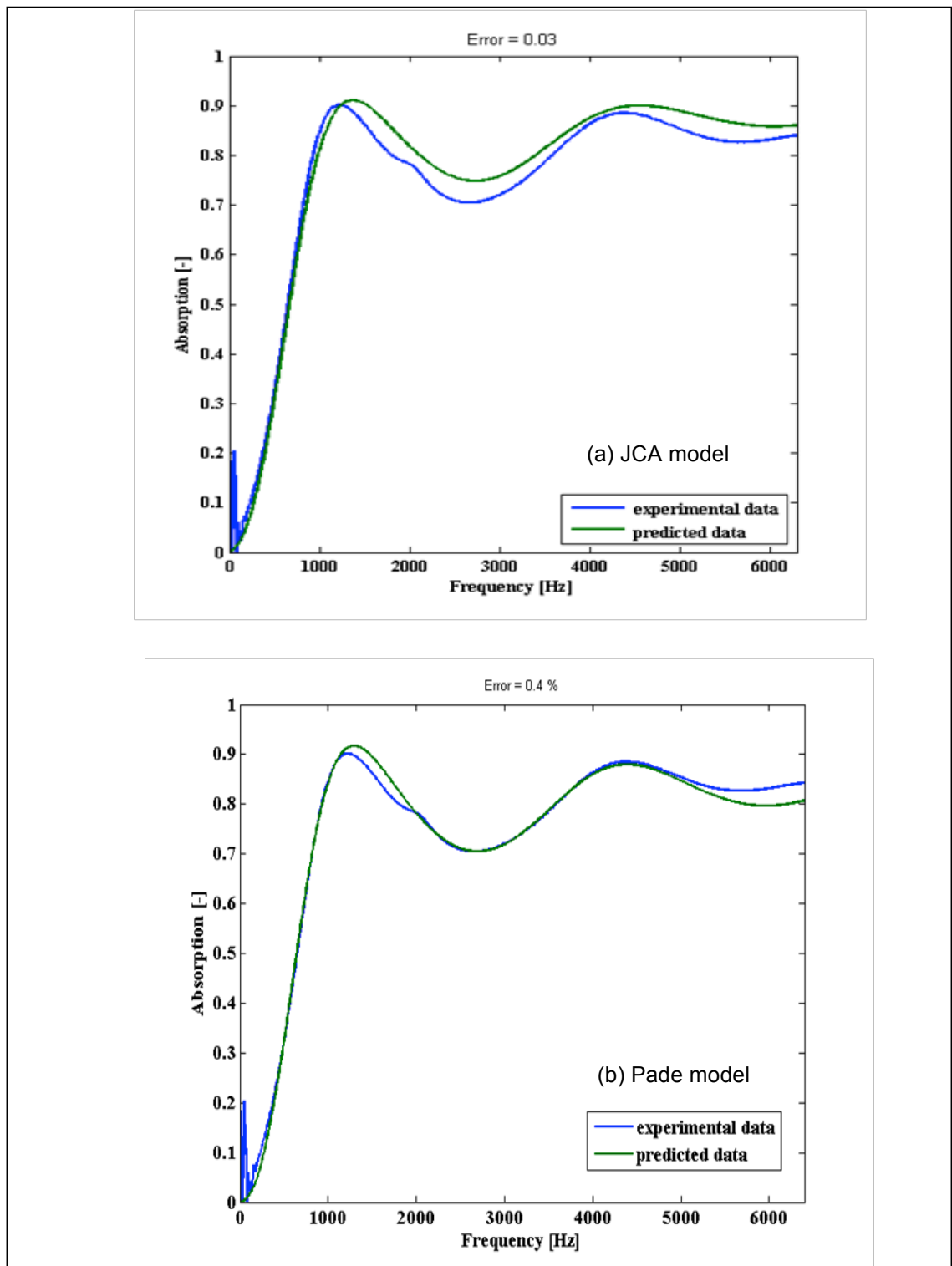


Figure 4.15: The measured and predicted absorption coefficient for porous specimen with 5% of surfactant produced with 3% of catalyst (sample C3S5); (a) JCA model and (b) Pade model

A summary of the deduced values from the JCA and Pade models of non-acoustical parameters for samples C3S0, C3S1, C3S2, C3S3, C3S4 and C3S5 is presented in Tables 4.3 and 4.4. A comparison of flow resistivity of these samples between the measured data and deduced data by both models are presented in figure 4.16. Figure 4.17 illustrates a comparison of porosity between the measured value and deduced value. The deduced values of tortuosity, the viscous and thermal characteristic lengths and standard deviation of pore size are presented in figures 4.18-4.20, which were plotted in at graph with a function of the amount of surfactant.

Table 4.3: The deduced non-acoustical properties by JCA model for the porous materials produced by varying the concentration of surfactants at constant catalyst 3%

Sample	At constant Catalyst (%)	Variation of Surfactant (%)	Flow Resistivity (N.s.m ⁻⁴)	Porosity (measuring)	Tortuosity	Viscous Characteristic Length	Thermal Characteristic Length
C3S0	3	0	33774	0.87	1.60	1.18E-05	5.87E-04
C3S1	3	1	37373	0.85	2.18	1.94E-05	1.50E-04
C3S2	3	2	48178	0.84	1.04	1.62E-05	2.52E-02
C3S3	3	3	32771	0.82	1.32	2.60E-05	2.01E-02
C3S4	3	4	33912	0.81	1.35	1.74E-05	4.67E-02
C3S5	3	5	43494	0.79	1.34	2.27E-05	4.00E-02

Table 4.4: The deduced non-acoustical properties by Pade model for the porous materials produced by varying the concentration of surfactants at constant catalyst 3%

Sample	At constant Catalyst (%)	Variation of Surfactant (%)	Flow Resistivity (N.s.m ⁻⁴)	Porosity	Tortuosity	Standard deviation of pore size
C3S0	3	0	51287	0.75	3.76	0.68
C3S1	3	1	52319	0.77	4.04	0.01
C3S2	3	2	42834	0.70	1.96	0.68
C3S3	3	3	29623	0.76	1.96	0.67
C3S4	3	4	30824	0.75	1.96	0.60
C3S5	3	5	30038	0.65	1.84	0.73

It was found that the measured data and deduced data from both models for these samples have a trend of flow resistivity decreasing as surfactant increases. It corresponds with increased larger pores when these samples have increased surfactant (see figure 3.49). The deduced values of the flow resistivity of these samples are slightly lower than the measured data, except the deduced values of C3S0 and C3S1 obtained from Pade model (see figure 4.16). The samples: C3S0 (without surfactant) and C3S1 (1% surfactant) have extremely complex pore structures. Moreover, standard deviation of pore size for sample C3S1 is 0.01 (shown in table 4.4). This shows, sample C3S1 cannot be adopted by Pade model, which has a complicated complex pore structure and connectivity.

The measured and deduced porosity of these samples have a shift to a lower value with surfactant is increased (see figure 4.17). But the deduced data of porosity from Pade model has a lower value than the measured data. It can be explained by the same reason as in the previous section. The samples in this case illustrate obviously bi-modal behaviour when the samples have increased amounts of surfactant. This is, prediction of Pade model obtained only porosity for the meso-pores.

For these samples the deduced tortuosity of the JCA and Pade models have a trend of decreasing tortuosity with increased concentration of surfactant except sample C3S1 (see figure 4.18). Because pore network of sample C3S1 contains variable pore sizes and more complex pore connectivity (see figure 3.48). Therefore, it increases the deduced tortuosity and flow resistivity values. Both the viscous and thermal characteristic lengths of these samples have a trend to increase with surfactant is increased. Furthermore, the thermal

characteristic length of all samples shown in table 4.3 and figure 4.19 illustrate clearly that is much larger than the viscous characteristic length. The impact of the viscous and thermal characteristic lengths between the sample without surfactant at 3% catalyst (C3S0) and the sample with the highest surfactant at 3% catalyst (C3S5) is 192% and 6814%, respectively. This corresponds with the increasing proportion of large pores as shown in figure 3.40 when these samples have an increase in the amount of surfactant.

The deduced standard deviation of pore size for these samples (shown in figure 4.20) give a range of 0.60-0.73 expect for sample C3S1 (as 0.01). The high deduced standard deviation of pore size can be explained by the wide pore size distribution of these samples as shown in figure 3.40 that contains more pores of variable in size.

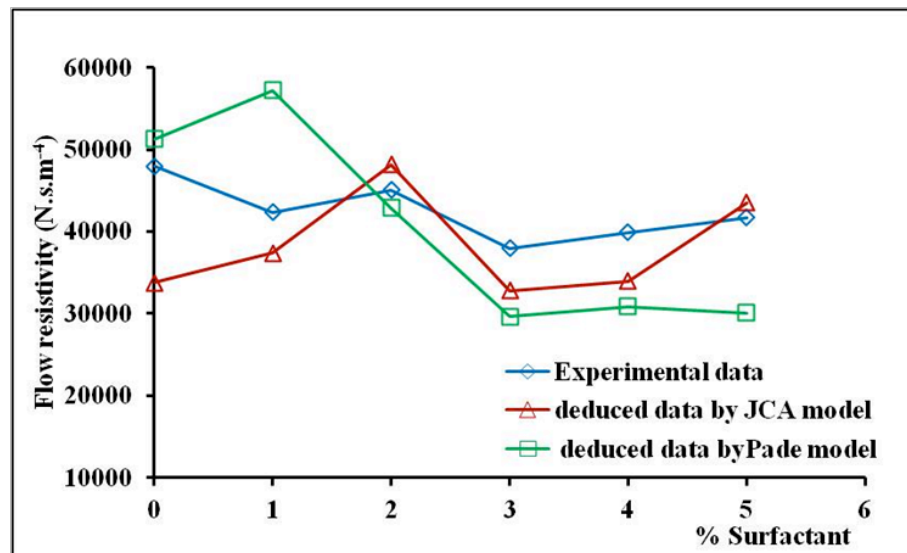


Figure 4.16: The measured and deduced flow resistivity values for porous samples produced by varying the concentration of surfactant and with 3% of catalyst.

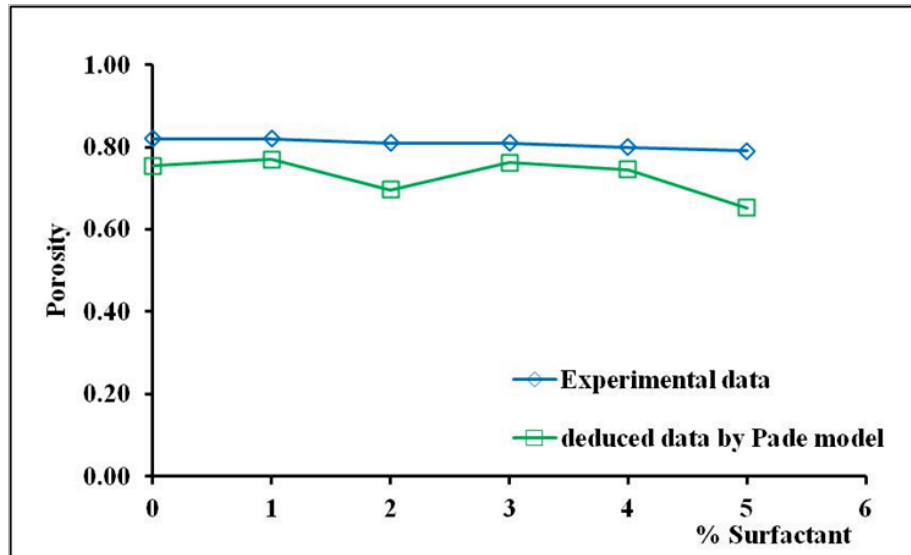


Figure 4.17: The measured and deduced porosity values for porous samples produced by varying the concentration of surfactant and with 3% of catalyst

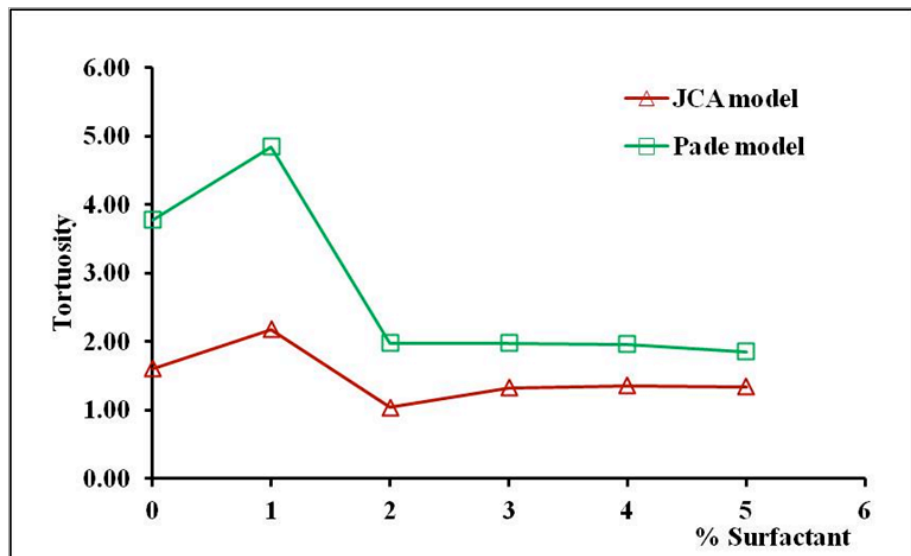


Figure 4.18: A comparison of deduced tortuosity values of two models for porous samples produced by varying the concentration of surfactant and with 3% of catalyst

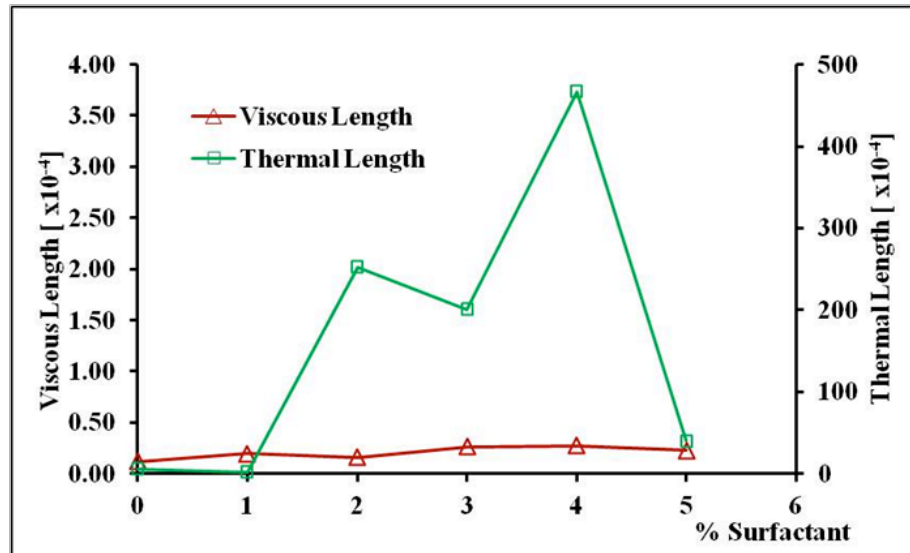


Figure 4.19: The deduced data of viscous length and thermal length for porous samples produced by varying the concentration of surfactant and with 3% of catalyst

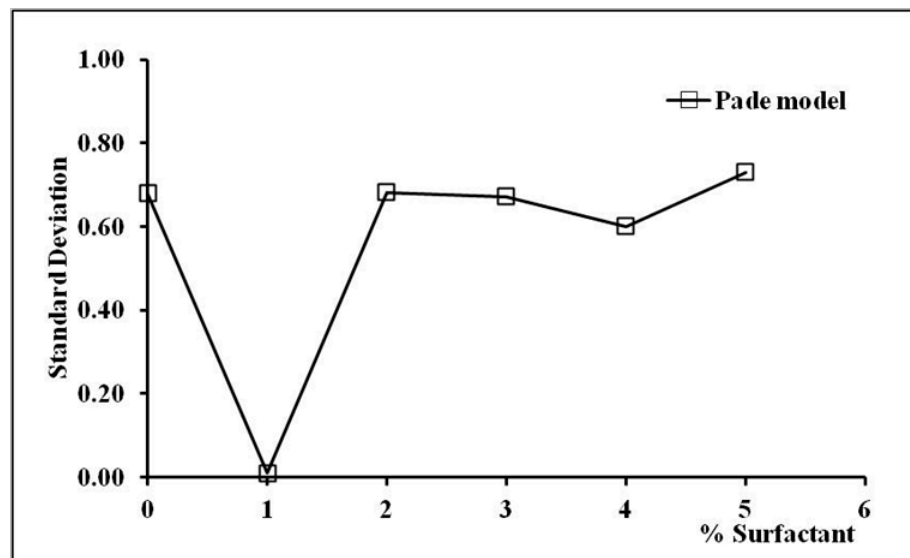


Figure 4.20: The deduced standard deviation of pore size for porous samples produced by varying the concentration of surfactant and with 3% of catalyst

4.5 Conclusions

The Johnson-Champoux-Allard (JCA) and Pade approximations were used in studying the acoustical behavior of the porous material samples produced by varying the amount of catalyst and surfactant in order to control the pore size. It was found that Pade model has a better fit to the measured data of acoustic absorption coefficient spectra than the JCA model. The deduced data by both models of flow resistivity and porosity from these samples has the same trend as the measured data. In addition, the deduced value of standard deviation of pore size for these materials corresponds to the pore size distribution obtained by the image analysis method. The deduced data of tortuosity and two characteristic lengths indicate that these porous materials have a pore system containing variable pore sizes and connected pores with a complex network. Finally, the modeling can help to describe the morphological characterisation of these porous material samples in terms of the non-acoustical properties.

Chapter five

5 The Porous Materials with Stratification

5.1 Introduction

Commercial porous materials have a poor performance of acoustical absorption in the low frequency range. To analyse the absorbing of acoustic materials in this range, Brouard et al. [70] proposed a general method of modelling acoustic fields in stratified media which include elastic solid, fluid and porous layers. However, these absorbing systems are discrete, i.e. they consist of a stack of several porous or micro-perforated layers. The work presented in this chapter is focused on improving absorption performance in the broad frequency range by using porous materials with continuous pore stratification. It is shown that materials with continuous pore stratification can be produced by the blending of recycled tyre granulates and polyurethane binder and controlling of expanding time in the chemical reaction process. This was achieved by the following two methods: first method used heat for control expanding time and second method used polyol to create open cells. The developed materials were studied acoustically and non-acoustically. Non-acoustical parameters of the pore stratification were measured and used to predict the acoustical properties of the developed materials. The prediction method was based on the Pade approximation model [68] and transfer matrix method [69].

This chapter presents the experimental setup, acoustic pore stratification data, absorption coefficient data, modeling method and predicted results. Production of porous materials with stratification, using recycled tyre granulates

has several advantage; low cost, waste disposal, protection of national resources and reduction of noise pollution.

5.2 Sample Preparation Procedure

Controlling the expanding time in foaming process is a key parameter for creating porosity stratification. This work has considered two methods for producing the porous materials with stratification. The first method, the expanding time was controlled by heat applied to the bottom surface of the container in which the material sample was placed. The second method was based on blending polyol with polyurethane binder in order to create an open cell. A cylindrical mould with an open top and terminated bottom was used for controlling the expanding in the foaming process. Each method experimental set up is discussed in the next section.

5.2.1 Sample Preparation by Applied Heat

This method makes use of a mould one end of this is attached to a hot plate. The diameter of this mould was 100mm and it was 150mm high. The raw material was prepared with polyurethane (PU) binder (Flexilon 457) which was supplied by Rosehill Polymers Ltd. This binder is based on methylene diphenyl diisocyanate (MDI), which contains 9.8-10.8% of isocyanate. The binder was added to tyre shred residue which was supplied by Credential Tyre Recycling Ltd. The sieve analysis data for tyre shred residue are shown in section 3.3 (chapter 3). The reactants listed in Table 5.1 were mixed in a 2-litre beaker with a spatula for 60 seconds. The resultant mixture was poured in the cylindrical mould and covered with a top lid. The bottom of this mould was heated by a

hotplate. The temperature was set at 80 °C which was found as an optimum in terms of the rate of reaction and the material quality attained as a result. The polyurethane polymerisation reaction is shown in Figure 5.1.

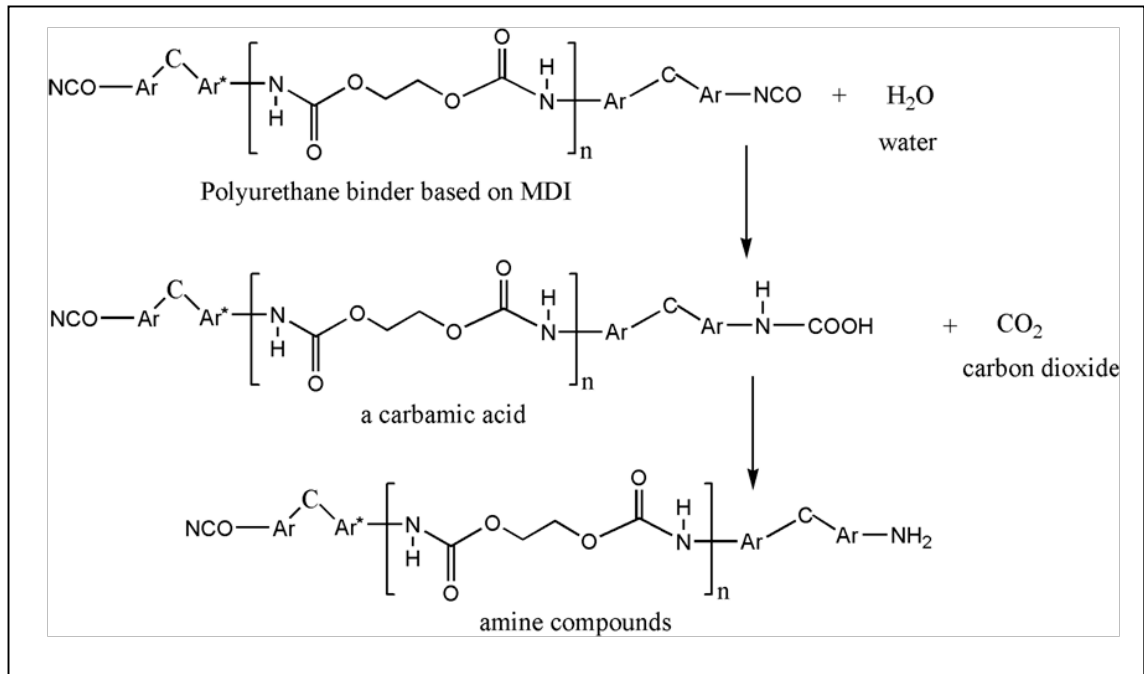


Figure 5.1: The polyurethane polymerization reaction

The polymerisation reaction occurred in the mould with bottom that was heated and the top was covered with a lid. Heat helps to decrease reaction time near the bottom surface of this mould. The reaction time relates directly to the expanding time in the foaming process. The lower part of the porous material sample in the container with heated bottom has a shorter expanding time and attains smaller pores. Carbon dioxide (CO_2) product from the bottom mould raises and it is trapped near the top lid of the mould. As a result of this process, the topside of the porous material sample attains larger pores. The polymerisation reaction took on average 90 min to complete. The sample was then removed from this mould and trimmed with a sharp knife to remove impervious polyurethane crust. This work prepared two 140mm samples

(sample 1: ST1 and sample 2: ST2), whose non-acoustical and acoustical properties were studied.

Table 5.1: The composition of the reactants

Reactants	% by weight
MDI	56.0
Water	22.0
Tyre shred residue	22.0

5.2.2 Sample Preparation Using a Low Molecular Weight Polyol

This method uses an open cylindrical mould to prepare porous material samples. The diameter of this mould was 100mm and it was 150mm high. The binder used in this experiment was Polyurethane (PU) binder (XP 2261) supplied by Chemique Adhesive and Sealant Ltd. This binder is based on methylene diphenyl diisocyanate (MDI), which contains 25-30 percents of isocyanate. A low molecular weight polyol (Flexilon 1117) was used in order to create a higher proportion of open cells. This polyol was supplied by Rosehill Polymers Ltd., it was based on polyether polyols and contained 1-5 percents of dibutyltin alkyl mercaptide. Tyre shred residue supplied by Credential Tyre Recycling Ltd., and comes in the granulated form, which is a mixture of nylon fibres and rubber grains bonded to the fibres. The reactants listed in Table 5.2 were mixed in a 2-litre beaker with a spatula for 60 seconds. The time selected for the mixing operation was found sufficient to ensure good mixing of the ingredients in the mix and to achieve an adequate level of aeration that was needed to help to initiate the polymerisation reaction. The resultant mixture was poured in a cylindrical mould with an open top. The chemical reactions of polyurethane polymerization were of two types. The first type reaction was polyurethane polymerization reacting with with water, which is illustrated in

figure 5.1. The second type of reaction is polyurethane polymerisation with polyol, which is illustrated in Figure 5.2.

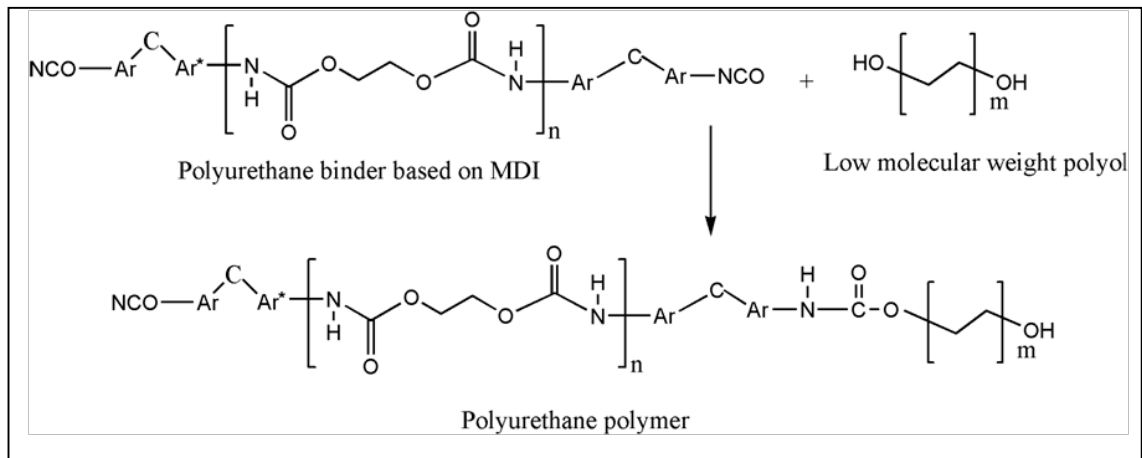


Figure 5.2: Chemical reaction of polyurethane polymerisation with polyol

The polymerisation reaction occurred in the mould with the top vented to the atmosphere and with the bottom blocked with a lid. Oxygen in the atmosphere helps to decrease reaction time at the surface of this material. The reaction time relates directly to expanding time in the foaming process. A short expanding time from the fast reaction of the foaming processes create small pores in the top layer of the material. In this method of sample preparation carbon dioxide (CO_2) products of the slower reaction at the bottom of the mould can be tapped by the top layers in the mould which solidify more rapidly. The slow polymerisation at the bottom of this mould had a longer expanding time. Therefore, this material contains larger pore sizes in the bottom layer. It was estimated that the reaction took on average 60 min to complete resulting in a fully consolidated sample of foam with a clear pore stratification.

Table 5.2: The composition of the material mix

Reactants	% by weight
MDI	46.0
Polyol	18.0
Water	18.0
Tyre shred residue	18.0

The fully consolidated sample was removed from the cylindrical mould. The top surface of this sample was uneven and the bottom surface contained an impervious residual layer. These layers were trimmed with a sharp knife to form a 140mm long porous cylinder with two perfectly flat interfaces. Photographs of the resultant material sample are shown in Figure 5.3. Two samples were prepared with (sample 1: SP1 and sample 2: SP2) and their acoustical and non-acoustical properties were examined.

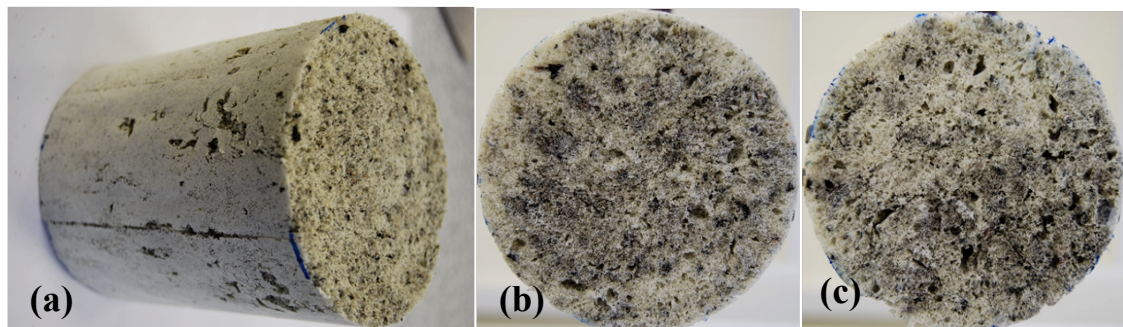


Figure 5.3: photographs of the resultant material sample; (a) whole, (b) top side of whole sample and (c) bottom side of whole sample

5.2.3 Material Characterisation methods

The process of material characterisation was carried out in three phases. The first phase of the experimental procedure was to measure the acoustical properties of the 140mm long, material sample in direct and reverse orientations in an impedance tube. This experiment was carried out in a two-microphone Bruel Kjael (BK4206) impedance tube at a normal angle of incidence and in the

frequency range of 50-1600 Hz. The second phase of experiments was to divide the material sample into two equal parts: Layer A and Layer B, each having the thickness of 70 mm. each of these two layers was then measured in the impedance tube in the direct and reverse orientations to study the effect of pore stratification. The final phase of the acoustic experiments was to split Layers A and B further to obtain four 35mm thick sub-layers: sub-layer C, D, E and F. Figure 5.4 illustrates the principle behind the process of dividing the 140mm material specimen into individual sub-layers. The acoustical properties of these four material specimens were measured in the impedance tube in a manner similar to that explained above.

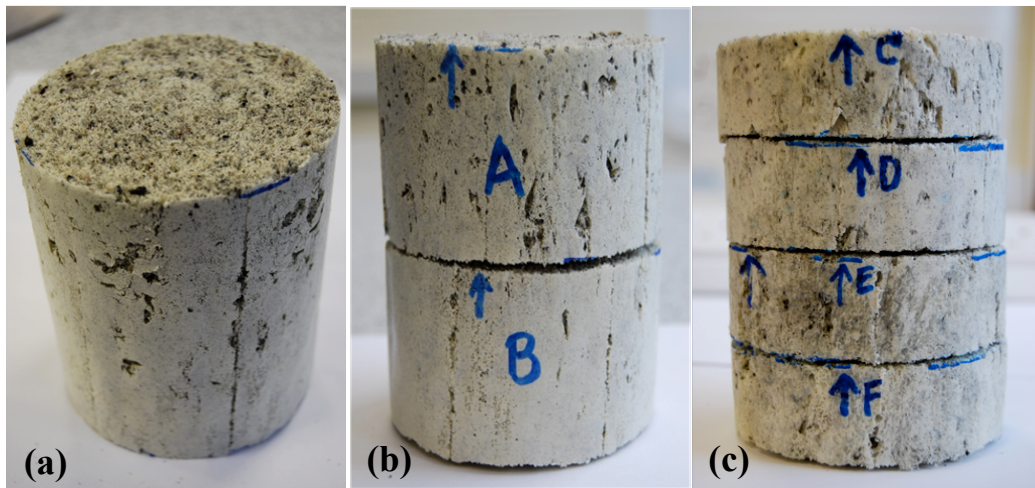


Figure 5.4: The procedure for splitting a 140mm sample into individual sub-layers: (a) original sample, (b) splitting in two 70mm layers, (c) splitting in four 35mm sub-layers.

The measurement procedure for determining the flow resistivity, porosity and density was explained in the section 3.4.4 (chapter 3). The pore size distribution was measured using the optical method detailed by Pispola et al [47]. Each side of sub-layer C, D, E and F had a photo taken by the microscope camera. The images were analysed using Optimax image analysis software

[48]. For this purpose five 20mm x 20mm non-equidistantly spaced areas on each of the 8 images were selected so that the mean pore size distribution in these specimens could be determined. Table 5.3 shows the relative positions on the sample surface at which these areas were selected. Figure 5.5 illustrates the process of the area selection for the image analysis. The detail of Optimax image analysis shows in the section 3.4.4.4 (chapter 3).

Table 5.3: The positions of areas on the image selected for the pore size distribution analysis (x,y) in terms of the sample radius R = 50mm.

Area label	P1	P2	P3	P4	P5
Co-ordinates (x,y)	(0,0)	(12.5,0)	(-37.5,0)	(0,25)	(0,-16.7)

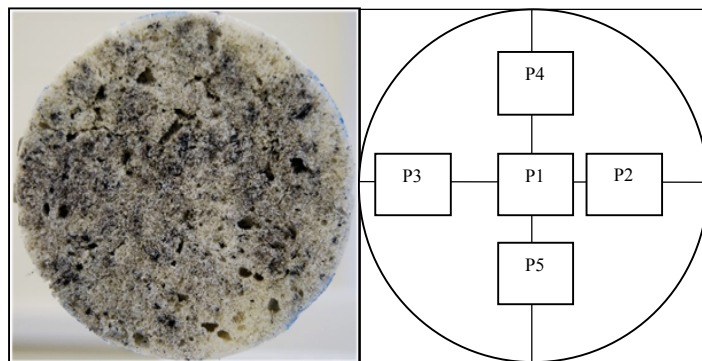


Figure 5.5: On the selection of the analysis area to determine the pore size distribution in a material specimen

5.3 Experimental Results

This section describes the non-acoustical and acoustical properties of the porous material sample with stratification that was produced by using the two methods of sample preparation.

5.3.1 Non-Acoustical Properties of Samples manufactured with Method 1

The material characterisation procedures detailed in Section 5.2.3 were used to determine the non-acoustical properties such as porosity (ϕ), density (ρ), flow resistivity (σ) and pore size distribution of sub-layer C, D, E and F. The measured value of these properties is shown in Figures 5.6-5.11.

The pore size distribution is an important non-acoustical property of porous materials and has an influence on sound propagation. Figures 5.6 (sample 1:ST1) and 5.7 (sample 2:ST2) show microscopic photographs of the top and bottom surfaces of sub-layers C, D, E and F. It was found that almost all photographs illustrate the presence of micro-pore and meso-pores. These photos were used for the determination of the pore size distribution of ST1 and ST2. In this work, the pore size distribution is presented by probability density function (PDF) of the pore size. Figures 5.8 (ST1) and 5.9 (ST2) present the mean pore size distribution data for all the four sub-layers. This data was obtained by averaging over the 10 sets of pore size distribution data that correspond to the 10 areas of the images taken on the top and bottom surfaces of these samples. The pore size distribution data illustrate clearly that the proportion of smaller pores increases with increasing sample depth. The bottom layer (sub-layer F) of all samples has the highest value of PDF in the micro-pore range (around 0.1 mm). The top layer (sub-layer C) of all samples has a higher value of PDF in the meso-pore range (1.00 mm.). Additionally, the sub-layers C, D and E has a closely value of PDF. This indicates that the pore size distribution of the sub-layers C, D and E are close to log-normal. It is clear that the faster polymerization reaction makes smaller pore sizes at the bottom

layer (sub-layer F), whereas the slower polymerization reaction creates larger pore size at the top layer sub-layer C to E (0-105 mm of the sample depth). This can be explained in term of the rate constant (k) that has a strong temperature dependence, increasing with the increased temperature. The rate constant can be defined by the Arrhenius equation [42]

$$k = Ae^{\left(\frac{-E_a}{RT}\right)}, \quad (5.1)$$

where A is the so-called pre-exponential factor or the A -factor, E_a is the activation energy and R is the gas constant. Therefore, these samples have different rate constants between the top layer and bottom layer. The polymerisation reaction at bottom layer of these samples is controlled by the temperature of the heated plate, whereas the polymerisation reaction at the top layer is controlled by the temperature in the room.

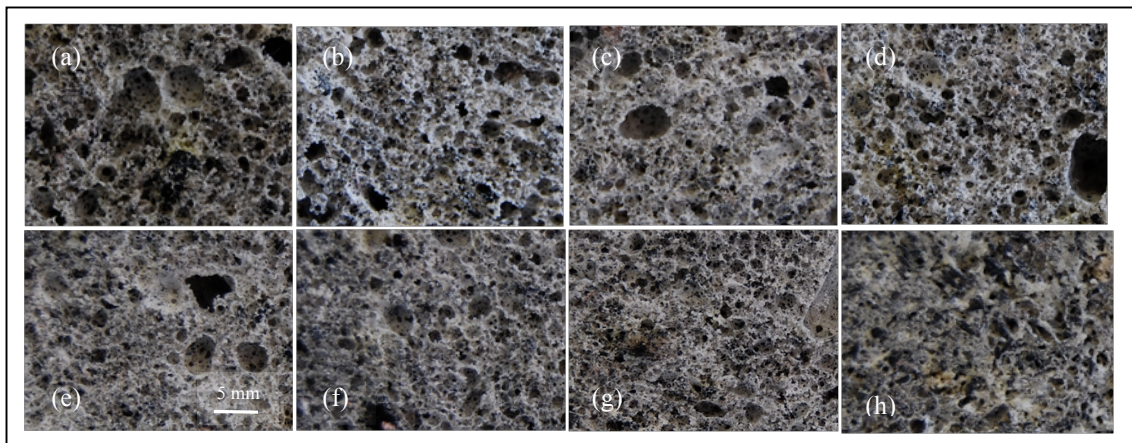


Figure 5.6: Microscopic images of the porous material with stratification for sample ST1; (a) sub-layer C, top side, (b) sub-layer C, bottom side, (c) sub-layer D, top side, (d) sub-layer D, bottom side, (e) sub-layer E, top side, (f) sub-layer E, bottom side, (g) sub-layer F, top side and (h) sub-layer F, bottom side

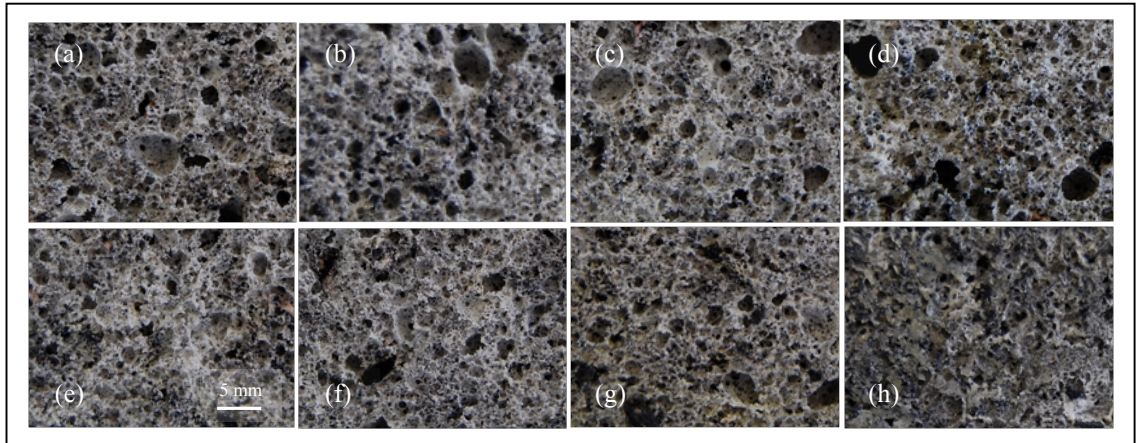


Figure 5.7: Microscopic images of the porous material with stratification for sample ST2: (a) Sub-layer C, top side, (b) sub-layer C, bottom side, (c) sub-layer D, top side, (d) sub-layer D, bottom side, (e) sub-layer E, top side, (f) sub-layer E, bottom side, (g) sub-layer F, top side and (h) sub-layer F, bottom side

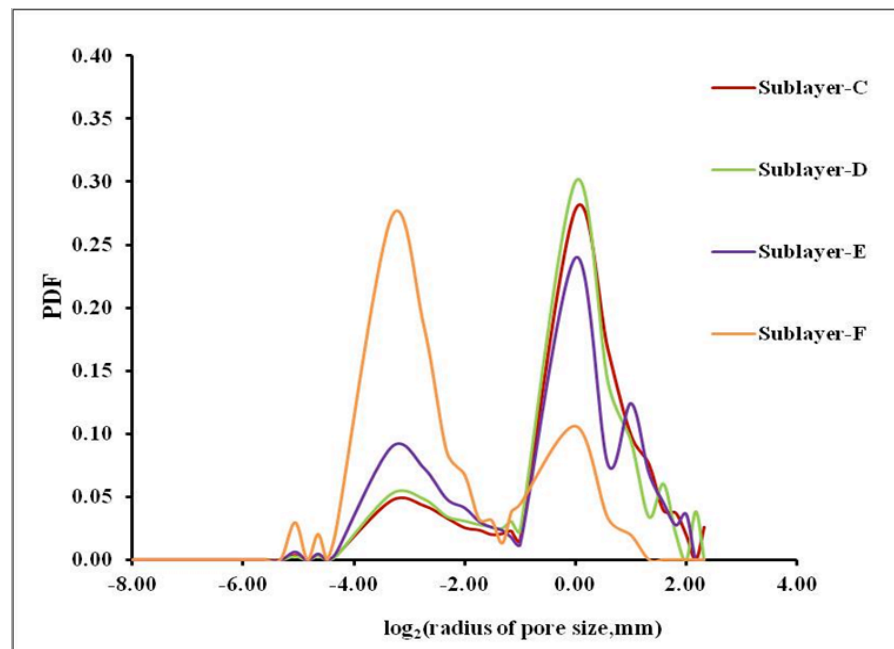


Figure 5.8: The probability density functions of the pore size for each of the four sub-layer of sample ST1.

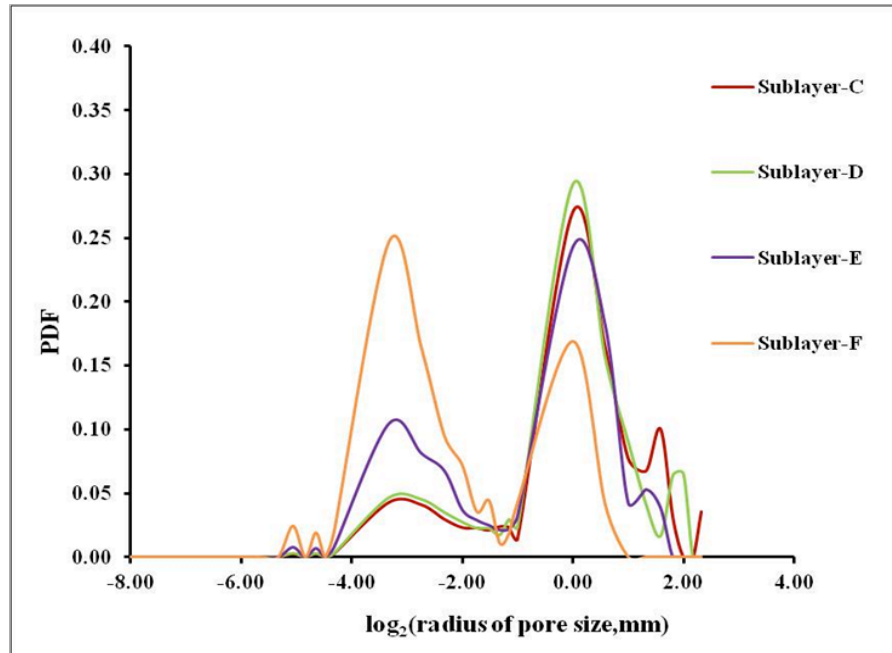


Figure 5.9: The probability density functions of the pore size of each of the four sub-layer of sample ST2.

Table 5.4 presents the average measured values and standard deviation (STD) of the porosity and density for sub-layers in samples ST1 and ST2, which were determined by averaging the data for 2 specimens taken from each of these samples. Figure 5.10 presents the porosity and density of samples ST1, ST2 as a function of the layer depth. The porosity of all samples reduces with the increased sample depth. The porosity of sub-layer C is similar to that for sub-layer D ($\phi = 0.92$) and it is slightly higher than that for sub-layer E ($ST1: \phi = 0.86, ST2: \phi = 0.89$). The porosity of sub-layer F is the lowest ($ST1: \phi = 0.59, ST2: \phi = 0.62$). The dependence of porosity on the layer depth is inverse to that measured for the density of ST1 and ST2, which is an expected result, which indicates that the ratio of open pore to close pore volumes is unlikely to change with depth. The density of these material layers increases with the increase layer depth (Figure 5.8). The density of sub-layer C ($ST1=191 \text{ kg/m}^3, ST2=180 \text{ kg/m}^3$) is lower than that for sub-layers D ($ST1=203 \text{ kg/m}^3,$

ST2=184 kg/m³) and sample E (ST1=270 kg/m³, ST2=214 kg/m³). But the density of sub-layer F 140 mm is relatively high (ST1=474 kg/m³, ST2=415 kg/m³).

Table 5.4: Summary of the porosity and density for ST1 and ST2

Sub-layer	Sample depth [mm]	Porosity				Density(kg/m ³)			
		ST1		ST2		ST1		ST2	
		Average	STD	Average	STD	Average	STD	Average	STD
C	35	0.92	0.007	0.93	0.014	191	7	180	14
D	70	0.92	0.007	0.92	0.016	203	7	184	16
E	105	0.86	0.023	0.89	0.009	270	23	214	9
F	140	0.59	0.011	0.62	0.017	474	11	415	17

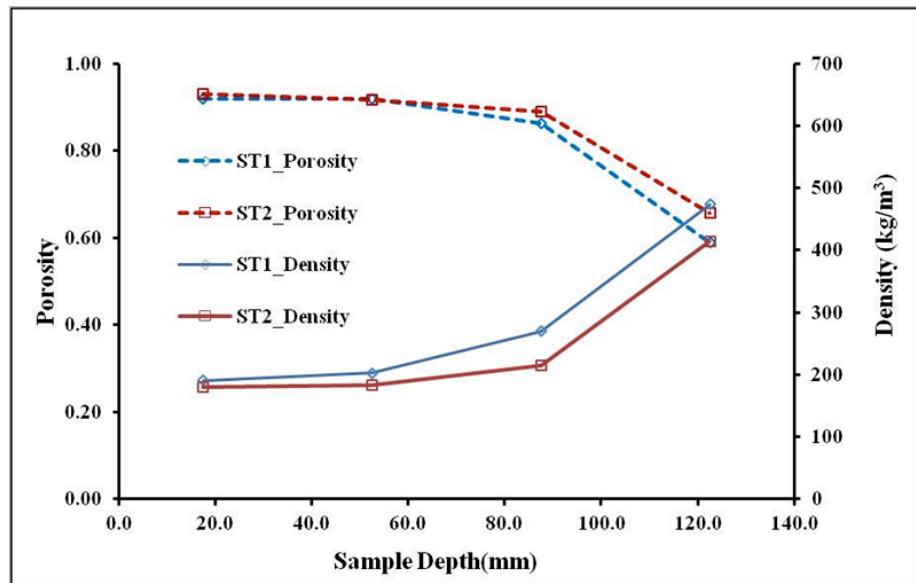


Figure 5.10: The dependence of the porosity and density on sample depth for samples ST1 and ST2

The flow resistivity of each sub-layer was measured in the flow resistivity rig for the normal and reverse sample orientation. The results are presented in Table 5.5. The average values of flow resistivity and porosity are plotted in the graph (see figure 5.11) as a function of the sample depth. It was found that the dependence of the flow resistivity with depth is inverse of the porosity dependence. Here, the flow resistivity rises at sample depth increase. The

flow resistivity of sub-layer C (ST1= 10306 N.s/m⁴, ST2= 10056 N.s/m⁴) is slightly lower than that for sub-layers D (ST1= 10665 N.s/m⁴, ST2= 10110 N.s/m⁴) and E (ST1 = 13528 N.s/m⁴, ST2= 11422 N.s/m⁴). The flow resistivity of sub-layer F is the highest (ST1= 167787 N.s/m⁴, ST2= 133417 N.s/m⁴). This illustrates very strong pore size stratification. This pore stratification of ST1 is characterized with a 33%, 248% and 1628% porosity, density and flow resistivity, respectively. In case of ST2, the impact is on porosity, density and flow resistivity which present 31%, 230% and 1327%, respectively. The non-acoustical properties of sub-layers C-E (0 - 105 mm depth) are similar and there are no evidence of strong pore stratification. Probably, the heat transfer from the hot plate into the sample is poor so that the reaction acceleration due to the flow of heat takes place mainly in the bottom sub-layer. Therefore, the fast polymerisation took place only in sub-layer F. In case of sub-layers C, D and E a more slower polymerisation reaction rate the same reaction rate which was relatively independent of depth.

Table 5.5. The flow resistivity data for samples ST1 and ST2

Sub-layer		Sample depth [mm]	Flow Resistivity (σ), [N.m.s ⁻⁴]	
			ST1	ST2
C	Top	0	10080	10024
	Bottom	35	10531	10090
	Average	17.5	10306	10057
D	Top	35	10642	10120
	Bottom	70	10688	10100
	Average	52.5	10665	10110
E	Top	70	12422	12048
	Bottom	105	14634	10795
	Average	87.5	13528	11422
F	Top	105	174950	120583
	Bottom	140	160624	146250
	Average	122.5	167787	133417

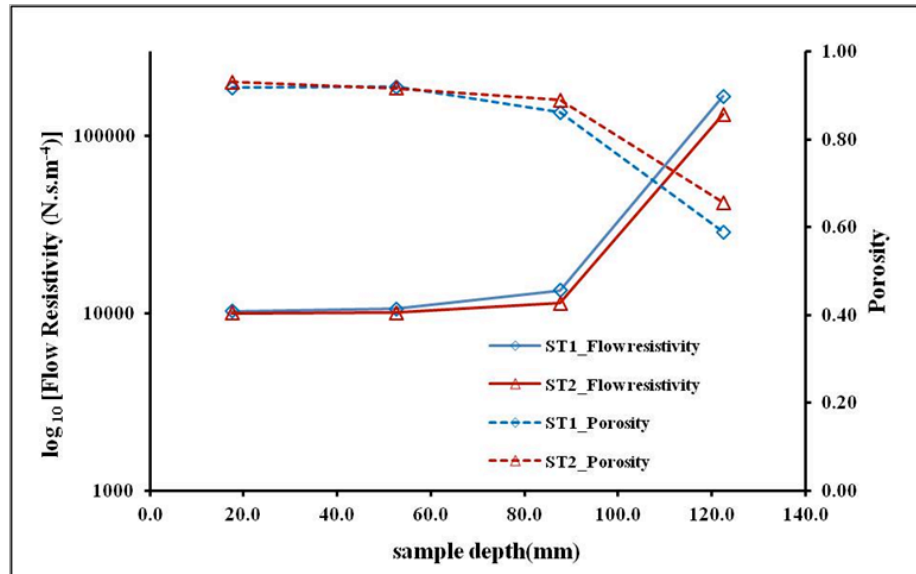


Figure 5.11: The dependence of the flow resistivity and porosity on layer depth for samples ST1 and ST2

5.3.2 Acoustic Absorption Coefficient of Samples manufactured with Method 1

Figure 5.12 shows the acoustic absorption coefficient spectra of 140mm thickness sample measured in the normal and reverse sample orientation in the impedance tube. There is a clear difference in these two absorption coefficient spectra. The absorption measured in the case of normal sample orientation (samples ST1, ST2) is higher than that measured in the case of reverse sample orientation in the frequency of 180-1600 Hz. The largest difference is observed in the frequency range below 180 Hz. This difference in the acoustical absorption spectra can be explained by the difference in the pore size distribution in the top (Figure 5.6(a) for ST1 and Figure 5.7(a) for ST2) and bottom (Figure 5.8(h) for ST1 and Figure 5.9(h) for ST2) side. Additionally, it can be explained by a higher proportion of meso-pore for topside of all samples

(fig 5.8-5.9) and a higher proportion of micro-pores is observed in the bottom side.

The acoustic absorption spectra of 70mm sub-layers A and B are shown in Figure 5.13 and the layout of these samples is shown in Figure 5.4. In the case of sub-layer A, it was found that absorption coefficient spectra taken for the sample in the normal and reverse orientations are close. It is an expected result, because the pore size distribution within sub-layer A is approximately uniform (see Figures 5.6-5.11). The absorption coefficient spectra of sub-layer A peaks in the frequency range of 400-1600 Hz. In the case of sub-layer B, the absorption coefficient measured for the normal sample orientation is much higher than that taken in the reverse sample orientation. It is clear that there is a strong pore size variation in sub-layer B.

Figure 5.14 presents the acoustic coefficient of sub-layers C-F. It is found that the absorption coefficient spectra of sub-layers C, D and E of sample ST1 are similar and peak in the higher frequency range which is explained by their relatively low and similar values of flow resistivity and porosity. The absorption coefficient spectra of sub-layers C, D and E of sample ST2 are also similar. In the case of sub-layer F, it was found that the absorption coefficient spectra have a large difference with those obtained for sub-layers C, D and E. There is a strong difference between the absorption coefficient measured in the normal and reverse sample orientation. The absorption coefficient measured in the reverse sample orientation of sub-layer F has the highest value in low frequency below 600 Hz. This illustrates that the bottom side of sub-layer F contains the smallest pores. This is supported by the results of the image analysis, which shows (images in Figure 5.6 and 5.7 and PDF data in Figures

5.8 and 5.9) that the highest proportion of pores in this sub-layer falls in the micro pore range. The flow resistivity of these sub-layer is high ($\sigma = 167787$ N.s/m⁴ for ST1 and $\sigma = 133417$ N.s/m⁴ for ST2). The acoustic absorption of sub-layers C, D and E is relatively high in the frequency range of 600-1600 Hz which is explained by a relatively high porosity and optimal flow resistance [71]. Sub-layers C, D and E are composed mainly of meso-pores as shown in Figure 5.6 (sample ST1) and Figure 5.7 (sample ST2).

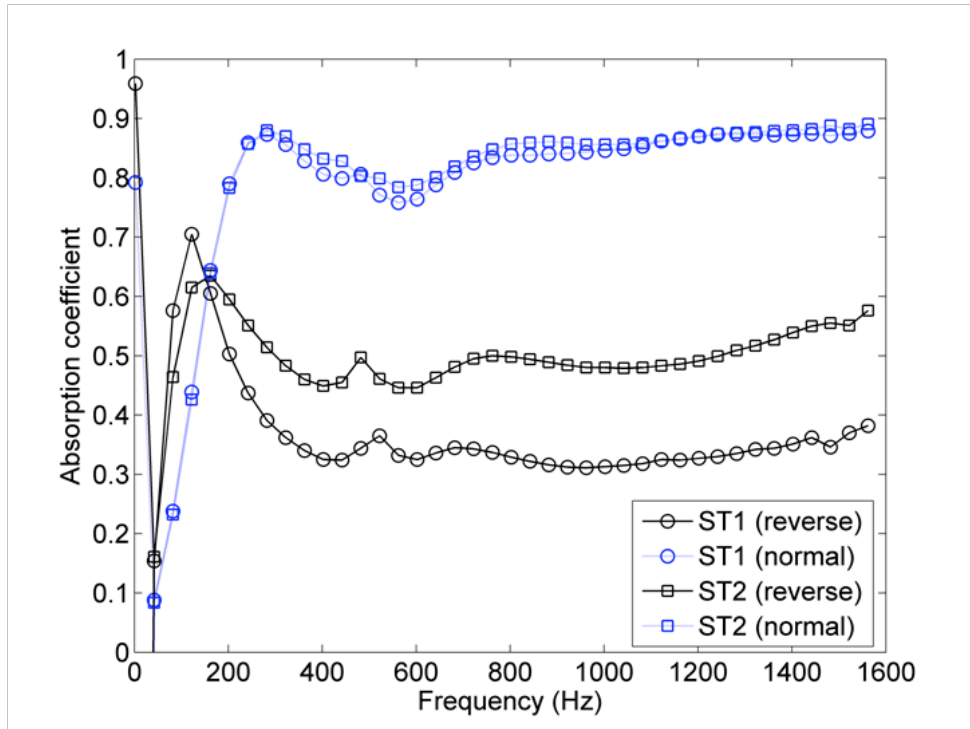


Figure 5.12: Absorption coefficient spectra of 140 mm thick sample of stratified porous materials (ST1 and ST2)

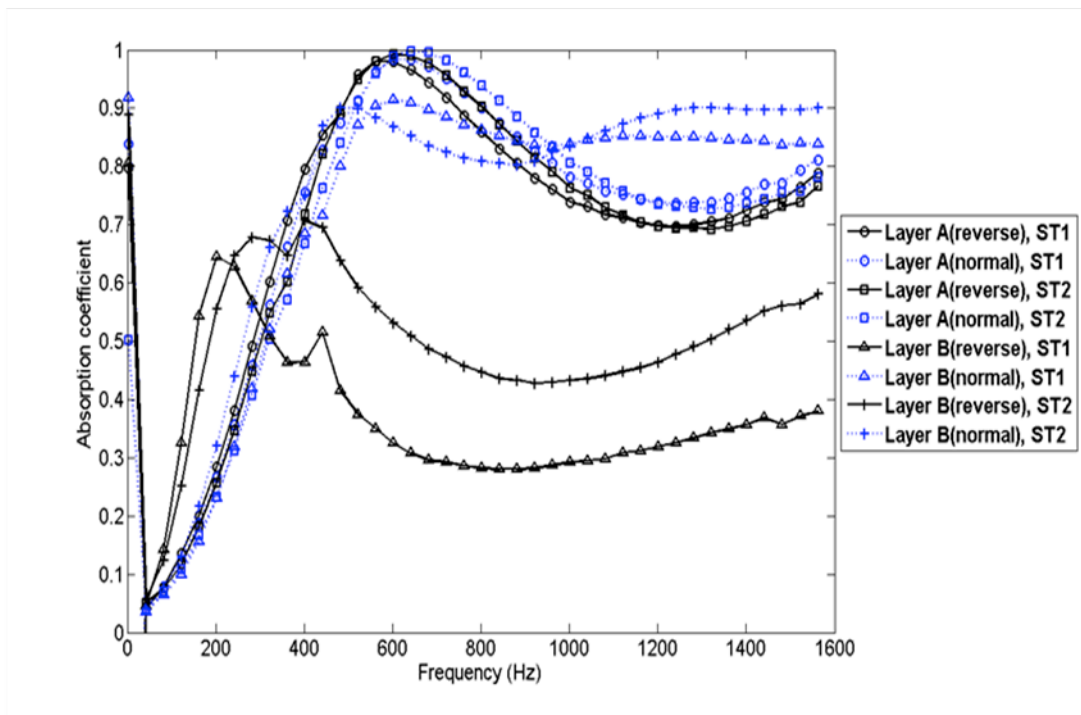


Figure 5.13: Absorption coefficient spectra of layer A and B of ST1 and ST2

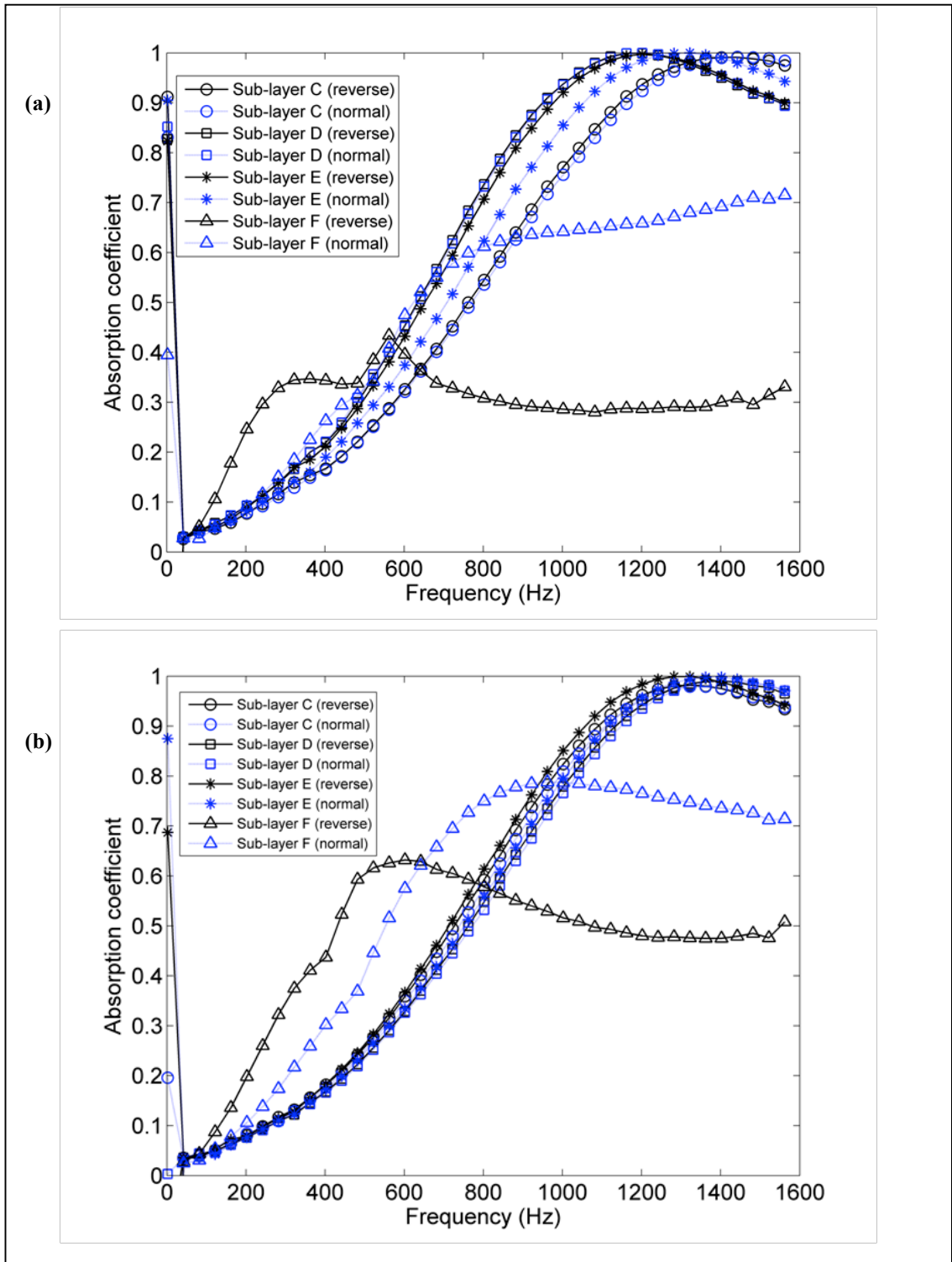


Figure 5.14: The absorption coefficient spectra of sub-layers C, D, E and F of: (a) sample ST1, and (b) sample ST2

5.3.3 The Non-Acoustical Properties of Samples manufactured with Method 2

This section describes the non-acoustical properties of the porous material samples (sample SP1 and Sample SP2) with stratification that was produced by using a low molecular weight polyol for controlling the expanding time in the foaming process.

The material characterisation procedures in Section 5.2.2 were used to determine the non-acoustical properties such as porosity (ϕ), density (ρ), flow resistivity (σ) and pore size distribution of sub-layers C, D, E and F. The measured values of these parameters are shown in Table 5.6. Figure 5.15 (Sample SP1) and Figure 5.16 (Sample SP2) show microscopic photographs of the top and bottom surfaces of sub-layers C, D, E and F. It was found that almost all photos contain a proportion of micro-and meso-pores. The images of the top layer (sub-layer C) show a larger proportion of micro-pores whereas the images of the bottom surface of sub-layer F show a larger proportion of meso-pores. The mean pore size distribution data of the four sub-layers are presented in Figures 5.17 for sample SP1 and 5.18 for sample SP2. These results were obtained by averaging over the 10 sets of the PDF data that correspond to 10 images of the top and bottom surfaces of the porous specimens.

The pore size distribution data illustrate that the proportion of larger pores increases with increasing sample depth. In the case of the top layer (sub-layer C), the pore size distribution is clearly bi-modal and it peaks around 1mm (meso-pores) and 0.1mm (micro-pores). In the case of the bottom layer (sub-

layer F), the pore size distribution is more close to log-normal and it peaks around 1mm. Between these two layers, there is a clear transition in the pore size distribution function from the bi-modal (sub-layer C) to log-normal (sub-layer F) as illustrated by the data presented in Figures 5.17 and 5.18. It is clear that the slower polymerisation reaction obtains a higher proportion of larger pores, whereas the faster polymerisation reaction obtains a higher proportion of smaller pores and broader pore size distribution. This can be explained in term of reaction rate [42] that is defined as the change in the concentration of reactant or product in the unit time. The expression of reaction rate in this case was shown in section 3.4.2 (expression 3.1).

In this work, the reaction rate can be measured by the amount of CO₂ products that are obtained from the polyurethane polymerization reaction. The chemical reaction of this polymerisation is illustrated in figure 5.2.

The obtained data indicate that the porous structure of the material samples produced with this production method appears clearly heterogeneous, i.e. there is a clear stratification in the pore size with the layer depth. The observed pore size stratification has an obvious influence on the porosity, density and flow resistivity which values are listed in Tables 5.6 and 5.7 for the four sub-layers of samples SP1 and SP2. The flow resistivity (Table 5.7) and density (Table 5.6) of SP1 and SP2 decrease with the layer depth increased. The flow resistivity as a function of depth changes by 590% and 400% for SP1 and SP2, respectively. The flow resistivity in sample SP2 is generally higher than that in sample SP1 for a given layer depth. It can be attributed to the difference in the pore size distribution. Sample SP2 (Figure 5.18) has a higher

proportion of micro-pores for a given sample depth than sample SP1 (Figure 5.17). This variation relates to the reproducibility of the production process.

The variation in the density and porosity in sample SP1 is relatively small, being 23% for the density and 3% for the porosity. In the case of sample SP2, these differences are 19 % for the density and 2% for the porosity. The porosity increases with the increased sample depth which can be explained by a higher proportion of meso-pores and lower proportion of micro-pores many of which collapsed during the polymerisation process resulting in a thicker porous frame and a larger proportion of partly closed pore. Because these samples result from the faster polymerisation reaction near the top, then the sub-layers close to top are likely to contain a higher proportion of close cells. The top layer (sub-layer C) has a larger ratio of smaller pore sizes, higher flow resistivity and lower porosity. On the other hand, the bottom layer (sub-layer F) has a larger proportion of larger pore sizes, lower flow resistivity and higher porosity.

Table 5.6: The porosity and density for sample SP1 and SP2.

Sub-layer	Sample depth [mm]	Porosity(ϕ)				Density(kg/m ³)			
		SP1		SP2		SP1		SP2	
		Average	STD	Average	STD	Average	STD	Average	STD
C	35	0.91	0.005	0.90	0.004	132	6	139	6
D	70	0.91	0.017	0.91	0.009	130	6	132	9
E	105	0.92	0.017	0.92	0.004	123	14	122	10
F	140	0.94	0.003	0.92	0.006	109	18	120	9

Table 5.7: The flow resistivity for samples SP1 and SP2

Sub-layer		Sample depth [mm]	Flow Resistivity (σ), [N.m.s ⁻⁴]	
			Sample 1(SP1)	Sample 2(SP2)
C	Top	0	81943	273806
	Bottom	35	81514	255823
	Average	17.5	81729	264815
D	Top	35	65000	217457
	Bottom	70	63829	209743
	Average	52.5	64415	213600
E	Top	70	32229	170286
	Bottom	105	31829	166286
	Average	87.5	32029	168286
F	Top	105	13877	66857
	Bottom	140	13749	65286
	Average	122.5	13813	66072

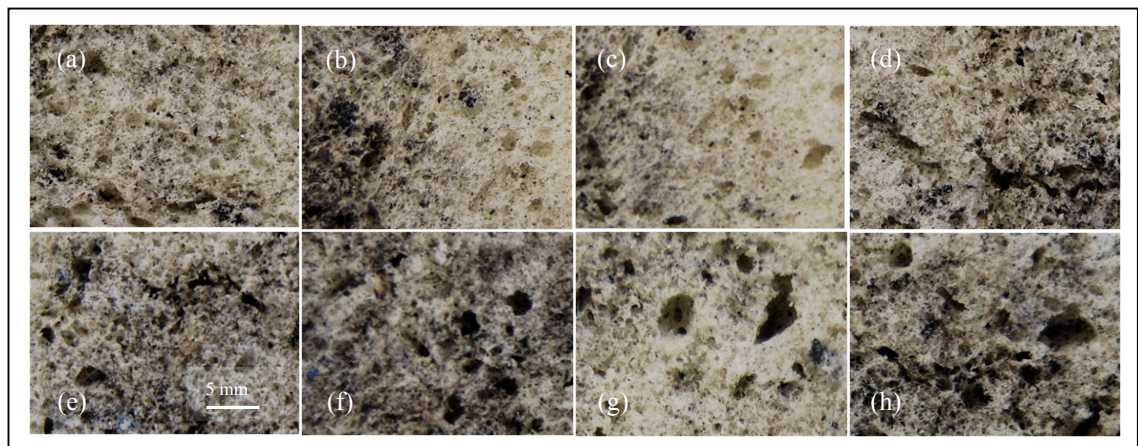


Figure 5.15: Microscopic images of the porous material with stratification for sample SP1: (a) sub-layer C, top side; (b) sub-layer C, bottom side; (c) sub-layer D, top side; (d) sub-layer D, bottom side; (e) sub-layer E, top side; (f) sub-layer E, bottom side; (g) sub-layer F, top side; and (h) sub-layer F, bottom side.

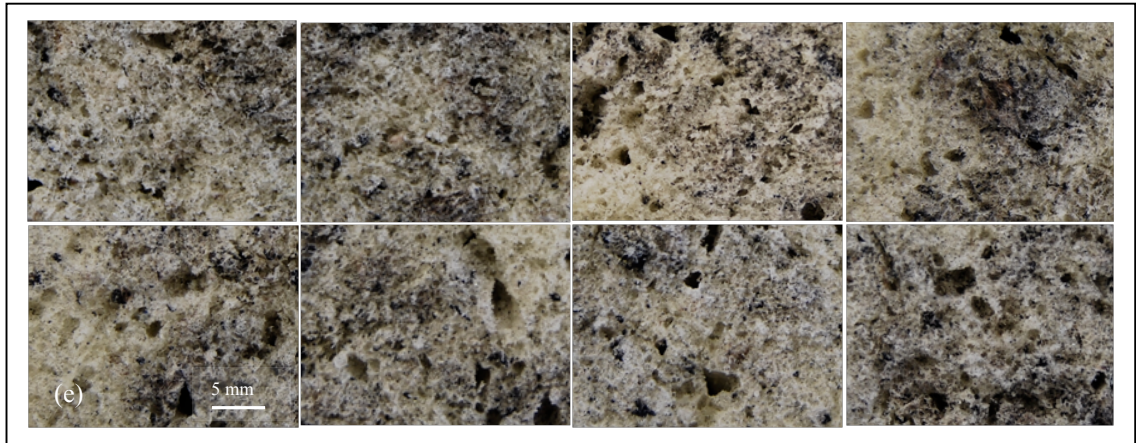


Figure 5.16: Microscopic images of the porous material with stratification for sample SP2: (a) sub-layer C, top side; (b) sub-layer C, bottom side; (c) sub-layer D, top side; (d) sub-layer D, bottom side; (e) sub-layer E, top side; (f) sub-layer E, bottom side; (g) sub-layer F, top side; and (h) sub-layer F, bottom side.

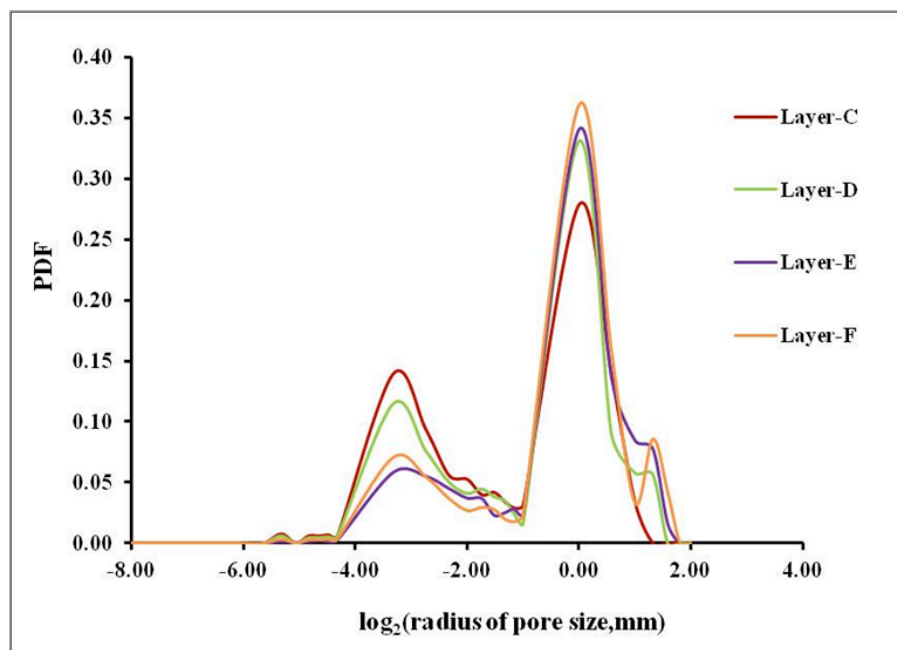


Figure 5.17: The probability density function of the pore size of each sub-layer of sample SP1

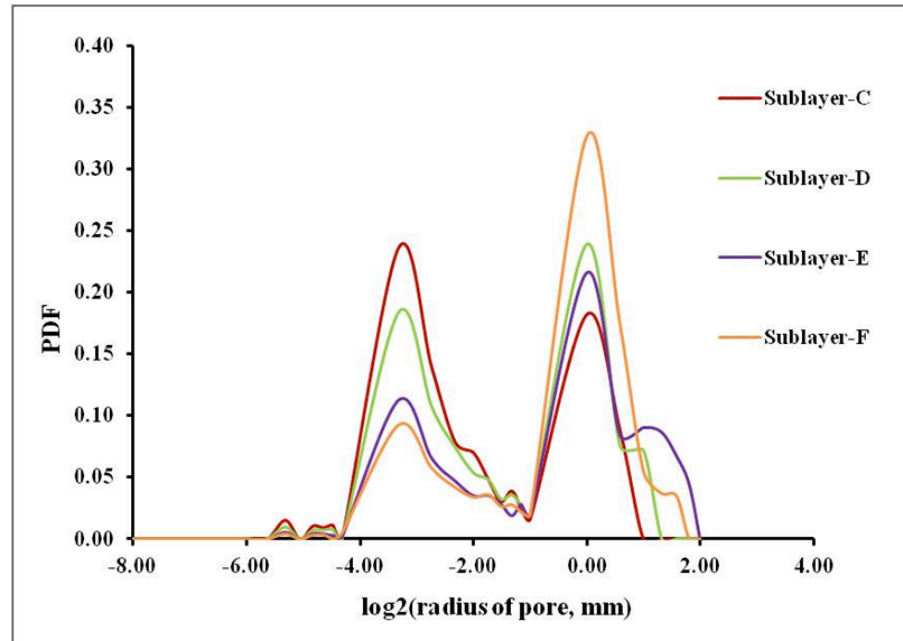


Figure 5.18: Probability density function of the pore size of each sub-layer of SP2

5.3.4 Acoustic Absorption Coefficient of Samples manufactured with Method 2

Figure 5.19 shows the acoustic absorption coefficient spectra of the original 140 mm thick samples in the normal and reverse orientations. It was found that the absorption coefficient between the normal and reverse orientation has a different value. The absorption coefficient of the topside (in normal orientation) of samples SP1 and SP2 is lower than that the bottom side (in reverse orientation). This difference can be explained by the variability in the pore size as a function of depth which shows the images of the topside showing smaller pores (fig. 5.15(a) for SP1 and fig. 5.16(a) for SP2) and bottom side showing larger pores (fig. 5.15(h) for SP1 and fig. 5.16(h) for SP2).

In order to study the pore stratification and its effect on the absorption coefficient, the original 140mm thick samples SP1 and SP2 were divided into

two sub-layers: sub-layer A and sub-layer B. The absorption coefficient data are shown in Figure 5.20. It was found that the absorption coefficient of sub-layers A and B in the normal and reverse orientation are different. This result suggests that samples SP1 and SP2 contain pores which size distribution depends on the layer depth.

In the next experiment, specimens A and B were divided into four sub-layers (C, D, E and F) which were 35 mm thick. The purpose of this experiment was to study absorption coefficient. This experiment provided more refined data on the pore stratification in samples SP1 and SP2. Figure 5.21 shows the acoustic coefficient spectra of sub-layers C - F measured in the normal and reverse orientations. Firstly, there is a clear difference in the absorption coefficient spectra determines for sub-layers C, D, E and F. It is clear that there is a pronounced pore stratification explained by a continuous change of the pore size with the layer depth which was controlled by expanding time during the polymerisation reaction. Secondly, the maximum value of the absorption coefficient spectra increases with the increased layer depth. This can be explained by a gradual increase in the proportion of meso pores with the increased layer depth (see Figures 5.17 and 5.18). Thirdly, there is still a measurable difference between the absorption coefficient for a porous specimen measured in the direct and reverse orientations. This result suggests that there is a fine variation in the pore size distribution within sub-layers C-F. Sub-layers C and D exhibit a higher absorption in the low frequency range (below 500 Hz). Sub-layer E has a higher absorption in the frequency range of 500-650 Hz, whereas the last (bottom) sub-layer F exhibits the highest absorption in the frequency range of 650-1600 Hz.

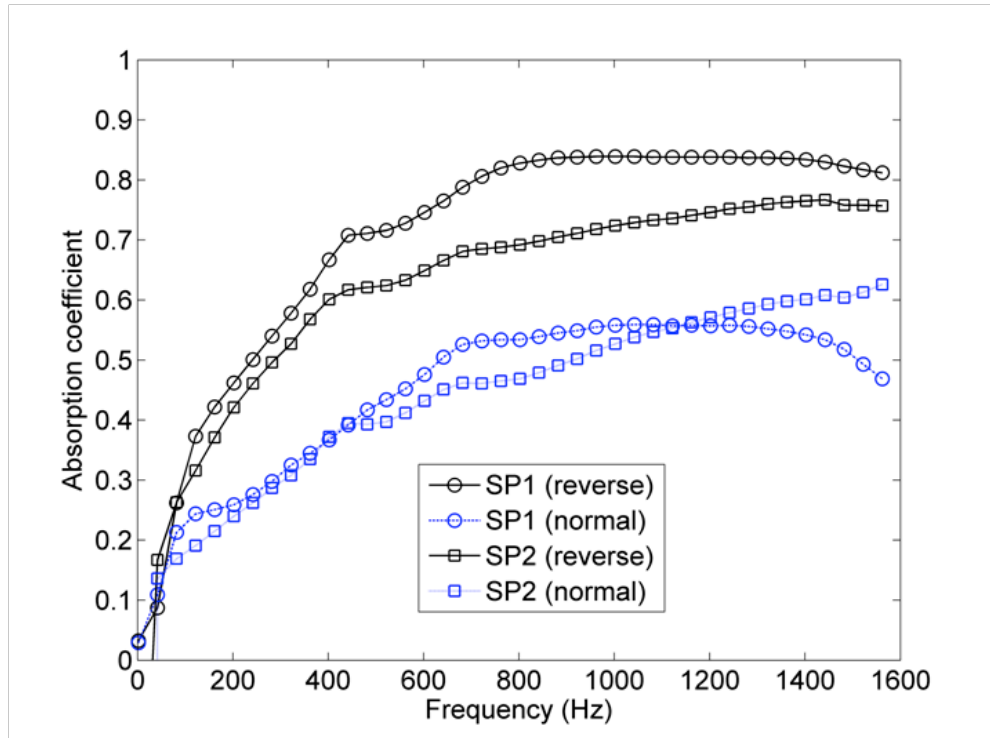


Figure 5.19: The absorption coefficient spectra of 140mm thick samples SP1 and SP2

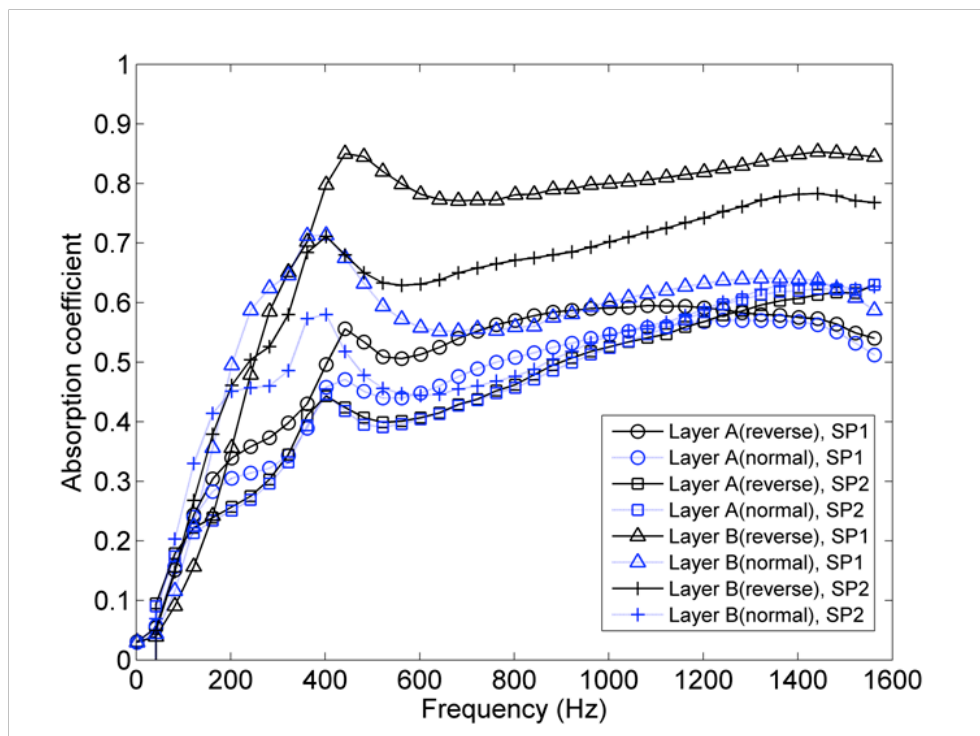


Figure 5.20: The absorption coefficient spectra of sub-layer A and B of samples SP1, SP2

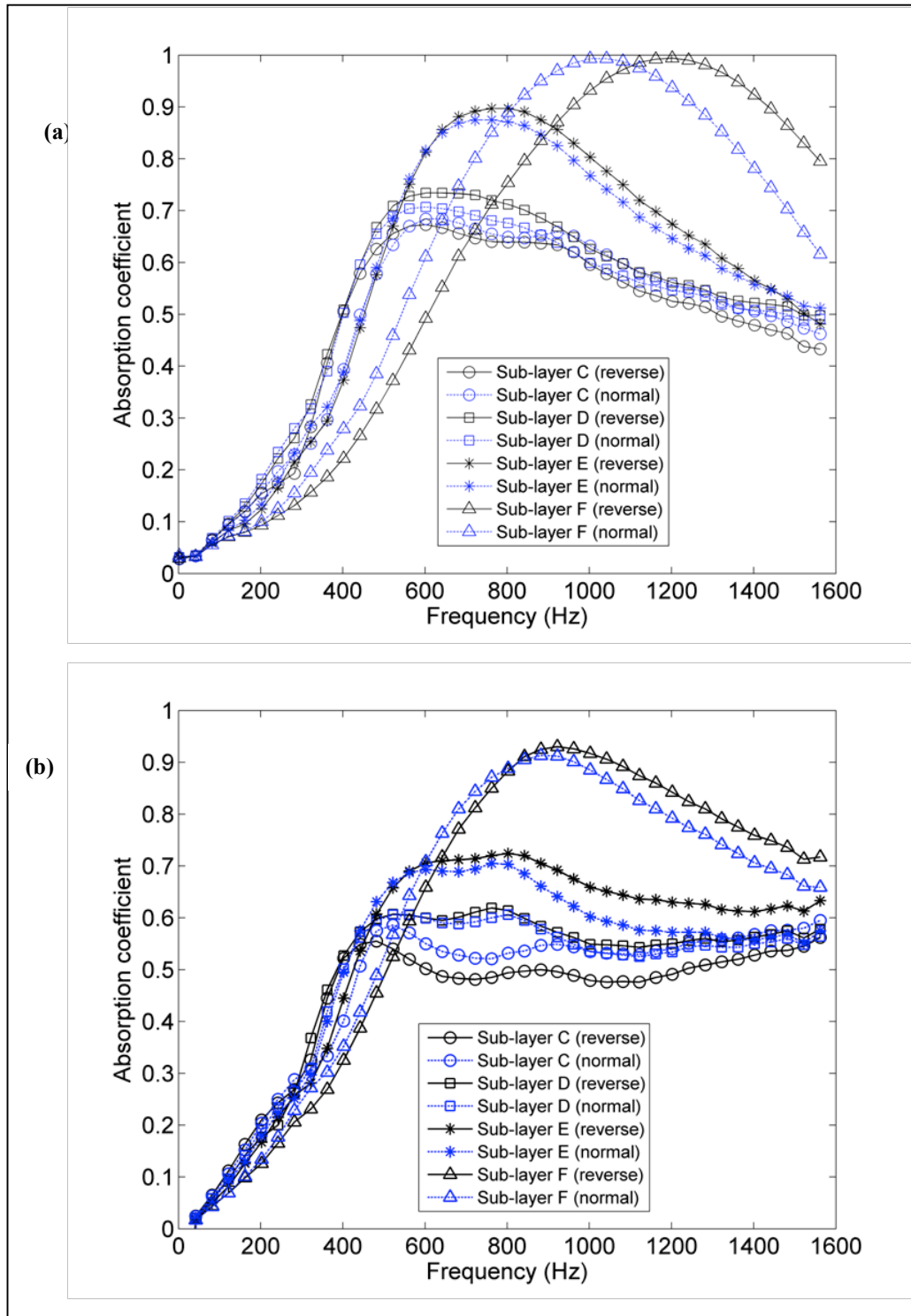


Figure 5.21: The absorption coefficient spectra of sub-layers C, D, E and F of: (a) sample SP1; (b) sample SP2.

5.4 Modeling of the Porous Materials Using Pade Approximations

In section 5.4 we presented the acoustical and non-acoustical data for porous material samples SP1 and SP2 with clear pore stratification. It was shown that the four individual sub-layers of these porous materials are characterised with different pore size distribution, porosity and flow resistivity values (see Tables 5.6 and 5.7). It was shown that the absorption coefficients of the four individual sub-layers are different when measured in the normal and reverse sample orientations. This section makes the use of a model to predict the sound absorption and non-acoustical properties of the individual sub-layers in the different orientations. A model for the acoustical properties of porous media with pore size distribution close to a log-normal was proposed by Horoshenkov *et al* [68], which is Pade approximation.

5.4.1 Acoustical Absorption Coefficient of individual sub-layers

The Pade approximation can predict accurately the behavior of the porous materials with the pore size distribution, which follows the log-normal law. This model provides a good fit for the acoustic absorption coefficient data obtained for sub-layers E and F (lower layers), which are mainly composed of meso-pores. It also provides a good fit to the data obtained for sub-layers D and C (upper layers), which exhibit a pronounced bi-modal pore size distribution (see Figure 5.17 and 5.18).

The Pade model was used in combination with a standard optimization algorithm to determine sets of non-acoustical parameters $x = \{\sigma, \phi, \alpha_\infty, \sigma_\phi\}$ which minimize the difference. The optimisation algorithm (see expression 4.23) was shown in section 4.4.1. This parameter inversion was carried out for $N = 750$ in

the frequency range of 100 – 1600 Hz that corresponds to the standard operational range for an impedance tube with a 100mm diameter.

Comparison between the deduced data and the experimental data for normal and reverse orientations of all sub-layers are presented in Figure 5.22 (for sample SP1) and in figure 5.23 (for sample SP2) in terms of the absorption coefficient spectra. The relative error between the measured and predicted absorption data can be calculated by the following expression 4.24 (shown in section 4.4.1). The non-acoustical properties obtained from modeling (Pade approximants) will be discussed in next section.

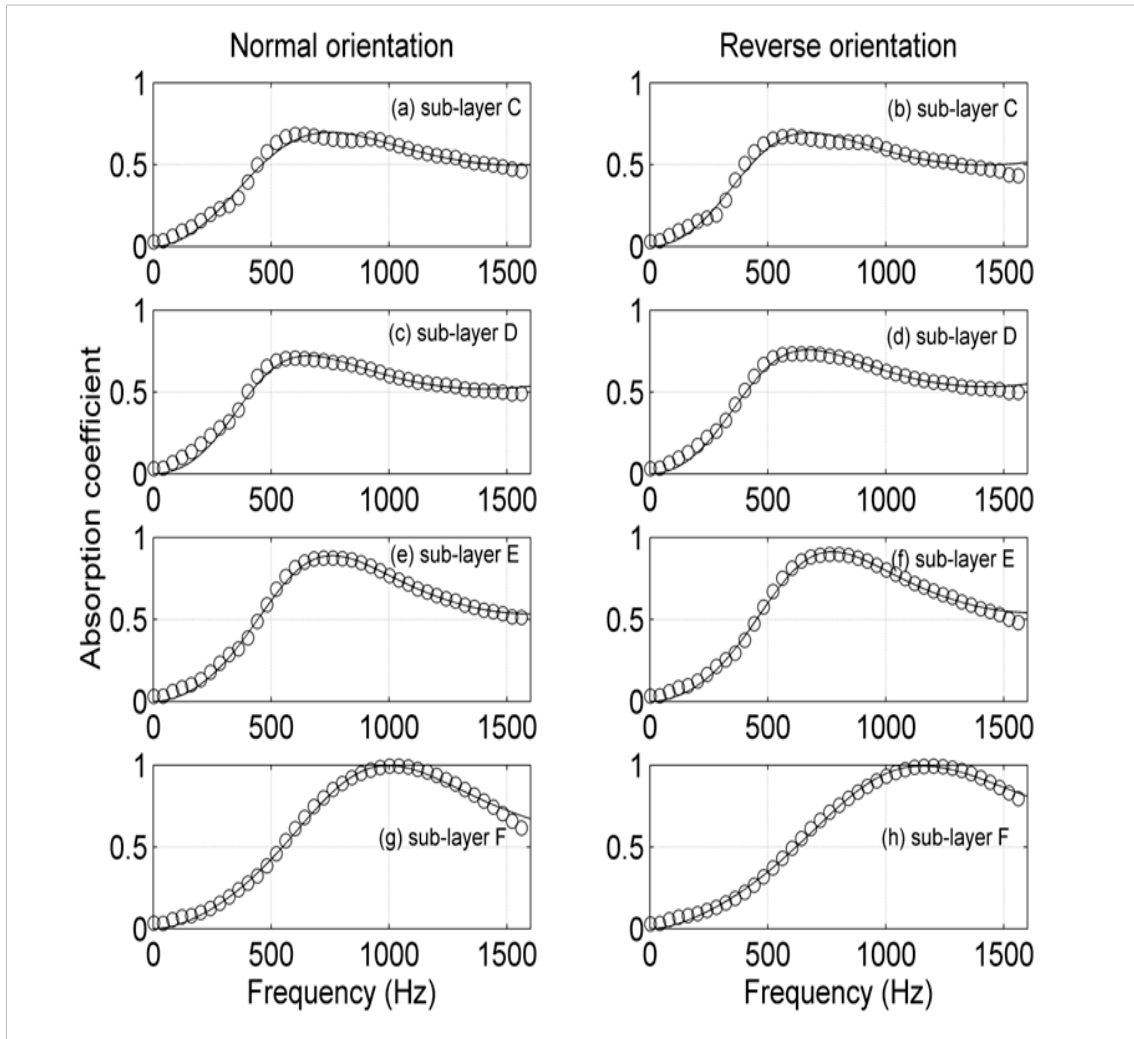


Figure 5.22: Comparison between the predicted data and experimental data of each sub-layer for SP1; (a) sub-layer C (normal), (b) sub-layer C (reverse), (c) sub-layer D (normal), (d) sub-layer D (reverse), (e) sub-layer E (normal), (f) sub-layer E (reverse), (g) sub-layer F (normal) and (h) sub-layer F (reverse)

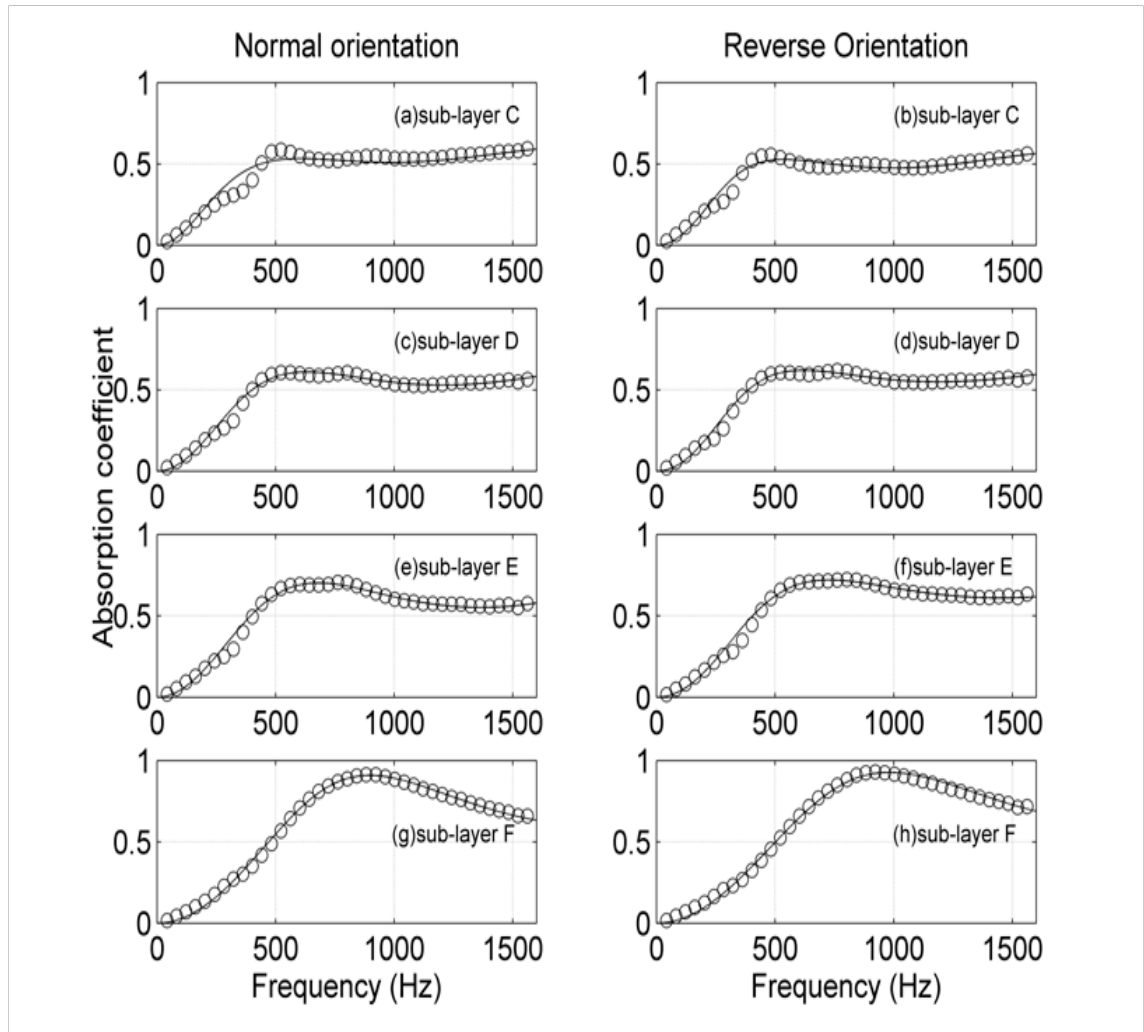


Figure 5.23: Comparison between the predicted data and experimental data of each sub-layer for SP2; (a) sub-layer C (normal), (b) sub-layer C (reverse), (c) sub-layer D (normal), (d) sub-layer D (reverse), (e) sub-layer E (normal), (f) sub-layer E (reverse), (g) sub-layer F (normal) and (h) sub-layer F (reverse)

A summary of the deduced values of non-acoustical parameters in the direct and reverse material sample orientations and their average values of sub-layers C-F is presented in Table 5.8 (for sample SP1) and in Table 5.9 (for sample SP2).

Table 5.8: The non-acoustical properties of all sub-layer of SP1 from Padé approximation

		Sample depth (mm)	Flow Resistivity σ , (N.m.s ⁻⁴)	Porosity ϕ	Tortuosity α_{∞}	Standard deviation, σ_{φ} (φ -units)
Layer-C	Top	0	75145	0.63	6.53	0.05
	Bottom	35	64469	0.65	6.04	0.58
	Average	17.5	69807	0.64	6.28	0.32
Layer-D	Top	35	45729	0.67	4.92	0.93
	Bottom	70	47729	0.72	5.72	0.73
	Average	52.5	46729	0.70	5.31	0.83
Layer-E	Top	70	29166	0.76	5.54	0.62
	Bottom	105	23012	0.77	5.19	0.74
	Average	87.5	26089	0.77	5.36	0.68
Layer-F	Top	105	14404	0.84	3.97	0.49
	Bottom	140	10001	0.87	3.12	0.52
	Average	122.5	12203	0.86	3.53	0.51

Table 5.9: The non-acoustical properties of all sub-layers of SP2 from Padé approximation.

		Sample depth (mm)	Flow Resistivity σ , (N.m.s ⁻⁴)	Porosity ϕ	Tortuosity α_{∞}	Standard deviation, σ_{φ} (φ -units)
Layer-C	Top	0	124880	0.76	6.60	0.47
	Bottom	35	110470	0.73	7.45	0.73
	Average	17.5	117675	0.75	7.02	0.60
Layer-D	Top	35	95793	0.75	7.34	0.45
	Bottom	70	78994	0.76	4.93	0.85
	Average	52.5	87394	0.75	6.10	0.65
Layer-E	Top	70	76205	0.78	7.78	0.15
	Bottom	105	62718	0.78	4.49	0.69
	Average	87.5	69462	0.78	6.05	0.42
Layer-F	Top	105	35781	0.79	4.66	0.23
	Bottom	140	33907	0.79	4.28	0.09
	Average	122.5	34844	0.79	4.45	0.16

Figure 5.24 presents a comparison of the average values between the measured and predicted flow resistivity in normal and reverse orientations for SP1 and SP2. The average values of flow resistivity were plotted in at graph with a function of the sample depth. The deduced flow resistivity measured for samples SP1 and SP2 reduces with the increased layer depth. The deduced

flow resistivity in these samples shows the same trend as the directly measured flow resistivity data. The flow resistivity deduced for the top and bottom sub-layers varies by 570% and 337% for samples SP1 and SP2, respectively. The difference between the deduced flow resistivity and its directly measured data is approximately 10%-17%.

The deduced flow resistivity for sample SP2 is generally higher than that for sample SP1. This can be explained by a higher deduced value of the tortuosity (Figure 5.26) and standard deviation (Figure 5.27) in the case of sample SP2. Additionally, sample SP2 has a lower measured value of porosity (see Table 5.6). These properties relate with flow resistivity and have an influence on sound propagation, therefore affecting the acoustic performance of these samples and explain the reason by which the acoustic absorption coefficient of SP2 is slightly lower than that of sample SP1 (Figure 5.21).

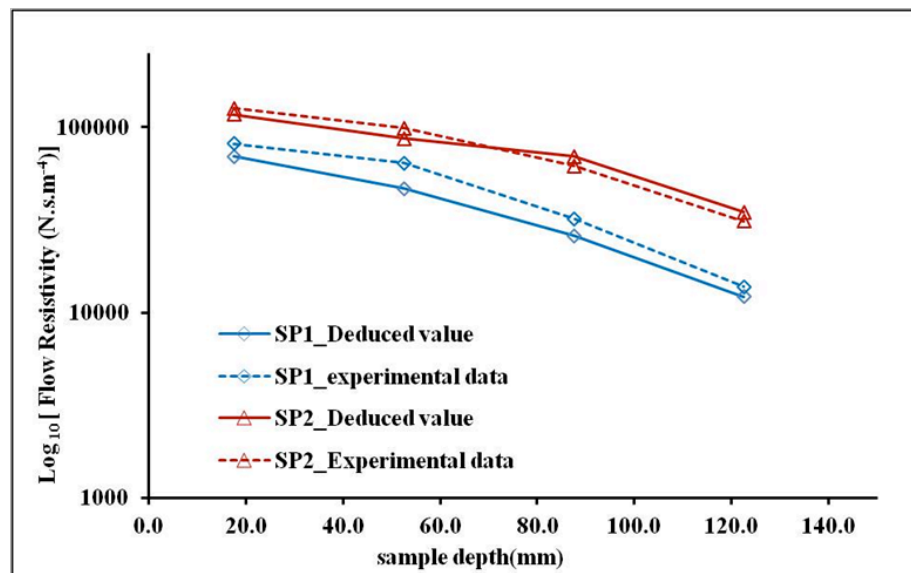


Figure 5.24: The dependence of the flow resistivity on the layer depth

Figure 5.25 shows the deduced porosity and corresponding experimental data for samples SP1 and SP2. It was found that the deduced porosity values agree well with the directly measured data and increase with as the increased layer depth. The deduced porosity exhibits a stronger dependence on the layer depth than that measured directly.

In comparison, the porosity from the experimental data gives evidently higher values than the porosity of the deduced value. It can be explained by previous reason and other reason as is following. In case of sub-layers C and D, comparison between the deduced value and the experimental data shows a large difference. This is the effect of the pore size distribution in sub-layers C and D, which are clearly bi-modal with peaks around 1mm (meso-pores) and 0.1mm (micro-pores). Probably, the model underestimates of the proportion of meso-pores present in this material case and it is lower than the directly measured value.

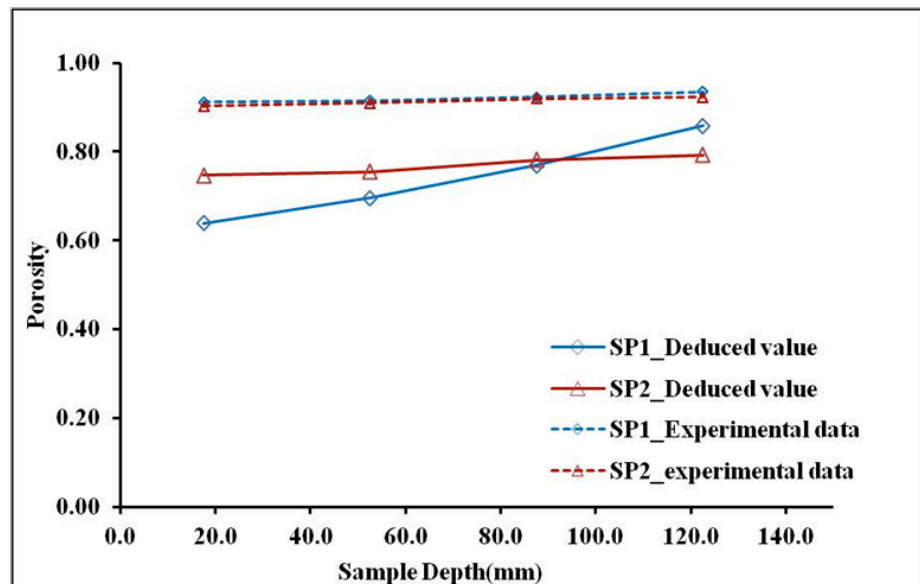


Figure 5.25: The dependence of porosity on the layer depth

Tortuosity is one of the non-acoustical properties, which has an influence on sound propagation and it relates closely with the pore size distribution, flow resistivity and porosity of the porous sample. The deduced values of tortuosity for samples SP1 and SP2 are shown in Tables 5.8 and 5.9. Figure 5.26 presents the average deduced values of the tortuosity for samples SP1 and SP2. It was found that these deduced values are very high. These dependences cannot be expressed via the porosity using the relations proposed by Berryman [72]

$$\alpha_{\infty} = 1 + \frac{1 - \phi}{2\phi} . \quad (5.2)$$

Expression (5.2) was used to calculate the tortuosity for these samples using the porosity data presented in Tables 5.8 and 5.9. The predicted tortuosity values are in range of $1.1 \leq \alpha_{\infty} \leq 1.29$. The high deduced value of tortuosity for these samples can be explained by the high proportion of partly closed pores of the material sample structure. The other reason, the pore structure has a more complex interconnectivity between pores of different sizes as illustrated in Figure 5.15 (a, b) and Figure 5.16 (a, b). Therefore, the pore morphology of these samples is difficult to characterise directly using 2-D images.

In comparison, top layers (sub-layer C) of SP1 and SP2 have higher the tortuosity values deduced than the bottom layer (sub-layer F). This can be explained by the amount of different pore sizes (see Figure 5.17 and 5.18). Here, the pore structure of sub-layer C contains two pore size regions; meso pore (1.00 mm) and micro pore (0.1 mm). The difference of PDF between two pore size regions is 14% and 6% in SP1 and SP2, respectively. These values are not a large change. It indicates that the sub-layer C is a bi-modal pore size distribution. Therefore, the deduced value results in tortuosity being high. In

the case of sub-layer F, it has a large difference of PDF, which is 34% and 24% in SP1 and SP2, respectively. Therefore, it is clear that the sub-layer F is a log-normal pore size distribution. Therefore, the deduced value of tortuosity for sub-layer F is decreased.

The tortuosity of SP2 has higher at tortuosity value deduced than SP1 over the entire sample depth (0-140 mm). This corresponds with the higher flow resistivity and lower porosity of the deduced value in SP2.

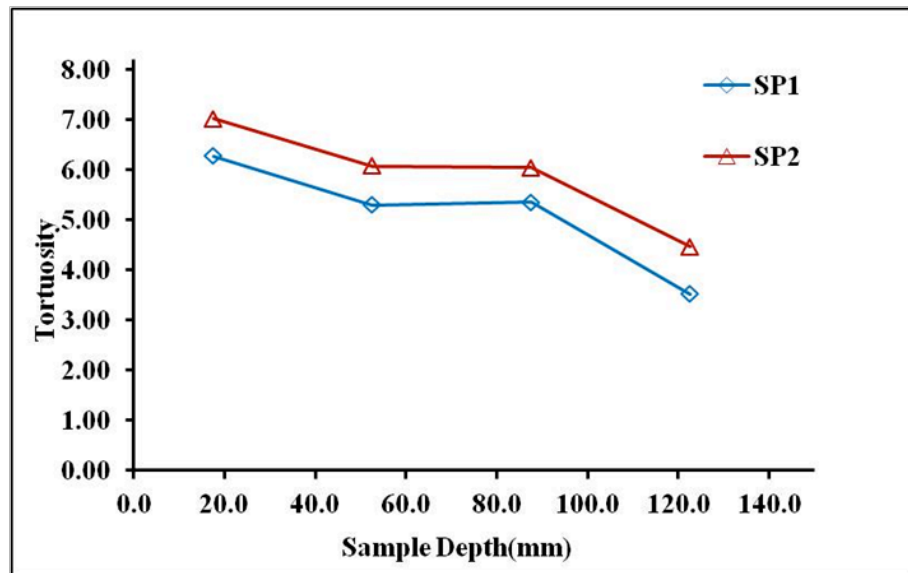


Figure 5.26: The dependence of the tortuosity on the layer depth

Standard deviation value of pore size of SP1 and SP2 obtained from modeling, which is presented in tables 5-8 and 5-9. Figure 5.26 shows the average deduced values of the standard deviation for SP1, SP2 and average of SP1-2 with a function of sample depth. It is found that the deduced standard deviation of sub-layer C is low. This result does not correspond with the PDF of SP1 and SP2 (fig. 5.17 and 5.18), which show broad pore size distribution. The sub-layer D has the highest value of the deduced standard deviation and after

sub-layer D, a trend of the deduced standard deviation value decreases continuously with increased sample depth. The Pade model used in this work, has assumes the pore size distribution is log-normal. This is an important reason, which was used to explain the result of the standard deviation. The other reason is the quality of the pore size distribution data which depends on the image contrast and software settings and the software analyze in 2-D images. Therefore, the 3-D pore structure in the stratified porous materials is hidden below the surface, which cannot be counted by this software.

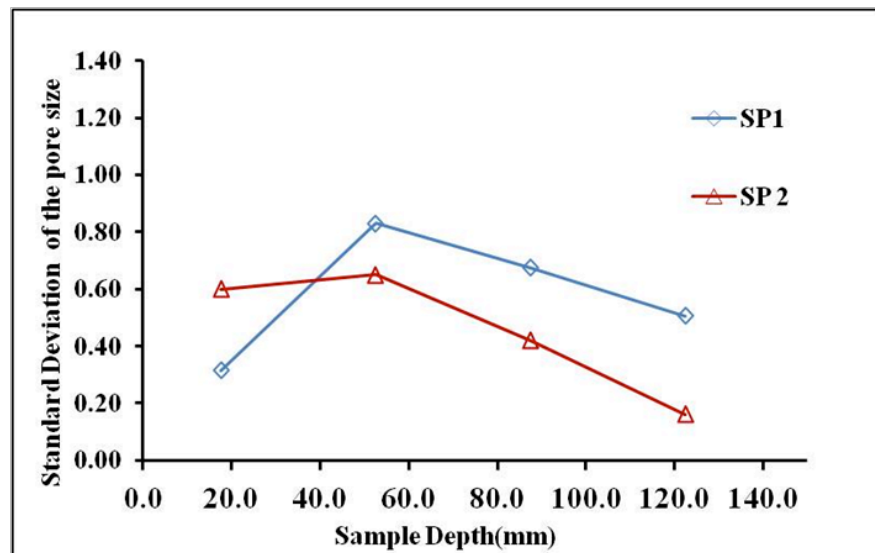


Figure 5.27: Standard deviation of pore size for SP1 and SP2

5.5 Acoustical modelling of porous media with stratification

The non-acoustical characteristics obtained in the previous section were used to predict the acoustic absorption coefficient of the porous sample with pore stratification. The acoustic absorption coefficient was predicted using a standard transfer matrix approach in which the surface (input) impedance of a stack of acoustic layers (fig. 5.28) can be predicted from the following expression [73]

$$z_{in}^{(n)}(\omega) = z_{n-1} \frac{z_{in}^{(n-1)} - z_{n-1} \tanh(ik_{n-1}h_{n-1})}{z_{n-1} - z_{in}^{(n-1)} \tanh(ik_{n-1}h_{n-1})} \quad (5.3)$$

Where z_n , k_n and h_n are the characteristic impedance, wave number and the thickness of the n -th layer in the stack. This formula is applied recursively starting with bottom layer 1 that typically rests on a perfectly reflecting wall or loaded with a semi-infinite air space. In the case of the rigid termination, the impedance at the interface between the bottom of the 2nd layer and the top of the 1st layer in the stack is given by $z_{in}^{(2)}(\omega) = z_1 \tanh(-ik_1h_1)$. The characteristic impedance and the wave number in eq. (5.3) can be determined from expressions (4.14) and (4.15) in section 4.3 using the averaged values of the four non-acoustical parameters listed in Tables 5-8 and 5-9. The absorption coefficient can then be calculated from

$$\alpha = 1 - \left| \frac{z_{in}^4 - 1}{z_{in}^4 + 1} \right|^2 \quad (5.4)$$

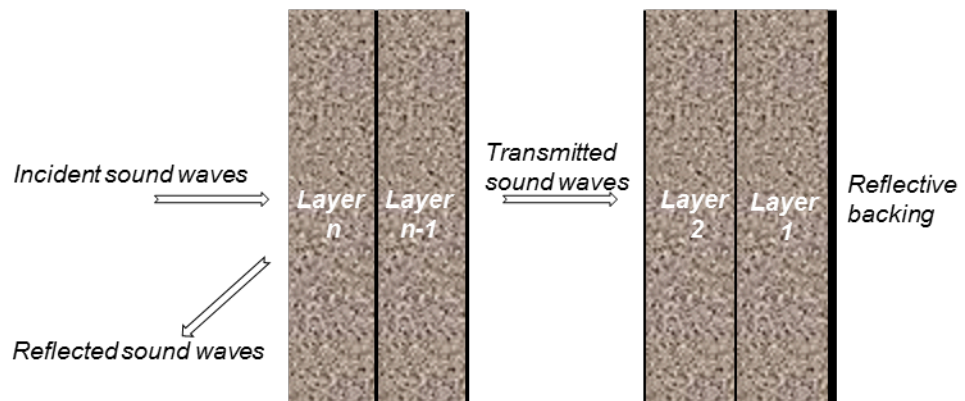


Figure 5.28 Illustration of sound wave incident to N-layers

The absorption coefficient of 140mm thickness sample of SP1 and SP2 was predicted by expression (5.4). The average value of four non-acoustical

parameters are shown in tables 5-8 and 5-9 were used by this model in order to predict the absorption coefficient for SP1 and SP2 which are presented in figures 5.29 and 5.30. These figures represent comparison between the predicted and measured absorption coefficient data. It was found that the absorption spectra of normal and reverse orientation correspond to sub-layer C (topside) and sub-layer F (bottom side). It illustrates obviously that this model captures closely the differences between the absorption coefficient data obtained for the two sample orientations. The predicted results are a good fit in the middle frequency range (between 600 and 1400 Hz). In case of the low frequency range, the predicted absorption spectra have slight differences with measured absorption data. The reason was used to explain for the performance of this model is as follows. The SP1 and SP2 samples have a complex pore size distribution. In this work, the porous material samples were assumed to be homogenous for this model. This is the main reason that affects the accurate results of predicted data. Therefore, the predicting of this model has a slight error between the predicted and measured absorption data.

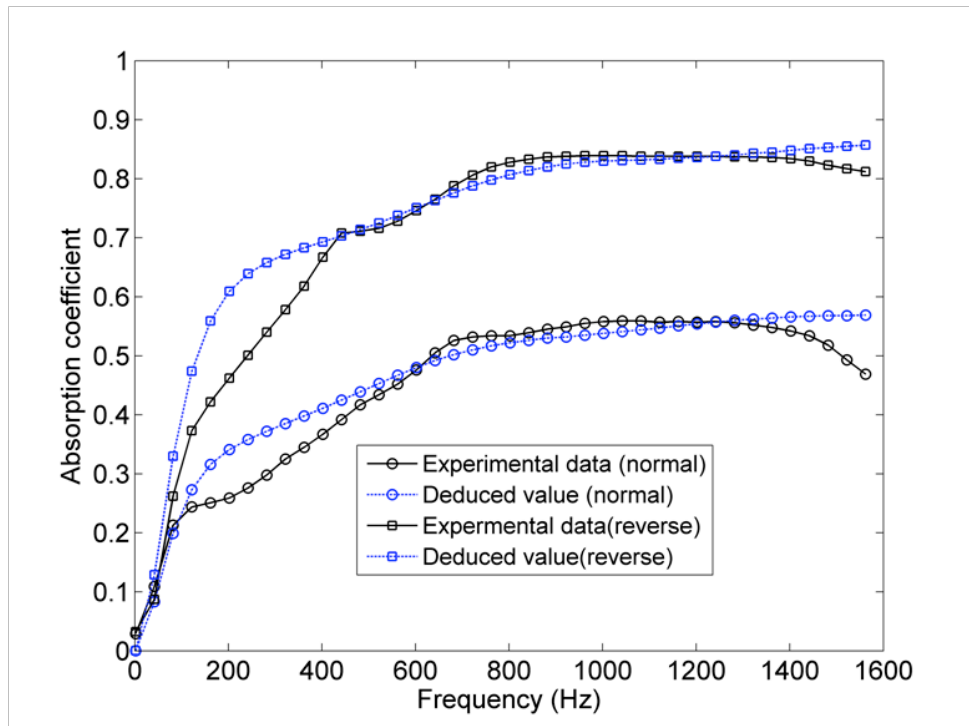


Figure 5.29: Comparison between the predicted and measured absorption coefficient spectra of the stratification material sample (SP1) in two different orientations

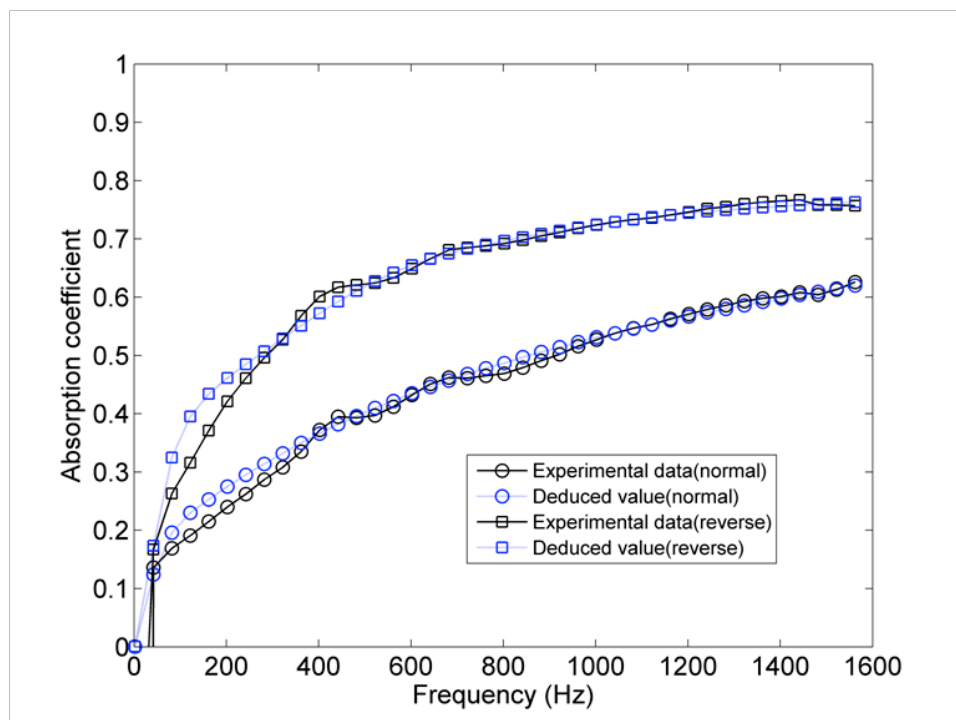


Figure 5.30: Comparison between the predicted and measured absorption coefficient spectra of the stratification material sample (SP2) in two different orientations

5.6 Conclusion

This chapter focused on the development a porous material with stratification. Reaction time is a main parameter that needs to be controlled in the foaming process in order to produce successful stratification. The reaction time has a very close relationship with expanding time, which is a main step of the foaming process for controlling cell growth. Therefore, the reaction time is a key parameter for controlling the pore size and pore size distribution of the porous materials. The pore size and pore distribution are a non-acoustical property and have an effect on the three non-acoustical properties such as flow resistivity, porosity and tortuosity. These non-acoustical properties have an influence on sound propagation into the porous materials and have a direct affect on the acoustical performance of the porous materials.

This work has considered two methods for producing porous materials with stratification. The first method, the stratified porous material was produced by blending polyurethane binder, water and tyre shred residue by applying heat at the 80 °C temperature, on the bottom surface for making the short expanding time. The difference of reaction rate between the top and bottom side affecting the pore size as is following: The topside contains a larger proportion of larger pore size because of having a slow reaction rate. The bottom side has a larger proportion of smaller pore size due to a fast reaction rate. The porous material result has an obviously difference in the pore size, porosity, density, flow resistivity and absorption coefficient between the top and bottom side. Furthermore, the pore size and porosity of this material sample decreases with increased sample depth. And the density and flow resistivity increases with the sample depth increasing. But the four non-acoustical properties and absorption

coefficient do not change gradually with increased sample depth. Therefore, a second method was developed in order to produce the porous material having the continuous pore stratification with increased sample depth. In the second method, the developed porous material was prepared by blending polyurethane binder, polyol, water and tyre shred residue in a cylindrical mould with an open top. The polyol helps to create the open cells and the oxygen in atmosphere helps to decrease reaction time at the surface of this porous material. Therefore, the topside of this porous material has a fast reaction rate and has large proportion of smaller pore size. The second method achieved the production of a porous material with continuous pore stratification. The four non-acoustical properties such as pore size, porosity, density and flow resistivity change gradually with increased sample depth. The stratified porous material in the second method has a difference of absorption coefficient in normal and reverse orientation. The absorption coefficient shifts gradually to higher value with increasing sample depth. Furthermore, this stratified porous material in the second method can improve the sound absorption over the frequency test due to changing the non-acoustical properties that are related to the sample depth. In this stratified porous material have a larger pore size, a lower flow resistivity, a higher porosity and a lower tortuosity as sample depth increase. The measured absorption coefficient was compared with predicted absorption data from the Pade Approximations. The model provides a good fit with the experimental data. The deduced value has a decreasing trend in the flow resistivity and increasing trend in the porosity when the sample depth is increased. The flow resistivity and porosity of the experimental data has the same trend as the deduced values. This material can be easily developed for

production at a large scale and have low cost due to the use of recycled tyre granulates.

Chapter Six

6 Study the Thermal property of Porous Materials

6.1 Introduction

This chapter investigates the thermal properties of porous material produced by using polyurethane binder mixed with granulated tyre waste. These porous materials were produced by varying the amount of catalyst and surfactant to achieve a higher proportion of closed pores. The details of the production process and the ingredients used in this process are detailed in the section 3.4.1. It is shown that the catalyst and surfactant have a strong influence on the pore dimensions and on the proportion of open, interconnected pores. This chapter attempts to quantify these effects in terms of the thermal conductivity coefficient.

6.2 Literature Review and Theoretical Background

6.2.1 Thermal insulation

Various types of materials are used for thermal insulation. These materials are wood, fiber, cork, fire brick, ceramic and plastic foams. The thermal insulation performance is explained by several factors: (1) the low volume fraction of polymer phase; (2) the small cell size that can suppress convection and reduce radiation through the cell walls; and (3) the poor conductivity of gas within the cell.

Several researches have focused on developing the various materials for thermal insulation. Modified concrete has been proposed by Khan and Prasad

[74], which decreases thermal conductivity with an increase in the fly ash content. Fiber reinforced fumed silica compact [75] and alumina fiber [76] were modified to prevent heat loss. Ye and et al. [77] have compared the thermal resistance between sheep-wool insulation and wool–hemp mixtures, both in the form of bonded insulation batts. It was found that the conductivity of the wool–hemp samples was not significantly different from the wool samples at the same density. Thus the use of hemp as an extender for wool in thermal insulation has no significant influence on the insulation properties under the test conditions. The model for calculation the thermal energy flux of two porous materials made of wool and polyester was developed by Wu and et al. [78]. It was found that decreasing fiber radius would significantly reduce the total thermal energy flux through the porous polymer materials. The fiber fractional volume had a significant influence on the thermal energy flux, and thereby the fiber fractional volume can be optimized in view of improving the thermal insulating performance of the porous polymer materials. Sureshkumar and et al. [79] have developed a novel and futuristic elastomeric insulation for case-bonded solid rocket motors (SRMs). The Elastomeric insulation based on ethylene propylene diene (EPDM) rubber as a primary polymer was blended with polychloroprene chlorosulphonated polyethylene (CSE) that was cast with composite propellant containing hydroxyl terminated polybutadiene (HTPB) as a polymeric binder. Polyurethane foam is a very versatile and useful material which can be used safely for applications [80], for example: polyurethane was used for pipes insulation for reducing the heat loss from district heating network [81]. Thermal conductivity of polyurethane foam was improved by modifying the reaction injection molding (RIM) [82]. Polyurethane foam was produced by

using binary gas mixtures (hydrochlorofluorocarbon, HCFC and carbon dioxide, CO₂) as physical blowing agents and ultrasonic excitation was applied to increase the rate of bubble nucleation. Best results such as low thermal conductivity and small bubbles were obtained when the polyol was mixed with the HCFC gas and saturated with carbon dioxide at 0.3 MPa, and foamed with ultrasonic nucleation.

6.2.2 Theoretical Basis

The phenomenon of heat flow through a porous material can be described by three heat transfer mechanisms: conduction, convection and radiation. These mechanisms are quantified by the thermal conductivities of gas and solid phases, convection heat-transfer coefficient and radiation heat-transfer coefficient. Alternatively, a porous material used for thermal insulation can be characterised in term of its overall thermal conductivity (λ) defined by Fourier's law as follows [83, 84]:

$$q = -\lambda \nabla T \quad (6.1)$$

where \mathbf{q} is the heat flux ($J/m^2 s$ or W/m^2), ∇T is temperature gradient and λ is the thermal conductivity given in the unit of $J/m s K$ or $W/m K$.

A non-steady heat conduction equation accounts for the difference in heat energy entering and leaving the material. That causes temperature to change with time (τ).

$$\rho C_p \frac{\partial T}{\partial \tau} = \frac{\partial}{\partial x} \left(\lambda \frac{\partial T}{\partial x} \right), \quad (6.2)$$

when the density (ρ) and specific heat (C_p) are constant. Therefore, the expression (6.2) can be rewritten:

$$\frac{\partial T}{\partial \tau} = a \frac{\partial^2 T}{\partial x^2} \quad , \quad (6.3)$$

where a is thermal diffusivity (m^2 /s) expressed in terms of the thermal conductivity, density and the specific heat

$$a = \frac{\lambda}{\rho C_p} \quad . \quad (6.4)$$

The thermal conductivity of the porous material can be calculated by four contributions [83]

$$\lambda^* = \lambda_s^* + \lambda_g^* + \lambda_c^* + \lambda_r^* \quad (6.5)$$

where λ_s^* is the conduction through the solid phase, λ_g^* is the conduction through the gas phase, λ_c^* is the convection within the cells and λ_r^* is the radiation through the cell walls and across the cell voids.

Heat convection is the heat transfer created by motion of fluids (liquid or gas), which is heat transfer rate between fluid and wall having different temperature, which can be defined by Newton's law [85, 86]

$$q = hA\Delta T \quad , \quad (6.6)$$

where q represents the rate of heat transfer by convection, A is a surface area and h is the convection heat-transfer coefficient. If Grashof number is > 1000 convection is considered. The Grashof number (Gr) represents the ratio of

buoyancy force to the viscous force in the free convection system, which can be expressed by [83, 85]

$$Gr = \frac{g\beta\Delta T_c l^3 \rho^2}{\mu^2} \quad , \quad (6.7)$$

where g is the acceleration of gravity, 9.81 m/s^2 , β is the volume coefficient of expansion for gas (for an ideal gas, $\beta = 1/T$), ΔT_c is the temperature difference across one pore (K), l is the pore size, ρ is the density of gas (kg/m^3) and μ is dynamic viscosity of gas (N s/m^2).

In contrast to the mechanism of conduction and convection, heat can be transferred from a surface of porous material at a higher temperature (T_1) to one at a lower temperature (T_0) with a perfect vacuum by the thermal motion of charged particles. This mechanism is electromagnetic radiation. The heat transfer in this case is called the thermal radiation, can be defined by Stephan's law

$$q_r^0 = \beta_1 \sigma (T_1^4 - T_0^4) \quad , \quad (6.8)$$

where β_1 is a constant (less than unity), which explains the emissivity of surface, $\sigma = 5.67 \times 10^{-8} \text{ W/m}^2 \text{ K}^4$ is Stephan's constant. The porous material is inserted between two surfaces for thermal insulation. In this way, the heat flux is reduced by the heat absorption of porous material and the reflection of cell wall. Therefore, the heat flux is reduced, which can be expressed by Beer's law [83]

$$q_r = q_r^0 \exp\left(-K_s \frac{\rho^*}{\rho_s} t\right) \quad , \quad (6.9)$$

where $K_s, (m^{-1})$ is the extinction coefficient of the solid, t is the uniform thickness of the porous material (which has unit of m), $\frac{\rho^*}{\rho_s}$ is the relative density of porous material, ρ^* is the density of porous material and ρ_s is the density of solid frame.

The relative density [83] is a physical property of a porous material, which depends on the material pore morphology that has various structural cell shapes such as honeycomb, open cell and close cell. The relative density of these structural cell shapes can be defined by the cell edge- length (l) and the cell wall thickness (t), which is low, when $t \ll l$.

For all honeycomb cells

$$\frac{\rho^*}{\rho_s} = C_1 \frac{t}{l} \quad (6.10)$$

For all open cells

$$\frac{\rho^*}{\rho_s} = C_2 \left(\frac{t}{l} \right)^2 \quad (6.11)$$

For all close cells

$$\frac{\rho^*}{\rho_s} = C_3 \frac{t}{l} \quad (6.12)$$

The heat flux (q_r) in expression (6.9) can be divided by the temperature gradient (using the approximations $dT/dx \approx (T_1 - T_0)/t$ and $T_1^4 - T_0^4 \approx 4\Delta T \bar{T}^3$, where \bar{T} represents the mean temperature, $(T_1 + T_0)/2$) and then q_r^0 is substituted by expression (6.8). Therefore, the thermal conductivity of porous material from the heat radiation becomes

$$\lambda_r^* = 4\beta_1 \sigma \bar{T}^3 t \exp\left(-K_s \frac{\rho^*}{\rho_s} t\right). \quad (6.13)$$

6.3 Thermal Conductivity Measurement

In this study, the determination of the thermal conductivity for the porous materials produced with variable catalyst and surfactant was carried out in BS 1902-5.8(1992) [87]. The thermal conductivity apparatus and experimental setup are shown in Figure 6.1. The test procedure and apparatus based on BS 1902-5.8(1992) consists of aluminium cylindrical columns split into three parts. The first (bottom) part of this equipment is an aluminium cylinder with 4 heaters 125mm long. Another aluminium cylinder is attached to the bottom part to transfer the heat. This aluminium cylinder is 150mm long and it has the diameter of 100mm. The top aluminium cylinder has 100mm diameter and it is 150mm long. Three thermal sensors are installed inside each of the two cylinders between which a 10mm thick material sample is placed (see Figure 6.1). The thermal sensors are spaced at 40mm. The steel bar-rack holds the top cylindrical column in order to protect the material sample compressed by the heavy weight column (see Figure 6.2). Thermal couples measured the temperature gradient, which was used to calculate the heat flux by

$$q = \frac{\lambda_{alu} (\Delta T_m) A}{d} \quad (6.14)$$

λ_{alu} is the thermal conductivity of aluminium (172 *Watts/(mK)*), ΔT_m (in K) is the mean temperature difference between thermocouples, **A** is the area of cross section of the aluminium cylindrical column (in m²) and *d* is the distance

between the thermocouple junctions (0.04 m). The thermal conductivity was then found from

$$\lambda = \frac{qd_s}{A\Delta T} \quad (6.15)$$

where λ is the thermal conductivity of the test sample at the mean temperature (*Watts/(m.k)*), d_s is the test sample thickness (in *m*), A is the cross sectional area of the test sample (in *m²*) and ΔT is temperature difference between thermal sensors 3 and 4 (in *K*) (see Figure 6.1 and 6.2).

Calibration and accuracy of thermal conductivity equipment can be found by measuring some commercial products (wool, wooden and PVC samples) with know value of thermal conductivity. The measured thermal conductivity of these commercial products was compared with thermal conductivity in a textbook [82]. In order to obtain accurate data for measuring thermal conductivity, the use of vermiculite around aluminium cylindrical column (see in Figure 6.2) helps to protect the heat loss due to air convection. The thermal conductivity equipment must be required to warm up before the measurement started. After loading specimen, temperature gradient of this equipment is developed until 100 °C by four heaters and is controlled by the cooling water.

This study used two material specimens of 100mm diameter and 10mm thickness to determine the thermal conductivity of the developed material formulation. The average thermal conductivity was then calculated. The results are shown in Tables 6.1 and 6.2.

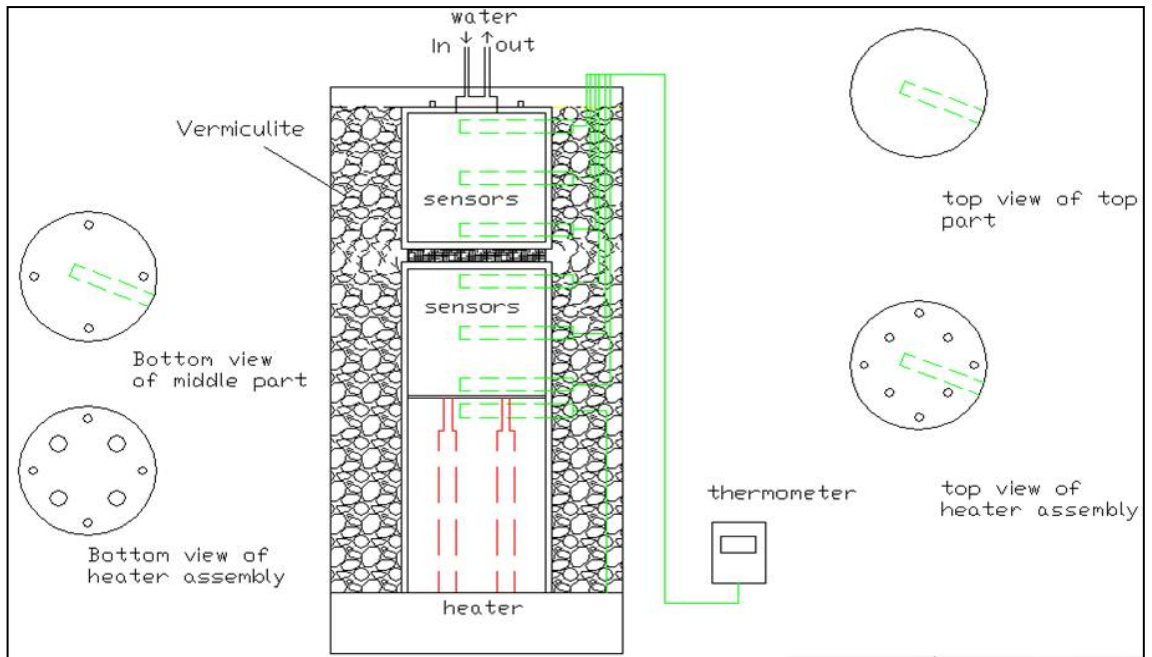


Figure 6.1 Illustration of thermal conductivity apparatus [88]

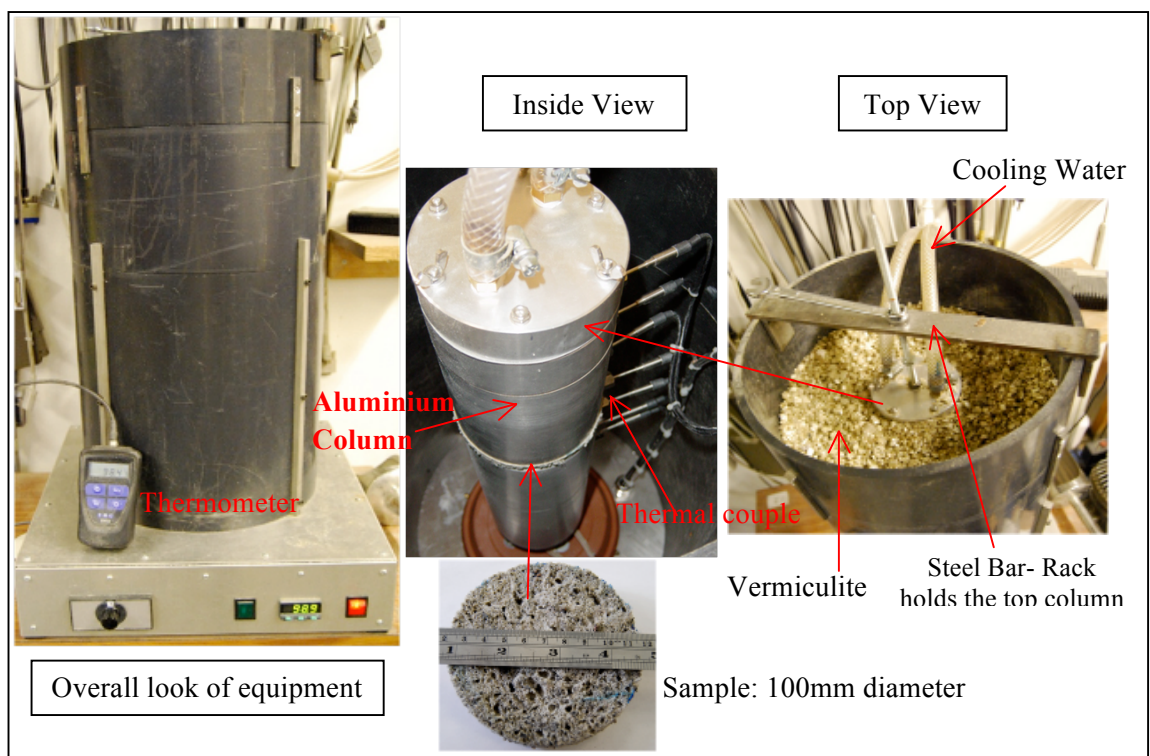


Figure 6.2: Experimental setup for determination thermal conductivity

6.4 Effect of the Catalysts on Thermal Conductivity

This section studied the thermal conductivity of the porous material samples produced by variable amounts of catalyst and using two polyurethane binders as: Flexilon 457 (higher % isocyanate) and Flexilon 1109 (lower % isocyanate) the details of the procedure are shown in the section 3.4.1. The thermal conductivity of the porous material samples: C0_M457, C1_M457, C2_M457, C3_M457, C0_M1109, C1_M1109, C2_M1109 and C3_M1109 were measured by the procedure method presented in the previous section. The results of these measurements are presented in Tables 6.1 and 6.2. Figures 6.3 and 6.4 show the influence of variable amounts of catalyst on the thermal conductivity by comparison with material density and porosity, respectively. The values of the thermal conductivity, density and porosity were plotted in a graph as a function of the amount of catalyst.

It was found that the thermal conductivity of these samples decreases with the increased concentration of catalyst. The difference between the thermal conductivity of the sample without catalyst (samples C0_M457 and C0_M1109) and of the sample with 3% catalyst (samples C3_M457 and C3_M1109) is 47% in the case of materials with a higher proportion of isocyanate. This difference is 44% in the case of the materials with a lower proportion of isocyanate. The lower thermal conductivity is observed in the samples with a larger proportion of smaller pores (see Fig. 3.39 and 3.40) which are attributed to a faster reaction rate and a shorter reaction time. The sample with the highest catalyst (3%) has the lowest thermal conductivity due to having a larger proportion of partly closed pore. The graphs in Figures 6.3 and 6.4 show clearly that the increasing catalyst affects to decrease thermal

conductivity, decrease density and increase porosity. It can be described in term of the volume fraction of solid of these porous material decreased that affect to decrease thermal conductivity.

It was found that the thermal conductivity of the porous materials with a lower proportion of isocyanate is lower than that of the samples produced with a higher proportion of isocyanate. It can be explained by the lower density and higher porosity which is achieved in the case of porous material made with a lower proportion of isocyanate. This indicates that the density and porosity has a strong influence on the volume fraction of solid have a strong influence on the thermal conductivity of porous material.

Table 6.1: The thermal conductivity of the porous materials produced with the polyurethane binder with a higher concentration of isocyanate (Flexilon 457) and concentration of catalyst.

Samples	Composition of Catalyst (%)	Thermal Conductivity (W/(mK))		
		Sample 1	Sample 2	Average
C0_M457	0	0.062	0.054	0.058±0.005
C1_M457	1	0.060	0.047	0.053±0.009
C2_M457	2	0.053	0.044	0.049±0.006
C3_M457	3	0.025	0.029	0.027±0.003

Table 6.2: The thermal conductivity of the porous materials produced with polyurethane binder with a lower concentration of isocyanate (Flexilon 1109) and variable amount of catalyst.

Samples	Composition of Catalyst (%)	Thermal Conductivity (W/(mK))		
		Sample 1	Sample 2	Average
C0_M1109	0	0.048	0.061	0.055±0.009
C1_M1109	1	0.034	0.048	0.041±0.010
C2_M1109	2	0.024	0.036	0.030±0.009
C3_M1109	3	0.023	0.025	0.024±0.001

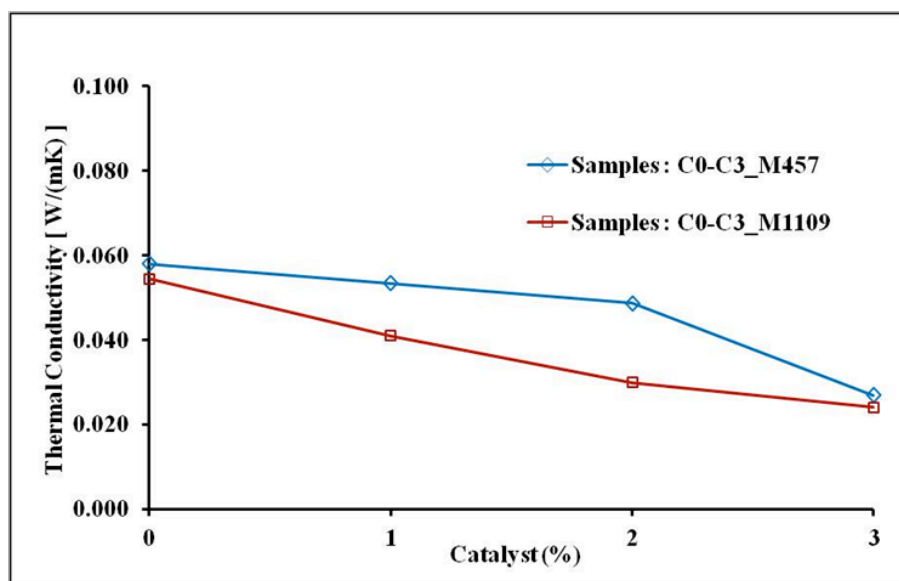


Figure 6.3: The influence of variable amount of catalyst on the thermal conductivity

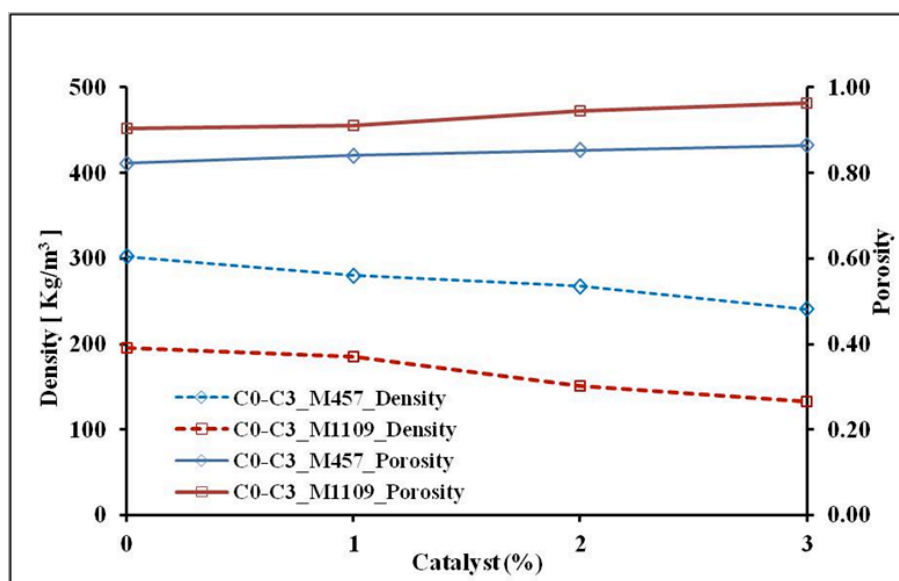


Figure 6.4: A comparison of the influence of the variable amount of catalyst on the density and porosity

The thermal conductivity of these porous materials (C0_M457, C1_M457, C2_M457, C3_M457, C0_M1109, C1_M1109, C2_M1109 and C3_M1109) was compared with commercial materials shown in Table 6.3. It was found that these porous materials have lower thermal conductivity than

AFS and Regopol samples. It can be explained by a lower porosity and a higher density of AFS and Regopol samples. In addition, these porous materials have the larger proportion of smaller pore size and closed pores.

Table 6.3: The physical properties and thermal conductivity of commercial products.

Samples	Company	Porosity	Density (kg/m ³)	Thermal Conductivity (W/(mK))
AFS (recycled nitrile rubber)	Armacell Uk Ltd.	0.79	242	0.07 (thickness 25mm)
Regopol (tyre crumb rubber)	CMS Acoustic Solutions Ltd.	0.21	830	0.12 (thickness 0.10mm)

6.5 Effect of Surfactants on the Thermal Conductivity

This section studies the thermal conductivity of the porous material samples produced with variable amounts of surfactant. These samples were manufactured according to the procedure detailed in the section 3.4.1. The results of these experiments are shown in Table 6.4. Figures 6.5 and 6.6 illustrate the influence of surfactant on the thermal conductivity, density and porosity. These figures also present the relation between the density, porosity and thermal conductivity.

It was found that the thermal conductivity of these sample increases when more surfactant is added to the material mix. The difference between the thermal conductivities of the sample without surfactant (S0) and the sample with 12% surfactant (S12) is 140 %. It can be explained by a larger proportion of larger pore size of sample S12 (shown in figure 3.45). The graphs in Figures 6.4 and 6.5 show clearly that increasing surfactant results in the increase in the

thermal conductivity, increased density and decreased porosity. This effect can be explained by the increased volume fraction of solid in these porous materials that affects to increase thermal conductivity. In addition, the porous materials in this case have lower thermal conductivity than commercial products (shown in Table 6.3). It can be explained by a lower density and a higher porosity of these porous materials.

Table 6.4: The thermal conductivity of the porous materials produced by varying the amount of surfactant

Samples	Composition of Surfactant (%)	Thermal Conductivity (W/(mK))		
		Sample 1	Sample 2	Average
S0	0	0.048	0.061	0.055±0.009
S2	2	0.051	0.061	0.056±0.007
S4	4	0.055	0.059	0.057±0.003
S6	6	0.070	0.061	0.066±0.006
S8	8	0.068	0.066	0.067±0.002
S10	10	0.078	0.065	0.071±0.009
S12	12	0.072	0.081	0.077±0.006

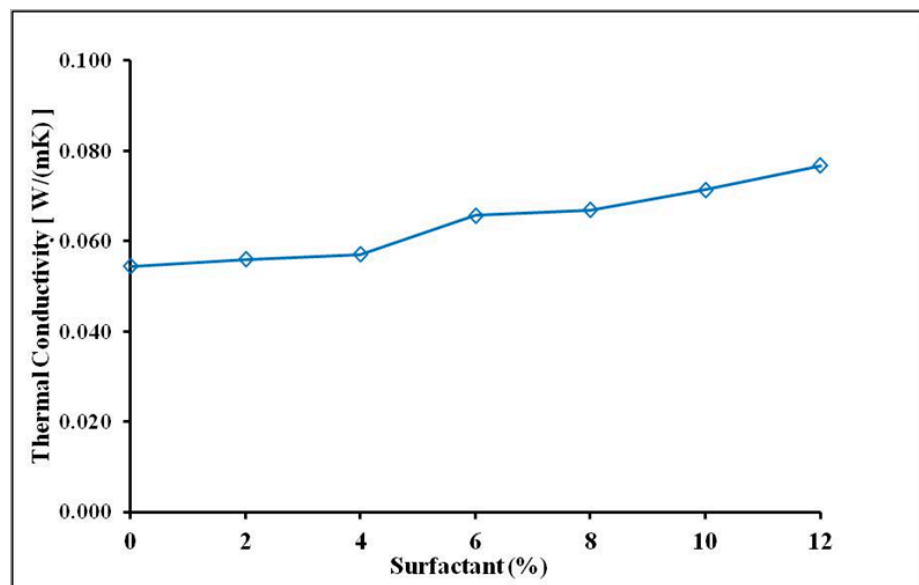


Figure 6.5: The influence of variable amount of surfactant on thermal conductivity

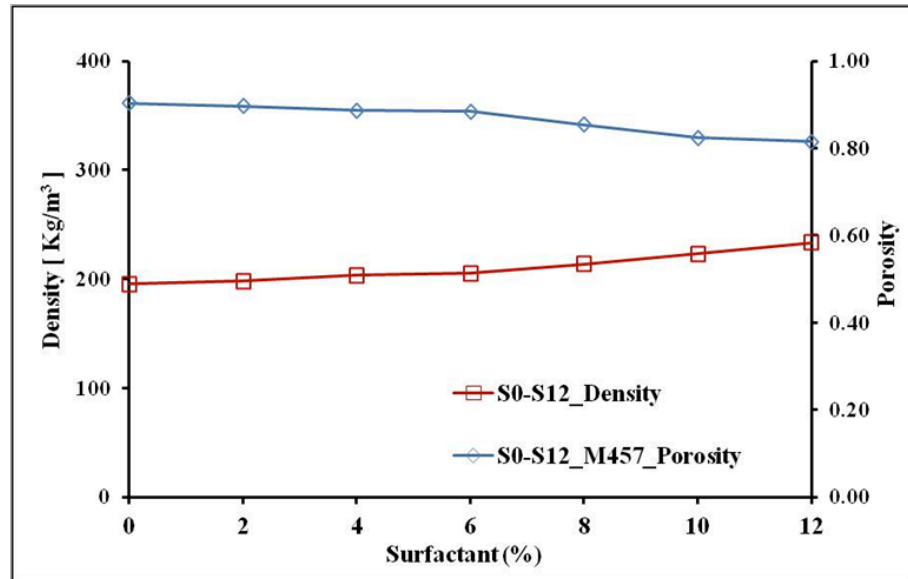


Figure 6.6: Comparison of the influence of variable amount of surfactant on density and porosity

6.6 Conclusion

This chapter studied the thermal conductivity of porous material produced by variable amounts of catalyst and surfactant. The pore size distribution of the manufactured materials is controlled by the catalyst, which also affects the material density, porosity and the thermal conductivity. The experimental results show clearly that the porous materials produced with more catalyst achieve a better thermal insulation. The thermal conductivity in these materials is close to that expected in good-quality commercial products used for thermal insulation. Typical requirements for materials for thermal insulation are: a close cell morphology, small cell size, poor conductivity of gas through the cell walls, low thermal conductivity of the frame material, low diffusivity of the solid frame and a low volume fraction of solid frame. The volume fraction of the solid frame directly controls the material density and porosity. Materials with a highest concentration of catalyst (C3_M457 and C3_M1109) have the lowest thermal

conductivity, larger proportion of smaller pores, lowest density and a highest porosity.

Materials with a higher concentration of surfactant exhibit a higher thermal conductivity. The thermal conductivity of the porous materials with no or small amount of surfactant is limited. It is found that surfactant added in the polyurethane mix helps to decrease the surface tension and enhance the foam stability. Therefore, the use of surfactant must be carefully controlled to improve obtained the desired proportion of closed, small pores which guarantee a low value of the thermal conductivity.

Chapter Seven

7 Summary and Conclusion

This research presents the development of porous absorbing materials that were produced with recycled tyre shred residue, polyurethane binder and other chemicals which were added to control the reaction time and amount of CO₂ produced as a result. It was found that the type and concentration of binder, catalyst and surfactant have an effect on the following material characteristics: density, porosity, pore distribution and the flow resistivity. These characteristics relate directly to the acoustical properties. The effect of each individual component added to the chemical formulation has been quantified. Specifically, it was found that an increased amount of tyre shred residue increases the reaction rate and results in an increased density, decreased porosity, increased flow resistivity and increased proportion of smaller pores. The material manufactured with the highest filler content (80% tyre shred residue) had the lowest acoustic absorption coefficient.

Water is a main reactant as a blowing agent in the production of the recycled porous materials. The amount of water used depends on stoichiometry of polyurethane polymerization reaction. The experimental results suggest that increasing the amount of water results in the increased reaction rate. Water helps to increase the porosity, decrease the flow resistivity and increase the proportion of larger pores.

Tyre shred residue used in this study has three main components: granulated rubber, nylon staple fibres and nylon filament fibres bonded to rubber, which was sieved by 12 sieves with different screen capture. It was found that the recycled porous material that was produced using tyre shred residue sieved by the largest hole size of screen capture that contains the largest proportion of nylon staple fibres and nylon filament fibres bonded to rubber, which has a slightly lower density, a higher porosity, a lower flow resistivity and a slightly higher sound absorption coefficient. But the resulting material produced by the larger proportion of granulated rubber (from the smallest hole size of screen capture) has a higher reaction rate, a higher density, a lower porosity and a higher flow resistivity.

The main work of a catalyst is to speed up the chemical reaction, which has a dominant effect on the reaction. Catalyst helps to increase the reaction rate and the proportion of yield (also called conversion). The reaction time which has a significant relationship with expanding time in the foaming process is a key component for controlling the pore size and pore distribution of the recycled porous materials. Adding more catalyst results in a larger proportion of smaller pores, decreased material density, increased porosity, increased flow resistivity and in a higher acoustical absorption coefficient in the lower frequency range. The experimental results show clearly that the pore size distribution has a great influence on the porosity and flow resistivity. The acoustical absorption performance of the recycled porous materials depends on these non-acoustical properties that directly control sound propagation in porous media.

Surfactant was used in this study in order to improve the mixing of components (such as tyre shred residue, water and polyurethane binder), reducing surface tension and preventing the collapse of cells. Adding both a catalyst and surfactant results in the produced recycled porous materials illustrated a more complex pore size distribution. The recycled porous materials produced by the increasing of surfactant and keeping catalyst at 3% contain a greater proportion of larger pores and exhibit the higher acoustical absorption coefficient in the higher frequency range.

The microstructural and acoustical properties of these materials were studied using Johnson-Champoux-Allard model (JCA) and Pade approximations model. The JCA model requires the knowledge of five non-acoustical parameters (porosity, flow resistivity, tortuosity and two characteristic lengths) to predict the acoustical behavior. It was shown that the model can provide a good agreement with the measured data. The Pade approximations model is based on four non-acoustical parameters (porosity, flow resistivity, tortuosity and standard deviation of pore size distribution). This model also provides an excellent agreement with experimental observations. These two models are capable of describing the morphological characteristics of these porous materials in term of their macro- and microstructure. This microstructure is complex and is affected by the amounts of catalyst and surfactant added to the initial mix.

This research has proved that it is possible to achieve an improved acoustical absorption in broad frequency range by producing the recycled materials with pore stratification. The study has considered controlling of the pore size distribution of the recycled materials by using different reaction time

(as a key parameter) over sample depth. The recycled porous materials produced by blending polyurethane binder, polyol, water and tyre residues in cylindrical mould with an open top have increased amounts of larger size pores with increased sample depth. The acoustical absorption coefficient of these recycled materials presented clearly show in the spectra there are differences in the normal and reverse orientations and shifts gradually to a higher value with increasing sample depth.

The acoustical behavior of the recycled porous materials with continuous pore stratification can be studied with the Pade approximation model and transfer matrix approach. For individual sub-layer of these materials, the agreement between the directly measured and deduced non-acoustical properties is close. Therefore, Pade approximations model is suitable for studying the acoustic behaviour of the recycled porous materials with pore stratification.

Finally, the thermal conductivity of the recycled porous materials produced by varying the amounts of catalyst and surfactant was studied. The experimental results illustrate that there is a relationship between the mean pore size, porosity, density and thermal conductivity. Materials produced with more catalyst have a higher proportion of smaller pores, a higher porosity and a lower density. These materials exhibit a lower value of thermal conductivity. However, the materials with more surfactant exhibit a higher thermal conductivity value. Therefore, the amount of surfactant used in the foaming process should be carefully controlled to provide sufficiently workable mix and stabilise the growth of bubbles in the expanding foam. Tables 7.1, 7.2 and 7.3

show the trends of non-acoustical, acoustical and thermal properties for the recycled porous materials produced in this study.

Table 7.1 The trends of the structural, acoustical and thermal properties for the effective porous materials when the composition increased

The Trends of these properties when these compositions increased							
Properties	Tyre shred residue	Water	Particle Size of Tyre Shred Residue	Catalyst (M457) Higher isocyanate	Catalyst (M1109) lower isocyanate	Surfactant	Catalyst and Surfactant
Reaction Rate	increase	increase	decrease	increase	increase	decrease	decrease
Reaction Time	decrease	decrease	increase	decrease	decrease	increase	increase
Pore Size	decrease	increase	increase	decrease	decrease	increase	increase
Porosity	decrease	increase	increase	increase	increase	decrease	decrease
Density	increase	decrease	decrease	decrease	decrease	increase	increase
Flow Resistivity	increase	decrease	decrease	increase	increase	decrease	decrease
Absorption Coefficient	Shift to a good absorption at low frequency	Shift to higher value at high frequency	Shift to higher value at high frequency	Shift to a good absorption at low frequency	Shift to a good absorption at low frequency	Shift to higher value at high frequency	Shift to higher value at high frequency
Thermal Conductivity	N/A	N/A	N/A	decrease	decrease	increase	N/A

Table 7.2 The trend of the non-acoustical and acoustical properties for the recycled porous materials with stratification produced by method 1


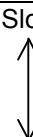

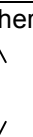








Sample Depth	Reaction Rate	Pore Size	Porosity	Density	Flow Resistivity	Absorption Coefficient
 increase	Slow	Larger	Higher	Lower	Lower	Shift to higher value at low frequency
						
	Fast	Smaller	Lower	Higher	Higher	

Table 7.3 The trend of the non-acoustical and acoustical properties for the recycled porous materials with stratification produced by method 2

Sample Depth	Reaction Rate	Pore Size	Porosity	Density	Flow Resistivity	Absorption Coefficient
 increase	Fast	Smaller	Lower	Higher	Higher	Shift to higher value at high frequency
						
	Slow	Larger	Higher	Lower	Lower	

Chapter Eight

8 Recommendation and Further Work

This research studied control of pore size in recycled porous materials by using catalysts and surfactants, and moreover this work achieved the production of recycled materials with pore stratification. At the present time, these recycled porous materials had only their non-acoustical properties and acoustical absorption coefficient studied. Therefore, the further work should be to study other acoustical properties (such as normalized surface impedance and impact sound insulation [89]), their mechanical properties (such as tensile strength, compressive strength, dynamic stiffness, Young's modulus, durability and fire resistance). The knowledge of these mechanical properties is important for applications in the areas of furniture manufacturing, automotive, building and construction.

This work can be improved in terms of the quality of measurement and experimental techniques. Determination of pore size and pore size distribution for porous material can be improved by using Scanning electron microscope (SEM), computer tomography and 3-D image analysis software. SEM can be used to characterise cell size and cell edge of a material to provide high-resolution images of the material surface. The 3D-image analysis gives more morphological details of the material microstructure such as cell shape, cell size and cell wall that cannot be unraveled by 2D imaging. These techniques help to provide more confidence and accuracy in the measured data.

Finally, the recycled material with pore stratification produced in this study with improved acoustical absorption in the broad frequency range should be investigated for the production on a larger scale and the methods for its characterisation should be further refined.

Reference

- [1] Horoshenkov, K. V. and Swift, M. J. (2001) "Acoustic properties of consolidated granular mixes," *Appl. Acoust.*, 62(6), pp. 665-690.
- [2] Lotfi, A, *Plastics Recycling*, available at:
<http://www.lotfi.net/recycle/plastic.html> (Accessed: 16 September 2011).
- [3] Scherirs, J. (1998) *Polymer Recycling*, John Wiley & Sons, pp. 415-463.
- [4] Kite Company, UK, *Plastic identification codes*, available at:
<http://www.kitepackaging.co.uk/services/wrap/Environmental-Glossary>
(Accessed: 16 September 2011).
- [5] Mantia, F.L. editor (2002) *Handbook of plastics recycling*, Rapra Technology Limited, pp. 148-171.
- [6] Kim, J.K. and Lee, S.H. (2000) "New technology of crumb rubber compounding for recycling of waste tires", *Journal of Applied Polymer Science*, 78, pp. 1573-1577.
- [7] Shojaei, A., Yousefian, H. and Saharkhiz, S. (2007) "Performance characterization of composite materials based on recycled high-density polyethylene and ground tire rubber reinforced with short glass fibers for structural applications", *Journal of Applied Polymer Science*, 104, pp. 1-8.
- [8] Colom, X., Canavate, J., Carrillo, F. And Sunol, J.J. (2009) "Effect of the particle size and acid pretreatments on compatibility and properties of

recycled HDPE plastic bottles filled with ground tyre powder”, *Journal of Applied Polymer Science*, 112, pp. 1882-1890.

[9] Colom, X., and et al. (2006) “Structural and mechanical studies on modified reused tyres composites”, *European Polymer Journal*, 42, pp. 2369-2378.

[10] Shanmugharaj, A.M., Kim, J.K. and Ryu, K.H. (2007) “Modification of rubber powder with peroxide and properties of polypropylene/rubber composites”, *Journal of Applied Polymer Science*, 104, pp. 2237-2243.

[11] Han, S.C. and Han, M.H. (2002) “Fracture behaviour of NR and SBR vulcanizates filled with ground rubber having uniform particle size”, *Journal of Applied Polymer Science*, 85, pp. 2491-2500.

[12] Li, Y., Zhao, S. And Wang, Y. (2011) “Microbial desulfurization of ground tire rubber by *Thiobacillus ferrooxidans*”, *Polymer Degradation and Stability*, pp.1-7.

[13] Lee, S.H., and et al. (2009) “The Effect of physical treatments of waste rubber powder on the mechanical properties of the revulcanizate”, *Journal of Applied Polymer Science*, 112, pp. 3048-3056.

[14] Qu, W., and et al. (2006) “Pyrolysis of waste tire on ZSM-5 zeolite with enhanced catalytic activities”, *Polymer Degradation and Stability*, 91, pp.2389-2395.

[15] Parres, F., Crespo-Amoros, J.E. and Nadal-Gisbert, A. (2009) “Characterization of fibers obtained from shredded tires”, *Journal of Applied Polymer Science*, 113, pp. 2136-3142.

- [16] Corsaro, R.D., and Sperling, L.H. (1990) Sound and Vibration Damping Polymer, ACS Symposium Series, pp. 20, 301, 366, 415.
- [17] Jaouen, L., Renault, A. And Deverge, M. (2008) "Elastic and damping characterization of acoustical porous materials; Available experimental methods and applications to a melamine foam", Applied Acoustics, 69, pp.1129-1140.
- [18] Chauhan, S., Karmarkar, A. And Aggarwal, P. (2009) "Damping behaviour of wood filled polypropylene composites", Journal of Applied Polymer Science, 114, pp. 2421-2426.
- [19] Yoon, K.H., Yoon, S.T. and Park, O.O. (2000) "Damping properties and transmission loss of polyurethane. I. Effect of soft and hard segment compositions", Journal of Applied Polymer Science, 75, pp. 604-611.
- [20] Adams, R.D. and Maheri, M.R. (2003) "Damping in advanced polymer-matrix composites, Journal of Alloys and Compounds", 355, pp. 126-130.
- [21] Jung, K.I., Yoon, A.W., Cho, K.Y. and Park, J.K. (2002) "Acoustic properties of nitrile butadiene rubber for underwater applications", Journal of Applied Polymer Science, 85, pp. 2764-2771.
- [22] Jung, K.I., Yoon, S.W., Sung, S.J. and Park, J.K. (2004) "Carbon black effect on the acoustic properties of nitrile butadiene rubber", Journal of Applied Polymer Science, 94, pp. 678-683.
- [23] Maekawa, Z. And Lord P. (1994) Environmental and Architectural Acoustic, Chapman and Hall, London, pp. 115.

- [24] LeninBabu, M.C. and Padmanabhan, C. (2010) "Noise control of a rectangular cavity using macro perforated po-roelastic materials", *Applied Acoustics*, 71, pp.418-430.
- [25] Arenas, J.P. and Crocker, M.J. (2010) "Recent trends in porous sound absorbing materials", *Sound & Vibration*, pp. 12-17.
- [26] Zhou, H., Li, B. And Huang, G. (2006) "Sound absorption characteristics of polymer microparticles", *Journal of Applied Polymer Science*, 101, pp. 2675-2679.
- [27] McRae, J.D., Naguib, H.E. and Atalla, N. (2010) "Mechanical and acoustic performance of compression molded open-cell polypropylene foams", *Journal of Applied Polymer Science*, 116, pp. 1106-1115.
- [28] Rodriguez-Perez, M.A., Alvarez-Lainez, M. And Saja, J.A. (2009) "Microstructure and physical properties of open-cell polyolefin foams", *Journal of Applied Polymer Science*, 114, pp. 1176-1186.
- [29] Lee, Y.E. and Joo, C.W. (2004) "Sound absorption properties of thermally bonded nonwovens based on composing fibers and production parameters", *Journal of Applied Polymer Science*, 92, pp. 2295-2302.
- [30] Yilmaz, N.D., Banks-Lee, P., Powell, N.B. and Michielsen, S. (2011) "Effects of porosity, fiber size, and layering sequence on sound absorption performance of needle-punched nonwovens", *Journal of Applied Polymer Science*, 121, pp. 3056-3069.
- [31] Long, M. (2006) *Architectural Acoustics*, Elsevier Inc., USA, pp. 249, 385.

- [32] Maekawa, Z. and Lord P. (1994) Environmental and Architectural Acoustic, Chapman and Hall, London, pp. 115-116.
- [33] Wirpsza, Z. (1993) Polyurethanes: Chemistry, Technology and Applications, Ellis Horwood Ltd., pp. 11-72.
- [34] Lee, S. and Randall, D. Editors (2002) The polyurethanes book, John Wiley & Sons, pp. 241-255.
- [35] Lee, S.T. editor (2000) Foam Extrusion: Principles and Practice, Technomic Publishing Company, Inc., pp.251-262.
- [36] University of Colorado, Chemistry and Biochemistry Department, (2011) Calculation of Theoretical Yield, available at:
<http://orgchem.colorado.edu/hndbksupport/labnb/theoryield.html> (Accessed: 20 September 2011).
- [37] Hepburn, C. (1982) Polyurethane Elastomers, Applied Science Publishers, pp.81-97.
- [38] Lee, S.T., Park, C.B. and Ramesh, N.S. (2007) Polymeric Foams: Technology and Science of polymeric foams, CRC Press, pp. 38-48, 60-72.
- [39] Parks, K.L. and Beckman, E.J. (1996) "Generation of Microcellular Polyurethane Foams via Polymerization in Carbon Dioxide. I: Phans Behavior of Polyurethane Precusors", Polymer Engineering and Science, 36, 19, 2404-2416.
- [40] Schildknecht, C.E. and Skeist, I. (1977), Polymerization Processes, Wiley, New York, pp. 642-647.

- [41] Ni, H., Yap, C.K. and Jin, Y. (2007) "Effect of curing moisture on the indentation force deflection of flexible polyurethane foam", *Journal of Applied Polymer Science*, 104, pp. 1679-1682.
- [42] Keeler, K. and Worthers, P. (2008) *Chemical Structure and Reactivity: an integrated approach*, Oxford: Oxford University Press, pp 409-415.
- [43] British Standards Institute (2001) *Acoustics- Determination of sound absorption coefficient and impedance in impedance tubes. Part 2: Transfer-function method. European Standard BS EN ISO 10534-2: 2010.*
- [44] International Standards Organization (1991) *ISO 9053: 1991. Acoustics - Materials for acoustical applications-Determination of airflow resistance.*
- [45] Leclaire, P., Umnova, O., Horoshenkov, K.V. and Maillet, L. (2003) "Porosity measurement by comparison of air volumes", *Review of Scientific Instruments*, vol. 74(3), pp.1366-1370.
- [46] Allard, J.F. and Champoux, Y. (1992) "New empirical equations for sound propagation in rigid frame fibrous materials" *J. Acoust. Soc. Am.*, 91(6), pp. 3346-3353.
- [47] Pispola, G., Horoshenkov, K.V. and Khan, A. (2007) Comparison of two modeling approaches for highly heterogeneous porous media, *J. Acoust. Soc. Am.*, 121(2), pp. 961-966.
- [48] Meyer Instruments Inc. Optimas version 5.2 Houston, US, available at: <http://www.meyerinst.com/html/optimas/optimas.htm> (Accessed: 24 July 2011).
- [49] Saunders, K.J.(1994) *Organic Polymer Chemistry*, 2nd ed., Blackie Academic & Professional., An Imprint of Chapman &Hall, pp 365-368.

- [50] Whittaker, A.G., Mount, A.R. and Heal, M.R. (2000) BIOS Instant Notes: Physical Chemistry, BIOS Scientific Publishers Limited, pp 136-141,
- [51] Rates of reaction – collision theory, available at:
<http://www.chemhume.co.uk/ASCHEM/Unit%203/14%20Reaction%20rates/Ratesc.htm> (Accessed: 26 July 2011).
- [52] Catalyst affects the rate of reaction, available at:
<http://cikguwong.blogspot.com/2011/02/chemistry-form-5-chapter-1-catalyst.html> (Accessed: 26 July 2011).
- [53] Khan, A., Horoshenkov, K.V. and Benkreira, H., A novel cold extrusion process for making vibro-acoustic products from recycled raw materials, 37th International Congress and Exposition on Noise Control Engineering, 26-29 October 2008, Shanghai, China.
- [54] Stinson, M.R. and Champoux, Y. (1992) "Propagation of sound and the assignment of shape factors in model porous materials having simple pore geometries", J. Acoust. Soc. Am., 91(2), pp. 685-695.
- [55] Attenborough, K. (1983) "Acoustical characteristics of rigid fibrous absorbents and granular materials", J. Acoust. Soc. Am., 73(3), pp. 785-799.
- [56] Attenborough, K. (1987) on the acoustic slow wave in air filled-granular media, J. Acoust. Soc. Am., 81(1), pp. 93-102.
- [57] Biot, M.A. (1956) Theory of propagation of elastic waves in a fluid-saturated porous solid. I. Low-frequency range, J. Acoust. Soc. Am., 28, pp. 168-178.

- [58] Biot, M.A. (1956) "Theory of propagation of elastic waves in a fluid-saturated porous solid. II. High-frequency range", J. Acoust. Soc. Am., 28, pp. 179-191.
- [59] Champoux, Y. and Stinson, M.R. (1992) "On acoustical models for sound propagation in rigid frame porous materials and influence of shape factor", J. Acoust. Soc. Am., 92(2), pp. 1120-1131.
- [60] Allard, J.F., Aknine, A. and Depollier, C. (1986) "Acoustical properties of partially reticulated foams with high and medium flow resistance" J. Acoust. Soc. Am., 79(6), pp. 1734-1740.
- [61] Allard, J.F., Bourdier, R. and Depollier, C. (1986) Biot waves in layered media, J. Appl. Phys., 60(6), pp. 1926-1929.
- [62] Allard, J.F., Depollier, C. and Rebillard, P. (1989) "Inhomogeneous Biot waves in layered media", J. Appl. Phys., 60(6), pp. 2278-2284.
- [63] Delany, M.E. and Bazley, N.E. (1970) "Acoustical properties of fibrous and absorbent materials, Applied Acoustics", 3, pp. 105-116.
- [64] Johnson, D.L., Koplik, J. And Dashen, R. (1987) "Theory of dynamic permeability and tortuosity in fluid-saturated pore media", J. Fluid. Mech., 176, pp. 379-402.
- [65] Champoux, Y. and Allard, J.F. (1991) "Dynamic tortuosity and bulk modulus in air-saturated porous media", J. Appl. Phys., 70(4), pp. 1975-1979.

- [66] Allard, J.F., Herzog, P., Lafarge, D. and Tamura, M. (1993) "Recent topics concerning the acoustics of fibrous and porous materials, *Applied Acoustics*, 39, pp. 3-21.
- [67] Horoshenkov, K.V., Attenborough, K. and Chandler-Wilde, S.N. (1998) "Pade approximants for the acoustical properties of rigid frame porous media with pore size distributions", *J. Acoust. Soc. Am.*, 104(3), pp. 1198-1209.
- [68] Horoshenkov, K.V. and Swift, M.J. (2001) "The acoustic properties of granular materials with pore size distribution close to log-normal", *J. Acoust. Soc. Am.*, 110(5), pp. 2371-2378.
- [69] Nelder, J. A. and Mead, R. (1965) "A simplex method for function minimization," *Computer Journal*, 7, 308-313.
- [70] Brouard, B., Lafarge, D. and Allard, J.F. (1995) "A general method of modeling sound propagation in layered media", *Journal of Sound and Vibration*, 183(1), pp.129-142.
- [71] Ingard, K.U. (1994) *Notes on Sound Absorption Technology*, Noise Control Foundation, USA.
- [72] Berryman, J. G. (1980) "Confirmation of Biot's theory," *Appl. Phys. Lett.* 37, pp. 382–384.
- [73] Brekhovskikh, L. M. (1973) *Waves in Layered Media*, Page 20, Nauka, Moscow, In Russian.
- [74] Khan, M.S. and Prasad, J. (2010) "Fly ash concrete subjected to thermal cyclic loads", *Fatigue Fract. Engng. Mater. Struct.*, 33, pp. 276-283.

- [75] Abe, H., Abe, I., Sato, K. and Naito, M. (2005) "Dry power processing of fibrous fumed silica compacts for thermal insulation", *J. Am. Ceram. Soc.*, 88(5), pp.1359-1361.
- [76] Harabi, A., Karboua, N. and Achour, S. (2011) "Effect of thickness and orientation of alumina fibrous thermal insulation on microwave heating in a modified domestic 2.45 GHz multi-mode cavity", *Int. J. Ceram. Technol.* pp. 1-9.
- [77] Ye, Z., Wells, M., Carrington, C.G. and Hewitt, N.J. (2006) "Thermal conductivity of and wool wool-hemp insulation", *Int. J. Energy Res.*, 30, pp. 37-49.
- [78] Wu, H., Fan, J. and Du, N. (2007) "Thermal energy transport within porous polymer materials: effects of fiber characteristics", *Journal of Applied Polymer Science*, 106, pp. 567-583.
- [79] Sureshkumar, M.S., Bhuvaneshwari, C.M., Kakade, S.D. and Gupta, M. (2008) "Studied on the properties of EPDM-CSE blend containing HTPB for case-bonded solid rocket motor insulation", *Polym. Adv. Technol.*, 19, pp. 144-150.
- [80] Hirschler, M.M. (2008) "Polyurethane foam and fire safety", *Polym. Adv. Technol.*, 19, pp. 521-529.
- [81] Bohm, B. and Kristjansson, H. (2005) "Single, twin and triple buried heating pipes: on potential savings in heat losses and costs", *Int. J. Energy Res.*, 29, pp. 1301-1312.

- [82] Koo, M.S., Chung, K. and Youn, J.R. (2001) "Reaction injection molding of polyurethane foam for improved thermal insulation, *Polymer Engineering and Science*, 41(7), pp. 1177-1186.
- [83] Gibson, L.J. and Ashby, M.F. (1988) *Cellular Solids: structure & properties*, Pergamon Press, Inc., Oxford, pp. 201-211.
- [84] Taine, J. and Petit, J.P. (1993) *Heat Transfer*, Prentice Hall, pp.3-24.
- [85] Holman, J.P. (1997) *Heat Transfer*, 8th edition, McGraw-Hill Companies, pp. 1-14, 338-341.
- [86] Zemansky, M. (1997) *Heat and Thermodynamics*, 4th edition, McGraw-Hill Companies, pp. 80-110.
- [87] British Standards Institute (1992) *British Standard (method 1902-508): Methods of testing Refractory materials, Part 5: Refractory and thermal properties: Section 5.8 Determination of thermal conductivity (split column method)*.
- [88] Ting, S.W. (2007) *Recycled carpet materials in application of noise, vibration and thermal insulation*. MPhil Thesis, University of Bradford.
- [89] Asdrubali, F. and D'Alessandro F. (2011) "*Impact sound insulation and viscoelastic properties of resilient materials made from recycled tyre granules*", *International Journal of Acoustic and Vibration*, 16(3), pp. 119-125.

APPENDIX A

List of Publications

1. Khan, A., Horoshenkov, K.V., Benkreira, H. and Mahasaranon, S., Tailoring of poro-elastic products from granular plastic and rubber waste using the cold extrusion technology, Euro Noise 2009, 26-28 October 2009, Edinburgh, UK.
2. Khan, A., Horoshenkov, K.V., Benkreira, H. and Mahasaranon, S., The use of stratification to improve the absorption of porous materials, Inter Noise 2010, 13-16 June 2010, Portugal.
3. Mahasaranon, S., Horoshenkov, K.V., Benkreira, H. and Khan, A., Acoustic Porous Materials Based on Polyurethane Foam and Granulated Tyre Waste, 2nd International Symposium-Frontiers in Polymer Science 2011, 29-31 May 2011, Lyon, France.
4. Benkreira, H., Khan, A., Horoshenkov, K.V. and Mahasaranon, S., Up-cycling of elastomeric waste residues into acoustic and thermal insulation, The Polymer Processing Society 27th Annual Meeting-PPS27, Marrakech, Morocco.
5. Mahasaranon, S., Horoshenkov, K.V., Khan, A. and Benkreira, H., The use of stratification to optimise the sound absorption of porous materials, Symposium on the acoustics of poro-elastic materials, 14-16 December 2011, Ferrara, Italy, (submitted)
6. Mahasaranon, S., Horoshenkov, K.V., Khan, A. and Benkreira, H., The effect of pore stratification on the acoustic absorption in open cell foams, Journal of Applied Physics, (submitted)

7. Geslain, A., Groby, J.P., Dazel, O., Mahasaranon, S., Horoshenkov, K.V, and Khan, A., Propagation of acoustic wave in one-dimensional macroscopically inhomogeneous porous material under the rigid frame approximation, Journal of the Acoustical Society of America, (submitted)

APPENDIX B

Average and standard deviation of absorption coefficient spectra of the porous materials produced by variable components in foaming production (studied in chapter 3)

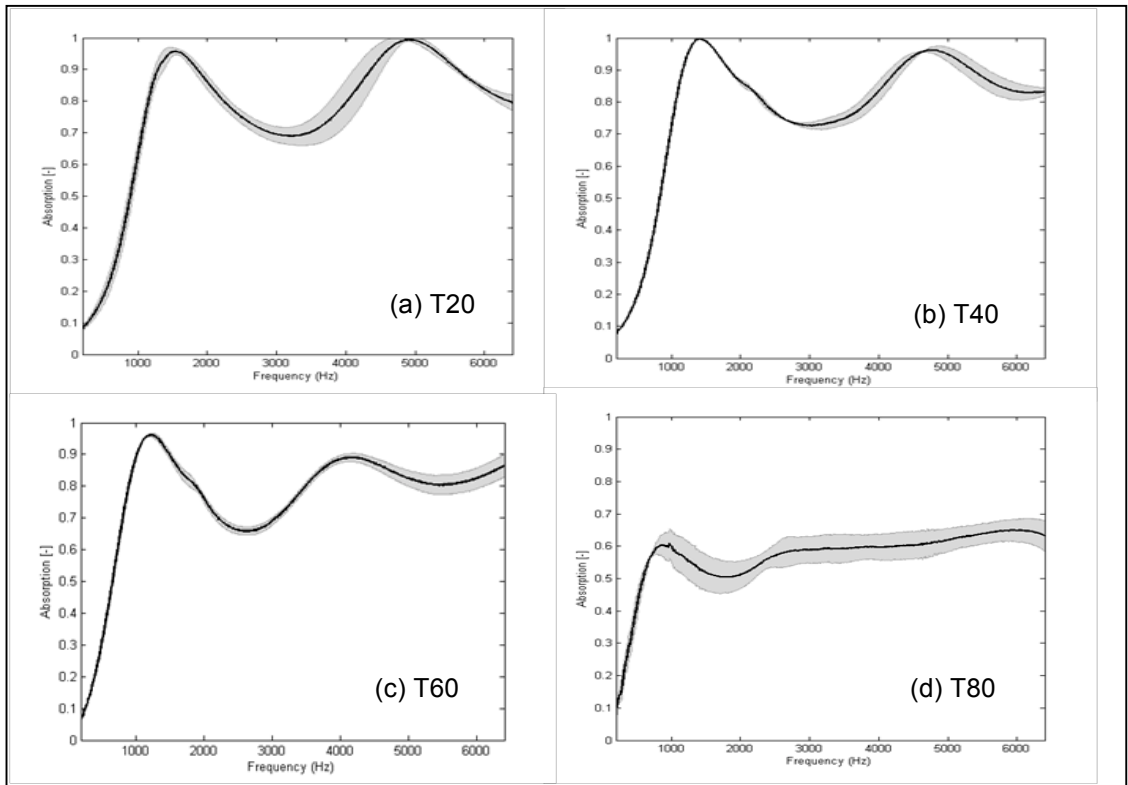


Figure B.1 Absorption coefficient spectra for the porous materials produced by the variable tyre shred residue; (a) 20%, (b) 40%, (c) 60% and (d) 80%

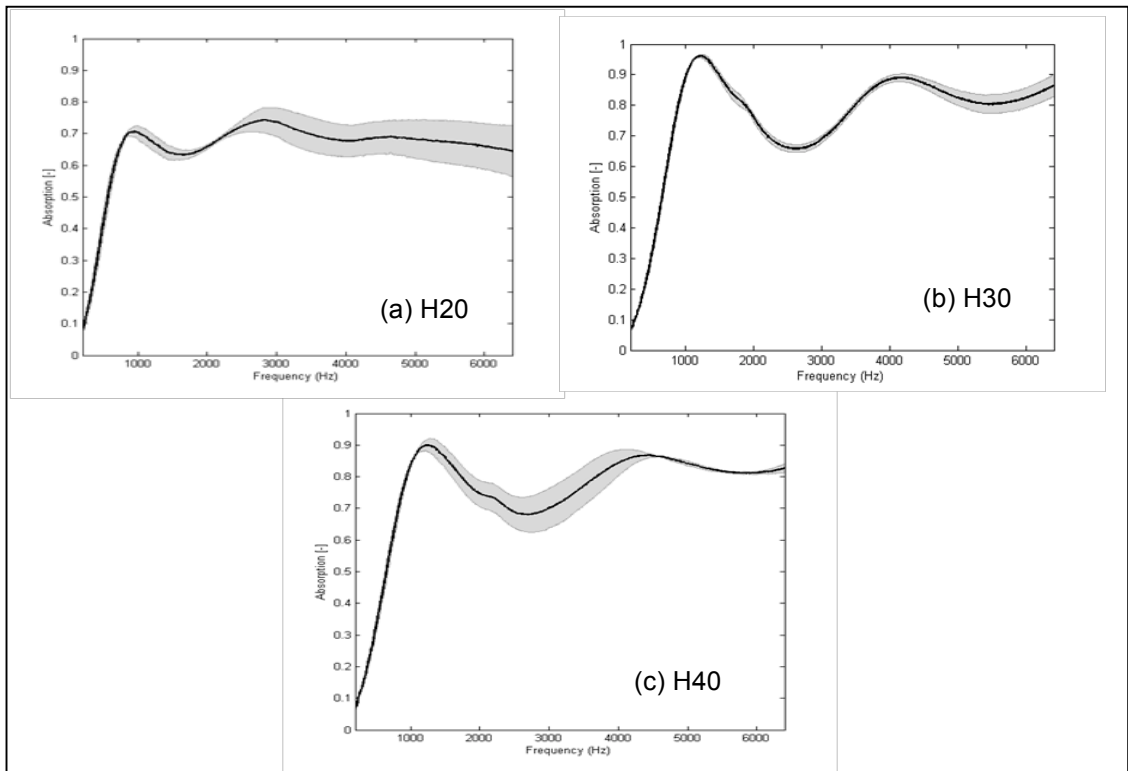


Figure B.2 Absorption coefficient spectra for the porous materials produced by the variable water; (a) 20%, (b) 30% and (c) 40%

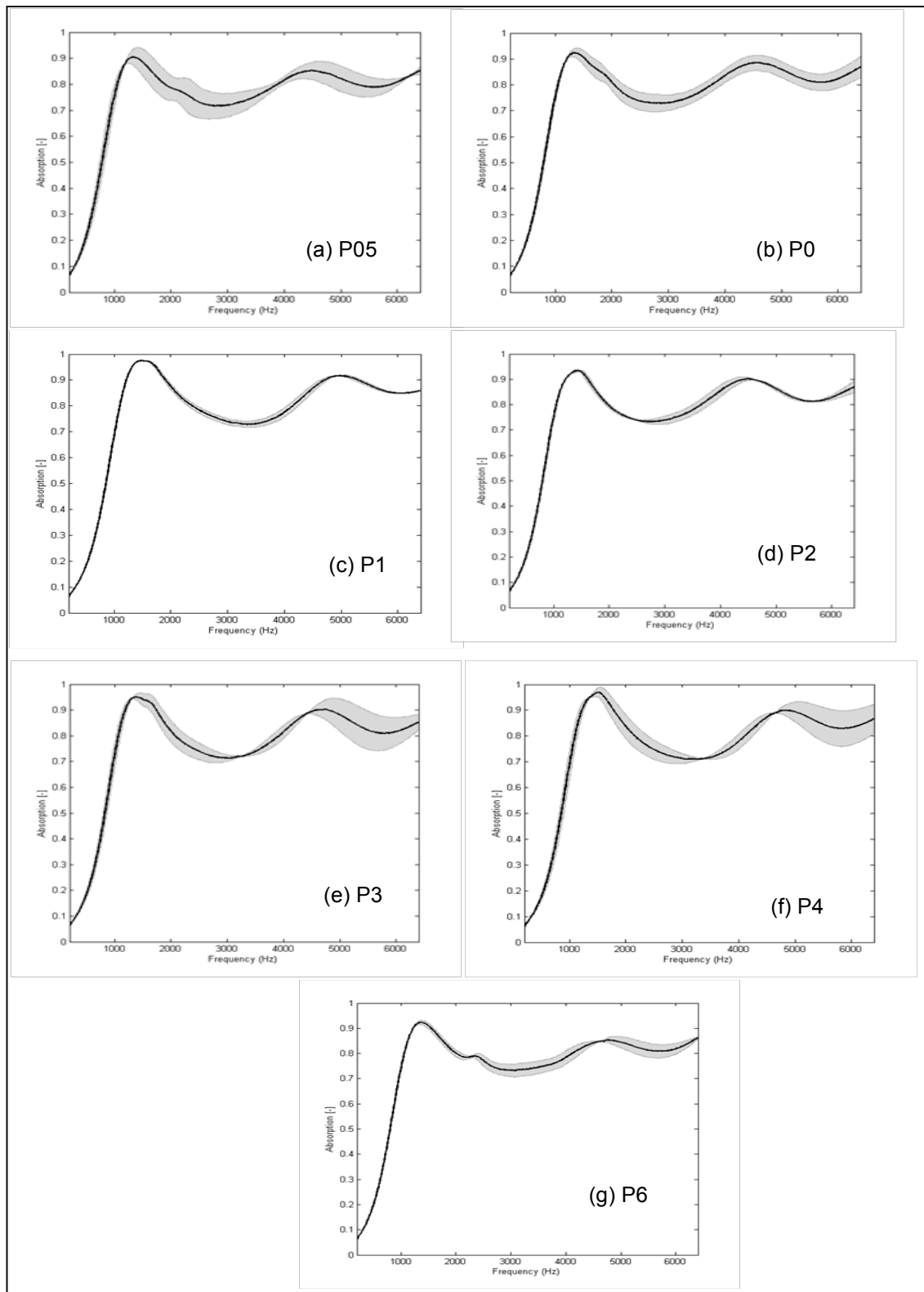


Figure B.3 Absorption coefficient spectra for the porous materials produced by tyre shred residue sieved having the different particle size followed on hole of screen capture (mm); (a) no sieve, (b) <0.5, (c) 1.0, (d) 2.0, (e) 3.35, (f) 4.0 and (g) > 6.67

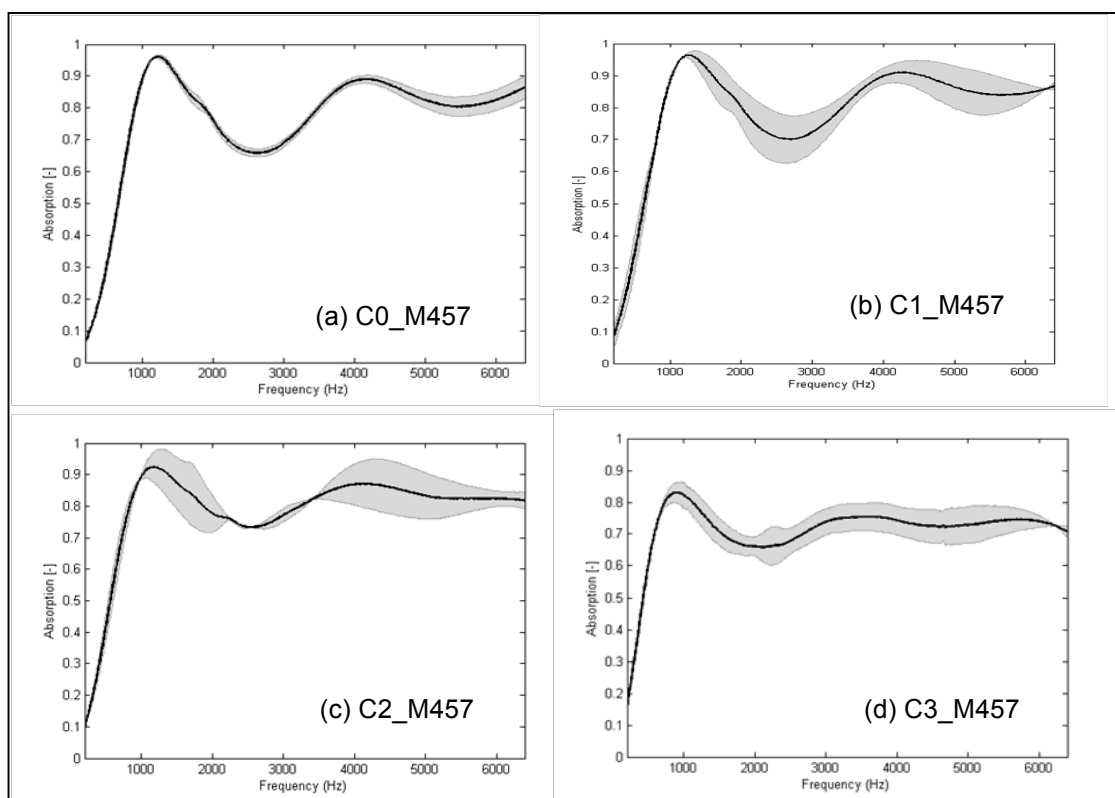


Figure B.4 Absorption coefficient spectra for the porous materials produced by polyurethane binder (Flexilon 457) and the variable catalyst; (a) 0%, (b) 1%, (c) 2% and (d) 3%

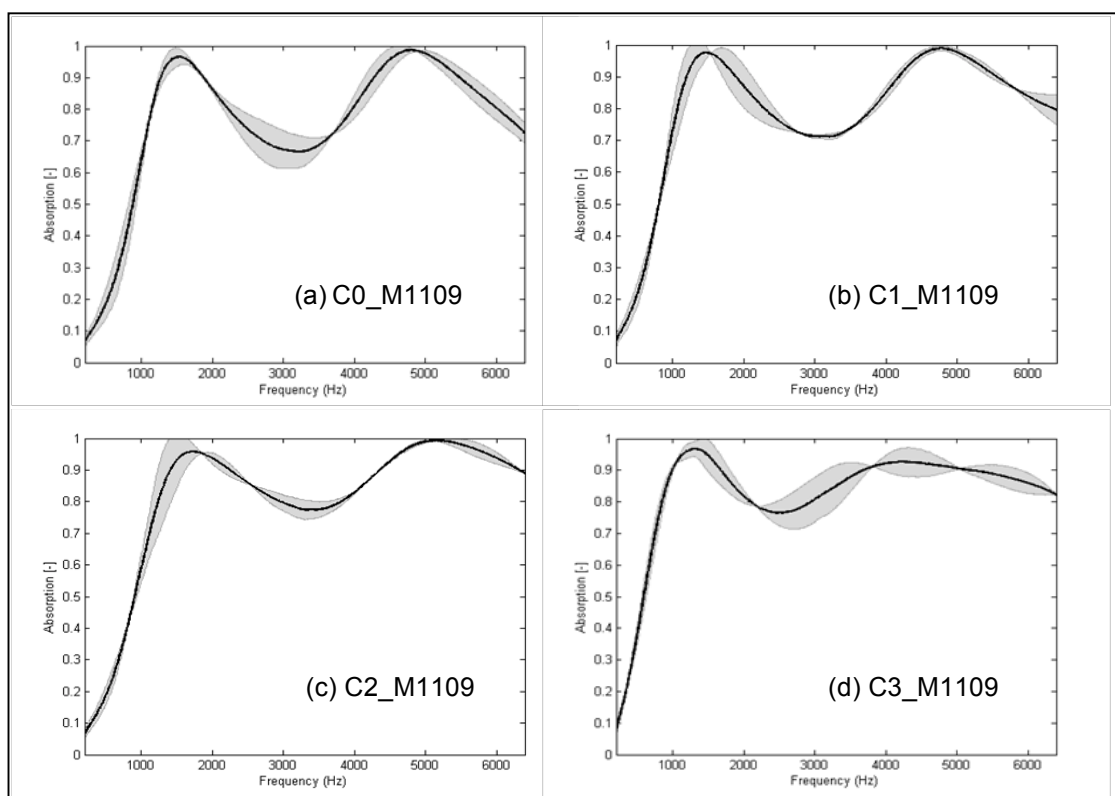


Figure B.5 Absorption coefficient spectra for the porous materials produced by polyurethane binder (Flexilon 1109) and the variable catalyst; (a) 0%, (b) 1%, (c) 2% and (d) 3%

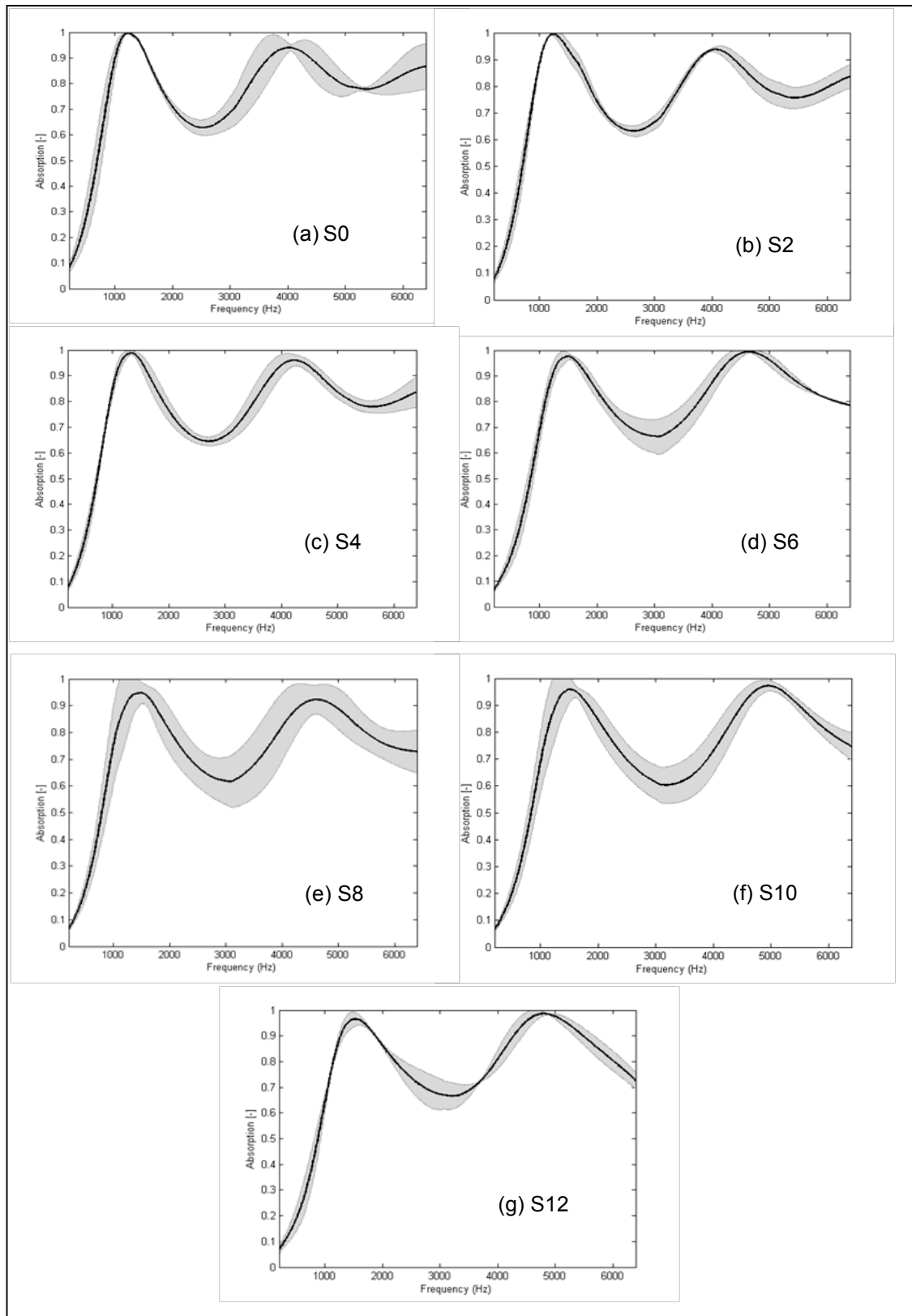


Figure B.6 Absorption coefficient spectra for the porous materials produced by the variable surfactant; (a) 0%, (b) 2%, (c) 4%, (d) 6%, (e) 8%, (f) 10% and (g) 12%

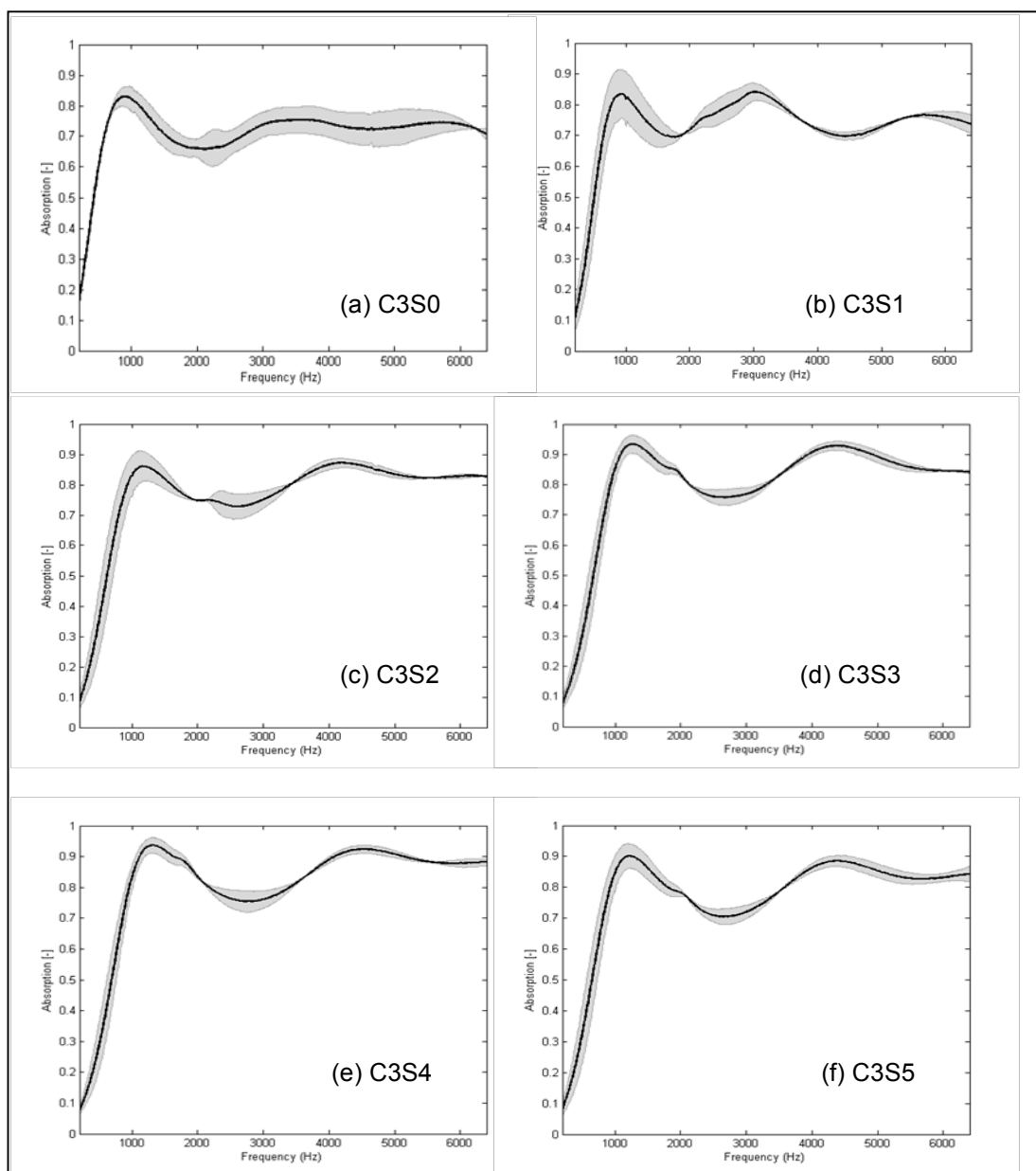


Figure B.7 Absorption coefficient spectra for the porous materials produced by the variable surfactant at 3% catalyst; (a) 0%, (b) 1%, (c) 2%, (d) 3%, (e) 4% and (f) 5%